APPLICATION OF LIGHT SCATTERING AND COMPUTATIONAL TECHNIQUES FOR INVESTIGATION OF MORPHOLOGICAL PROPERTIES OF SMALL PARTICLES USING A DESIGNED AND FABRICATED LASER BASED SETUP

A thesis submitted in partial fulfillment of the
requirements for award of the degree of
Doctor of Philosophy

Sanchita Roy

Regn. No. 010 of 2011

School of Science and Technology
Department of Physics
Tezpur University

December, 2011

Application of light scattering and computational techniques for investigation of morphological properties of small particles using a designed and fabricated laser based setup

Abstract

Light scattering is one of the most powerful techniques for probing the properties of small particles, in various scientific disciplines. These particles may be aerosols, cloud particles, dust particles, etc. of different origin, and are normally suspended in the atmosphere, but may also be present in other types of media. An understanding of light scattering behavior of isolated spherical or non-spherical particles, where the particles range from nanometer to micrometer size, are a vital requirement for investigating various physical characteristics (such as size, shape, refractive index etc.) and developing applications which depend on light scattering. Some of the processes and applications are optical diagnostics of industrial aerosols and combustion, applications in remote sensing with light detection and ranging (*Lidar*) systems, environmental issues like visibility and haze, astrophysical issues such as effect of interstellar dust on propagation of stellar radiation and applications in the area of Nano-science and Nano-technology etc. Knowledge of aerosol optical properties assumes significant importance in the wake of studies strongly correlating airborne particulate matter with adverse health effects.

An exact way to characterize the scattering properties is to consider how the brightness and polarization of scattering depend on the wavelength λ, of incident light and the geometry of observations (characterized mainly by the phase angle). For example, total intensity and polarization response are linked to the respective shape and size of scatterers. The properties of light

scattered by such particles or from a volume element containing aggregate of such particles depend on different parameters like:

i. size and dispersion of size of particles
ii. shape and dispersion of shape of particles
iii. density of particles in a unit volume
iv. structure of aggregates which may be fluffy, fractal, dense etc.
v. optical properties like permittivity, absorption, isotropy etc.
vi. quality of particle surfaces like smoothness, roughness, porosity, etc.

The scattering properties of small particulate matter are determined not only by their own and the medium's refractive indices but also by state of polarization of the incident light. The angular scattering dependency of small particles is very important because it helps for better understanding of radiation transfer through the medium containing the scatterer.

This field has become a subject of deep interest with its ever expanding importance as documented by the current research topics and increasing number of publications. Moreover, there are thousands of aerosols and other particulate matter which are of importance and yet to be studied. Light scattered by small particles can either be computed or measured in the laboratory. This subject is actively being pursued, especially for non-spherical particles. Optical measurements of small particulate matter in the laboratory are an important source for retrieval of information on light scattering since it is a non-destructive technique. The invention of laser made such studies feasible, so that detection and characterization of such particles can be done to a high level of accuracy. In 1950, Kerker and V.K.L Mer developed a method where they showed that by using either the polarization ratio or the phase angle of the scattered light as a function of scattering angle, they could determine information about the size of the particle. Ever since, other workers have continued with their efforts to design improved light scattering

instruments for better experimental observation of scattered light and calculate the scattering matrix elements with greater accuracy. On the other hand, using the existing theories on electromagnetic radiation or light scattering theories, theoretical predictions of the expected scattering patterns can be made by using assumed trial values of some important parameters of characteristic properties of such particles. In this regard, computer simulations using trial values and existing light scattering theories, have produced appreciable results. With the development of more sophisticated lasers and instruments for detection of scattered light, laser based characterization of particulate matter has become an area of very active research. Again, the fast development of computer hardware and software has made it possible to have faster data acquisition and do analysis of scattering patterns of particles with different morphological characteristics.

The subject of light scattering is mainly governed by Maxwell's electromagnetic theory of light. There are various theoretical approaches which involves computational techniques to explain the experimentally observed light scattering pattern of small particles. These theories can be divided into volume-based theories, such as the integral equation and differential equation methods, and surface-based theories. Well known integral equation methods are the discrete dipole approximation (DDA) and the volume integral equation method (VIEM). One useful differential equation method is the finite difference time domain method (FDTD). Among surface based theories, both Mie theory and Waterman's T-matrix method provide solutions of Maxwell's equations on the boundary conditions of the scattering objects. While Mie theory provides closed solutions for spherical particles in a plane wave field, T-matrix method supplies numerical solutions for non-spherical, but most often rotationally symmetric particles. The crucial advantage of the T-matrix, relating the scattered and incident field coefficients, is that it can be computed very fast and in an easy manner.

The widely used Mie theory and T-matrix theory treats exactly the scattering of electromagnetic radiation by small particles and yields angular intensity distribution of scattered light and also the scattering and extinction coefficients. It takes into account the change of polarization state of the scattered light when light of some particular state of polarization is incident on a medium. The polarization state of the scattered light is related to the polarization state of the incident light by a 4x4 matrix. This matrix, frequently called the Mueller matrix and is a characteristic of the medium.

The sixteen elements of the matrix are each functions of the scattering angle. In almost all practical cases, symmetry reduces the number of elements in the scattering matrix. For a system of randomly oriented particles, the number of independent parameters reduces to ten, and for spherical particles, for the general scattering matrix it reduces to four.

To describe polarization states of scattered light, the formalism is based on the Stokes vector. The Mueller scattering matrix describes the relation between incident and scattered Stokes parameters if the individual particles have spherical symmetry.

Again, computer simulation has become an important tool nowadays, which enables one to predict the behavior of complex systems which is otherwise not possible to calculate analytically. Simulation is a powerful technique that involves modeling, computer- programming and statistics for solving a wide variety of problems. Computer simulation of experiments provide better insight into the experiments done in laboratory, besides being relatively inexpensive, faster and easier method for performing an experiment on the computer. Moreover, for systems which involve thousands and thousands of variables, the complications caused by uncertainty are also very large. Thus, for such problems simulation becomes an essential tool for many researchers. It is worth mentioning that an approach that many workers have been pursuing to understand the phenomenon of light scattering better, is to

use computational models that simulate light propagation in scattering media. They used Monte Carlo algorithms that were based on the Stokes-Mueller formalism. The Monte Carlo method is used for simulating the light scattering patterns of small particles when illuminated with some source of light, for example, laser light. Using any of the theories of light scattering, Monte Carlo method simulates the elements of the Mueller matrix for any given particle or scattering volume element, which can then be plotted to yield the respective scattering patterns. In the recent years, various research groups have implemented Monte Carlo simulation in various computer languages. This technique has been used in many applications including diagnostic and therapeutic applications and atmospheric sciences. This simulation technique proved to be a very successful tool in verifying the experimental observations obtained by use of the different investigating instruments, as well as lending support and improving the current theoretical models, like Mie theory and T-matrix approach, for interpreting scattering phenomenon.

Despite such advanced numerical techniques being available, the results of laboratory and *in situ* experiments do not completely fit with the existing techniques, especially for particles with complicated morphology. This is because of the limitations of such theories when applied to complex particles, and to some extent because of the imprecisions that may be present in the experimental setup. Combined efforts on improving and developing computation and experimentation can produce better results. Thus, an attempt was made to improve computation and instrumentation for light scattering investigations of small particles. In fact, this attempt is the basis of this thesis.

We have designed and fabricated a laser based laboratory light scattering instrument. The system uses a photomultiplier tube detector (H 5784-20, Hamamatsu, Japan) and can be operated at three different wavelengths, 632.8nm, 594.5nm and 543.5nm respectively. The sources were used alternatively for studying the scattering properties as a function of the

scattering angle. The instrument was designed to carry out light scattering investigations of both natural and artificial small particulate matter to account for recording the volume scattering function $\beta(\theta)$ (which equals S_{11}) and linear polarization ratio, $P(\theta)$ (which equals $-S_{12}/S_{11}$). The instrument could be used to measure scattered light signals from an angle of 10° to 170° for θ (polar angle), and from 10° to 60° for φ (azimuthal angle). The influence of φ is noticeable only for aligned particles.

Light scattered from samples passes through optical components comprising of appropriate analyzers, and is sensed by the PMT detector. The signals are interfaced to a dedicated data acquisition system to store the recorded data. The data obtained from the experimental setup is then compared with the theoretical predictions based on established theories like Mie theory and T-matrix theory. The performance of any light scattering setup is evaluated by conducting experiments on perfectly spherical particles and then comparing the results with the theoretical Mie calculations.

Test measurements were made on Polystyrene latex spheres at three different wavelengths followed by comparison with Mie calculations for such spherical particles to ensure the accuracy and reliability of the setup. The results of measured $\beta(\theta)$ and $P(\theta)$ for these particles validated that the setup is efficient and reliable for performing light scattering investigations on small particulate matter. Thus, extensive experiments were performed on other particles also.

Some of the particles investigated using the setup are semiconductor particles (in the form of micron-sized and nanoparticles) like CdS and ZnSe, particles like Titania (TiO_2) and ZnO, and also biological particles like *Camellia sinensis* dust (tea dust), bacteria like *Mycobacterium smegmatis* and *Staphylococcus aureus*. As a mathematical and numerical basis for the analysis of observed data from experiments performed on the above mentioned particles, Mie theory and T-matrix theory were used. These theories are often

used for solving light scattering problems for homogeneous and composite particles having sizes not too large when compared to the wavelength of incident light. Light scattering investigations on all the particles showed very interesting results, especially for the biological particles. For characterizing size as well as morphology of the particles under investigation, we also used various analytical techniques such as Transmission electron microscopy (TEM) and Scanning electron microscopy (SEM). Energy dispersive X-Ray analysis (EDS) was also performed for composition analysis of some samples of special interest. The detailed results and discussions about quantification of light scattering measurements on all these particles are presented in this thesis.

Again, a simulation program *simscat.c,* was developed to simulate both the scattering phase function and the degree of linear polarization. The program was based on Monte Carlo code and developed in standard C-language. Simulation of propagation and scattering of the laser light, after interaction with small particles were done for better understanding of the physical processes and verification of experimental results. The technique is used to calculate volume scattering phase function $\beta(\theta)$ and linear polarization ratio $P(\theta)$. The closeness of agreement or disagreement between these results of all the simulated particles is discussed extensively in this thesis. Details of the source code of the program *simscat.c* and the results obtained for different particles by using this program, is a significant part of this thesis.

The thesis is explicitly divided into six chapters. The background and motivation of our research work is contained in the introductory Chapter- 1. Chapter- 2 presents an overview of the established theories like Mie theory and T-matrix theory and its significant role in light scattering studies. The details of design considerations and fabrication of the laser based light scattering system and instrumentation is presented in Chapter- 3. Investigations, measurements and results by using the light scattering

instrument on different particulate matter are presented in Chapter- 4. In Chapter- 5, details about Monte Carlo simulation technique used for light scattering analysis of various small particulate systems are presented. The concluding Chapter- 7 highlights on the summary of the whole work and future prospectives of light scattering studies.

DECLARATION

I hereby declare that the thesis entitled "**Application of light scattering and computational techniques for investigation of morphological properties of small particles using a designed and fabricated laser based setup**" being submitted to the School of Science and Technology, Tezpur University, Tezpur, Assam in partial fulfillment for the award of the degree of Doctor of Philosophy in Physics is a record of original research work carried out by me. Any text, figures, theories, results or designs that are not of own devising are appropriately referenced in order to give credit to the original author(s). I also declare that neither this work as a whole nor a part has been submitted to any other University or institute for any degree, diploma, associateship, fellowship or any other similar title or recognition.

Date: 26.12.2011

Place: Tezpur

(Sanchita Roy)
School of Science and Technology
Department of Physics
Tezpur University, Napaam
Assam-784028, India

Tezpur University

CERTIFICATE

This is to certify that the thesis entitled "**Application of light scattering and computational techniques for investigation of morphological properties of small particles using a designed and fabricated laser based setup**" submitted to the School of Science and Technology, Tezpur University in partial fulfillment for the award of the degree of Doctor of Philosophy in Physics is a record of research work carried out by **Ms. Sanchita Roy** under my supervision and guidance.

All helps received by her from various sources have been duly acknowledged.

No part of this thesis has been submitted elsewhere for award of any other degree.

(Dr. G. A. Ahmed)
Supervisor, Associate Professor
School of Science and Technology
Department of Physics
Tezpur University, Tezpur

Date : 26 - 12 - 2011
Place: Tezpur, Assam, India

I would like to dedicate this work to

My parents

Smt. Manjusree Roy

and

Sri Bhupendra Chandra Roy

Acknowledgements

First and foremost I would like to express my sincere gratitude to my Ph.D. supervisor Dr. Gazi A. Ahmed, Associate Professor, Department of Physics, Tezpur University for his dynamic and scrupulous supervision that I have received throughout the endeavor of my Ph. D. work at Tezpur University. He was always there with stimulating discussions and new suggestions, and also willing to let things develop in unexpected ways. His ongoing confidence in me helped me to accomplish this work.

I want to convey my sincere thanks to Prof. A. Choudhury, Prof. A. Kumar, Prof. J. K. Sarma, Dr. N. S. Bhattacharyya, Dr. N. Das, Dr. D. Mohanta, Dr. P. Deb, Dr. M. K. Das, Dr. A. Pathak and Dr. K. Baruah of Dept. of Physics, Tezpur University for their encouragement, criticism and inspiration to carry out this work. I would like to thank Prof. Alak K. Buragohain and Nilakshi Barua of Dept. of Molecular Biology and Bio-technology, Tezpur University for their fruitful discussions and valuable suggestions during my Ph. D. work. I would also like to thank Mr. Ratan Baruah, Mr. Jayanta Bora and Mr. Pradyumna K. Choudhury of Tezpur University for rendering help in different types of microscopic and other analysis techniques.

I would like to thank all my seniors, juniors, colleagues and friends of Tezpur University who have supported me during my research work, specially, Ankur, Mayuri, Nayanmoni, Nomita, Rupjyoti, Meenakshi, Durga da, Isha, Sovan, Ranjan, Vishal, Gautam and Rajib.

Special thanks go to the members of "Researchhelp Google Group for their help in providing research articles related to my Ph. D. work.

I acknowledge the help extended by Mr. Ajanta Pathak, Mr. Umesh Patir, Mr. Narayan Sarma and Mr. Prakash Kurmi in official works.

I am indebted to my parents, my brother Jintu and my sister Sumi for their love, constant encouragement, support and inspiration.

I wholeheartedly acknowledge and extend my sincere thanks to my husband Simanta for his cooperation and support at all times. I owe great debt to him for the pain and sacrifice in dealing family responsibilities during my absence. I must admit the sacrifice and support of my daughter Upashrita (Mamti) too, who managed herself in different difficult times even without my presence near her. She has enriched my life beyond measure.

I offer my love to my niece Anishka, Banisha and nephew Leon. I sincerely acknowledge the support of my sister-in-law Ritika and brother-in-law Avinash. I would also like to thank my mother-in-law, Dipankarda, Mainubou, Matuba and Rubalda.

I am thankful to Saswati Mashi and Rana Mesho, uncle and aunt Purabi and Alok Bhattacharjee, uncle Timir Chakrabortty, my school teachers of K. V. Duliajan, specially, Mrs. Ena Borbora and Sri R. L. Singh, for their encouragement and blessings. I thank my family friends with special mention of Mamon and Ankur Chakrabarty, and Arup K. Borgohain.

I thank my bosom friend Anupama Chakrabarty for her never ending support, encouragement and inspiring words.

My deepest gratitude goes to Dr. Sanjeev Kr. Bhattacharyya who always came up with a solution in my times of doubt. His valuable suggestions were very much beneficial for completion of this work. I specially thank him for the consistent help and support rendered even in his busy schedule and despite being not near.

I take the opportunity to thank Tezpur University for providing me the research facility and the University community for helping me in carrying out my research work. I acknowledge the help extended by the Central Library staff of Tezpur University.

Finally, I would like to sincerely acknowledge the financial support received from the Department of Science and Technology, Ministry of Science and Technology, Government of India, New Delhi, for the project grant (Sanction No. SR/WOS-A/PS-20/2007, dated-04/08/2008) under the Women Scientist-A Scheme.

Date: 26.12.2011

Sanchita Roy

(Sanchita Roy)

CONTENTS

Abstract		i
Declaration		ix
Certificate		x
Acknowledgements		xi
Contents		xv
List of Tables		xix
List of figures		xx

Chapter I

Introduction to Laser Based Light Scattering System

1.0	General Introduction	1
1.1	Light Scattering theories	3
1.2	Light scattering by small particles: a perspective	14
1.3	Motivation and Objectives	23
1.4	Instruments for light scattering studies	26
1.5	Introduction to the presented work	33

Chapter II

Theory of Extinction and Scattering

2.0	General Introduction	35
2.1	Maxwell equations and its importance	36
2.2	Scattering matrix and scattering coefficients	38
2.3	Extinction, Absorption and Scattering: An overview	52
2.4	Mie theory	56
2.5	T-matrix method	67

Chapter III

Design considerations of the laser based light scattering system and instrumentation

3.0		General Introduction	75
3.1		Light scattering setup	78
3.2		He- Ne Laser source	82
3.3		Simulation Chamber	83
3.4		Delivering and Collection Optics	83
3.5		Photodetector units	84
	3.5.1	Photomultiplier tube power supply	90
	3.5.2	Sensitivity Adjustment of the photomultiplier tube	91
3.6		Photomultiplier tube rotating unit	91
	3.6.1	Driver circuit of the stepper motor	93
	3.6.2	Power supply for stepper motor	94
	3.6.3	The C program for generating sequence for driving stepper motor	95
3.7		Scattering Sample	96
	3.7.1	Refractive index matching basin and Sample cell (for sample in a liquid suspension)	97
	3.7.2	Sample holder for particles embedded in a matrix medium	97
3.8		Computer interfacing and data acquisition system	98
	3.8.1	Data acquisition system- Type I	98
	3.8.2	Data acquisition system- Type II General Description and Installation	106
3.9		Data Reduction Procedure	122
	3.9.1	Data reduction for sample in suspension.	122
	3.9.2	Data reduction for sample embedded in matrix medium.	129
3.10		Validation of the Light scattering setup	130
3.11		Data Processing	139

CHAPTER IV

Investigations and Results with Light Scattering System

4.0		General Introduction	140
4.1		Overview of investigations made on different samples	140
4.2		Cadmium Sulphide (CdS)	141
4.3		Zinc Selenide (ZnSe)	150
4.4		Titanium dioxide (TiO_2) or Titania	159
4.5		Zinc oxide (ZnO)	166
4.6		*Staphylococcus aureus*	173
4.7		*Camellia Sinensis (Tea)* dust and *Mycobacterium smegmatis*	181
	4.7.1	Sample preparation and Antimycobacterial Assay of *Camellia Sinensis* dust particles	184
4.8		Error Analysis	197
4.9		Comparison with reported work	200

CHAPTER V

Simulation of Light scattering

5.0		General Introduction	202
5.1		Monte Carlo Simulation of Light scattering	203
5.2		An original Monte Carlo technique	205
	5.2.1	Sampling Random Variables	206
	5.2.2	Programming method	208
	5.2.3	Flowchart for Monte Carlo simulation	209
5.3		Computation Results and comparison with Experimental Results	211
	5.3.1	Simulation of CdS	211
	5.3.2	Simulation of *Staphylococcus aureus*	213
	5.3.3	Simulation of ZnSe	215
5.4		Conclusion	218

CHAPTER VI
Conclusion and Future Prospects 219

References 224

List of publications 257

CHAPTER I

Introduction to Laser Based Light Scattering System

1.0 General Introduction

Light is scattered by almost all objects in the known Universe. Hence, process of light scattering and its applications is a very important area of study and research. It is important to understand the mechanism and effects of interaction between light and matter.

The way in which light is scattered by an obstacle is governed by its physical properties, therefore, in principle, it is possible to extract some or all information about the scatterer by analyzing the scattered light. This technique of extracting information about objects by observing and analyzing the light that is scattered by the objects is called the light scattering technique. The light scattering technique has been used to infer information about the size, shape, refractive index etc. of different types of particles in various scientific disciplines. The technique finds great importance in scientific disciplines like atmospheric science, astronomy, oceanography, radar meteorology, colloidal chemistry, biophysics, geology, remote sensing, light detection and ranging (lidar) systems, environmental monitoring like visibility and haze, climate modeling, ocean optics, astrophysical issues, and nanoscience issues which are currently hot topics in science and technology. Areas of interest mostly hold for colloids, aerosols, hydrosols, bio-particles, macromolecules, astrophysical particles etc. [1 - 24, 263 - 267]. Many instruments based on this technique have been developed and used for characterizing such particles, spherical and non-spherical, ranging in size from nanometers to micrometers [2, 25 - 33]. As it is a non-destructive technique, it is very useful for routine measurements on such particles, especially the atmospheric, astrophysical and bio-particles, which are not

easily accessible otherwise by other techniques [34 - 42]. This makes light scattering technique a vital diagnostic tool.

The scattering of light may be thought of as the redirection of light that takes place when an electromagnetic (EM) wave (i.e. an incident light ray) encounters an obstacle or non-uniformity which is the scattering particle in this case (figure 1.1). When an EM wave is incident upon a particle, it interacts with the particle, and the electrons orbiting within the particle's constituent atoms and molecules, especially on the surfaces of the particle. The electrons are perturbed periodically with the same frequency (υ_0) as the electric field of the incident wave [43]. Fractional energy of these excited charges is reradiated in all directions as electromagnetic energy and results in secondary radiation which is the *scattered light*, and some of the energy contributes to the internal energy of the system, called *absorption*. Almost all the light scattered by the particle is emitted with same frequency (υ_0) of the incident light, a process referred to as elastic scattering. In general, scattering may be defined as:

Scattering= Excitation + Reradiation

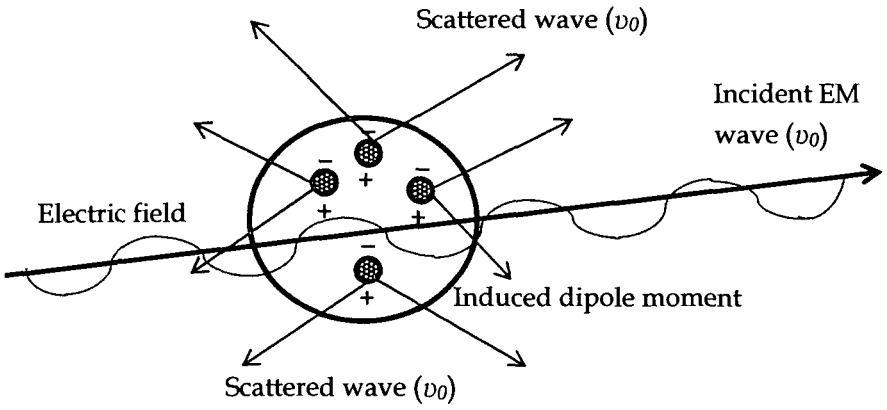

Figure 1.1: Light scattering by an induced dipole moment.

Both scattering and absorption remove energy from a beam of light traversing the medium leading to attenuation of the beam. This attenuation is called *extinction*. We may define extinction as:

Extinction= Scattering + Absorption

The scattering is said to be elastic or coherent if the scattered light has same frequency with that of the incident light. Rayleigh scattering, Mie scattering are examples of elastic scattering. In the inelastic scattering the frequency of the scattered light is different from that of the incident light frequency. Raman scattering, on the other hand is an example of inelastic scatterings.

1.1 Light Scattering theories

Maxwell's equations are the basis of theoretical analysis and computational methods describing light scattering. Exact solutions to Maxwell's equations are only known for selected geometries, such as spherical particles. Light scattering by particles is a branch of computational electromagnetics dealing with electromagnetic radiation scattering and absorption by particles. In case of geometries for which analytical solutions are known (such as spheres, cluster of spheres, infinite cylinders), the solutions are typically calculated in terms of infinite series. In case of more complex geometries and for inhomogeneous particles, the original Maxwell's equations are discretized and solved. Multiple-scattering effects of light scattering by particles are treated by radiative transfer techniques (RTE)[44] .

If light traverses in perfectly homogenous medium, it is not scattered. Only inhomogeneities cause scattering. Scattering is usually divided into two types: single scattering and multiple scattering [45 - 49]. In single scattering, the number of particles in a scattering medium is sufficiently small and their separation is sufficiently large compared to the wavelength of the incident light. That is, in the neighborhood of any collection of particles, the total field scattered by all the particles is small when compared with the total external

field. The total scattered field is just the sum of the fields scattered by the individual particles, each of which is acted upon by the external field in isolation from the other particles. That is, light scattered by N particles is N times the light scattered by one particle. The mutual distance between each particle should be approximately 3 times the radius of a single particle to be recognized as single scattering [50]. Multiple scattering occurs if the density of particles is high, that is, if the particles are very close to each other compared to the wavelength. Each of the particles in the scattering medium not only scatters the incident light, but this scattered light also suffers successive scattering by the neighboring particles. There is multiple scattering, when an increase in the number of particles does not induce proportionally the same increase in the scattered intensity. Again, multiple scattering can be identified when the extinction increases faster than that expected from the number of particles in the scattering medium.

The scattering laws do not depend directly on the size of the particle but rather on the ratio a/λ, where "a" is the characteristic size of the particle and "λ" the wavelength of incident light. So, we take into account the size parameter in light scattering studies, which is $x = ka = 2\pi a/\lambda$, where "k" is the wave vector. Each of these approximations corresponds to a particular type of scattering and is valid in a particular domain of size parameter and refractive index. Some such types of scattering are Rayleigh scattering, Rayleigh-Gans scattering, Anomalous diffraction, Mie scattering, Geometrical optics etc. Among the approximations the two important theoretical backgrounds for light scattering studies are Rayleigh scattering and Mie scattering. Rayleigh scattering was originally formulated and applied to explain light scattering from small, dielectric (non-absorbing), spherical particles. The theory of Mie scattering comprehends the general spherical scattering solution (absorbing or non-absorbing). In the present work, we have considered cases of single elastic scattering where the scattered light has the same frequency as the incident light.

In recent years, extensive work has been done by many researchers to study both spherical and non-spherical particles by light scattering technique. The earliest solution to the electromagnetic scattering problem based on symmetry assumptions is Mie's solutions for spherical particles. However, it cannot accommodate well for the description of non-spherical particles. For any lower degree of symmetry, the scattering problem needs to be resolved numerically [51 - 55], because retrievals accounting for particle non-sphericity are not well defined methodologically and technically.

The convenient availability of Mie solution has resulted in the widespread practice of approximately treating non-spherical particles assuming as if they were spheres to which the theory is applicable, but the scattering properties of non-spherical particles differ both qualitatively and quantitatively from those of volume - or surface-equivalent spheres [46]. Among typical examples of complex scattering objects are clouds, aerosols, a particle suspension, tissue sample or isolated morphologically complex particle etc. Due to the complexity of theory for shapes other than spherical, similar computation (like Mie theory) became cumbersome [46, 47, 56, 57]. The fact became evident from the works reported during 1970's [46, 47]. Since then, several attempts were made to develop numerical techniques based on semi-empirical approach through a modification of the Mie solution and ray tracing technique etc. [58, 59]. However, the approach failed to describe some noteworthy optical phenomena like halos, arcs, pillars and zenith-enhanced lidar backscatter observed for ice crystals [60], interstellar polarization caused by dust grains oriented by cosmic magnetic fields [61], single-scattering lidar and radar depolarization observed for cirrus clouds and precipitation for cirrus clouds etc. [62 - 65]. Over the past two decades, efforts have been made by many researchers to understand and demonstrate the effect of non-sphericity of particles on light scattering [66 - 71]. In fact, it became evident from the increasing number of reports on development of advanced numerical tools and approximations for computing the scattered

electromagnetic radiation by such particles. The scattering properties of non-spherical particles can now be computed theoretically to a fair amount of accuracy, although there are a lot of limitations in these new techniques.

All exact theories and numerical techniques for computing the scattered electromagnetic field of non-spherical particles also are based on Maxwell's equations either analytically or numerically. All the numerical techniques for computing electromagnetic scattering by non-spherical particles mostly fall into two broad categories, Differential and Integral. Differential equation methods compute the scattered field by solving the vector wave equation in the frequency or time domain, whereas, Integral equation methods are based on volume or surface integral corresponding to Maxwell's equations [46]. Some of the approaches and approximations which are used for such non-spherical particles are Separation of Variables Method (SVM), Finite Difference Time Domain Method (FDTDM), Finite Element Method (FEM), Point Matching Method (PMM), Method of Moments (MoM) or Volume Integral Equation Method (VIEM), Discrete Dipole Approximation (DDA), T-Matrix Method (TMM) etc.

The above mentioned methods and approximations, in addition to Mie theory are applicable to particle having size comparable to the wavelength of light. The approaches, theories and approximation methods applicable to light scattering are briefly described below:

- **Rayleigh scattering:** It is one of the first light scattering theories given by Lord Rayleigh. It is the elastic scattering of light by particles much smaller than the wavelength of the light i.e., $a << \lambda$, and having size parameter, $x = 2\pi a/\lambda << 1$. The particles may be individual atoms or molecules. It is usually applicable to particles that are optically "soft" (i.e. with a refractive index $n \approx 1$). In this type of scattering, it is assumed that the incident field inside and near the particle almost behaves like an electrostatic field and the internal field to be homogenous [48].

- **Rayleigh-Gans scattering:** It is also elastic scattering where the size of particle is large (larger than Rayleigh particles) but with small refractive index and small absorption. The size parameter ka is such that $|n\text{-}1| << 1$ and $ka|n\text{-}1| << 1$. It is possible to obtain relatively simple approximate expressions for scattering matrix elements using Rayleigh-Gans (RG) approximation. The method is valid for small polarizability contrasts and small phase shifts [72].
- **Raman scattering:** When light encounters molecules in the air, the predominant mode of scattering is elastic scattering, called Rayleigh scattering. It is also possible for the incident photons to interact with the molecules in such a way that energy is either gained or lost so that the scattered photons are shifted in frequency (usually lower than the frequency of the incident photons). Such inelastic scattering is called Raman scattering. Like Rayleigh scattering, the Raman scattering depends upon the polarizability of the molecules. For polarizable molecules, the incident photon energy can excite vibrational modes of the molecules, yielding scattered photons which are diminished in energy by the amount of the vibrational transition energies. Raman scattering can also involve rotational transitions of the molecules from which the scattering occurs. Studies on Raman scattering or Raman effect has been gaining popularity over the years since powerful monochromatic laser sources could provide the scattering power [73 - 75].
- **Anomalous diffraction:** Using the Huygens and Babinet principles, van de Hulst considered the problem of light scattering and extinction by a particle having size bigger than the wavelength of light but with small refractive index, i.e. $|n\text{-}1| << 1$. The range of applicability of the anomalous diffraction theory for the scattering amplitude is limited by small angles;

however the formulas for the cross-sections became good approximations for a wide class of particles. By using anomalous diffraction approximation (ADA), it was observed that the extinction efficiency as a function of size parameter, and for $|n| << 1.69$, the ADA agrees well with the results predicted by Mie theory [76]. Thus, the ADA can be easily applied to non-spherical particles, and provide scattering information for nonspherical particles with intermediate size parameter and moderate refractive indices [8, 76, 77].

- **Mie scattering:** It is an elastic scattering where the size of particle is comparable to the wavelength of the incident light, i.e. $a \approx \lambda$. It is an exact analytical solution to the Maxwell's equations for spherical particles [45, 48].The theory was proposed by Gustav Mie in 1908 [78 - 81], but before that, Lorenz in 1891 studied this phenomenon [82, 83]. In fact, it is the first well-known theoretical framework to explain scattering and extinction of light by small particles embedded in homogenous medium. Mie theory is extensively used by many researchers to develop more accurate and approximate analytical solutions and calibrate new scattering instruments based on light scattering techniques, because of its simplicity, accuracy and efficiency. Mie's 1908 paper is a landmark in the development of electromagnetic theory, computation and measurement techniques which is evident from the number of citations (about 4000 journals) [79]. In the recent years, major effort has been made to develop fast and comprehensive numerical algorithms and computer programs based on Mie theory [84 - 97]. Mie solutions are implemented in a number of codes written in different computer languages such as Fortran, C etc. These solutions are in terms of infinite series and include calculation of scattering phase function, extinction, scattering, absorption

efficiencies and other parameters such as asymmetry parameter or radiation torque. Computations have been made for scattering of polydisperse systems of spherical particles; however, limited work has been done for scattering from ensemble of homogenous spherical particles with very large size parameters [95, 98].

- **Geometrical Optics Approximation (GOA):** It is a method used for computing light scattering by particles much larger than the wavelength of light, i.e., $a > \lambda$. This approximation method is otherwise known as Ray tracing or Ray optics approximation [46, 99 - 105]. GOA is based on the assumption that the incident plane wave can be represented as a collection of independent parallel rays. The effect of each ray interacting with the surface of particle obeys the Snell's law and Fresnel's equations. Again, particles much larger than wavelength of light also scatters light by the phenomenon of diffraction and removes energy from the light wave diffracted by the particle. In the far field, this diffracted component of scattered light can be approximated by the Fraunhofer diffraction theory. The sampling of all the rays originating from geometric reflection, refraction and Fraunhofer diffraction on the particle projection yields a quantitative representation of the particle scattering properties.
- **Separation of Variables Method (SVM):** This method is used to solve the electromagnetic scattering problem for a prolate or an oblate spheroid in the respective spheroidal coordinate system. It is based on expanding the incident, internal, and scattered fields in the vector spheroidal wave functions. The expansion coefficients of the incident fields which are known are computed analytically, whereas the unknown expansion coefficients of the internal and scattered fields are determined through the requirement of boundary conditions. The SVM for single

homogenous, isotropic spheroids was pioneered by Oguchi (1973) and Asano and Yamamoto (1975), and was significantly improved by Voshchinnikov and Farafonov (1993) [106 - 108]. The method was successfully applied to obtain exact analytical solutions of problems involving scattering of electromagnetic waves by core-mantle spheroids, optically active spheroids, coated spheroids, concentric multi-layered spheres, homogenous isotropic cylinders and spheroids, lossy dielectric spheroids etc. [46, 109 - 114]. The main advantage of SVM is that it can produce very accurate results, particularly for spheroidal particles.

- **Finite Difference Time Domain Method (FDTDM):** It is a numerical method which uses finite difference in time and space to solve the Maxwell's time dependent curl equations [115 - 119]. In this method, the space containing a scattering particle is discretized by using a grid mesh and the existence of the particle is represented by assigning suitable electromagnetic constants like permittivity, permeability, and conductivity over the grid points. This method makes it possible to have the evolution in time of the electromagnetic field in space by iterative computing among the initial value of field. The FDTDM computes the near field in time domain, thus a special near to far field transformation must be pursued in order to compute the scattered field in the far field region. The method is one of the most efficient computational methods to analyse the interaction of electromagnetic waves with scatterers, particularly, those with complicated geometry and inhomogeneous compositions. In recent years, there has been wide application of this method in study of biological cells [120], human tissues [121], atmospheric non spherical particles, cirrus clouds etc. [123 - 124].
- **Finite Element Method (FEM):** The finite element method is a differential equation method that computes the scattered time-

harmonic electric field by solving numerically the vector Helmholtz equation (and not the Maxwell's equation as in FDTDM), subject to boundary conditions at the particle surface [46, 125]. In this method the scatterer is embedded in a finite computational domain that is discretized into many small-volume cells called elements with about 10-20 elements per wavelength. The unknown field values are specified at the nodes of these elements. Unlike FDTDM, where the scattering particle is discretized in a cubic grid leading to a staircase approximation of the shape of the particle, in FEM the particle shape can be discretized by using variety of elements of different shapes, such as triangular and rectangular for two-dimensional problems (2D) and tetrahedral for elements for three-dimensional problems (3D) [46, 126, 127]. The FEM computations are spread over the entire computational domain rather than confined to the scatterer itself. This makes FEM computations rather time consuming, limited to size parameters less than 10 approximately and requires a lot of memory. Extensive work has been done in diverse fields using this method [46, 127 - 131].

- **Point Matching Method (PMM):** In this differential equation technique, the incident and internal fields are expanded in vector spherical wave functions (VSWFs) regular at origin, and the scattered field outside the scatterer is expanded in outgoing VSWFs. The expansion coefficients of the incident field are known, whereas the expansion coefficients of the internal and scattered fields are found by truncating the expansions to a finite size matching the fields at the surface of the scatterer by application of appropriate boundary conditions. The method is accurate if the particle is not too large, and displays symmetry [50]. On the other hand, for large size parameters, it requires a lot of programming effort and computation time [132]. PMM has

been successfully used for particles like coated axisymmetric particles, spheroidal hydrometeors, etc. [46, 50, 127, 132 - 135].

- **Method of Moments (MoM) or Volume Integral Equation Method (VIEM):** This method is based on a volume integral. The total electric field is the sum of the incident field and an integral on the volume of the particle [46, 50]. Physically the internal field is represented at each point of the volume V by a sum of the incident field and the field induced by sources at all internal points including the self-point. The major advantage of VIEMs are that they automatically satisfy the radiation condition at infinity, and are confined to the scatterer itself; and can be applied to homogenous, anisotropic and optically active scatterers [135, 137]. However, the main drawback is its low computational accuracy.
- **Discrete Dipole Approximation (DDA):** The method was originally derived by Purcell and Pennypacker in 1973. This method is another version of MoM. It is based on partitioning a particle into N number of elementary polarizable units called dipoles. In DDA, a scattering particle of arbitrary shape is treated as a three-dimensional assembly of dipoles. The electromagnetic field experienced by such dipole is the superposition of the external field and the fields scattered by all other dipoles [138 - 142]. DDA is applicable to arbitrary shaped, inhomogenous, anisotropic and optically active particles. The disadvantage of this method is that the numerical accuracy is low, and improves only with the increase in number of cells.
- **T-Matrix Method (TMM):** The T-matrix method (TMM) was first introduced by Waterman in 1971 for single homogenous scatterers, and was subsequently generalized to multi-layered scatterers and arbitrary clusters of non-spherical particles and non-spherical chiral scatterers [143 - 147]. The TMM is based on

expanding the incident field in VSWFs regular at the origin and expanding the scattered field outside a circumscribing sphere of the scatterer in VSWFs regular at infinity. The expansion coefficients of the scattered field are related to the incident fields by transition matrix, and can be used to compute any scattering characteristic of a non-spherical particle. This method is also popularly known as Extended Boundary Condition Method (EBCM), Null Field Method (NFM), Schekunoff equivalent current method, or Ewald-Oseen Extinction theorem [148 - 158]. The main advantage of this method is that it is highly accurate, fast, and applicable to particles with equivalent-sphere size parameters exceeding 100 [159 - 161]. The elements of the *T* matrix are independent of the incident and scattered fields and depend only on shape, size parameter, and refractive index of the scattering particle and on its orientation with respect to the reference frame. Thus, *T* matrix needs to be computed only once and then can be used in computations for any direction of incident and scattered light. Conversely, the incident field can be fixed, and the particle can be rotated. The main drawback of TMM is the loss of efficiency for particles with large aspect ratio or with shape without axial symmetry. However, recent improvements on TMM has made the method applicable to particles having larger size parameter (exceeding 100), and the fact is reported in a current review [161]. Thus, TMM is a suitable approach to check the accuracy of GOA and its modifications at lower frequencies. The limitation of TMM is that the scatterer must be isotropic, and should have a linear response to the incident electromagnetic field. Among all the above mentioned techniques, the T-matrix method to calculate the 4x4 scattering matrix of both spherical and non-spherical particulate matter has led to successful interpretation of many

observations [162 - 167]. T-matrix method may be applicable to any kind of shape but the most practical applications are centered on spheroidal, cylindrical and chebyshev particles [163, 166].

Theoretical approach does not involve expensive instrumentation, but accurate computation for realistic polydispersions of irregular particles is practically difficult. Again, experimental measurements on both natural and artificial particles are possible; however, it is incapable of measuring all scattering characteristics simultaneously and accurately, and characterizing a sample precisely. Thus, it is clear that only a combination of theoretical and experimental approaches can lead to a better understanding of electromagnetic scattering by small particles, particularly non-spherical particles.

In this entire thesis, we have considered the case of elastic scattering only (that is, the scattered light has same frequency as the incident light). Effects like Raman-effect, or any quantum transitions are excluded.

1.2 Light scattering by small particles: a perspective

Scattering and absorption of light by small particles is a very important tool for visualization and diagnostic applications. An understanding of the phenomena of light scattering by small particles (ranging from nanometer to micrometer scale), especially particles like aerosols, cloud particles, dust particles, etc. which are normally suspended in the atmosphere but may also be present in other types of media, is a vital requirement for investigating various physical processes and developing applications. The intensity of light scattered by a particle, or collection of particles is a function of the angle between incident and the scattered radiation, and the wavelength of incident light. The light scattering mechanism by such particles [2, 3, 152,168 - 171] or from a volume element containing such particles, also depend on the

characteristics of the particles themselves, or their collective properties. Small particles or volume elements containing such particles possesses a large number of characteristic properties like shape and dispersion of shape of particles, size and dispersion of size of particles, density, aggregate structure (fluffy, fractal, tenacious, dense, etc.), refractive index , absorption properties, the homogeneity of their internal structure and the quality of their surfaces like roughness, etc. In other words, the angular dependency is also a function of these characteristic properties. It is important to study angular scattering dependency of small particulate matter for retrieval of information about size, shape, refractive index etc., and better comprehension of the radiative transfer process. Special areas of its importance and application are discussed below.

Atmospheric applications: Even if the air looks clear, it nearly contains millions of solid particles and liquid droplets, some of which we probably inhale every day. These pervasive iotas of matter are known as aerosols, and they can be found in the air over oceans, deserts, mountains, forests, ice, and every ecosystem in between. They float in Earth's atmosphere and range in size from a few nanometers (less than the width of the smallest viruses) to several tens of micrometers. True aerosols range from 10^{-7} to 10^{-4} cm in diameter, though turbulent media can keep particles 100 times larger in dispersion, as is often the case with fog, cloud and dust particles [2, 30]. All these particles possess a distinct and very often complicated morphology. Aerosol is usually defined as a form of colloid, in which microscopic particles of highly polymerized aggregate of liquid or solid substances are lumped together and are dispersed in a gas. Despite their small size, they have major impacts on our climate and our health, and holds significant importance in the wake of studies strongly correlating airborne particulate matter with adverse health effects. Through the mid-1990s considerable attention was paid to study the scattering properties as well as the size, shape, and orientation of

aerosols having size greater than the probing wavelength (Visible or UV scattering) [2, 169, 170]. Key aerosol groups include sulfates, organic carbon, black carbon, nitrates, soot aerosols, volcanic ashes, snow or ice crystals, mineral dust, and sea salt. In practice, many of these terms are imperfect, as aerosols often clump together to form complex mixtures. The effects of scattering, extinction or polarization change by aerosols, cloud or haze on radar and satellite communications, meteorology, pollutant quantification etc. were broadly investigated by light scattering techniques [172 - 178].

A large mass fraction of the Earth's atmosphere contains irregular mineral dust particles [179, 180], considerable fraction of cometary aerosols and aerosols of biological origin [177 - 200]. Changes in stratospheric ozone concentrations occur after major volcanic eruptions, like Mt. Pinatubo in 1991 and Eyjafjallajokul in 2010, where tons of volcanic aerosols were blown into the atmosphere [30]. The dispersal of volcanic aerosols has a drastic effect on the Earth's atmosphere. Following an eruption, large amounts of sulphur dioxide (SO_2), hydrochloric acid (HCl) and ash are spewed into the Earth's stratosphere. Light scattering investigation of such aerosols is important for climate modeling, remote sensing and developing atmospheric correction algorithms [201, 202].

Again, an important constituent of Earth's atmosphere is water vapor. In recent years, measurements of water vapor droplets on controlled environment provided vital information about water droplet size distribution in air, and its importance in the formation of rain clouds [1, 38, 202]. Formation of clouds takes place when a volume of air becomes saturated with water vapor and excess water condenses rapidly on aerosol particles to form water droplets, which means the aerosol particles act as cloud condensation nuclei. The increment of such nuclei in the atmosphere affects the radiative properties of clouds

[38, 47]. It is noteworthy to mention that clouds play an important role in Earth's atmospheric radiative balance [203 - 215]. An important constituent of clouds (cirrus clouds) are ice crystals. The scattering-phase functions are highly dependent on the crystal morphology and orientation. Proper information on scattering-phase function leads to developing reliable methods for optical and microphysical properties of ice clouds, based on bidirectional reflectance measurements from space, and remote-sensing applications [212]. The ice crystals present in cirrus clouds generally have hexagonal shapes, and are present in the form of aggregates and bullete rosettes. It is practically difficult to retrieve information of such complex particles, particularly for smaller sizes [213, 214]. However, studies on ice analogue crystals, which have same shape and refractive index as the real ice crystals, have produced appreciable results [24, 37, 215]. In other words, scattering, absorption and polarization data of cloud particles reveals essential information for climate modeling; Development of remote sensing techniques are required to gather knowledge of cloud optical depth, temperature, and size of ice crystals; Fluxes; Heating rates from air, ground, and space etc. [46,206, 216].

Another type is the sea salt aerosol, which is mostly spread over the oceans and has been recognized as the dominant aerosol contributor to clear sky albedo over oceans [217]. It is produced by evaporation of sea spray induced by wind. Depending upon the aerosol optical properties and the surface albedo, aerosols may exert warming or cooling effect of the atmosphere [218].

Astrophysical applications: Light scattering technique is an essential tool for assessing the physical properties of small particles and aggregates in the solar system or the interstellar medium [169, 170, 219]. Remote sensing observations of the linear polarization of light scattered by dust particles in cometary comae, diffused or circumstellar

dust clouds, interplanetary dust cloud, planetary rings, and asteroidal regoliths etc. are used to deduce physical properties of their constituent particles [181]. Again, properties of terrestrial aerosols are important as their properties are found to be similar to that of planetary regoliths, cometary dust etc. [220 - 222]. Terrestrial aerosols are considered as important contributors to light scattering in marine atmosphere, and is demonstrated by studies that found the presence of Sahara dust and volcanic ash in marine environment [223]. Most solid particles in the terrestrial and planetary atmospheres, and other solar system bodies like asteroids and comets, consist of irregular mineral particles. Some irregular particles like Hematite (Fe_2O_3), Graphite and Titania (TiO_2) are currently an important topic of astronomical discussions [71, 196 - 200, 214]. Hematite is believed to be the main constituent for red color appearance of Mars. Investigations have revealed that rutile titania dust particles are thought to be the nucleation sites in oxygen-rich circumstellar shells, and is also an essential component of lunar regolith [214, 224]. Soot can also be an important component of atmospheric aerosols. Carbonaceous soot is believed to be one of the most prevalent contributors of particulates in atmospheres [225, 226]. Again, composition of cometary dust particles were investigated *in-situ* by the dust mass impact spectrometer (CIDA) onboard, the NASA spacecraft STARDUST, which substantiated that interstellar dust is a mixture of carbonaceous and silicate particles, irregular in shape and highly porous in nature [42, 227, 228]. The fragility, fluffiness, and complicated morphology of such particles make it a very difficult task to characterize the observed scattered light, even with ever-increasing computation models [46, 148, 229] or classical laboratory measurements. Yet, light scattering experiments *in-situ,* under microgravity conditions has produced good results [31, 41, 182 - 184].

Biological applications: The light scattered from bio-particles, particularly polarized light, carries information about the optical, geometrical, and even esoteric properties of these bio-particles. Changes in cell morphology, internal arrangement and metabolic activity causes change in radius, refractive index and absorption, thereby changing the scattered signal [34, 189, 190, 230 - 232]. It has been demonstrated by Bickel how the 16 elements of Mueller matrix, S_{ij}, can type human blood cells, do autopsies, distinguish between different types of white blood cells, bacteria, and study life cycle and degradation as bio-particles undergoes biologically significant changes [34]. Again, light scattering technique has been used to study red blood cells (RBC) by different workers, and produced interesting results [233 - 236].

These bio-particles may be present in water or may remain suspended in the atmosphere as bio-aerosols as well. Natural water has different constituent of particles like bacteria, algae, virus, colloids, phytoplankton, ions etc., and are termed as hydrosols. Seventy percent of the surface of the Earth is covered by water, which significantly effects the planetary albedo and climate [232, 237, 238]. A complex absorption spectrum and a significant amount of scattering is exhibited by the water molecules, when there is fluctuation in the refractive index due to small variations in the salt composition [239]. For example, backscattering by clean ocean water alone contributes as much as eighty percent of total backscattering coefficient in the blue spectral region. Whereas, during phytoplankton bloom, and atmospheric dust deposition in oceanic water, the backscattering coefficient is dominated by plankton species, and mineral particles (of atmospheric dust deposits) having high index of refraction [237]. The growth and decay of phytoplankton bloom, radiance from water bodies, marine environment, and similar ecological information are constantly

monitored and collected by satellite remote-sensing [240]. Therefore, it is important to know scattering properties of such constituent hydrosols in order to find information about the nature of scatterers, and predict the type of environment of light underwater [35, 232]. Recent studies on scattering, absorption, and backscattering efficiency of marine water, and hydrosols delivered tremendous information useful for interpreting satellite imagery, and to develop radiative transfer algorithms to study ecosystems [232, 241 - 250].

Again, spread of some pathogenic aerosols (bio-aerosols) in the environment may cause threat to human health, especially for respirable size of aerosols ranging between 1-10 μm [188]. In the area of fluorescence by particles the detection and identification of *Bacillus subtilis* subsp. niger (BG) bio-aerosol spores, and kaolin dust is a significant step forward [251]. In the fields of occupational hygiene and environmental monitoring, there is international recognition of the need for new techniques and instrumentation for the detection and monitoring of potentially hazardous respirable airborne particulates, especially in working environments. It requires advanced systems for such detections which are proficient in providing important information of such life-threatening aerosols. Among the several techniques developed so far, the sensors based on elastic scattering is quite promising as the technique could provide information about size, shape and quality of particle surface[34, 190, 252 - 258]. Optical-scattering techniques are widely used as a means of counting and sizing airborne particles on an individual basis and are personified in a number of commercial instruments. In general these instruments do not attempt to assess particle shape but rather attribute a spherical-volume-equivalent size to each measured particle, based on an empirical or theoretical calibration function [174]. Because of the possibility to describe more realistic scattering phenomena, light

scattering is now also used in new domains such as oceanography, colloidal chemistry, biophysics, among others.

Nanoscience applications: *Optical effects of small metallic particles* and clusters have been a topic of great interest over more than three millennia, and have evolved from cluster science to nanoscience and nanotechnology in due course. The area of nanoscience and nanotechnology is gaining significant attention due to the interesting properties displayed by materials at this nano-scale [259, 261, 367]. In recent years, a lot of effort has been made in the development of science and technology at the nanometer scale, covering from growth and characterization of nanoparticles, to manufacturing devices with such particles. The shape and size of low-dimensional materials are crucial parameters to determine their physical, optical and electronic properties [262 - 267]. Nanosize particles are also used in chemical and biological sensor development. The sensitivity of these sensors to detect any physical or chemical change depends directly on the shape, size, size distribution of constituent particles, emphasizing the significance of nanoparticle characterization [259].

There are several methods for the characterization of nanoparticles, namely, Laser Light Scattering (LSS) techniques, Scanning Electron Microscopy (SEM), Transmission Electron Microscopy (TEM), Atomic Force Microscopy (AFM), Scanning Near field Optical Microscopy (SNOM) and Scanning Tunneling Microscopy (STM), Scanning mobility particle sizer, and centrifugal sedimentation etc. [48]. Among these methods, light scattering techniques are some of the most versatile techniques for *in-situ* morphological measurement, size distribution measurement and determination of shapes of such nanoparticles (in some cases), especially when they are suspended in optically inactive solution [21, 264 - 269]. Recently, particle sizing on the nanometer scale by optical techniques, far exceeding the diffraction

limit of the UV radiation, have been reported [262]. On the other hand, some other workers have successfully investigated the sizes and shapes of nanoparticles using dynamic light scattering (DLS) techniques [263, 270]. Experimental and theoretical work on identifying nanosphere sizes using LSS in the UV range (λ ~ 250-390 nm) has also been reported [266]. Also, possibility of Mie scattering by nanoparticles with different particle sizes are being investigated [271 - 273]. Again, semiconductor and metal nanoparticles are potential candidates for its applications in sub-wavelength photonic, and optoelectronic devices; non-linear optics; optical data storage; bio-sensors etc. [269]. Light scattering studies is an imperative tool for *in-situ* monitoring and tuning such particles for proper applicability. Metallic nanoparticles are known to exhibit distinct optical phenomenon, especially Surface Enhanced Raman Scattering (SERS), relative to bulk form of metals at optical wavelengths [274 - 276]. The extremely large electromagnetic field enhancements associated with these plasmon resonances are of considerable importance for nanoscience [260]. Characterization of nanoparticles and structures has become crucial to understand and study nano self-assembly processes and bottom up building processes. The problem has interesting applications in characterizing micro structures on flat substrates and development of surface scanners [277]. Most of the previous work on particle characterization is concentrated on particles embedded in a dielectric medium rather than on particles interacting with an interface.

Simulation techniques and applications: Another approach that many workers have been taking to understand the phenomenon of light scattering better is to use computational models that simulate light propagation in scattering media [278, 279]. They used Monte Carlo algorithms that were based on the Stokes-Mueller formalism. In a recent interesting paper, Monte Carlo simulation results of diffusely

backscattered intensity patterns that arise from illumination of a turbid medium with a polarized laser beam has also been reported. A Monte Carlo algorithm has also been developed which accurately models the single-scattering event according to Mie -theory and keeps track of the polarization state of individual photons in multiple scattering media [280]. There are also other reported works which showed the successful implementation of Monte Carlo simulation technique [233, 280 - 295]. Monte Carlo simulation of propagation of a short light beam through turbulent oceanic flow has also been reported [296]. Such Monte Carlo methods [279, 287, 288, 296] of solving light scattering problems have been proved to be very successful tools in verifying the experimental observations obtained by use of the different investigating instruments as well as lending support and improving the current theoretical models, like Mie theory and T-matrix approach, for interpreting scattering phenomenon.

1.3 Motivation and Objectives

There are various theoretical approaches and computational techniques which describe the experimentally observed scattering of light by small particles. Some such theories are mentioned in section 1.2. Variety of laboratory measurements, both *in-situ* and *ex-situ* of visible and infra-red light scattering were performed to determine the phase function and extinction, polarization and depolarization characteristics of natural and artificially generated cirrus cloud crystals [297, 298], scattering matrix elements of hydrosols [35, 232], backscattering Mueller matrix for atmospheric aerosols [30, 168, 299], etc. Still, the complete structure, size, composition and optical parameters of thousands of aerosols and other particulate matters are yet to be done. Many leading journals pointed the necessity of clear understanding of the radiative properties of aerosols for a wide variety of such applications. Again, natural particles are often complex (in terms of size, shape, size distribution, refractive index etc.) and show discrepancies between the

theoretical and experimentally measured results. Thus, it becomes difficult to characterize and model such particles. In order to overcome such discrepancies and to improve upon the performance, usefulness and quality of light scattering theories, we need to collect sufficient scattering data. Moreover, it is important to compare experimental measurements with simulations for understanding the results in a better way [300]. Despite such advanced numerical techniques being available, the results of such techniques do not completely fit with the results of laboratory and *in-situ* experiments, especially for particles with complicated morphology. This is because of the limitations of such theories when applied to complex particles, and to some extent because of the imprecisions that may be present in the experimental setup. Combined efforts on improving and developing computation, and experimentation can produce better results.

In order to improve upon measurement techniques and computation involved in light scattering studies, we need to improve instrumentation, so that it can be used to characterize different particulate matter including nanoparticles. More precise experimental error reduction techniques should be followed during scattering-data collection. In order to yield a better result, it is necessary to find out complete morphology of particles based on high resolution microscopic techniques. Moreover, powerful and fast algorithms to compute light scattering pattern of complex shapes and extreme refractive indices is a prerequisite for obtaining improved results. Thus, in our work an attempt was made to improve computation and instrumentation, and its proper utilization for light scattering investigations of small particles. In fact, this attempt is the basis of this thesis. The objectives of this thesis are outlined below:

- Design and fabricate an efficient and reliable laser based system using He-Ne and diode laser, for light scattering studies.

- Performance optimization of the setup by calibrating with standard sample.
- Use the setup for experimental investigation of different particulate matter (aerosols, other suspended particles, bio-particles etc.)
- Carry out simulations of light scattering by these particles, and comparing with established theoretical results and experimental results.

As a mathematical and numerical basis for the analysis of the observed experimental data of small particulate matter, Mie-theory and T-matrix approach has been specifically used in our research, for spherical and non-spherical particles not too large compared to the incident wavelength of light.

Remarks on the choice of Mie theory:

There are several reasons for choosing Mie theory for light scattering studies. They are discussed below:

- It provides complete analytical solution of classical scattering problem using Maxwell's equations (including the absorbing host medium).
- It is the simplest, accurate and efficient method used for light scattering studies of homogenous particles.
- It allows the calculation of the Mueller matrix elements.
- Though Mie solution is presented for spherical particles, it acts as a guide to describe first order optical effects in non- spherical small particles also.
- The theory can be further extended to study coated, clustered and stratified spherical particles.
- It is a fast algorithm and requires less memory for its execution.

Remarks on the choice of the T-matrix approach:

There are several reasons for our choice of the T-matrix algorithm for the numerical calculation. They are enumerated below:

- It can be adapted to both spherical and non-spherical particles, most often to rotationally symmetric particles.
- It allows averaging on all orientations of particles.
- It allows the calculation of the Mueller matrix elements.
- T-matrix approach allows multiple scattering modeling.
- As the main part of the solution is analytically calculated, corresponding numerical errors are low.
- It is a very fast algorithm, and can be adapted to different geometries.

1.4 Instruments for light scattering studies

There are several important components in a light scattering setup, for experimental observation of light scattered by small particles. During the past few decades, manual and automated methods have been developed which satisfy requirements of many scattering setups [253]. Calculation of all the 16 elements of 4x4 Mueller scattering matrix is possible by using a laser-based light scattering setup. This matrix operator completely determines the transformation of the incident light of any arbitrary polarization state after scattering, and in fact is a characteristic matrix of the scattering object. In 1950, Kerker and V.K.L Mer developed a method where they showed that by using either the polarization ratio or the phase angle of the scattered light as a function of scattering angle, they could determine information about the size of the particle [238]. B. S. Pritchard and W. G. Elliot did the first measurement of the scattering matrix elements by using a simple subtraction method [25]. The accuracy of measurement was significantly improved by implementing polarization modulation techniques [190, 301 - 306]. In the 1980's, a sophisticated, fully computerized setup was built by P. Stammes, F.Kuik, and

H. Volten, in the Department of Physics and Astronomy, Free University, Amsterdam to investigate laser light scattering and was later improved by J. W. Hovenier [2, 46, 47, 304]. However, the standard light scattering techniques used to characterize the micron and sub-micron size particles do not have the fine resolution needed for characterizing nano-sized particles, for which exploration of nanoparticles by light scattering tools has not been realized yet, to their fullest potential. Again, in order to have a better understanding of interaction of light with matter in microgravity, for describing planetary formations and to understand the properties of scattering aggregates, several projects like PROGRA2 (Propriétés Optiques des Grains Astronomiques et Atmosphériques) and the ICAPS (Interaction in Cosmic and Atmospheric Particle Systems) have been carried out by Levasseur Regourd, Hadamcik and Worms [31, 41, 182 - 184, 219]. Since then, other workers have continued with their efforts to design instruments for better experimental observation of scattered light and calculate the scattering matrix elements with greater accuracy. Some such advanced light scattering setups were developed by D. Daugeron, M. T. Valentine, P. H. Kaye, Z. Ulanowski, O. Munoz and G. A. Ahmed, and used for its successful implementation [24, 27, 30, 32, 38, 307].

The common instruments, with remote sensing capability, efficiency for providing realistic measurements in the atmosphere, and also incorporating laser sources, namely, the Nephelometer, the Transmissiometer, the Point visibility meter and the LIDAR (Light Detection and Ranging) systems are briefly described below:

(a) Nephelometer

An instrument for angular light scattering measurements is called a nephelometer [25, 301, 308 - 311], or a polar nephelometer, shown in figure 1.2. It comprises of some essential elements, like collimated light source, and an arm that can be rotated about the scattering sample. The detector system which collects the light scattered within a small solid angle, is mounted on the arm positioned on the scattering plane. The

light source may be a tungsten-halogen, high-pressure mercury or xenon lamp, or otherwise, a laser. The detector consists of a lens, followed by an aperture to limit angular acceptance of the detector.

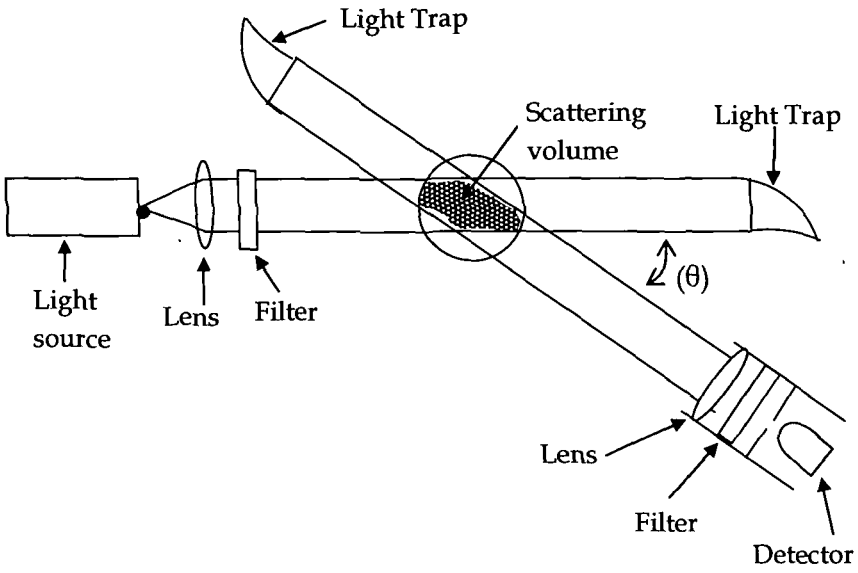

Figure 1.2: A polar nephelometer.

The scattering volume which consequently changes with the change in angular distribution is determined by intersection of the incident beam with the detector field of view. Since the arm containing the detector interferes with the incident beam, it is practically not feasible to make scattering measurements at angles close to 180°, with conventional nephelometers. Sometimes, angular light scattering measurements are classified as either absolute or relative. In an absolute measurement the ratio of scattered irradiance I_s to incident irradiance I_i, which is directly related to a factor $dC_{sca}(\theta)/d\Omega$, called the differential scattering cross section is determined. In a relative measurement the irradiance is referred to some arbitrary scattering angle, say 10°, so that,

$$\frac{I_s(\theta)}{I_s(10°)} = \frac{I_s(\theta)/I_i}{I_s(10°)/I_i} = \frac{dC_{sca}(\theta)/d\Omega}{dC_{sca}(10°)/d\Omega}$$

Relative measurements are considerably easier to make and are the type most commonly reported. A nephelometer yields information regarding volume scattering coefficients and consequently information of shape and size of the sample under investigation.

(b) Transmissiometer

A common instrument used for measuring light transmittance is called a transmissiometer [25, 312]. In Earth's atmosphere, the transmission in visible portion of spectrum is mainly affected by scattering. Optical transmission of a particular medium is defined as the ratio of the initial intensity to the final intensity of light after it passes through the medium. The essentials of a practical transmissiometer are shown in figure 1.3.

Light from a point source is collimated by a lens, if necessary, and then transmitted through the particulate sample, and finally focused by a lens onto a detector through a pinhole. In particular, light scattered in the forward direction only, is detected. The ratio of the final flux P in a light beam to the initial flux P_o is the *Transmittance* T of an optical path.

$$T = \frac{P}{P_o}$$

For a homogeneous path of length D, a transmissiometer gives the extinction coefficient σ as

$$T = e^{-\sigma D}$$

This information is used to measure absorption, visibility and find number densities of the samples under investigation [25, 312 - 317].

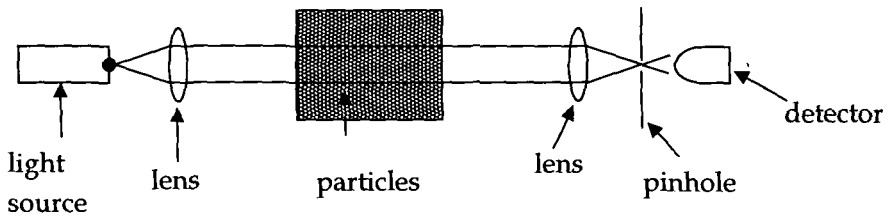

Figure 1.3: An ideal Transmissiometer.

(c) Point Visibility Meter

A compact instrument capable of measuring the atmospheric extinction coefficient, or otherwise, amount of light scattered along a particular forward direction is called the Point visibility meter (PVM)[318]. The extinction coefficient σ is found from the empirical law relating σ to the scatterer at this angle [318, 319]. The schematic diagram of a point visibility meter is shown in figure 1.4.

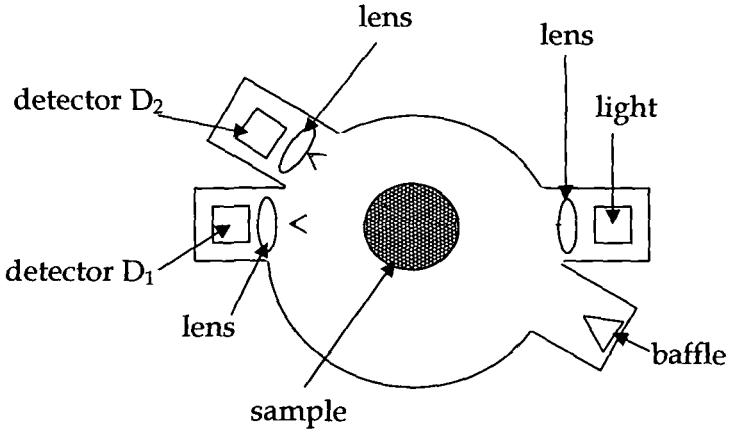

Figure 1.4: Block schematic of Point visibility meter (PVM).

The particulate sample scatters the radiation emitted by the light source. A fraction of the radiation scattered in the forward direction is collected by the scattering detector D_2 at an angle θ, and the unscattered

radiation is collected by the reference detector D_1. The empirical law derived from the observations [38] of linear dependence of the extinction coefficient σ on intensity of radiation scattered $\beta(\theta)$, that is,

$$\frac{\beta(\theta)}{\sigma} = \text{constant}$$

at an optimum angle between 30° and 40° is the basis on which the PVM is operated.

(d) Lidar

Lidar, which is an acronym for Light Detection And Ranging, is used for laser remote sensing of atmospheric properties from a single location [320]. It comprise of a laser source and a photo-receiver which measures the backward scattering of light. In this system, the projection of a short laser pulse is followed by reception of a portion of the radiation reflected from a distant target or from atmospheric constituents such as molecules, aerosols, clouds, or dust, as shown in figure 1.5. The incident laser radiation interacts with the constituents of such matter, causing variations in the intensity and wavelength, according to the strength of this optical interaction and the concentration of the interacting species in the atmosphere. Accordingly, information on the composition and physical state of the atmosphere can be inferred from the lidar data. In addition, the range to the interacting species can be determined from the temporal delay of the backscattered radiation.

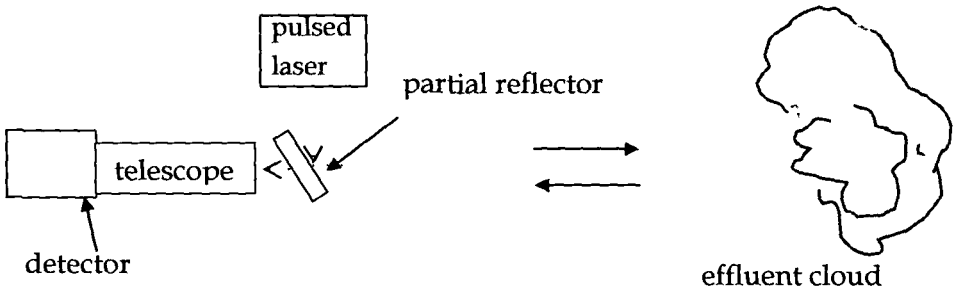

Figure 1.5: Schematic of a lidar

By generating a light beam of high power and small angular divergence, it becomes an advantage of lidar over projector sounding systems which were used before. Moreover, as lasers are capable of producing powerful pulses of short duration, there is possibility of measuring time-dependent measurements, which includes integral optical measurements of the medium, as well as their spatial distribution. The basic lidar principles outlined above may be expressed formally by the following lidar equation.

$$P_r(R) = P_o\left(\frac{c\tau}{2}\right)\beta(R)A_r R^{-2}\, exp\left[-2\int_0^R \sigma(r)dr\right]$$

where P_r is the instantaneous received power at time t, P_o is the transmitted power at time t_o, c is the velocity of light, τ is the pulse duration, β is the volume backscattering coefficient of the atmosphere, R is the range, A_r is the effective receiver area, and σ is the volume extinction coefficient of the atmosphere.

There are different types of Lidar systems, which are classified as:

- **Atmospheric backscatter lidar:** In this type, the lidar transmits one laser wavelength and detects changes in the backscatter due to the aerosols, or dust in the atmosphere.
- **Differential-absorption lidar (DIAL):** It is a type of lidar which measures the concentration of a molecular species in the atmosphere by transmitting two wavelengths, only one of which is absorbed, and detects the difference in the intensity of the returns at the two wavelengths.
- **Fluorescence lidar:** This type uses two wavelengths, just as in the case of DIAL system, but, in addition, uses spectrometric techniques to separate the wavelength-shifted fluorescence signal from the strong Rayleigh backscatter in the atmosphere.

- **Raman and Doppler lidar:** In this type, there is a single-wavelength laser, and sophisticated detection techniques to spectrally determine the wavelength shifted signal from the strong background due to Rayleigh or Mie scattering.

Since the time of Fiocco and Smullin, who were the first to use a laser for atmospheric studies in 1962, Lidar technology has reached a high degree of sophistication. Lidar plays an important role in remote sensing of the atmosphere and the related issues like multiple scattering, depolarization ratios, transmission effects, noise, atmospheric optical turbulence, and speckle, and are still open to research so that Lidar systems can be further improved. Although lidar systems are very expensive, it is the most prevalent, and is used to explore different scientific disciplines. [321 - 325].

1.5 Introduction to the presented work

In regard of the kind of light scattering systems mentioned in the above sections, the work in this thesis proposes the design considerations of a modified and improved version of laser based light scattering system. The system is coupled to a microprocessor linked data recording and processing unit. Primary focus was on the development of a fast, reliable, efficient, portable and far more accurate light scattering system. Successive effort was made to extend the applicability of this system to a variety of particulate matter.

Chapter I of this thesis gives an introduction to the light scattering system and the associated instrumentation, and simulation.

Chapter II of the thesis reviews the theories of extinction and scattering to bring forward the significance of the parameters monitored by the designed and fabricated light scattering system. It also emphasizes on the significance of light scattering theories like Mie theory and T-matrix method, which are

required to compute scattering matrix elements in order to support the light scattering system which was used in determination of two important elements of the scattering matrix.

Chapter III of the thesis presents the design and instrumentation of the light scattering system and provides information of every unit of the system in detail. The data acquisition systems tested with the light scattering system is also discussed in this chapter. Technique applied for correction of systematic errors, and an overview of the data processing software used for the light scattering system are also presented in this chapter.

Chapter IV of the thesis presents the results of the experimental investigations carried out in the simulation chamber on variety of particles using the light scattering system, and followed by method of comparison of experimental results with the theoretically derived results. Significant findings from the investigations are also laid down in this chapter. Here the reported works of other authors on the subject of extinction and scattering are also presented for relative assessment with the work presented in this thesis.

Chapter V of the thesis presents details of Monte Carlo simulation technique which was developed and implemented for simulating the light scattering of some small size distributed particles.

Chapter VI of the thesis lays down the conclusions drawn from the work presented in the thesis and gives suggestions for future improvements in the light scattering system as well as the simulation technique.

CHAPTER II

Theory of Extinction and Scattering

2.0 General Introduction

Two important electromagnetic theories required for processing the data acquired from our designed and fabricated laser-based light scattering system is presented in this chapter. Section 2.1 presents basic Maxwell's equations required for presenting the Poynting vector in a form required for developing the Stokes parameters. In Section 2.2, relation between incident and scattered fields and the Stokes parameters are developed, and presented. Combination of this relation and the Stokes parameters lead to the formation of the Mueller matrix for scattering, and the first two elements of which are assessed by the light scattering system. In Section 2.3, the cross-sections of extinction, absorption and scattering are derived and are then used in forming the theory for extinction co-efficient. In Section 2.4, we present the Mie theory to explain the angular variations of the scattered light, as the theory successfully explains multitude of scattering observations for spherical particles. We have considered Mie theory for explanation of most of the experiments. In Section 2.5, we present the numerical method of T-matrix approach, which was also used in our work. An overview of the computer program based on Mie theory and T-matrix method which were used to calculate theoretical values of scattering coefficients over size distributions, and which may be co-related with experimental results are also presented in the end of this section. Thus, this chapter presents the original efforts in the thesis at measuring the scattering matrix elements in a format compatible with the light scattering system, together with molding the established theory of scattering coefficients suitable for automation.

2.1 Maxwell equations and its importance

The analytical and numerical basis for describing scattering properties of media composed of small discrete particles is formed by the classical electromagnetic theory. We start by formulating the Maxwell equations and constitutive equations to derive the simplest plane-wave equations, which will lead to the introduction of fundamental quantities like the Stokes parameters. The mathematical depiction of all classical optics phenomena is based on the following set of Maxwell equations for electromagnetic field at interior points in matter.

$$\nabla.\boldsymbol{D} = \rho \qquad \textbf{2.1.1}$$

$$\nabla x\boldsymbol{E} = -\partial\boldsymbol{B}/\partial t \qquad \textbf{2.1.2}$$

$$\nabla.B = 0 \qquad \textbf{2.1.3}$$

$$\nabla x\boldsymbol{H} = J + (\partial D/\partial t) \qquad \textbf{2.1.4}$$

where, t is the *time*, E is the *electric field*, H is the *magnetic field*, B is the *magnetic induction*, D is the *electric displacement*, ρ is the macroscopic free *charge density* and J is the *current density*. The continuity equation which is inherent in the Maxwell's equations is given by

$$(\partial\rho/\partial t) + \nabla.J = 0 \qquad \textbf{2.1.5}$$

and can be derived by using equation 2.1.1 and equation 2.1.4. The vector fields in equations 2.1.1 - 2.1.4 are related by electric displacement and the magnetic field, given by

$$D = \varepsilon_0 E + P \qquad \textbf{2.1.6}$$

$$H = (1/\mu_0)(B-M) \qquad \textbf{2.1.7}$$

where, P is the *electric polarization* or average electric dipole moment per unit volume, M is the *magnetization* or average magnetic dipole moment per unit volume, ε_0 is the *electric permittivity*, and μ_0 is the *magnetic permeability* of free space. Since equations 2.1.1 - 2.1.7 are inadequate for unique determination of

electric and magnetic fields, they must be supplemented with so-called *constitutive relations*, given by

$$J = \sigma E \qquad \textbf{2.1.8}$$

$$B = \mu H \qquad \textbf{2.1.9}$$

$$P = \varepsilon_0 \chi E \qquad \textbf{2.1.10}$$

where, σ is the *conductivity*, μ is the *permeability*, and χ is the *electric susceptibility*. The constants σ, μ, and χ, depend upon the medium under consideration, and are termed as *material constants*. We assume all these material constants to be independent of field, position and direction respectively, which mean a condition satisfying linearity, homogeneity and isotropy, throughout the thesis. It is noteworthy that Maxwell equations are strictly valid only for points in the neighbourhood of which the physical properties of the medium, as characterized by σ, μ, and χ, vary continuously. However, if there is an interface separating one medium from another, then E, D, B and H may be discontinuous. The boundary conditions at such an interface can be formulated by using integral equivalents of Maxwell equations [47]. For the boundary conditions, the equations are as follows:

(i) There is a discontinuity in the normal component of D:

$$(D_2 - D_1).\hat{n} = \rho_s \qquad \textbf{2.1.11}$$

where, $\hat{n}$ is the unit vector directed along the local normal to the interface separating media 1 and 2 while pointing towards media 2, and ρ_s is the surface charge density.

(ii) There is a discontinuity in the tangential component of H:

$$\hat{n} \times (H_2 - H_1) = J_s \qquad \textbf{2.1.12}$$

where, J_s is the surface current density. However, media with finite conductivity cannot support surface currents, so that

$$\hat{n} \times (H_2 - H_1) = 0 \qquad \textbf{2.1.13}$$

(iii) The normal component of B and the tangential component of H are continuous:

$$(B_2 - B_1).\ \hat{n} = 0 \qquad 2.1.14$$

$$\hat{n} \times (E_2 - E_1) = 0 \qquad 2.1.15$$

The boundary conditions are useful in solving the Maxwell equations in different adjacent regions with continuous physical properties and then relating the partial solutions to determine the fields throughout the space.

2.2 Scattering matrix and scattering coefficients

The Maxwell equations [45, 74] for the electromagnetic field in a region where free charge density $\rho_F = 0$ and current density $J_F = 0$ are given as

$$\nabla.E = 0 \qquad 2.2.1$$

$$\nabla xE = -\mu\ (\partial H/\partial t) \qquad 2.2.2$$

$$\nabla.H = 0 \qquad 2.2.3$$

$$\nabla xH = e\ (\partial E/\partial t) \qquad 2.2.4$$

where, μ and ε are the permeability and permittivity respectively of the medium. Thus, it follows that if the refractive index of the medium is given as $n = n' + in''$, then

$$E = E_0\, e^{(-k''.x)}\ e^{(ik'.x - i\omega t)} \qquad 2.2.5$$

$$H = H_0\, e^{(-k''.x)}\, e^{(ik'.x - i\omega t)} \qquad 2.2.6$$

where, $k = k' + ik''$ and ω are the wave vector and angular frequency respectively. The Poynting vector S specifies the magnitude and direction of the rate of transfer of electromagnetic energy at all points of space, given by

$$S = (1/2)Re\{(\varepsilon/\mu)^{1/2}(E.E^*)\}\hat{e} \qquad 2.2.7$$

where, E^* is the complex conjugate of E and $\hat{e}$ is the direction of propagation. Assuming the wave with wavelength λ to be moving in the z direction, the above equation becomes

$$S = (k/2\omega\mu) \mid E_o \mid^2 e^{(-4\pi n'' z/\lambda)} \hat{e} \qquad \textbf{2.2.8}$$

This gives the modulus of S as

$$\mid S \mid = (k/2\omega\mu)\, I \qquad \textbf{2.2.9}$$

Here, I denote the irradiance with dimension of energy per unit area and time. As the wave traverses the medium, the irradiance may be given from 2.2.8 and 2.2.9 as,

$$I = I_o e^{(-a' z)} \qquad \textbf{2.2.10}$$

where,

$$a' = 4\pi n''/\lambda \qquad \textbf{2.2.11}$$

is the absorption co-efficient and

$$I_o = (k/2\omega\mu) \mid E_o \mid^2 \qquad \textbf{2.2.12}$$

is the irradiance at $z = 0$. Also if there is no absorption in the medium then $n'' = 0$ and 2.2.9 becomes

$$\mid S \mid = (k/2\,\omega\mu) I_o \qquad \textbf{2.2.13}$$

The equations 2.2.12 and 2.2.13 are now in a form that can be used for development of the Stokes parameters, which in turn can be used in developing the Mueller matrix for scattering. When a beam of incident light interacts with an obstacle, there is a modification in the intensity and state of polarization of the incident light, in addition to change in the direction of the incident beam after scattering, along any polar (θ) or azimuthal angle (φ). The direction of propagation of the incident light is taken as the z-axis. Any point in the particle is chosen as the origin of a rectangular Cartesian co-ordinate system (x,y,z),where x and y axes are orthogonal to the z-axis and to each other but are otherwise arbitrary. The orthogonal basis vectors $\hat{e}_x$, $\hat{e}_y$, $\hat{e}_z$ are in the directions of the positive x, y and z axes. The direction of scattering may also be given in terms of $\hat{e}_r$, $\hat{e}_\theta$ and $\hat{e}_\varphi$ which are the orthonormal basis vectors associated with the spherical polar co-ordinate system (r, θ, φ).

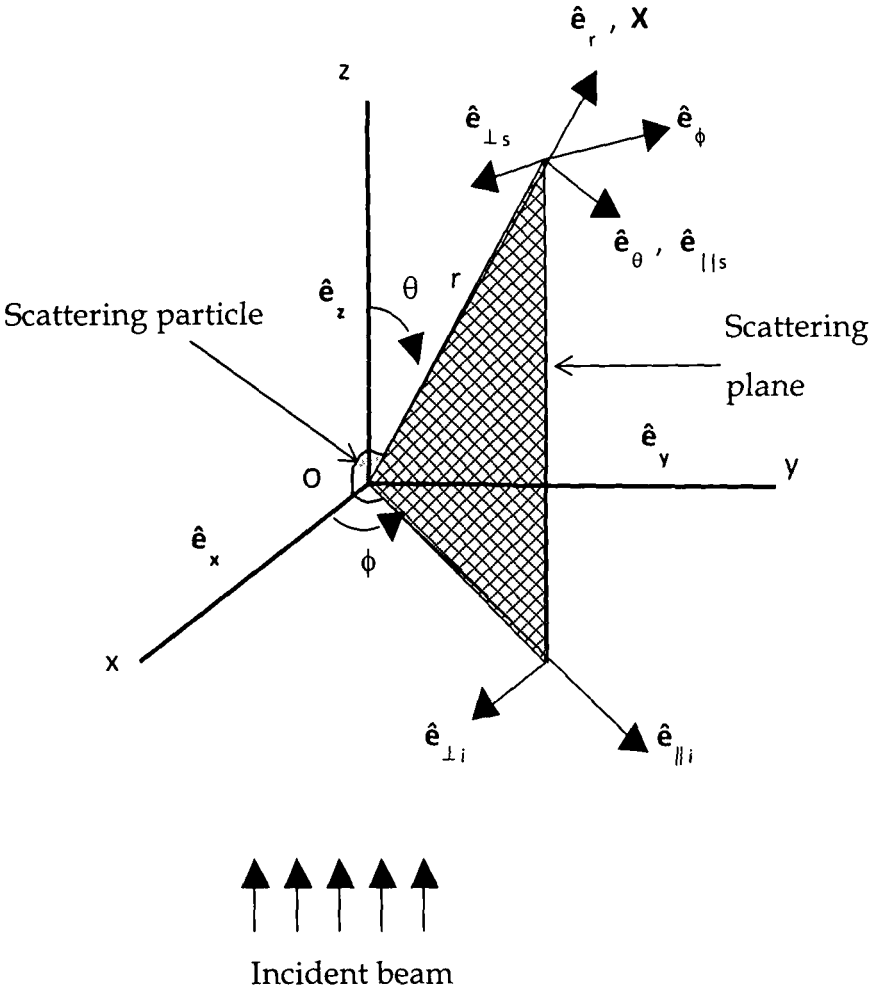

Figure 2.1: Scattering by a particle

Here θ is the scattering angle and $\hat{e}_r$ and $\hat{e}_z$ defines the scattering plane. The scattering plane is distinctively determined by the azimuthal angle φ except when $\hat{e}_r$ is parallel to the z-axis. In these two instances, that is $\hat{e}_r = \pm \hat{e}_z$, any plane containing the z-axis is a suitable scattering plane. The incident field E_i, which lies in the x-y plane can be resolved into parallel component $E_{||i}$, and perpendicular component $E_{\perp i}$ with respect to the scattering plane, thus leading to the relation

$$E_i = (E_{o||}\hat{e}_{||i} + E_{o\perp}\hat{e}_{\perp i})\, e^{(ikz-i\omega t)} = E_{||i}\hat{e}_{||i} + E_{\perp i}\hat{e}_{\perp i} \qquad \textbf{2.2.14}$$

again,

$$\hat{e}_{\perp i} = \sin\varphi\, \hat{e}_x - \cos\varphi\, \hat{e}_y \qquad \textbf{2.2.15}$$

$$\hat{e}_{||i} = \cos\varphi\, \hat{e}_x + \sin\varphi\, \hat{e}_y \qquad \textbf{2.2.16}$$

$$\hat{e}_{\perp i} \times \hat{e}_{||i} = \hat{e}_z \qquad \textbf{2.2.17}$$

$$\hat{e}_{\perp i} = -\,\hat{e}_\varphi \qquad \textbf{2.2.18}$$

$$\hat{e}_{||i} = \sin\theta\, \hat{e}_r + \cos\theta\, \hat{e}_\theta \qquad \textbf{2.2.19}$$

The x and y components of E_i may be denoted by E_{xi} and E_{yi}, which leads to

$$E_{||i} = \cos\varphi\, E_{xi} + \sin\varphi\, E_{yi} \qquad \textbf{2.2.20}$$

$$E_{\perp i} = \sin\varphi\, E_{xi} - \cos\varphi\, E_{yi} \qquad \textbf{2.2.21}$$

In the far field region where $kr>>1$, the scattered field E_s is nearly transverse ($\hat{e}_r.\boldsymbol{E}_s = 0$) and has the asymptotic form [353]

$$E_s \sim (e^{ikr}/-ikr)A \quad kr>>1 \qquad \textbf{2.2.22}$$

where, $\hat{e}_r.A = 0$ and A is the θ and φ dependent vectorial scattering amplitude. Again, $\boldsymbol{E}_s$ in the far field region can be written as

$$E_s = E_{||s}\hat{e}_{||s} + E_{\perp s}\hat{e}_{\perp s} \qquad \textbf{2.2.23}$$

also,

$$\hat{e}_{||s} = \hat{e}_\theta \qquad \textbf{2.2.24}$$

$$\hat{e}_{\perp s} = -\hat{e}_\varphi \qquad \textbf{2.2.25}$$

$$\hat{e}_{\perp s} \times \hat{e}_{||s} = \hat{e}_r \qquad \textbf{2.2.26}$$

where, the basis vectors $\hat{e}_{||s}$ and $\hat{e}_{\perp s}$ are parallel and perpendicular to the scattering plane respectively. Thus, considering the equations 2.2.14 to 2.2.26 the required relation between incident and scattered fields in matrix form may be given as

$$\begin{pmatrix} E_{\parallel s} \\ E_{\perp s} \end{pmatrix} = \frac{e^{ik(r-z)}}{-ikr} \begin{pmatrix} S_2 & S_3 \\ S_4 & S_1 \end{pmatrix} \begin{pmatrix} E_{\parallel i} \\ E_{\perp i} \end{pmatrix} \qquad \textbf{2.2.27}$$

where the matrix elements S_j (j=1,2,3,4) depends on θ and φ. The matrix is the resulting amplitude scattering matrix. The amplitude scattering matrix describes the transformation of θ and φ components of the incident plane-wave into the components of scattered plane-wave. The amplitude scattering matrix depends on the direction of incident and scattered light as well as on the size, morphology, orientation of the scattering object with respect to the coordinate system. The matrix also gives the total field, thereby providing complete description of the scattering pattern.

The relation between the incident and scattered fields is an essential part in the development of the Mueller matrix for scattering, and is derived by taking the case of scattering by a single particle, as shown in figure 2.1. The intensity and polarization of a beam of light can be completely defined by Stokes vector I= (I, Q, U, V), where I is the total intensity, Q is the difference between the polarization intensities at 0° and 90° to the scattering plane, U is the difference between the polarization intensities at +45° and -45° to the scattering plane, and V is the difference between left and right circular polarization intensities [45 - 47].

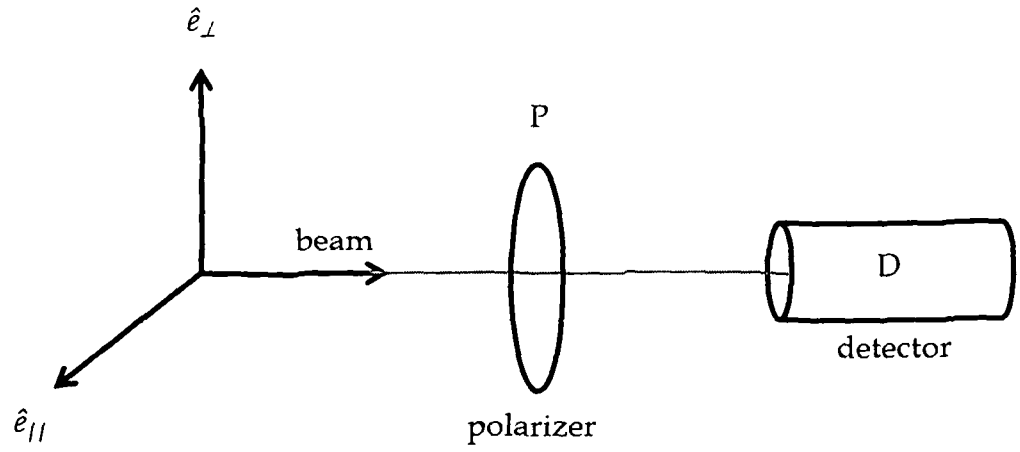

Figure 2.2: Schematic of setup for finding Stokes parameters.

In order to derive the Stokes parameters, a series of hypothetical experiments which can be performed with an arbitrary monochromatic beam, a detector, and various polarizers, in a non-absorbing medium are considered, and shown in figure 2.2. The detector responds to irradiance independently of the polarization state, and the polarizers are assumed to be ideal. The electric field E is referred to horizontal and vertical orthogonal axes, $\hat{e}_{||}$and $\hat{e}_\perp$ respectively, and E_o is given as

$$E_o = E_{||}\hat{e}_{||} + E_\perp\hat{e}_\perp \qquad \textbf{2.2.28}$$

Case 1: With no polarizers.

If there is no polarizer in the beam, the irradiance I recorded by the detector is given by

$$I = I_{||} + I_\perp \qquad \textbf{2.2.29}$$

or using 2.1.12 and 2.1.13 by,

$$I = (k/2\omega\mu_o)(E_{||}E_{||}^* + E_\perp E_\perp^*) \qquad \textbf{2.2.30}$$

Case 2: With horizontal and vertical Polarizers.

Let P be a horizontal polarizer as shown in figure 2.2; the amplitude of the transmitted wave is $E_{//}$and the irradiance $I_{//}$recorded by the detector is $(k/2\omega\mu_o)E_{//}E_{//}^*$. Again, let P be a vertical polarizer; then the amplitude of the transmitted wave is $E_\perp$ and the irradiance $I_\perp$ recorded by the detector is $E_\perp E_\perp^*$. The difference between these two measured irradiances is

$$I_{//} - I_\perp = (k/2\omega\,\mu_o)(E_{//}E_{//}^* - E_\perp E_\perp^*) \qquad \textbf{2.2.31}$$

Case 3: +45° and -45° polarizers.

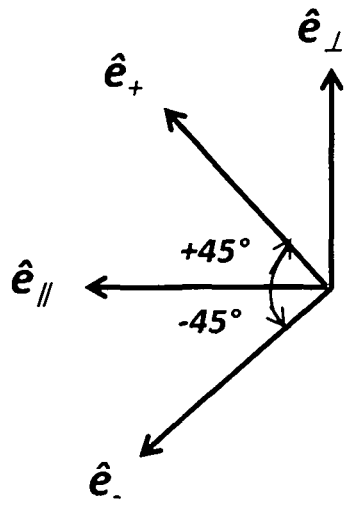

Figure 2.3: Schematic representation of the basis vectors.

An orthonormal set of basis vectors $\hat{e}_+$ and $\hat{e}_-$, which are obtained by rotating $\hat{e}_{//}$ by +45° and -45° , as shown in figure 2.3 may be introduced. Since,

$$\hat{e}_+ = (1/2)^{1/2}(\hat{e}_{//} + \hat{e}_+) \qquad \textbf{2.2.32}$$

$$\hat{e}_- = (1/2)^{1/2}(\hat{e}_{//} - \hat{e}_\perp) \qquad \textbf{2.2.33}$$

Therefore, electric field E_o may be written as

$$E_o = E_+\hat{e}_+ + E_-\hat{e}_- \qquad \textbf{2.2.34}$$

where,

$$E_+ = (1/2)^{1/2} (E_{||} + E_{\perp}) \qquad \textbf{2.2.35}$$

$$E_- = (1/2)^{1/2} (E_{||} - E_{\perp}) \qquad \textbf{2.2.36}$$

Now if P is a +45° polarizer as shown in figure 2.2, then the amplitude of the transmitted wave is

$$(k/2\omega\,\mu_o)(E_{||}E_{||}^* + E_{||}E_{\perp}^* + E_{\perp}E_{||}^* + E_{\perp}E_{\perp}^*)/2 \qquad \textbf{2.2.37}$$

Again, if P is a -45° polarizer then the irradiance of the transmitted wave is

$$I_- = (k/2\omega\,\mu_o)(E_{||}E_{||}^* - E_{||}E_{\perp}^* - E_{\perp}E_{||}^* + E_{\perp}E_{\perp}^*)/2 \qquad \textbf{2.2.38}$$

The difference between these two irradiances is

$$I_+ - I_- = (k/2\omega\,\mu_o)(E_{||}E_{\perp}^* + E_{\perp}E_{||}^*) \qquad \textbf{2.2.39}$$

Case 4: With circular polarizers.

Another set of basis vectors $\hat{e}_R$ and $\hat{e}_L$ are defined as

$$\hat{e}_R = (1/2)^{1/2} (\hat{e}_{||} + i\hat{e}_{\perp}) \qquad \textbf{2.2.40}$$

$$\hat{e}_L = (1/2)^{1/2} (\hat{e}_{||} - i\hat{e}_{\perp}) \qquad \textbf{2.2.41}$$

These basis vectors represent right-circularly and left-circularly polarized waves and are orthonormal in the sense that $\hat{e}_R.\hat{e}_R^* = 1$, $\hat{e}_L.\hat{e}_L^* = 1$, $\hat{e}_R.\hat{e}_L^* = 0$ and $\hat{e}_L.\hat{e}_R^* = 0$. Thus we may write the incident field as

$$E_o = E_R\hat{e}_R + E_L\hat{e}_L \qquad \textbf{2.2.42}$$

where,

$$E_R = (1/2)^{1/2} (E_{||} - iE_{\perp}) \qquad \textbf{2.2.43}$$

$$E_L = (1/2)^{1/2} (E_{||} + iE_{\perp}) \qquad \textbf{2.2.44}$$

Now if P is a right-handed polarizer, then the transmitted irradiance I_R is

$$I_R = (k/2\omega\,\mu_o)(E_{||}E_{||}^{*} - iE_{||}^{*}E_{\perp} + iE_{\perp}^{*}E_{||} + E_{\perp}E_{\perp}^{*})/2 \qquad \textbf{2.2.45}$$

Again if P is a left-handed polarizer, then the transmitted irradiance I_L is

$$I_L = (k/2\omega\,\mu_o)(E_{||}E_{||}^{*} + i\,E_{\perp}E_{||||}^{*} - iE_{||}\,E_{\perp}^{*} + E_{\perp}E_{\perp}^{*})/2 \qquad \textbf{2.2.46}$$

The difference between these two irradiances is

$$I_R - I_L = i(k/2\omega\,\mu_o)(\,E_{\perp}^{*}E_{||} - E_{||}^{*}E_{\perp}) \qquad \textbf{2.2.47}$$

Therefore the required Stokes parameters I, Q, U, V are

$$I = (k/2\omega\,\mu_o)(E_{||}E_{||}^{*} + E_{\perp}E_{\perp}^{*}) \qquad \textbf{2.2.48}$$

$$Q = (k/2\omega\,\mu_o)(E_{||}E_{||}^{*} - E_{\perp}E_{\perp}^{*}) \qquad \textbf{2.2.49}$$

$$U = (k/2\omega\,\mu_o)(E_{||}E_{\perp}^{*} + E_{\perp}E_{||}^{*}) \qquad \textbf{2.2.50}$$

$$V = i(k/2\omega\,\mu_o)(E_{||}E_{\perp}^{*} - E_{\perp}E_{||}^{*}) \qquad \textbf{2.2.51}$$

Now, a physically realizable Stokes vector must satisfy the condition $I^2 \geq Q^2 + U^2 + V^2$ [74]. This inequality can be expressed as

$$P = \frac{\sqrt{Q^2+U^2+V^2}}{I} \leq 1 \qquad \textbf{2.2.52}$$

where, P is the *degree of polarization* of the scattered light [45]. When P equals 1, the light is entirely polarized. Again, the *degree of linear polarization*, and *circular polarization* are given by respective equations

$$P_{lp} = \frac{\sqrt{Q^2+U^2}}{I} \leq 1 \qquad \textbf{2.2.53}$$

$$P_{cp} = \frac{V}{I} \leq 1 \qquad \textbf{2.2.54}$$

where, $\sqrt{Q^2+U^2+V^2}$, $\sqrt{Q^2+U^2}$, and V represents the intensity of the total polarized, linearly polarized, and circularly polarized light respectively. When $U = 0$, the degree of linear polarization takes the form

$$P_{lp} = \frac{Q}{I} \leq 1 \qquad 2.2.55$$

Moreover, for $U = 0$, we can express P_{lp} as [45, 47],

$$P_{lp} = -\frac{Q}{I} = \frac{I_\perp - I_\parallel}{I} \qquad 2.2.56$$

or, $$P_{lp} = \frac{I_\perp - I_\parallel}{I} = \frac{I_\perp - I_\parallel}{I_\perp + I_\parallel} \qquad 2.2.57$$

where, $I_{//}$ and $I_{\perp}$ are the intensities of scattered light parallel and perpendicular to the scattering plane respectively.

Now, in case of scattering of the incident field by a particle the time averaged Poynting vector S at any point in the medium surrounding the particle can be written as the sum of three terms.

$$S = (1/2)Re(E_2 \times H_2) = S_i + S_s + S_{ext} \qquad 2.2.58$$

where,

$$S_i = (1/2)Re(E_i \times H_i^*) \qquad 2.2.59$$

$$S_s = (1/2)Re(E_s \times H_s^*) \qquad 2.2.60$$

$$S_{ext} = (1/2)Re(E_i \times H_s^* + E_s \times H_i^*) \qquad 2.2.61$$

where, S_i is the Poynting vector associated with the incident wave and is independent of position if the medium is non-absorbing. S_s is the poynting vector of the scattered field and S_{ext} is the poynting vector arising because of interaction between the incident and scattered waves. E_i and H_i represents the incident with and E_s and H_s represents the scattered field. If a suitably collimated detector of detector area ΔA is placed at a distance r from the particle in the far field region, with ΔA aligned normal to $\hat{e}_r$, and if $\hat{e}_r$ is not too near the forward direction $\hat{e}_z(\theta = 0^\circ)$, the detector will record a signal proportional to

$$S_s.\hat{e}_r \Delta A \qquad 2.2.62$$

on condition that ΔA is sufficiently small such that S_s does not vary greatly over the detector. From 2.2.22, and 2.2.59 to 2.2.60 it follows that

$$\mathbf{S}_s.\hat{\mathbf{e}}_r \Delta A = \frac{k}{2\omega\mu_0}\frac{|\mathbf{A}|^2}{k^2}\Delta\Omega \qquad \textbf{2.2.63}$$

where

$$\Delta\Omega = \Delta A/r^2 \qquad \textbf{2.2.64}$$

is the solid angle subtended by the detector . Hence it is possible to obtain $|A|^2$ as a function of direction, to within a solid angle $\Delta\Omega$ by recording the detector response at various positions on a hemisphere surrounding the particle. By incorporating various polarizers in front of the detector and proceeding in a manner identical to the method used in finding relations 2.2.48 to 2.2.51, the Stokes parameters of the light scattered by a particle is obtained as

$$I_s = (k/2\omega\,\mu_o)(E_{\parallel s}E_{\parallel s}^* + E_{\perp s}E_{\perp s}^*) \qquad \textbf{2.2.65}$$

$$Q_s = (k/2\omega\,\mu_o)(E_{\parallel s}E_{\parallel s}^* - E_{\perp s}E_{\perp s}^*) \qquad \textbf{2.2.66}$$

$$U_s = (k/2\omega\,\mu_o)(E_{\parallel s}E_{\perp s}^* + E_{\perp s}E_{\parallel s}^*) \qquad \textbf{2.2.67}$$

$$V_s = i(k/2\omega\,\mu_o)(E_{\parallel s}E_{\perp s}^* - E_{\perp s}E_{\parallel s}^*) \qquad \textbf{2.2.68}$$

Thus relations 2.2.27, 2.1.48 - 2.1.51 and 2.2.65 - 2.2.68 yields

$$\begin{pmatrix} I_s \\ Q_s \\ U_s \\ V_s \end{pmatrix} = \frac{1}{k^2r^2}\begin{pmatrix} S_{11} & S_{12} & S_{13} & S_{14} \\ S_{21} & S_{22} & S_{23} & S_{24} \\ S_{31} & S_{32} & S_{33} & S_{34} \\ S_{41} & S_{42} & S_{43} & S_{44} \end{pmatrix}\begin{pmatrix} I_i \\ Q_i \\ U_i \\ V_i \end{pmatrix} \qquad \textbf{2.2.69}$$

where

$$S_{11} = (1/2)(|S_1|^2 + |S_2|^2 + |S_3|^2 + |S_4|^2) \qquad \textbf{2.2.70}$$

$$S_{12} = (1/2)(|S_2|^2 - |S_1|^2 + |S_4|^2 - |S_3|^2) \qquad \textbf{2.2.71}$$

$$S_{13} = Re(S_2S_3^* + S_1S_4^*) \quad \textbf{2.2.72}$$

$$S_{14} = Im(S_2S_3^* - S_1S_4^*) \quad \textbf{2.2.73}$$

$$S_{21} = (1/2)(|S_2|^2 - |S_1|^2 - |S_4|^2 + |S_3|^2) \quad \textbf{2.2.74}$$

$$S_{22} = (1/2)(|S_2|^2 + |S_1|^2 - |S_4|^2 - |S_3|^2) \quad \textbf{2.2.75}$$

$$S_{23} = Re(S_2S_3^* - S_1S_4^*) \quad \textbf{2.2.76}$$

$$S_{24} = Im(S_2S_3^* + S_1S_4^*) \quad \textbf{2.2.77}$$

$$S_{31} = Re(S_2S_4^* + S_1S_3^*) \quad \textbf{2.2.78}$$

$$S_{32} = Re(S_2S_4^* - S_1S_3^*) \quad \textbf{2.2.79}$$

$$S_{33} = Re(S_1S_2^* + S_3S_4^*) \quad \textbf{2.2.80}$$

$$S_{34} = Im(S_2S_1^* + S_4S_3^*) \quad \textbf{2.2.81}$$

$$S_{41} = Im(S_2^* S_4 + S_3^* S_1) \quad \textbf{2.2.82}$$

$$S_{42} = Im(S_2^* S_4 - S_3^* S_1) \quad \textbf{2.2.83}$$

$$S_{43} = Im(S_1S_2^* - S_3S_4^*) \quad \textbf{2.2.84}$$

$$S_{44} = Re(S_1S_2^* - S_3S_4^*) \quad \textbf{2.2.85}$$

Thus the required 4×4 scattering matrix is represented by equation 2.2.69, and is the Mueller matrix for scattering by a single particle. The Mueller matrix represents the transformation performed on the incident Stokes parameters by the particles in the scattering volume, as a result of single scattering event [47]. The elements of the matrix carry the signature of the scatterer and this scattering information can reveal the characteristics of the scatterer. It is possible to calculate each element of the matrix as a function of the scattering angle, along with proper adjustment of the delivering and collection optics combinations as shown in figure 2.4 [354]. In this figure, the scattering matrix elements of a particle is measured by using an arrangement of polarizer to select the state of polarization of the incident light, an analyzer

to pass the desired state of polarization of the scattered light for detection, and a photo-detector which should essentially be insensitive to the polarization.

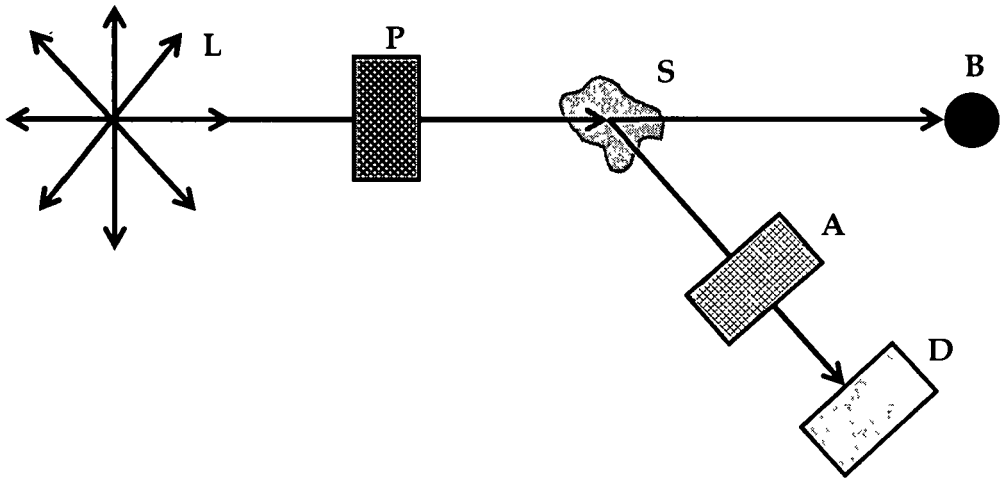

Figure 2.4: Schematic diagram of arrangement for determining of Mueller matrix arrangement. **L**: Randomly polarized incident laser beam; **P**: Polarizer; **S**: Scattering centre; **B**: Beam stop; **A**: Analyzer; **D**: Polarization insensitive photodetector.

The equivalent mathematical expression of the arrangement in figure 2.4 is given by

$$I_s(\theta) = \left[\frac{1}{kD^2}\right] S_A S(\theta) S_P I_i \qquad 2.2.86$$

where, I_s and I_i are the Stokes vector of the scattered and incident light respectively, θ is the scattering angle, S_A and S_P are the Mueller matrices of the analyzer and polarizer respectively [239].

The elements S_{11} and S_{12} are related to the measurements made by the designed and fabricated light scattering system. When equation 2.2.69 is used in developing the Mie theory, one can realize the possibility of measurements of these elements. If the individual particles have spherical symmetry, the Mueller matrix which is a function of the scattering angle θ (given by equation 2.2.69) reduces to a form containing eight non-zero elements out of which six elements are independent [45]. The angular dependence of various elements of the scattering matrix either provide a direct measure of the physical

properties of the scattering medium, or are indicative of their physical properties such as size, shape, surface morphology, and also optical properties such as refractive index etc.[46].The elements may be described in the table below.

Table 2.1: Scattering matrix elements and their interpretation.

S_{11}	Transformation of total intensity of incident light; element is proportional to the phase function; provides information about the general size.
S_{12}	Depolarization of linearly polarized light parallel and perpendicular to the scattering plane (S_{21} is the reverse case); dependent on size, shape and complex refractive index of the scatterers.
S_{13}	Depolarization of linearly polarized light ±45° to the scattering plane(S_{31} is the reverse case); orientation effects can cause non-zero elements.
S_{14}	Depolarization of circularly polarized light (S_{41} is the reverse case); presence of optical activity indicated by presence of non-zero element; helical structures; circular intensity differential scattering (CIDS) measures ($-S_{14}/S_{11}$); most often zero for non-oriented ensembles of particles.
S_{22}	Transformation of linearly polarized incident light (±90°) to linearly polarized scattered light (±90°); deviation from S_{11} is an important indication of presence of non-spherical particles.
S_{23} , S_{32}	Transformation of linearly polarized incident light (±45°) to linearly polarized scattered light (±90°)(S_{32} is the reverse case); non-zero element indicates presence of non-random orientation of particles.
S_{24} , S_{42}	Transformation of circularly polarized incident light to linearly polarized scattered light (±90°)(S_{42} is the reverse case); non-zero element indicates presence of non-random orientation of particles.
S_{34} , S_{43}	Transformation of circularly polarized incident light to linearly polarized scattered light (±45°)(S_{43} is the reverse case); element is strongly dependent on size and complex refractive index of the scatterers.
S_{33},	Transformation of linearly polarized incident light (±45°) to linearly polarized scattered light (±45°); deviation from S_{44} is an important indication of presence of non-spherical symmetry.
S_{44}	Transformation of circularly polarized incident light to circularly polarized scattered light; deviation from S_{33} is an important indication of presence of non-spherical symmetry.

2.3 Extinction, Absorption and Scattering: An overview

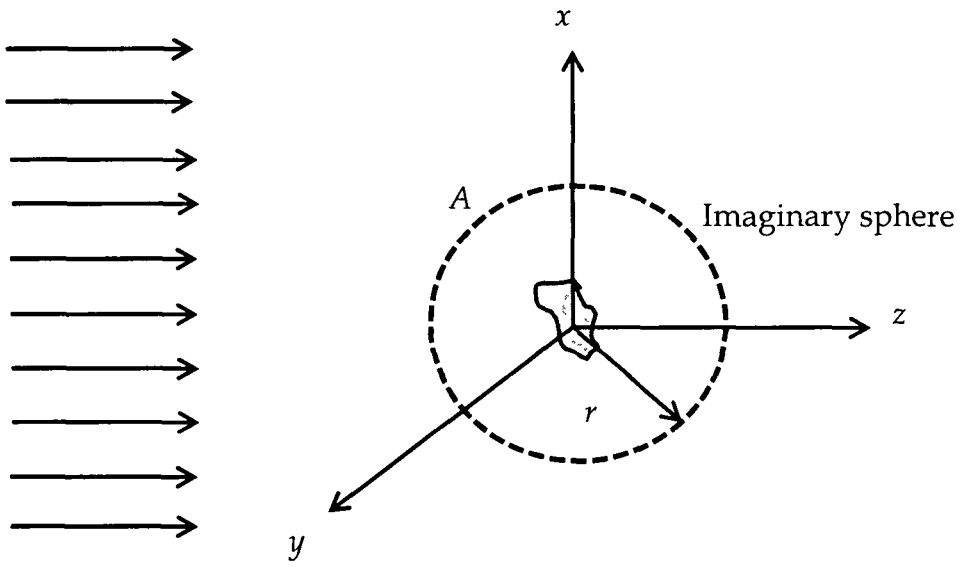

Figure 2.5: Extinction by a single particle.

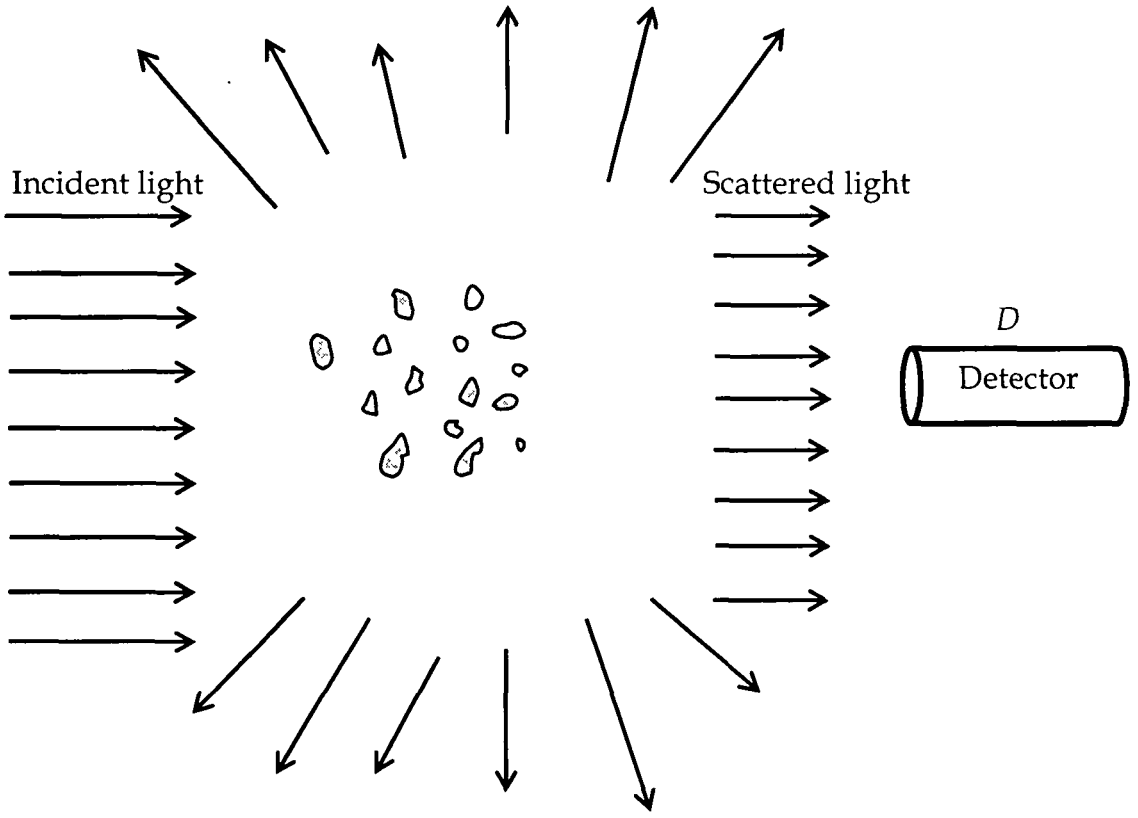

Figure 2.6: Extinction by a collection of particles.

When one or more particles are placed in a beam of electromagnetic radiation, electromagnetic energy received by a detector D downstream from the particles (shown in figures 2.5 and 2.6), and the rate at which the energy is received by the detector may be denoted by U. If the particles are removed, the power received by the detector is U_o, where $U_o > U$. Thus, the presence of the particles results in *extinction* of the incident beam. If the medium in which the particles are embedded is non-absorbing, the difference $U_o - U$ is accounted for by *absorption* in the particles, and *scattering* by the particles. This extinction depends upon the chemical composition of the particles, and their size, shape, refractive index, orientation, the surrounding medium, density, polarization state, and frequency of the incident beam.

Let us now consider the case of extinction by a single arbitrary particle. In order to investigate extinction by a single arbitrary particle embedded in a non-absorbing medium, and illuminated by a plane wave, an imaginary sphere of radius r is constructed around the particle as in figure 2.5. Then the net rate W_a at which electromagnetic energy crosses the surface A_{sph} of this sphere is

$$W_a = -\int_{A_{sph}} \mathbf{S}.\hat{\mathbf{e}}_r dA \qquad \textbf{2.3.1}$$

where S is the Poynting vector. If $W_a > 0$, energy is absorbed within the sphere. But the medium is non-absorbing, which implies that W_a is the rate at which energy is absorbed by the particle. Because of the Stoke's parameters 2.2.48-2.2.51 and Poynting vectors 2.2.58-2.2.61, W_a may be written as the sum of three terms

$$W_i = -\int_{A_{sph}} \mathbf{S}_i.\hat{\mathbf{e}}_r dA \qquad \textbf{2.3.2}$$

$$W_s = \int_{A_{sph}} \mathbf{S}_s.\hat{\mathbf{e}}_r dA \qquad \textbf{2.3.3}$$

and

$$W_{ext} = -\int_{A_{sph}} \mathbf{S}_{ext} . \hat{\mathbf{e}}_r \, dA \qquad \textbf{2.3.4}$$

Now, W_t vanishes identically for a non-absorbing medium. W_s defines the rate at which energy is scattered across the surface A_{sph}. Therefore W_{ext} is the sum of the rate of energy absorbed and scattered. Thus,

$$W_{ext} = W_a + W_s \qquad \textbf{2.3.5}$$

The incident electric field $\boldsymbol{E}_i = E\hat{e}_x$ is taken to be x-polarized for convenience. As the medium is non-absorbing, W_a is independent of the radius r of the imaginary sphere. Therefore r may be chosen to be sufficiently large such that it is in the far-field region where

$$E_s \sim \frac{e^{ik(r-z)}}{-ikr} XE \qquad \textbf{2.3.6}$$

$$H_s \sim \frac{k}{\omega\mu} \hat{\mathbf{e}}_r \times E_s \qquad \textbf{2.3.7}$$

and $\hat{e}_r$. $X = 0$. As a reminder that the incident light is x-polarized, the symbol X is used for the *vector scattering amplitude*. As $kr \to \infty$ the limiting values of W_{ext} becomes [45]

$$W_{ext} = I_i \, (4\pi/k^2) \, Re\{(X.\hat{e}_x)_{\theta=0}\} \qquad \textbf{2.3.8}$$

where I_i is the incident irradiance. Now, the cross-section of extinction, C_{ext} ,which has dimension of area becomes

$$C_{ext} = W_{ext} / I_i = (4\pi/k^2) \, Re\{(X.\hat{e}_x)_{\theta=0}\} \qquad \textbf{2.3.9}$$

By the analogy of equation 2.3.5, C_{ext} may be written as the sum of C_{abs}, the cross-section of absorption, and C_{sca} , the cross-section of scattering.

$$C_{ext} = C_{abs} + C_{sca} \qquad \textbf{2.3.10}$$

where

$$C_{abs} = W_{abs} / I_i \qquad \textbf{2.3.11}$$

and

$$C_{sca} = W_s / I_i \qquad \textbf{2.3.12}$$

From 2.2.2-2.2.4 and 2.2.6-2.2.7 we have,

$$C_{sca} = \int_0^{2\pi}\int_0^{\pi} \frac{|\mathbf{X}|^2}{k^2 r^2} r^2 \sin\theta \, d\theta \, d\phi = \int_{4\pi} \frac{|\mathbf{X}|^2}{k^2} d\Omega \qquad \textbf{2.3.13}$$

The quantity $|\mathbf{X}|^2 / k^2$ is the differential scattering cross-section and $dC_{sca}/d\Omega$ physically specifies the angular distribution of the scattered light, that is, the amount of light for unit incident irradiance scattered into a unit solid angle about a given direction.

Now if N is the number of particles per unit volume of the medium through which extinction of light is taking place then the irradiance is attenuated according to the expression (2.2.10) , which can be represented using 2.3.10 - 2.3.13 as

$$I = I_o e^{-\sigma z} \qquad \textbf{2.3.14}$$

where

$$\sigma = NC_{ext} = NC_{abs} + NC_{sca} \qquad \textbf{2.3.15}$$

is the extinction co-efficient. The extinction co-efficient for a mixture of different particles may be represented as

$$\sigma = \sum_j N_j C_{ext,j} \qquad \textbf{2.3.16}$$

where N_j is the number of particles of type j per unit volume and $C_{ext,j}$ is the corresponding extinction cross-section.

2.4 Mie theory

Mie theory is most suitable for investigation of small particulate matter, and to successfully explain extinction and scattering by such particles, which are mostly spherical at the detectable levels [45, 48, 74]. In this thesis, Rayleigh and Raman scattering are left out as the particles being investigated were neither very small nor possessed the appropriate density to be explained by these two theories.

It is noteworthy that scattered radiation behaves as a spherical wave in the far-field zone, and thus the problem of light scattering is solved in spherical coordinate system. Now, because of the linearity of Maxwell equations, the electric fields (incident field E_i, scattered field E_s , and inner field E_{in}) can be expanded in vector spherical harmonics, generating complete set of linear combinations. Mie theory begins by expanding the incident plane x-polarized wave given by

$$\boldsymbol{E}_i = E_o e^{(ikz - i\omega t)} \hat{\boldsymbol{e}}_x \qquad \textbf{2.4.1}$$

And expressed in spherical polar co-ordinates as

$$\boldsymbol{E}_i = E_o e^{ikr\cos\omega} \hat{\boldsymbol{e}}_x \qquad \textbf{2.4.2}$$

where

$$\hat{\boldsymbol{e}}_x = \sin\theta \cos\varphi \, \hat{e}_r + \cos\theta \cos\varphi \hat{e}_\theta - \sin\varphi \hat{e}_\varphi \qquad \textbf{2.4.3}$$

$\boldsymbol{E}_i$ is expressed in vector spherical harmonics as,

$$\mathbf{E}_i = \sum_{m=0}^{\infty} \sum_{n=m}^{\infty} (a_{emn} \mathbf{M}_{emn} + a_{omn} \mathbf{M}_{omn} + b_{emn} \mathbf{N}_{emn} + b_{omn} \mathbf{N}_{omn}) \qquad \textbf{2.4.4}$$

$\boldsymbol{E}_s$ is expressed in vector spherical harmonics as,

$$\mathbf{E}_s = \sum_{m=0}^{\infty} \sum_{n=m}^{\infty} (p_{emn} \mathbf{M}_{emn} + p_{omn} \mathbf{M}_{omn} + q_{emn} \mathbf{N}_{emn} + q_{omn} \mathbf{N}_{omn}) \qquad \textbf{2.4.5}$$

and $\boldsymbol{E}_{in}$ is expressed in vector spherical harmonics as,

$$\mathbf{E}_{in} = \sum_{m=0}^{\infty}\sum_{n=m}^{\infty}(c_{emn}\mathbf{M}_{emn} + c_{omn}\mathbf{M}_{omn} + d_{emn}\mathbf{N}_{emn} + d_{omn}\mathbf{N}_{omn}) \qquad \textbf{2.4.6}$$

with the vector spherical harmonics being given by the relations,

$$\mathbf{M}_{emn} = \frac{-m}{\sin\theta}\sin m\phi P_n^m(\cos\theta)z_n(\rho)\hat{\mathbf{e}}_\theta - \cos m\phi\frac{dP_n^m(\cos\theta)}{d\theta}z_n(\rho)\hat{\mathbf{e}}_\phi$$

2.4.7

$$\mathbf{M}_{omn} = \frac{m}{\sin\theta}\cos m\phi P_n^m(\cos\theta)z_n(\rho)\hat{\mathbf{e}}_\theta - \sin m\phi\frac{dP_n^m(\cos\theta)}{d\theta}z_n(\rho)\hat{\mathbf{e}}_\phi$$

2.4.8

$$\begin{aligned}\mathbf{N}_{emn} = {} & \frac{z_n(\rho)}{\rho}\cos m\phi n(n+1)P_n^m(\cos\theta)\hat{\mathbf{e}}_r \\ & + \cos m\phi\frac{dP_n^m(\cos\theta)}{d\theta}\frac{1}{\rho}\frac{d}{d\rho}[\rho z_n(\rho)]\hat{\mathbf{e}}_\theta \\ & - m\sin m\phi\frac{P_n^m(\cos\theta)}{\sin\theta}\frac{1}{\rho}\frac{d}{d\rho}[\rho z_n(\rho)]\hat{\mathbf{e}}_\phi\end{aligned}$$

2.4.9

$$\begin{aligned}\mathbf{N}_{omn} = {} & \frac{z_n(\rho)}{\rho}\sin m\phi n(n+1)P_n^m(\cos\theta)\hat{\mathbf{e}}_r \\ & + \sin m\phi\frac{dP_n^m(\cos\theta)}{d\theta}\frac{1}{\rho}\frac{d}{d\rho}[\rho z_n(\rho)]\hat{\mathbf{e}}_\theta \\ & + m\cos m\phi\frac{P_n^m(\cos\theta)}{\sin\theta}\frac{1}{\rho}\frac{d}{d\rho}[\rho z_n(\rho)]\hat{\mathbf{e}}_\phi\end{aligned}$$

2.4.10

where, P_n^m are the Associated Legendre Polynomials of degree n and order m, z_n is a Bessel function, $\rho = kr$, k being the propagation constant, is a dimensionless parameter. a_{emn} , a_{omn} , b_{emn} and b_{omn} are the expansion co-efficient of the incident field, p_{emn} , p_{omn} , q_{emn} and q_{omn} are the expansion co-efficient of the scattered field, and c_{emn} , c_{omn} , d_{emn} and d_{omn} are the expansion co-efficient of the inner field respectively. The orthogonality of all the vector

spherical harmonics implies that the expansion co-efficients in 2.4.4 are of the form

$$a_{emn} = \frac{\int_0^{2\pi}\int_0^{\pi} \mathbf{E}_i . \mathbf{M}_{emn} \sin\theta \, d\theta \, d\phi}{\int_0^{2\pi}\int_0^{\pi} |\mathbf{M}_{emn}|^2 \sin\theta \, d\theta \, d\phi} \qquad \textbf{2.4.11}$$

with similar expressions for a_{omn} , b_{emn} and b_{omn}. It follows from 2.4.3, 2.4.6 and 2.4.9, together with the orthogonality of sine and cosine, that $a_{emn} = b_{omn} = 0$ for all m and n. Moreover, the remaining co-efficients vanish unless m=1 for the same reason.

The expansion coefficients that finally remain after calculation are

$$a_{o1n} = i^n E_0 \frac{2n+1}{n(n+1)} \qquad \textbf{2.4.12}$$

and

$$b_{e1n} = -iE_0 i^n \frac{2n+1}{n(n+1)} \qquad \textbf{2.4.13}$$

Now since the incident field is finite at the origin it is required that, from the two spherical Bessel functions [355]

$$j_n(\rho) = \sqrt{\frac{\pi}{2\rho}} J_{n+1/2}(\rho) \qquad \textbf{2.4.14}$$

and

$$y_n(\rho) = \sqrt{\frac{\pi}{2\rho}} Y_{n+1/2}(\rho) \qquad \textbf{2.4.15}$$

where J_ν and Y_ν are the Bessel functions of first and second kind, z_n in the vector spherical harmonics be the spherical Bessel funtion $j_n(\rho)$ as it is well

behaved at the origin. Since the spherical Bessel function satisfy the recurrence relations

$$z_{n-1}(\rho) + z_{n+1}(\rho) = \frac{2n+1}{\rho} z_n(\rho) \qquad \textbf{2.4.16}$$

and

$$(2n+1)\frac{d}{d\rho} z_n(\rho) = n z_{n-1}(\rho) - (n+1) z_{n+1}(\rho) \qquad \textbf{2.4.17}$$

from the first two orders,

$j_0(\rho) = (\sin \rho)/\rho$ and $j_1(\rho) = \sin\rho/\rho^2 - \cos \rho$

$y_0(\rho) = -(\cos \rho)/\rho$ and $y_1(\rho) = -\cos \rho)/\rho^2 - (\sin \rho)/\rho$

higher order terms can be generated. Hence the superscript (1) is appended to vector spherical harmonics involving $j_n(\rho)$. The expansion of the plane wave in spherical harmonics finally takes the form

$$\mathbf{E}_i = E_0 \sum_{n=1}^{\infty} i^n \frac{2n+1}{n(n+1)} (\mathbf{M}_{o1n}^{(1)} - i\mathbf{N}_{e1n}^{(1)}) \qquad \textbf{2.4.18}$$

and the corresponding incident magnetic field is obtained from the curl of **2.3.18** as

$$\mathbf{H}_i = \frac{-k}{\omega\mu} E_0 \sum_{n=1}^{\infty} i^n \frac{2n+1}{n(n+1)} (\mathbf{M}_{e1n}^{(1)} + i\mathbf{N}_{o1n}^{(1)}) \qquad \textbf{2.4.19}$$

When the plane x-polarized wave is incident on a homogeneous, isotropic sphere of radius a, the fields inside the particle are given as

$$\mathbf{E}_{in} = \sum_{n=1}^{\infty} E_n (c_n \mathbf{M}_{o1n}^{(1)} - i d_n \mathbf{N}_{e1n}^{(1)}) \qquad \textbf{2.4.20}$$

and

$$\mathbf{H}_{in} = \frac{-k}{\omega\mu_1}\sum_{n=1}^{\infty} E_n(d_n\mathbf{M}_{e1n}^{(1)} + ic_n\mathbf{N}_{o1n}^{(1)}) \qquad \textbf{2.4.21}$$

where, $E_n = i^n E_0 \frac{(2n+1)}{n(n+1)}$, μ_1 is the permeability of the sphere and c_n and d_n are the expansion co-efficients. In case of the scattered field the expressions arrived at are

$$\mathbf{E}_s = \sum_{n=1}^{\infty} E_n(ia_n\mathbf{N}_{e1n}^{(2)} + b_n\mathbf{M}_{o1n}^{(2)}) \qquad \textbf{2.4.22}$$

and

$$\mathbf{H}_s = \frac{k}{\omega\mu}\sum_{n=1}^{\infty} E_n(ib_n\mathbf{N}_{o1n}^{(2)} + a_n\mathbf{M}_{e1n}^{(2)}) \qquad \textbf{2.4.23}$$

where a_n and b_n are the expansion co-efficients and the superscript (2) appended to the vector spherical harmonics indicate that the Bessel function z_n in these harmonics is the spherical Hankel function

$$h_n(kr) \sim \frac{(-i)e^{ikr}}{ikr} \qquad kr>>n^2 \qquad \textbf{2.4.24}$$

For simplifying the vector spherical harmonics it is found to be convenient to define two functions

$$\pi_n = \frac{P_n^1}{\sin\theta} \qquad \textbf{2.4.25}$$

and

$$\tau_n = \frac{d}{d\theta}P_n^1 \qquad \textbf{2.4.26}$$

which can be computed by beginning with π_0=0 and π_1=1 since they follow the recurrence relations

$$\pi_n = \frac{2n-1}{n-1}\mu\pi_{n-1} - \frac{n}{n-1}\pi_{n-2} \qquad \textbf{2.4.27}$$

$$\tau_n = n\mu\pi_n - (n+1)\pi_{n-1} \qquad \textbf{2.4.28}$$

where $\mu = \cos\theta$ **2.4.29**

$$\pi_n(-\mu) = (-1)^{n-1}\pi_n(\mu) \qquad \textbf{2.4.30}$$

$$\tau_n(-\mu) = (-1)^n\tau_n(\mu) \qquad \textbf{2.4.31}$$

and $\pi_n + \tau_n$ and $\pi_n - \tau_n$ are orthogonal **2.4.32**

The vector spherical harmonics 2.4.7 - 2.4.10 with m=1 in the expansions of the internal fields 2.4.20 and 2.4.21 and the scattered fields 2.4.22 and 2.4.23 can now be written in a more concise form as

$$\mathbf{M}_{o1n} = \cos\phi\,\pi_n(\cos\theta)z_n(\rho)\hat{\mathbf{e}}_\theta - \sin\phi\,\tau_n(\cos\theta)z_n(\rho)\hat{\mathbf{e}}_\phi \qquad \textbf{2.4.33}$$

$$\mathbf{M}_{e1n} = -\sin\phi\,\pi_n(\cos\theta)z_n(\rho)\hat{\mathbf{e}}_\theta - \cos\phi\,\tau_n(\cos\theta)z_n(\rho)\hat{\mathbf{e}}_\phi \qquad \textbf{2.4.34}$$

$$\mathbf{N}_{o1n} = \sin\phi\,n(n+1)\sin\theta\,\pi_n(\cos\theta)\frac{z_n(\rho)}{\rho}\hat{\mathbf{e}}_r + \sin\phi\,\tau_n(\cos\theta)\frac{[\rho\,z_n(\rho)]'}{\rho}\hat{\mathbf{e}}_\theta + \cos\phi\,\pi_n(\cos\theta)\frac{[\rho\,z_n(\rho)]'}{\rho}\hat{\mathbf{e}}_\phi \qquad \textbf{2.4.35}$$

$$\mathbf{N}_{e1n} = \cos\phi\,n(n+1)\sin\theta\,\pi_n(\cos\theta)\frac{z_n(\rho)}{\rho}\hat{\mathbf{e}}_r + \cos\phi\,\tau_n(\cos\theta)\frac{[\rho\,z_n(\rho)]'}{\rho}\hat{\mathbf{e}}_\theta - \sin\phi\,\pi_n(\cos\theta)\frac{[\rho\,z_n(\rho)]'}{\rho}\hat{\mathbf{e}}_\phi \qquad \textbf{2.4.36}$$

where the prime indicates differentiation, a process that is aided by the identity

$$\frac{d}{d\rho}z_n = \frac{n\,z_{n-1} - (n+1)z_{n+1}}{2n+1} \qquad \textbf{2.4.37}$$

Now the boundary conditions at the boundary between the spherical particle and the medium are given as

$$(\boldsymbol{E}_i + \boldsymbol{E}_s - \boldsymbol{E}_1) \times \hat{\boldsymbol{e}}_r = 0 \qquad \textbf{2.4.38}$$

$$(\boldsymbol{H}_i + \boldsymbol{H}_s - \boldsymbol{H}_1) \times \hat{\boldsymbol{e}}_r = 0 \qquad \textbf{2.4.39}$$

and may be written in component form as

$$E_{i\theta} + E_{s\theta} = E_{1\theta} \qquad \textbf{2.4.40}$$

$$E_{i\varphi} + E_{s\varphi} = E_{1\varphi} \qquad \textbf{2.4.41}$$

$$H_{i\theta} + H_{s\theta} = H_{1\theta} \qquad \textbf{2.4.42}$$

$$H_{i\varphi} + H_{s\varphi} = H_{1\varphi} \qquad \textbf{2.4.43}$$

Hence from the orthogonality of $\sin\varphi$ and $\cos\varphi$, the orthogonality relations 2.4.32, the boundary conditions 2.4.40 - 2.4.43, the expansions 2.4.18 - 2.4.23 and the expressions 2.4.33 - 2.4.36 for the vector spherical harmonics, four linear equations are eventually obtained in the expansion coefficients as

$$j_n(mx)c_n + h_n(x)b_n = j_n(x) \qquad \textbf{2.4.44}$$

$$\mu[mxj_n(mx)]'c_n + \mu_1[xh_n(x)]'b_n = \mu_1[xj_n(x)]' \qquad \textbf{2.4.45}$$

$$\mu m j_n(mx)d_n + \mu_1 h_n(x)a_n = \mu_1 j_n(x) \qquad \textbf{2.4.46}$$

$$[mxj_n(mx)]'d_n + m[xh_n(x)]'a_n = m[xj_n(x)]' \qquad \textbf{2.4.47}$$

where the prime indicates differentiation with respect to the argument in parenthesis and the size parameter x and the relative refractive index m are

$$x = ka = \frac{2\pi Na}{\lambda} \qquad \textbf{2.4.48}$$

$$m = \frac{k_1}{k} = \frac{N_1}{N} \qquad \textbf{2.4.49}$$

and N_1 and N are the refractive indices of particle and medium, respectively. Solving the four simultaneous equations 2.4.44 - 2.4.47, the scattering coefficients are obtained as

$$a_n = \frac{\mu m^2 j_n(mx)[xj_n(x)]' - \mu_1 j_n(x)[mxj_n(mx)]'}{\mu m^2 j_n(mx)[xh_n(x)]' - \mu_1 h_n(x)[mxj_n(mx)]'} \qquad \textbf{2.4.50}$$

$$b_n = \frac{\mu_1 j_n(mx)[xj_n(x)]' - \mu j_n(x)[mxj_n(mx)]'}{\mu_1 j_n(mx)[xh_n(x)]' - \mu h_n(x)[mxj_n(mx)]'} \qquad \textbf{2.4.51}$$

These coefficients are further simplified by introducing the Riccati-Bessel functions [48]

$$\psi_n(\rho) = \rho\, j_n(\rho) \qquad \textbf{2.4.52}$$

and $\xi_n(\rho) = \rho\, h_n(\rho)$ **2.4.53**

with ξ_n also represented as,

$$\xi_n = \psi_n - i\chi_n \qquad \textbf{2.4.54}$$

where $\chi_n(\rho = -\rho y_n(\rho)$ is a Ricatti-Bessel function with y_n given by 2.4.15. If the permeability μ_1 and μ of the particle and the surrounding medium, respectively, is the same , then 2.4.50 and 2.3.51 become

$$a_n = \frac{m\psi_n(mx)\psi_n'(x) - \psi_n(x)\psi_n'(mx)}{m\psi_n(mx)\xi_n'(x) - \xi_n(x)\psi_n'(mx)} \qquad \textbf{2.4.55}$$

$$b_n = \frac{\psi_n(mx)\psi_n'(x) - m\psi_n(x)\psi_n'(mx)}{\psi_n(mx)\xi_n'(x) - m\xi_n(x)\psi_n'(mx)} \qquad \textbf{2.4.56}$$

Since the series expansion 2.4.22 and 2.4.23 of the scattered field is uniformly convergent, the series can be terminated after n_c terms and the resulting error is arbitrarily small for all kr if n_c is sufficiently large. Now if $kr>>n_c^2$, substituting the asymptotic relation 2.4.24 and its derivative,

$$\frac{dh_n}{d\rho} \sim \frac{(-i)^n e^{i\rho}}{\rho} \qquad \textbf{2.4.57}$$

which is obtained by using the identity 2.4.37, in the truncated series of 2.4.22 and 2.4.23, yields the transverse components of the scattered electric field as

$$E_{s\theta} \sim E_0 \frac{e^{ikr}}{-ikr} \cos\phi \; S_2(\cos\theta) \qquad \textbf{2.4.58}$$

and

$$E_{s\phi} \sim -E_0 \frac{e^{ikr}}{-ikr} \sin\phi \; S_1(\cos\theta) \qquad \textbf{2.4.59}$$

where,

$$S_1 = \sum_n \frac{2n+1}{n(n+1)} (a_n \pi_n + b_n \tau_n) \qquad \textbf{2.4.60}$$

and

$$S_2 = \sum_n \frac{2n+1}{n(n+1)} (a_n \tau_n + b_n \pi_n) \qquad \textbf{2.4.61}$$

and the series are terminated after n_c terms. The relation between incident and scattered field amplitudes therefore becomes

$$\begin{pmatrix} E_{\parallel s} \\ E_{\perp s} \end{pmatrix} = \frac{e^{ik(r-z)}}{-ikr} \begin{pmatrix} S_2 & 0 \\ 0 & S_1 \end{pmatrix} \begin{pmatrix} E_{\parallel i} \\ E_{\perp i} \end{pmatrix} \qquad \textbf{2.4.62}$$

From this relation 2.4.62 and using the 4x4 Mueller matrix for scattering from 2.2.69, the relation between incident and scattered Stokes parameters follows as

$$\begin{pmatrix} I_s \\ Q_s \\ U_s \\ V_s \end{pmatrix} = \frac{1}{k^2 r^2} \begin{pmatrix} S_{11} & S_{12} & 0 & 0 \\ S_{12} & S_{11} & 0 & 0 \\ 0 & 0 & S_{33} & S_{34} \\ 0 & 0 & -S_{34} & S_{33} \end{pmatrix} \begin{pmatrix} I_i \\ Q_i \\ U_i \\ V_i \end{pmatrix} \qquad \textbf{2.4.63}$$

where,

$$S_{11} = \tfrac{1}{2}(|S_2|^2 + |S_1|^2) \qquad \textbf{2.4.64}$$

$$S_{12} = \tfrac{1}{2}(|S_2|^2 - |S_1|^2) \qquad \textbf{2.4.65}$$

$$S_{33} = \tfrac{1}{2}(S_2^* S_1 + S_2 S_1^*) \qquad \textbf{2.4.66}$$

$$S_{34} = \frac{i}{2}(S_1 S_2^* - S_2 S_1^*) \qquad \textbf{2.4.67}$$

If the incident light is unpolarized then due to relations 2.2.48 - 2.2.51 the Stoke's parameters of the scattered light in 2.4.63 become

$$U_s = V_s = 0 \qquad \textbf{2.4.68}$$

$$Q_s = (1/k^2 r^2)\, S_{12}\, I_i \qquad \textbf{2.4.69}$$

$$I_s = (1/k^2 r^2)\, S_{11}\, I_i \qquad \textbf{2.4.70}$$

Thus, $S_{11}(\theta)$ characterizes the scattered light intensity as a function of scattering angle θ , and is related to the scattered intensities $I_{/\!/}$ and $I_{\perp}$ by the relation

$$S_{11} = \frac{I_{/\!/} + I_{\perp}}{2} \qquad \textbf{2.4.71}$$

There is no role of orientation on the light scattering properties of homogenous spherical particles. In case of optically inactive homogenous spherical particles, $S_{11} = S_{22}$ and $S_{33} = S_{44}$. Out of the six non-zero elements of the matrix depicted by equation 2.4.63, the measurements of S_{11} and S_{12} requires randomly polarized incident light. Therefore, these two elements are the most important ones for study of atmospheric, interplanetary, biological and cometary particles which scatters randomly polarized incident light like sunlight [354].

It is worth mentioning that according to the theory of self-preserving size distribution [356] which suggests that in a unit volume of

natural aerosols, the sizes of the particles is given by a distribution function. For volume of particles having gamma distribution, the distribution is given by

$$N(a) = p\, a^{\gamma} e^{-\eta a} \qquad \textbf{2.4.77}$$

where a is the radius of the particle and p, γ, η are parameters of the distribution related to the density of scattering particles N_{tot} by

$$N_{tot} = p\eta^{-(\gamma+1)}\Gamma(\gamma+1) \qquad \textbf{2.4.78}$$

where again γ and η are related to the particle modal radius a_c corresponding to the peak of the distribution by

$$a_c = \gamma/\eta \qquad \textbf{2.4.79}$$

Hence, if the particle density N_{tot} is fixed, the gamma distribution 2.4.77 is completely specified by the index γ and the modal radius a_c. Since the Stokes parameters of the light scattered by a collection of randomly separated particles are the sum of the Stokes parameters of the light scattered by the individual particles, therefore the scattering matrix for such a collection is merely the sum of the individual particle scattering matrices, provided linear dimension of the volume occupied by the scatterers is small compared with the distance at which the scattered light is observed. Thus, for an ensemble of axially symmetric, and randomly oriented particles illuminated by unpolarized light, the volume scattering coefficient $\beta(\theta)$ [356] is obtained by integrating S_{11} as given by 2.4.70 over the size distribution $N(a)$ and is given as,

$$\beta(\theta) = \frac{1}{k^3}\int_0^{\infty} S_{11}(\theta) N(a)\, da \qquad \textbf{2.4.80}$$

Again, for an ensemble of particles, the degree of linear polarization which was originally defined by equation 2.2.57 is expressed by the form

$$P(\theta) = -\frac{\langle S_{12}(\theta)\rangle}{\langle S_{11}(\theta)\rangle} = \frac{I_{\perp} - I_{\parallel}}{I_{\perp} + I_{\parallel}} \qquad \textbf{2.4.81}$$

Thus it is evident from equations 2.4.69, 2.4.70 and 2.4.80 that experimental measurements of I_s and I_i (scattered intensity and incident intensity of light) using unpolarized light source will yield experimental $\beta(\theta)$ and $P(\theta)$ values, a fact that is consistently used in the light scattering system.

2.5 T-matrix method

The T-matrix method was originally introduced by Waterman for computing electromagnetic scattering by single, homogenous and arbitrary shaped particle based on Huygen's principle [46]. The method is based on expanding the incident and the scattered waves in appropriate vector spherical wave functions and relating these expansions by means of a transition matrix or T-matrix. An interesting feature of this method is that it reduces exactly to Mie theory when the scattering particle is a homogenous or layered sphere composed of isotropic materials. The T-matrix method is the most convenient approach to evaluate optical properties of very complex irregular particles, like fluffy aggregates [4, 41].

It has been already shown in equations 2.1.1 - 2.1.4 and equations 2.1.11 - 2.1.15 that the linearity of Maxwell equations and boundary conditions enables one to find the solution of electromagnetic scattering problem for spherical particles in a form of expansion of incident and scattered fields into vector harmonics. Thus, because of this linearity, there exists a relational matrix which relates the incident waves to scattered waves (equation 2.4.62). The T-matrix method is also based on the same principle. But, in addition to a very simple spherical geometry that is applied to Mie theory, this approach degenerates the electromagnetic field on basis of functions adapted to more complex geometries of scatterers. T-matrix is an exact method in which the incident, scattered and internal fields are expanded into vector spherical harmonics, just like Mie theory. Mathematically, the fields are given by equations 2.4.1 - 2.4.6 and representing a set of linear equations. Since it is a differential equation of second order there exist two independent solutions. In case of Mie theory, they are formulated in the form

$$\phi_e(\varphi) = \cos(m\varphi)$$

$$\phi_o(\varphi) = \sin(m\varphi) \qquad \textbf{2.5.1}$$

where, subscripts e and o denote even and odd respectively. The complete solution is given by a linear combination as

$$\phi(\varphi) = A_m \cos(m\varphi) + B_m \sin(m\varphi) \qquad \textbf{2.5.2}$$

In order to simplify any further derivations, equation 2.5.2 can be replaced by the linear combinations of complex functions $e^{im\varphi}$ and $e^{-im\varphi}$ as

$$\phi(\varphi) = C_m e^{im\varphi} + C_{-m} e^{-im\varphi} \qquad \textbf{2.5.3}$$

where, C_m and C_{-m} are, in general complex numbers. Thus, the even and odd expansions are reduced to only one coefficient, and equations 2.4.4 - 2.4.6 of section 2.4 takes the form

$$\mathbf{E}_i = \sum_{n=1}^{\infty} \sum_{m=-n}^{n} (a_{mn}\mathbf{M}_{mn} + b_{mn}\mathbf{N}_{mn}) \qquad \textbf{2.5.4}$$

$$\mathbf{E}_s = \sum_{n=1}^{\infty} \sum_{m=-n}^{n} (p_{mn}\mathbf{N}_{mn} + q_{mn}\mathbf{N}_{mn}) \qquad \textbf{2.5.5}$$

$$\mathbf{E}_{in} = \sum_{n=1}^{\infty} \sum_{m=-n}^{n} (c_{mn}\mathbf{M}_{mn} + d_{mn}\mathbf{N}_{mn}) \qquad \textbf{2.5.6}$$

Inserting the generating functions Ψ_{emn} and Ψ_{omn} (after combining the odd and even components into one equation, that is Ψ_{mn}) into the vector function, we can write the vector harmonics **M** and **N** as [47]

$$\mathbf{M}_{mn}(kr, \theta, \varphi) = \gamma_{mn}\, h_n^{(1)}(kr)\, \mathbf{C}_{mn}(\theta, \varphi) \qquad \textbf{2.5.7}$$

$$\mathbf{N}_{mn}(kr, \theta, \varphi) = \gamma_{mn} \left\{ \frac{\mathrm{P}_{mn}(\theta,\varphi)}{kr} h_n^{(1)}(kr)\, n(n+1) + \frac{\mathrm{B}_{mn}(\theta,\varphi)}{kr} \frac{d\left[kr\, h_n^{(1)}(kr)\right]}{d(kr)} \right\}$$

$$(r > r_>) \qquad \textbf{2.5.8}$$

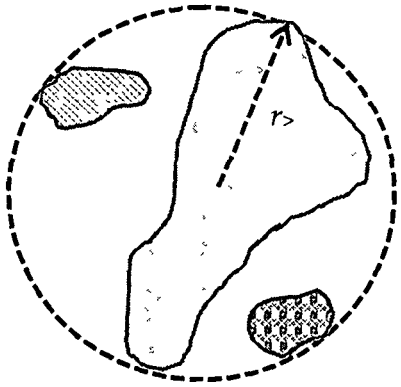

Figure 2.7: Cross section of an arbitrary shaped, finite scattering object.

where k is the wave number and $r_>$ is the radius of the smallest circumscribing sphere of the scatterer centered at the origin of the laboratory coordinate system, as shown in figure 2.7. In the above equation 2.5.8,

$$\gamma_{mn} = d_n \sqrt{\frac{(n-m)!}{(n+m)!}} \qquad 2.5.9$$

is a normalization factor originating from

$$P_n^{-m}(\cos\theta) = (-1)^m \frac{(n-m)!}{n+m)!} P_n^m(\cos\theta) \qquad 2.5.10$$

and

$$d_n = \sqrt{\frac{(2n+1)}{4\pi n(n+1)}} \qquad 2.5.10(a)$$

$$\mathbf{C}_{mn}(\theta,\varphi) = \left[\hat{\theta}\frac{im}{\sin\theta} P_n^m(\cos\theta) - \hat{\varphi}\frac{d}{d\theta} P_n^m(\cos\theta)\right] e^{im\varphi} \qquad 2.5.11$$

$$\mathbf{B}_{mn}(\theta,\varphi) = \left[\hat{\theta}\frac{d}{d\theta} P_n^m(\cos\theta) + \hat{\varphi}\frac{im}{\sin\theta} P_n^m(\cos\theta)\right] e^{im\varphi} \qquad 2.5.12$$

$$\mathbf{P}_{mn}(\theta,\varphi) = \hat{\mathbf{r}}\ P_n^m(\cos\theta)\ e^{im\varphi} \qquad 2.5.13$$

In analogy with equations 2.4.18 and 2.4.22 the electric fields of incident and scattered waves are

$$\mathbf{E}_t(\mathbf{r}) = \sum_{n=1}^{\infty}\sum_{m=-n}^{n}\left[a_{mn}R_g\mathbf{M}_{mn}(k_{out}\mathbf{r}) + b_{mn}R_g\mathbf{N}_{mn}(k_{out}\mathbf{r})\right] \qquad \textbf{2.5.14}$$

$$\mathbf{E}_s(\mathbf{r}) = \sum_{n=1}^{\infty}\sum_{m=-n}^{n}\left[p_{mn}\mathbf{M}_{mn}(k_{out}\mathbf{r}) + q_{mn}\mathbf{N}_{mn}(k_{out}\mathbf{r})\right] \qquad \textbf{2.5.15}$$

The symbol R_g means that the Hankel function $h_n^{(1)}$ is replaced by spherical Bessel function z_n. The functions $Rg\mathbf{M}_{mn}$ and $Rg\mathbf{N}_{mn}$ are regular (finite) at the origin, while the use of outgoing functions $\mathbf{M}_{mn}$ and $\mathbf{N}_{mn}$ in equation 2.5.15 ensures that the scattered field satisfies the so-called radiation condition at infinity (i.e., the transverse component of the scattered electric field decays as $1/r$, whereas the radial component decays faster than $1/r$ with $r \to \infty$). The requirement that $r > r_>$ in equation 2.5.15 means that the scattered field is expanded in the functions $\mathbf{M}_{mn}$ and $\mathbf{N}_{mn}$ only outside the smallest circumscribing sphere of the scatterer (figure 2.7). It can be shown that the expansion coefficients of the plane incident wave are given by simple analytical formulas as follows [46]

$$a_{mn} = 4\pi(-i)^m i^n d_n \mathbf{E}_0^{inc}.\mathbf{C}_{mn}^*(\nu^{inc})\exp(-im\varphi^{inc}) \qquad \textbf{2.5.16}$$

$$b_{mn} = 4\pi(-i)^m i^{n-1} d_n \mathbf{E}_0^{inc}.\mathbf{B}_{mn}^*(\nu^{inc})\exp(-im\varphi^{inc}) \qquad \textbf{2.5.17}$$

Owing to the linearity of Maxwell equations and constitutive relations, the relation between the expansion coefficients of scattered and incident fields must also be linear. Thus we may write

$$p_{mn} = \sum_{n'=1}^{\infty}\sum_{m'=-n'}^{n'}\left[a_{m'n'}T^{11}_{mnm'n'} + b_{m'n'}T^{12}_{mnm'n'}\right] \qquad \textbf{2.5.18}$$

$$q_{mn} = \sum_{n'=1}^{\infty}\sum_{m'=-n'}^{n'}\left[a_{m'n'}T^{21}_{mnm'n'} + b_{m'n'}T^{22}_{mnm'n'}\right] \qquad \textbf{2.5.19}$$

or in matrix form, it can be expressed as

$$\begin{bmatrix} \mathbf{p} \\ \mathbf{q} \end{bmatrix} = \mathbf{T} \begin{bmatrix} \mathbf{a} \\ \mathbf{b} \end{bmatrix} = \begin{bmatrix} \mathbf{T}^{11} & \mathbf{T}^{12} \\ \mathbf{T}^{21} & \mathbf{T}^{22} \end{bmatrix} \begin{bmatrix} \mathbf{a} \\ \mathbf{b} \end{bmatrix} \qquad 2.5.20$$

where **T** is the so-called transition matrix or *T-matrix*, and is the cornerstone of T-matrix approach. It can be seen that the column vector of the expansion coefficients of the scattered field is obtained by multiplying the T-matrix and the column vector of the expansion coefficients of the incident field. For the asymptotic behavior in the far field zone [47] we have

$$z_n(kr) = h_n^{(1)}(kr)_{r\to\infty} \sim \frac{(-i)^{(n+1)} e^{ikr}}{kr} \qquad 2.5.21$$

And therefore equations 2.5.7 and 2.5.8 are transformed into the forms:

$$\mathbf{M}_{mn}(kr,\theta,\varphi)_{kr\to\infty} = \gamma_{mn} \frac{(-i)^{(n+1)} e^{ikr}}{kr} \mathbf{C}_{mn}(\theta,\varphi) \qquad 2.5.22$$

$$\mathbf{N}_{mn}(kr,\theta,\varphi)_{kr\to\infty} = \gamma_{mn} \frac{(-i)^{n} e^{ikr}}{kr} \mathbf{B}_{mn}(\theta,\varphi) \qquad 2.5.23$$

Substituting the asymptotic formulas 2.5.22 and 2.5.23 in equation 2.5.15 yields

$$\mathbf{E}_s(r) = \frac{e^{ikr}}{kr} \sum_{n=1}^{\infty} \sum_{m=-n}^{n} i^{-n} \left[-ip_{mn} \mathbf{C}_{mn}(\theta^{sca},\varphi^{sca}) + q_{mn} \mathbf{B}_{mn}(\theta^{sca},\varphi^{sca}) \right] \qquad 2.5.24$$

Finally using equations 2.5.16-2.5.19, 2.5.22 and 2.5.23 yields

$$\begin{aligned} \mathbf{S}(\hat{\mathbf{n}}^{sca}\hat{\mathbf{n}}^{inc}) = \frac{1}{k_1} \sum_{n=1}^{\infty} \sum_{n'=1}^{\infty} \sum_{m=-n}^{n} \sum_{m'=-n'}^{n'} \alpha_{mnm'n'} \left[T^{11}_{mnm'n'} \pi_{mn}(\nu^{sca}) \pi_{m'n'}(\nu^{inc}) \right. \\ + T^{21}_{mnm'n'} \tau_{mn}(\nu^{sca}) \pi_{m'n'}(\nu^{inc}) + T^{12}_{mnm'n'} \pi_{mn}(\nu^{sca}) \tau_{m'n'}(\nu^{inc}) \\ \left. + T^{22}_{mnm'n'} \tau_{mn}(\nu^{sca}) \tau_{m'n'}(\nu^{inc}) \right] \exp\left[i(m\varphi^{sca} - m'\varphi^{inc}) \right] \end{aligned} \qquad 2.5.25$$

where, $\mathbf{S}(\hat{\mathbf{n}}^{sca}\hat{\mathbf{n}}^{inc})$ represents another form of amplitude scattering matrix and yields the elements of the amplitude scattering matrix are as follows:

$$S_{11}(\hat{\mathbf{n}}^{sca}\hat{\mathbf{n}}^{inc}) = \frac{1}{k_1}\sum_{n=1}^{\infty}\sum_{n'=1}^{\infty}\sum_{m=-n}^{n}\sum_{m'=-n'}^{n'} \alpha_{mnm'n'}[T^{11}_{mnm'n'}\pi_{mn}(\nu^{sca})\pi_{m'n'}(\nu^{inc}) + T^{21}_{mnm'n'}\tau_{mn}(\nu^{sca})\pi_{m'n'}(\nu^{inc}) + T^{12}_{mnm'n'}\pi_{mn}(\nu^{sca})\tau_{m'n'}(\nu^{inc}) + T^{22}_{mnm'n'}\tau_{mn}(\nu^{sca})\tau_{m'n'}(\nu^{inc})]\exp[i(m\varphi^{sca} - m'\varphi^{inc})]$$

2.5.26

$$S_{12}(\hat{\mathbf{n}}^{sca}\hat{\mathbf{n}}^{inc}) = \frac{1}{k_1}\sum_{n=1}^{\infty}\sum_{n'=1}^{\infty}\sum_{m=-n}^{n}\sum_{m'=-n'}^{n'} \alpha_{mnm'n'}[T^{11}_{mnm'n'}\pi_{mn}(\nu^{sca})\tau_{m'n'}(\nu^{inc}) + T^{21}_{mnm'n'}\tau_{mn}(\nu^{sca})\tau_{m'n'}(\nu^{inc}) + T^{12}_{mnm'n'}\pi_{mn}(\nu^{sca})\pi_{m'n'}(\nu^{inc}) + T^{22}_{mnm'n'}\tau_{mn}(\nu^{sca})\pi_{m'n'}(\nu^{inc})]\exp[i(m\varphi^{sca} - m'\varphi^{inc})]$$

2.5.27

$$S_{21}(\hat{\mathbf{n}}^{sca}\hat{\mathbf{n}}^{inc}) = \frac{1}{k_1}\sum_{n=1}^{\infty}\sum_{n'=1}^{\infty}\sum_{m=-n}^{n}\sum_{m'=-n'}^{n'} \alpha_{mnm'n'}[T^{11}_{mnm'n'}\tau_{mn}(\nu^{sca})\pi_{m'n'}(\nu^{inc}) + T^{21}_{mnm'n'}\pi_{mn}(\nu^{sca})\pi_{m'n'}(\nu^{inc}) + T^{12}_{mnm'n'}\tau_{mn}(\nu^{sca})\tau_{m'n'}(\nu^{inc}) + T^{22}_{mnm'n'}\pi_{mn}(\nu^{sca})\tau_{m'n'}(\nu^{inc})]\exp[i(m\varphi^{sca} - m'\varphi^{inc})]$$

2.5.28

$$S_{22}(\hat{\mathbf{n}}^{sca}\hat{\mathbf{n}}^{inc}) = \frac{1}{k_1}\sum_{n=1}^{\infty}\sum_{n'=1}^{\infty}\sum_{m=-n}^{n}\sum_{m'=-n'}^{n'} \alpha_{mnm'n'}[T^{11}_{mnm'n'}\tau_{mn}(\nu^{sca})\tau_{m'n'}(\nu^{inc}) + T^{21}_{mnm'n'}\pi_{mn}(\nu^{sca})\tau_{m'n'}(\nu^{inc}) + T^{12}_{mnm'n'}\tau_{mn}(\nu^{sca})\pi_{m'n'}(\nu^{inc}) + T^{22}_{mnm'n'}\pi_{mn}(\nu^{sca})\pi_{m'n'}(\nu^{inc})]\exp[i(m\varphi^{sca} - m'\varphi^{inc})]$$

2.5.29

where,

$$\alpha_{mnm'n'} = i^{n'-n-1}(1)^{m+m'}\left[\frac{(2n+1)(2n'+1)}{n(n+1)n'(n'+1)}\right]^{\frac{1}{2}}$$

2.5.30

$$\pi_{mn}(\nu) = \frac{md^n_{0m}(\nu)}{\sin\nu}, \quad \pi_{-mn}(\nu) = (-1)^{m+1}\pi_{mn}(\nu)$$

2.5.31

$$\tau_{mn}(\nu) = \frac{dd^n_{0m}(\nu)}{d\nu}, \quad \tau_{-mn}(\nu) = (-1)^m\tau_{mn}(\nu)$$

2.5.32

The scattering characteristics of any particle can be computed if the amplitude matrix is calculated. Specifically, the Stokes phase matrices are given by equation 2.2.70 [46]. Alternatively, equations 2.3.9, 2.5.24, 2.5.16 and 2.5.17 yield

$$C_{ext} = -\frac{1}{k_1^2 E_0^{inc_2}} \mathrm{Re} \sum_{n=1}^{\infty} \sum_{m=-n}^{\infty} [a_{mn}(p_{mn})^* + b_{mn}(q_{mn})^*] \qquad 2.5.33$$

Furthermore, the formula for the scattering cross section follows from equation 2.3.13, and the condition of orthogonality and normalization conditions for vector spherical harmonics as

$$C_{sca} = -\frac{1}{E_0^{inc_2}} \int_0^{2\pi} d\varphi^{sca} \int_0^{\pi} d\nu^{sca} \sin\nu^{sca} E_1^{sca}(\nu^{sca}, \varphi^{sca})^2 \qquad 2.5.34$$

$$C_{sca} = -\frac{1}{k_1^2 E_0^{inc_2}} \sum_{n=1}^{\infty} \sum_{m=-n}^{n} [p_{mn}^2 + q_{mn}^2] \qquad 2.5.35$$

An important feature of T-matrix approach is that T-matrix depends only on the physical and geometrical characteristics of the scattering particle such as size parameter, shape, refractive index, and orientation with respect to the laboratory frame of reference, whereas completely independent of the direction of propagation and state of polarization of the incident and the scattered fields. This leads to the fact that T-matrix needs to be computed only once and can be used for calculation of any direction of incident or scattered field, and any state of polarization the fields [45, 46, 92, 101, 166].

In this chapter we have presented an overview of the two important theoretical approaches, Mie theory and T-matrix method, which were used in our light scattering studies. We have used established computer programs [97,357, 358] to compute scattering matrix elements for different ensemble of homogenous spherical and non-spherical particles having different size parameter, incorporating subjective values of incident wavelength, radius of particle and refractive index. The programs were used to correlate and analyze the results obtained from our experimental measurements on

different particles. We have used Mie theory for light scattering investigation of particles like Cadmium sulphide (CdS), Zinc selenide (ZnSe), Zinc oxide (ZnO), *Staphylococcus aureus, Mycobacterium smegmatis* and *Camellia sinensis;* and T-matrix method for Titanium dioxide (TiO_2), which will be presented in Chapter IV of the thesis.

CHAPTER III

Design considerations of the laser based light scattering system and instrumentation

3.0 General Introduction

This chapter presents the design aspects of the laser based light scattering system and describes the instrumentation. Section 3.1 gives complete description about the light scattering system in detail. Section 3.2 to Section 3.8 deals with the individual components of the light scattering system. Section 3.9 presents the data reduction procedure which was used to eliminate the error in the measurement of scattering and linear polarization phase functions and gives the method of rectification of this error. Section 3.10 presents description about the validation of the light scattering setup. Finally, section 3.11 presents an overview of the software for processing the data obtained with the light scattering system which yields extinction coefficients and scattering coefficients.

Here the basic parameter measured is the variations of light intensity due to scattering or absorption with the intensities, after being converted to electrical signal, obtained in units of voltage. The technique of measurement used in this research work is (i) to observe the scattered intensity of light from different angles, (ii) to compute the scattering coefficient. These are the basic considerations through which the light scattering setup was developed and verified by precise observations of light scattering behavior of different types of small particles like CdS, ZnSe, TiO_2, ZnO, *Stapphylococcus aureus, Camellia sinensis* and *Mycobacterium smegmatis.*

Light scattering investigation of CdS particles were carried out by using an existing earlier light scattering setup comprising of 16 static silicon detectors [327].

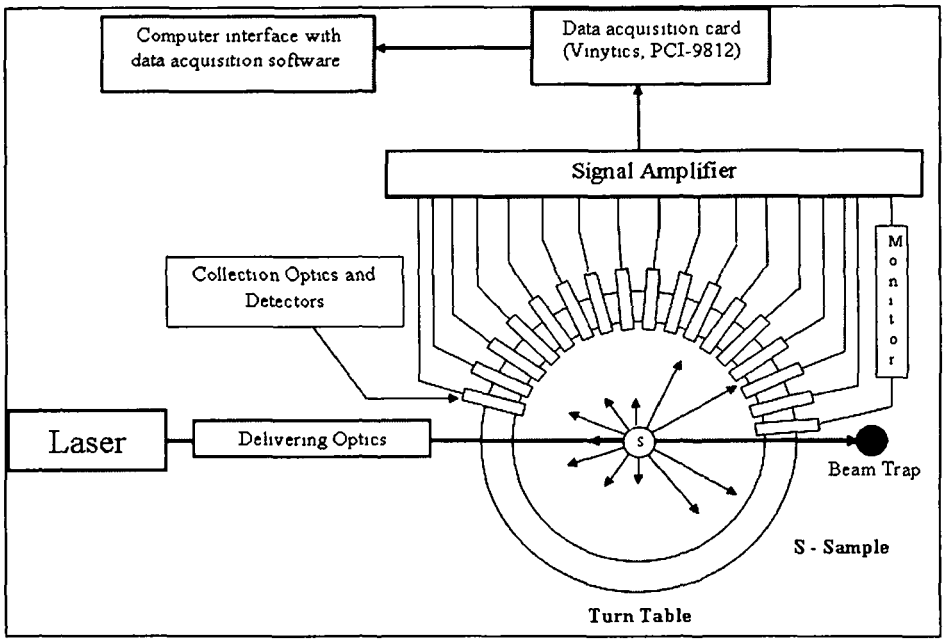

Figure 3.1: Schematic diagram of the existing earlier light scattering setup.

This setup consists of a He-Ne laser source (Melles Griot), controlled sample holders, arrangements of 16 photodetectors, each separated by an angular distance of 10°, data acquisition system and associated instrumentation. Light beam from the He-Ne laser source passes through the delivering optics. The laser light is scattered by the sample when it is placed in a sample holder positioned at the center of the circular disc. The scattered light intensity could be sensed by the arrangements of 16 static Si detectors (BPW34), each of which has a large sensitive area of 7.5mm^2 mounted on the circular disc. This arrangement is further connected to a high gain, low noise OPAMP (LM 301 AN) based amplifier circuit. The amplified signals are interfaced to a dedicated data acquisition system having 12 bit resolution. The whole array of the 16 detectors can be rotated simultaneously about an axis perpendicular to the plane of the circular disc. Analyzers used for the He-Ne laser wavelength determines the state of polarization of the light scattered from the particles after it is sensed by the detector.

On the other hand, light scattering experiments for ZnSe, TiO_2, ZnO, *Stapphylococcus aureus, Camellia sinensis* and *Mycobacterium smegmatis* were carried out by using a modified version of light scattering setup [253]. Figure 3.2(a) shows a schematic diagram of this setup. This modified and improved setup, used for the measurement of the scattering properties of small particles was designed and fabricated in the Optoelectronics and Photonics Research Laboratory, Department of Physics, Tezpur University, Assam, India. The modified light scattering setup uses a photomultiplier tube detector. Here, the plane of reference is the scattering plane, i.e., the plane containing the incident and the scattered light. The arrangement of polarizers was optional and was used specifically in the experiments while measuring the polarization phase function. Light scattered from samples passes through arrangement of collection optics comprising of appropriate analyzer. The laser light get scattered by the particles of sample placed at the scattering centre held by a mechanical support. The scattered light intensity signal was sensed by the photomultiplier tube (H 5784 - 20, Hamamatsu, Japan) which is movable along both polar and azimuthal angles, θ and φ respectively. The signals are interfaced to a steadfast data acquisition system to store the recorded data. The system could be used to measure scattered light signals from an angle of 10° to 170° for θ, and from 10° to 60° for φ, to subsequently account for recording the volume scattering. However, we know that the dependence on φ plays a vital role and is taken into account for aligned particles. The whole setup is enclosed in a box painted black from inside to cutoff electromagnetic noise, and beam stop is used to minimize the intensity of stray reflections at tactical points.In the present work, the design and instrumentation of the modified and improved setup constitute a significant part in this thesis.

3.1 Light scattering setup

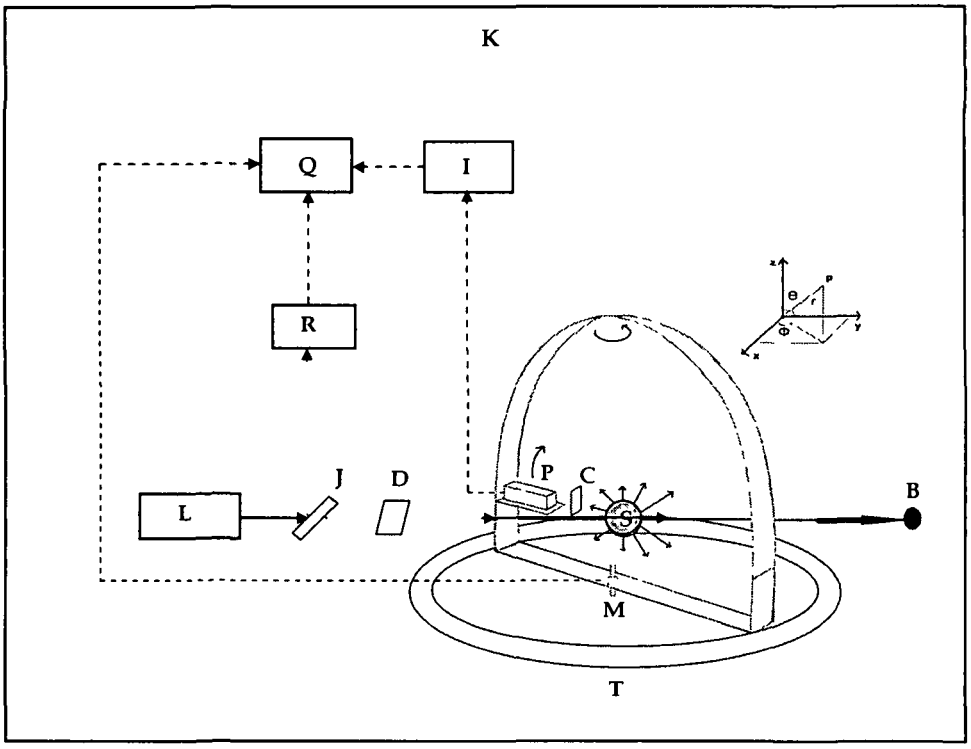

Figure 3.2(a): Schematic diagram of the light scattering setup. **L**: Laser; **J**: Beam splitter; **D**: Delivering optics; **R**: Reference detector; **M**: Stepper motor; **P**: Photomultiplier tube; **C**: Collection optics; **S**: Scattering centre; **B**: Beam stop; **I**: Data acquisition card; **Q**: Computer interface with the Data acquisition software and Stepper motor; **K**: Simulation chamber; **T**: Turn table.

Figure 3.2 (b): Photograph of the light scattering setup.
L: Laser; **J:** Beam splitter; **R**: Reference detector; **P:** Photomultiplier tube; **S:** Scattering centre; **M:** Stepper motor; **Q**: Computer interface with the Data acquisition software and Stepper motor; **K**: Simulation chamber; **B**: Beam stop; **T**: Turn table; **U**: UPS; **Z**: Mechanical jack.

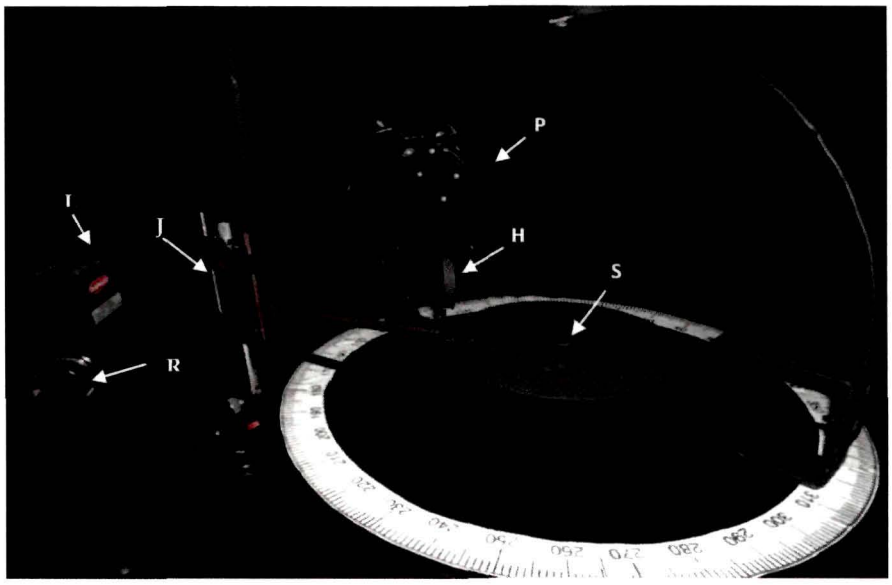

Figure 3.2(c): Close side view of the light scattering setup.
L: Laser; **J:** Beam splitter; **R**: Reference detector; **P:** Photomultiplier tube; **S:** Scattering centre; **H:** Pinhole.

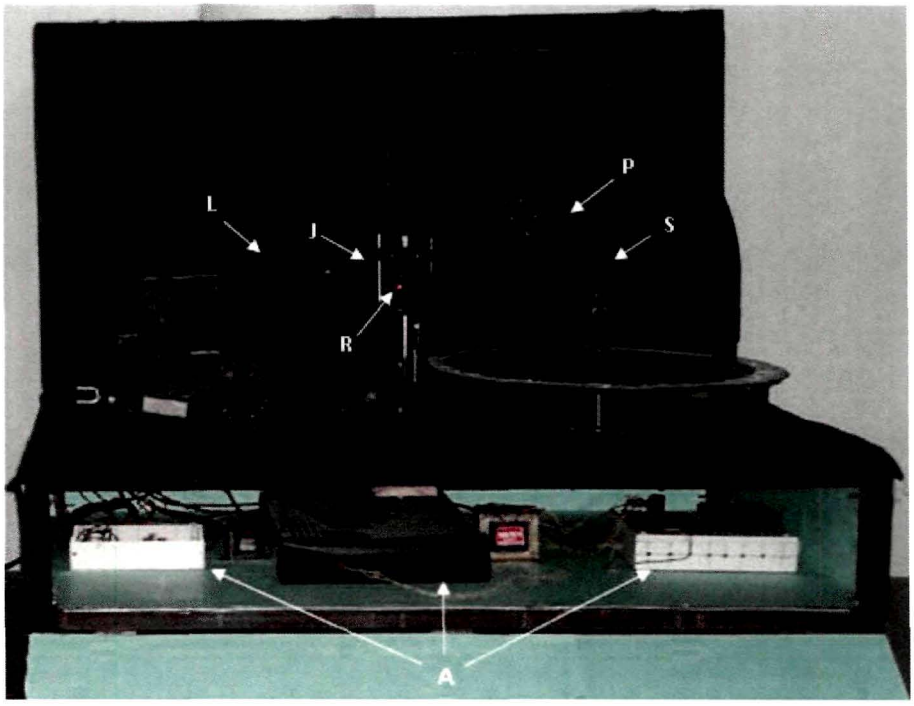

Figure 3.2(d): Close side view of the light scattering setup.
L: Laser; **J:** Beam splitter; **R**: Reference detector; **P:** Photomultiplier tube; **S:** Scattering centre with sample; **A:** Associated instrumentation.

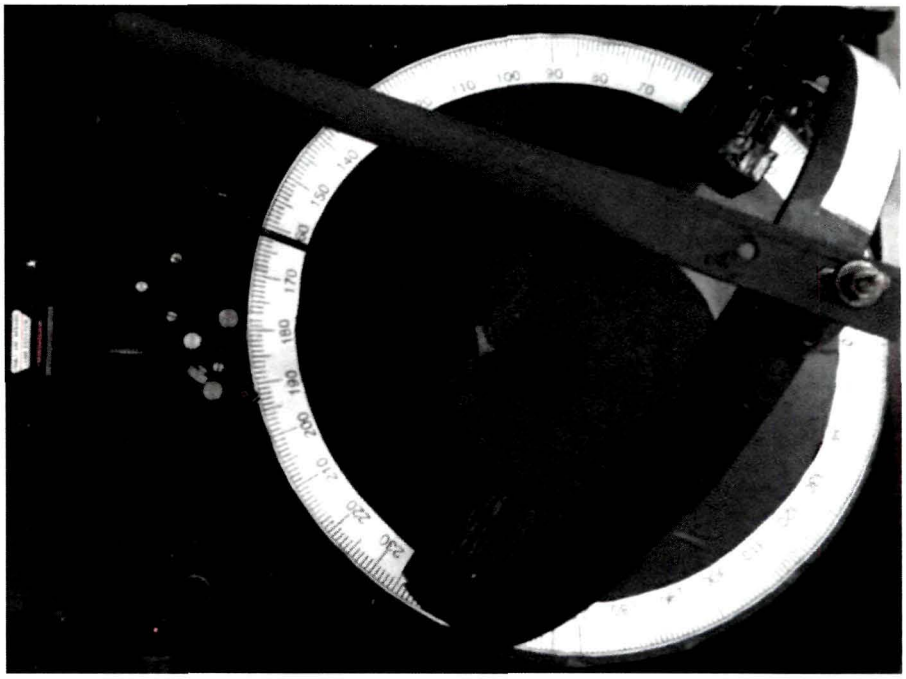

Figure 3.2(e): Top view of the light scattering setup.

The essential components of the setup are a laser source, beam splitter, reference photodetector, delivering and collection optics, scattering center with controlled sample holders, a photomultiplier tube detector, data acquisition system and associated instrumentation and beam stop, shown in figures 3.2(a) to 3.2(d). The top view of the light scattering setup is shown in figure 3.2(e). Inside the simulation chamber K, the beam from the laser source ***L*** is split by the beam splitter ***J***, gets scattered by the sample ***S***, and suffers extinction and scattering due to the constituents of the scattering volume inside the sample holder, while the reflected beam enters the photodetector ***R*** which is meant for reference. The scattered light intensity signal passes through the collection optics system ***C***, and is sensed by the photomultiplier tube ***P***. The angles of optical elements are measured counterclockwise when looking in the direction of propagation of the light. The particular configuration of the optical components used in the setup allows to measure first two matrix elements $S_{11}(\theta)$ and $S_{12}(\theta)$ of the Mueller scattering matrix given in equation 2.2.69 in Chapter II, in order to measure the volume scattering function $\beta(\theta)$ and degree of linear polarization $P(\theta)$. The scan of other elements of the Mueller matrix in principle, can be obtained by incorporating different configurations of the optical components [2]. The signal from *P* is fed via the data acquisition card ***I*** (analog-to-digital converter unit) to the computer ***Q***. The stepper motor controlled unit ***M*** is also connected to ***Q***. The following sections describe the individual components in detail.

3.2 He- Ne Laser source

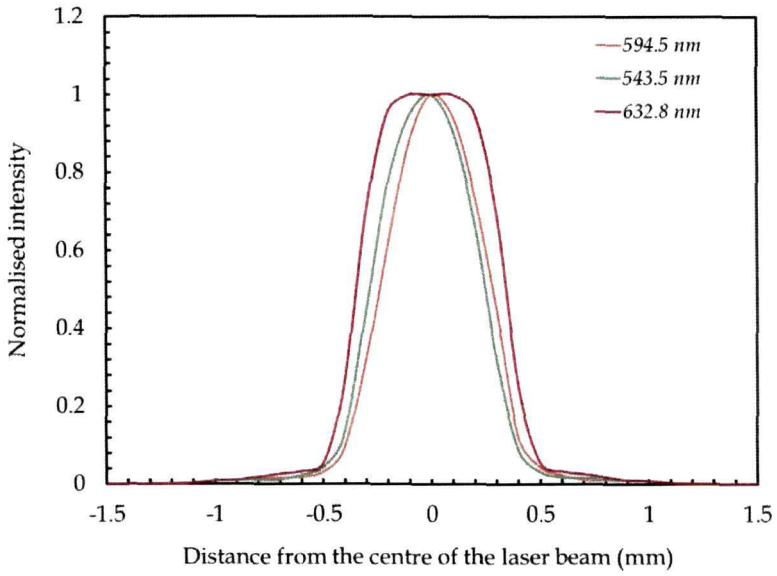

Figure 3.3: Intensity profiles of the laser beams measured at 200 mm for 543.5, 594.5 and 632.5 nm laser wavelengths.

Three He–Ne laser source (***L*** in figure 3.2 (a) and 3.2(b)) (Jain Laser-Tech, Mumbai, India) emitting at light at wavelengths 543.5 nm, 594.5 nm and 632.8 nm with an output power of 0.35mW, 0.35 mW and 2.0 mW, respectively, were alternately used as incident light sources. It was observed that the diameter of the beam cross-section was approximately 1 mm. The distance between the source and the scattering center was 200mm. The beam intensity was observed and it was found to be almost homogeneous (figure 3.3). The intensity was also monitored for 60 seconds and there were no fluctuations in the intensity observed for all the three wavelengths and the beam intensity was almost flat top in the case of 632.8 nm, whereas it was Gaussian in the case of 594.5 and 543.5 nm as shown in figure 3.3. Moreover, all our samples under investigation showed negligible non-resonant absorption at these wavelengths as verified from UV-vis absorption spectra. The laser source is mounted on a fabricated stand whose base can be leveled by screws for alignment of the beam.

3.3 Simulation Chamber

The essential components of the light scattering setup like the laser source, scattering centre, optical components like polarizers and analyzers, detectors are installed inside an alluminium enclosure, The enclosure is painted in matt black colour from inside. The beam stop ***B***, is held fixed to the wall of the enclosure which faces the direction of propagation of the laser beam. This ensured minimizing stray reflections and reducing unwanted electromagnetic noise. The enclosure was 100 cm in length, 57 cm in breadth and 50 cm in height. Other necessary components like data acquisition system and associated instrumentation are placed outside the enclosure for convenience (figure 3.2(b)).

3.4 Delivering and Collection Optics

We have devoted major part of our research in measurement of the volume scattering function $\beta(\theta)$, and degree of linear polarization $P(\theta)$, for different scattering particles. We know that measurement of $\beta(\theta)$ and $P(\theta)$ is related to the first two elements of the Mueller matrix, that is S_{11} and S_{12} , as mentioned in Section 2.4 in the preceding chapter. The measurement of these two elements requires a randomly polarized source of incident light. Therefore, no polarizers were used in the delivering optics unit in order to maintain the random polarization of the incident beam from the He-Ne lasers as shown in figure 3.4. Again for measurements, detectors were essentially used to measure the intensity of three states of polarization of scattered light. The three states of polarization are un-polarized, perpendicular and parallel polarized light. For this purpose, analyzers optimized for the wavelength of He-Ne laser were used in front of the detector **D** as shown in figure 3.4

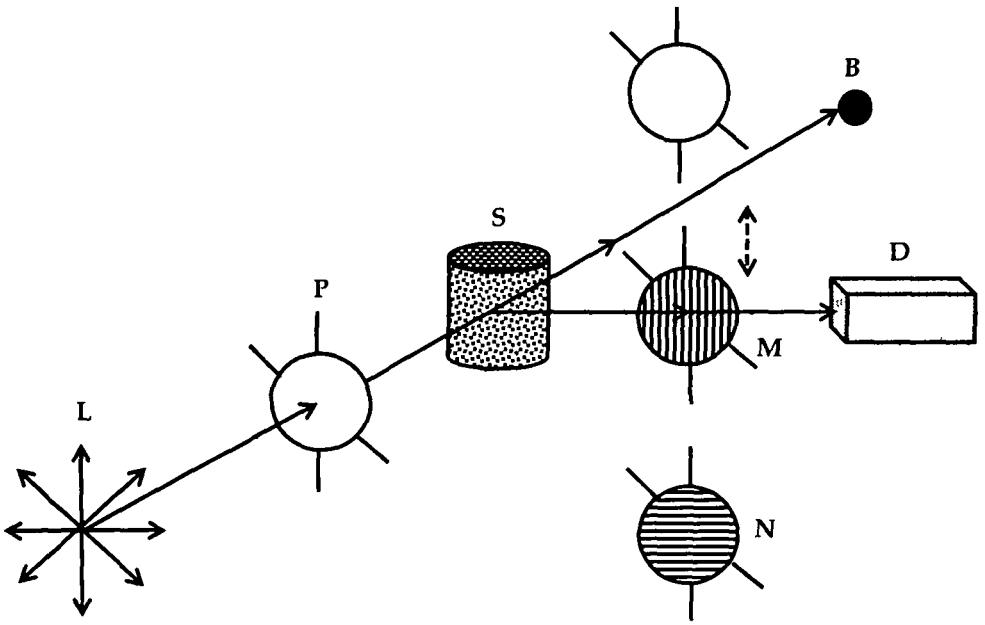

Figure 3.4: Schematic diagram of delivering and collection optics unit. **L:** Randomly polarized incident laser light; **P**: No polarizer; **S**: Scattering centre; **M:** Linear polarizer (⊥); **N:** Linear polarizer (||); **D**: Detector; **B:** Beam stop.

3.5 Photodetector units

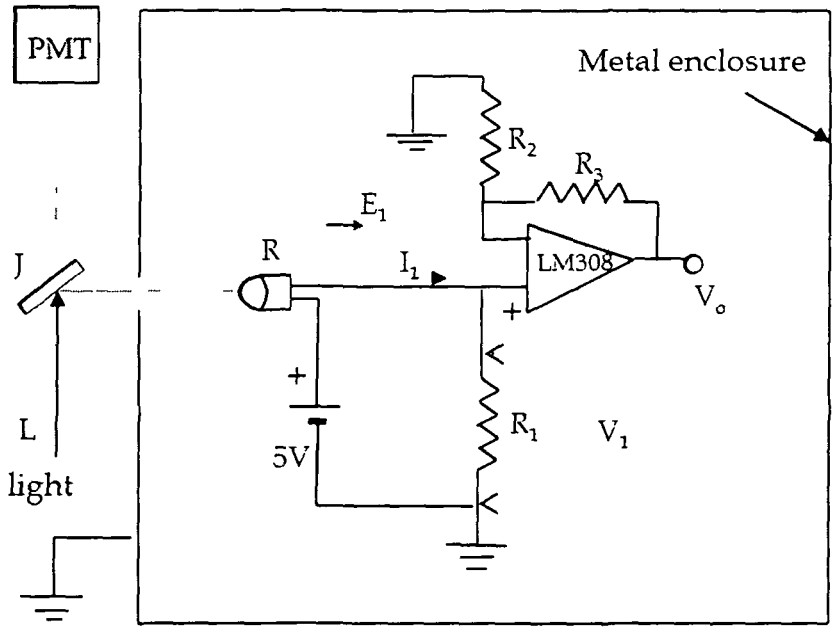

Figure 3.5: Photodetector unit with circuitry.

(i) The silicon phototransistor based photodetector unit is shown schematically in figure 3.5. This type of detector has been used as a reference detector in our modified light scattering setup. The beam splitter splits the incoming incident light beam into two components, one component is received by the phototransistor ***R*** shown in figure 3.2(a) which again is connected to the data acquisition system, and the other component falls on the scattering volume and is scattered by it. The phototransistor ***R*** produces photocurrent I_1, and a bias voltage of +5 volts is provided to R. I_1 produces a voltage drop V_1 across the load resistance R_1. V_1 is then amplified by the LM308 [327] operational amplifier based stage by A_1 times. The power supply lines have capacitors connected to ground to bypass any ripple present in the dc supply.

Here ***R*** is a highly sensitive npn silicon phototransistor [328] of type TIL - 81. Figure 3.6 shows the dimension and figure 3.7 shows the working circuit of TIL - 81 based photodetector. The base terminal is not present as it remains floating. The specifications of the phototransistor which is suitable for the light scattering system as it makes the system portable, compact and efficient (at 25° centigrade) are given in table 3.1 below. The light current versus radiation profile of TIL - 81, shown in figure 3.8 fits well with the intensity of the laser source of the light scattering system.

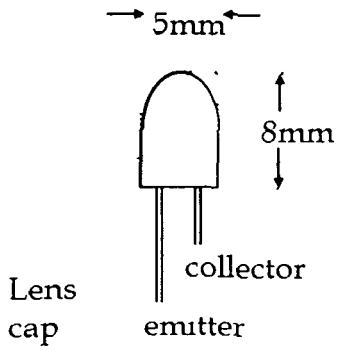

Figure 3.6: TIL - 81 phototransistor

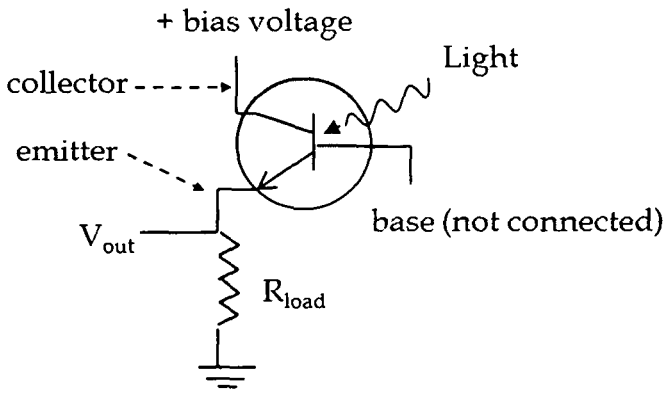

Figure 3.7: TIL - 81 phototransistor working circuit

Table 3.1: Specification of TIL - 81

Parameter	TIL- 81	Unit
Collector to emitter voltage	45(max)	V
Light current (at collector to emitter voltage) at intensity of light on the photodetector = 10mW/cm²	5 6	V mA
Dark current (at collector to emitter voltage), and Intensity of light on the phototransistor = 10mW/cm²	10 100	V nA
Saturation voltage (at collector current = 10mA)	0.4	V
Turn-on time (at collector to emitter voltage), (collector current), (load resistance)	8 10 2 100	µs V mA Ω
Turn-off time (at collector to emitter voltage), (collector current), (load resistance)	7 10 2 100	µs V mA Ω
Operating Temperature	+25	^{0}C

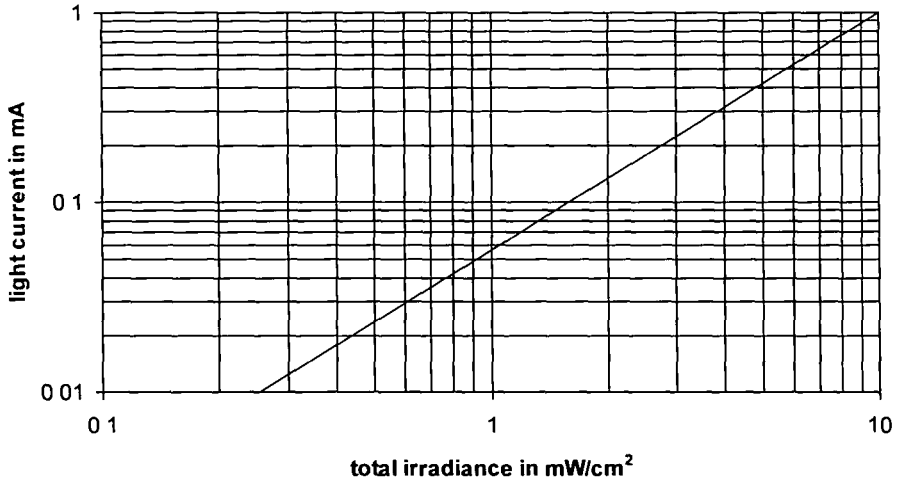

Figure 3.8: Light current versus irradiance graph of TIL-81 phototransistor. Normalized to collector current = 6mA (collector to emitter voltage = 5V) and intensity of light on the phototransistor = 10mW/cm².

The graph in figure 3.8 gives the relationship between V_1 and the incident intensity of light E_1 on R as

$$(1/6)(V_1 / R_1) = 0.0562 (E_1)^{1.25} \qquad \textbf{3.5.1}$$

where the factor (1/6) comes due to the fact that the specification graph in figure 3.8 is normalized at phototransistor current I_1 = 6mA and E_1=10mW/cm².

The output of the LM308 based amplifier is fed to one channel of the analog-to-digital converter unit. Amplification factor A_1 is adjusted, with the reference laser beam allowed to fall on the detector to such a value that V_o is less than 5 volts, as it is the maximum value that can be used as the input to the analog-to-digital converter unit.

The eight pin LM308 operational amplifier [327] is chosen as it can be used as a high speed, low drift and low input current amplifier. The following specifications of LM308 satisfies the requirements of the light scattering system -

Supply voltage = ±18 volts.

Power dissipation = 500 mW.

Input voltage = ±15 volts.

Input resistance = 70 MΩ.

Common mode rejection ratio = 110 dB.

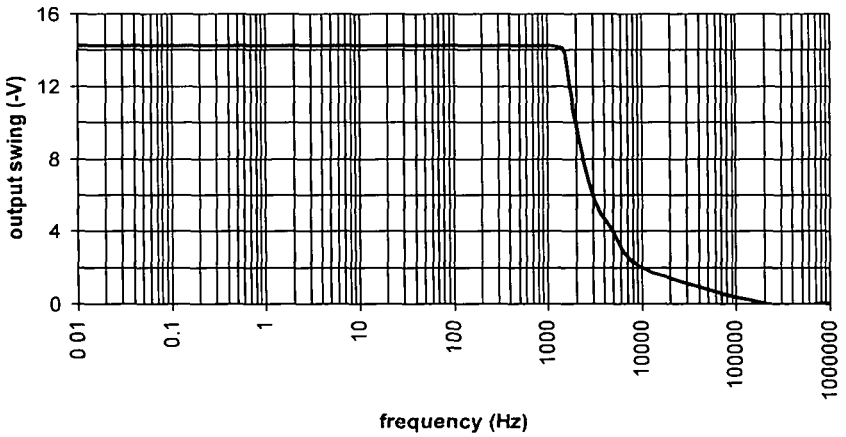

Figure 3.9: Large signal frequency response of the LM308 with pin number 8 connected to ground via a 30pf capacitor.

Moreover, pin number 8 of the LM308 is connected to ground via a 100pf capacitor as it improves rejection of power supply noise by a factor of ten. It has a linear frequency response within the low frequency range in which the air quality monitoring system operates as shown in figure 3.9. The amplified signals are interfaced to a data acquisition system having a resolution of 12 bit for data recording and analysis.

(ii) The photomultiplier based scattering photodetector (*P* in figure 3.2(a)) for detecting scattered light is shown in figure 3.10. We have used a photomultiplier tube (Model: **H 5784 - 20**, Hamamatsu, Japan) to measure the scattered intensity of light.

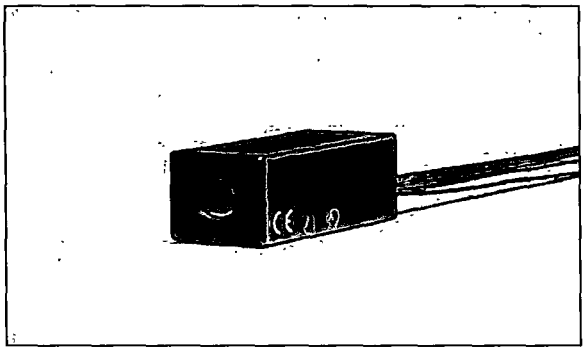

Figure 3.10: Photomultiplier tube (**H 5784-20**)

The **H 5784 - 20** photo sensor module is comprised of a metal package photomultiplier tube, low power consumption high voltage power supply and low noise amplifier. The electrical current from the photomultiplier tube is converted to a voltage by an amplifier for easy signal processing. The **H5784-20** is highly resistant to noise since the amplifier is installed near the anode output pin of the photomultiplier tube. The amplifier feedback resistance of $1M\Omega$ allows a current to voltage conversion factor of $1V/\mu A$, and covers a frequency bandwidth from DC to 20 *kHz*.

Table 3.2: Specification of Photomultiplier tube H 5784 - 20

Parameter	H 5784 - 20	Unit
Input Voltage	±11.5 to ±15.5	V
Max. input Voltage	±18.0	V
Max. Input Current	±9/-1	mA
Max. Output signal Voltage	+10 (Load resistance 10 kΩ)	V
Max. Control Voltage	+1.0 (Input impedance 100 kΩ)	V
Effective area	Φ8	mm
Peak sensitivity wavelength	630	nm
Ripple noise (peak to peak, Max.)	2	mV
Operating Ambient Temperature	+5 to +50	^0C

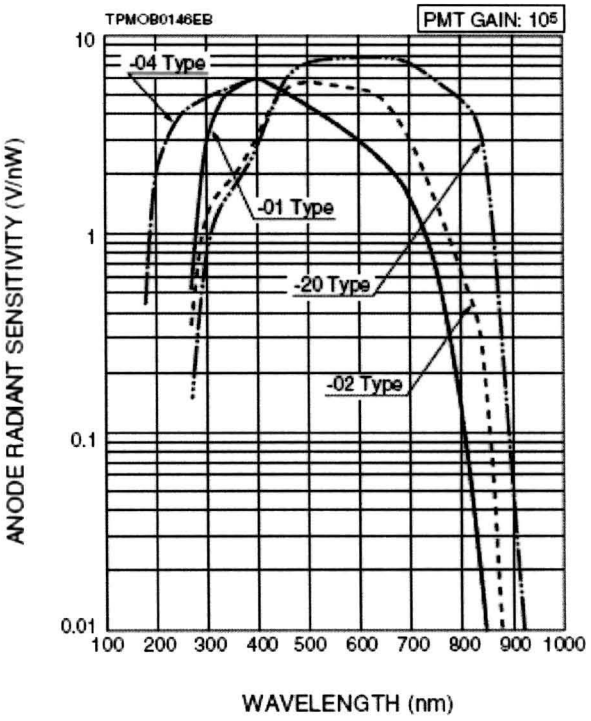

Figure 3.11: Characteristics of Anode radiant sensitivity of PMT

The Anode radiant sensitivity of photomultiplier tube is shown in figure 3.11. The '-20 Type' marked curve give the sensitivity vs. wavelength of the H5784-20 photomultiplier tube.

3.5.1 Photomultiplier tube power supply

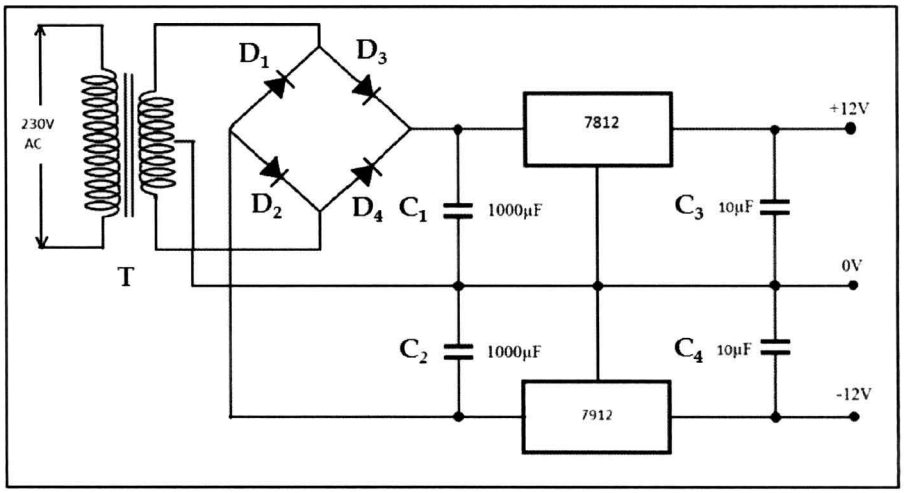

Figure 3.12: Circuit diagram of PMT power supply

A ±12V power supply is required for the photomultiplier tube. Figure 3.12 shows circuit diagram of power supply. The transformer T steps down the AC mains voltage and diodes D_1, D_2, D_3 and D_4 does the rectification. Capacitors C_1 and C_2 does filtering. C_3 and C_4 are decoupling capacitors. IC 7812 and 7912 are used for the purpose of voltage regulation in which the former is a positive 12V regulator and later is a negative 12V regulator. The output of 7812 will be +12V and that of 7912 is -12V.

3.5.2 Sensitivity Adjustment of the photomultiplier tube

There are two methods for sensitivity adjustment

i. Voltage programming

ii. Resistance programming

The sensitivity was adjusted by resistance programming method. Block diagram of resistance programming is given in figure 3.13.

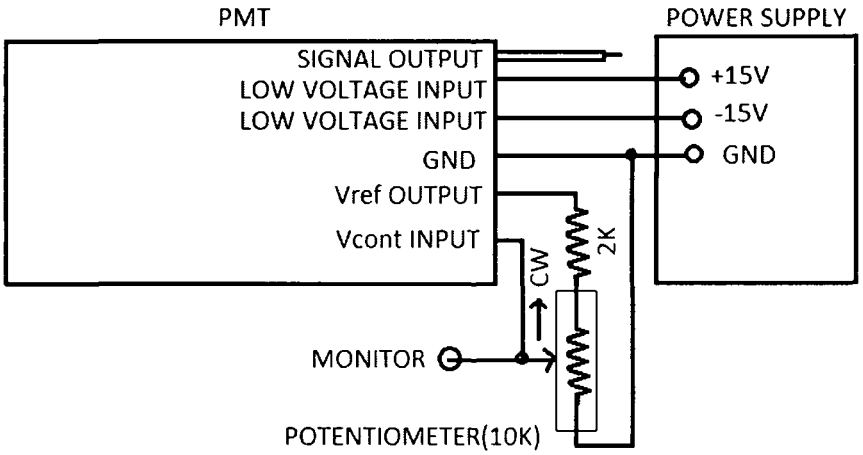

Figure 3.13: Block diagram of Resistance programming

3.6 Photomultiplier tube rotating unit

The photomultiplier tube could be rotated by using a stepper motor. The stepper motor was a brushless, synchronous electric motor that could divide a full rotation into a large number of steps. The motor position could be controlled precisely without any feedback mechanism. The stepper motor effectively had multiple 'toothed' electromagnets arranged around a central gear-shaped piece of iron (figure 3.14). The electromagnets were energized by

an external control circuit. In order to make the motor shaft turn, one electromagnet was supplied with power at first and as a result it enabled the tooth of the gear to get attracted to the tooth of the electromagnet due to magnetic effect. In this way, when the tooth of the gear is aligned to the first electromagnet, they are slightly offset from the next electromagnet. So, when the next electromagnet is turned off, the gear rotates slightly to align itself with the next one, and this process is repeated. There are two basic winding arrangements for electromagnetic coil in two phase stepper motors, namely unipolar and bipolar. In this setup, the photomultiplier tube was rotated by using a unipolar stepper motor. The image of the stepper motor used in our setup is shown in figure 3.14 and the block diagram of the stepper motor control system is shown in figure 3.15.

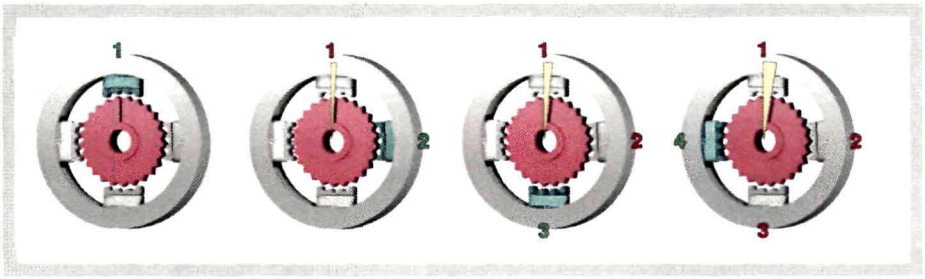

Figure 3.14: Rotation of the stepper motor shaft

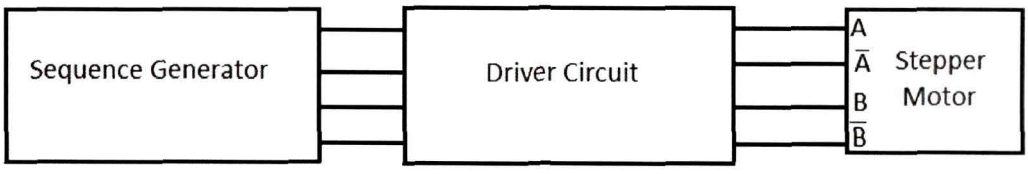

Figure 3.15: Block diagram of stepper motor control system

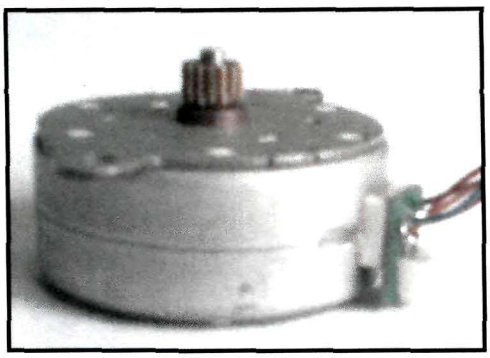

Figure 3.16: Image of the Stepper motor

The photograph of the Stepper motor is shown in figure 3.16. The sequence needed to run the stepper motor was generated by using computer and we got the output sequence through the parallel port of the computer. Since the parallel port output current and voltage was not enough for driving stepper motor, we also needed a driver circuit which is made using MOSFET IRF540.

3.6.1 Driver circuit of the stepper motor

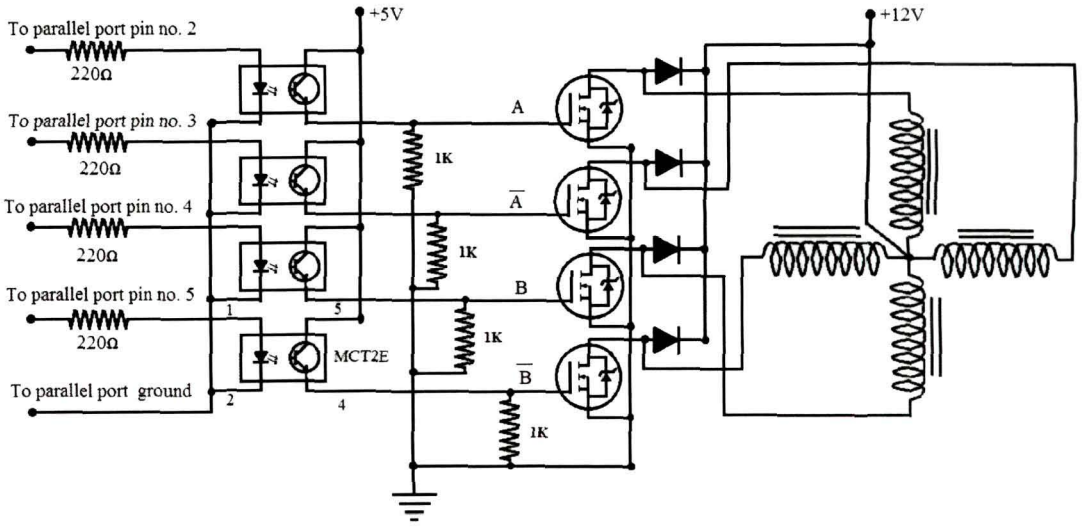

Figure 3.17: Circuit diagram of stepper motor driver

Here the MOSFET acts as a switch. When 'A' is high (+5V), the 1st MOSFET conducts and the current is passed through the stepper motor coil. When 'A' is low, the MOSFET does not conduct and no current passes through the

motor coil. It is the same case for all other MOSFETs. As the motor is an inductive load, a free-wheeling diode is connected across the load to dissipate any back e.m.f. generated by the motor when the MOSFET turns it off. Circuit diagram of the stepper motor driver circuit is shown in figure 3.17. For the safety of the mother-board we have used Optocouplers (MCT2E).

3.6.2 Power supply for stepper motor

The functioning of stepper motor requires +12V and 2A power supply. Since a single 7812 IC cannot give 2 amps current, the output current was increased by paralleling two 7812 IC . The circuit diagram and driver circuit of stepper motor power supply is shown in figures 3.18 and 3.19 respectively.

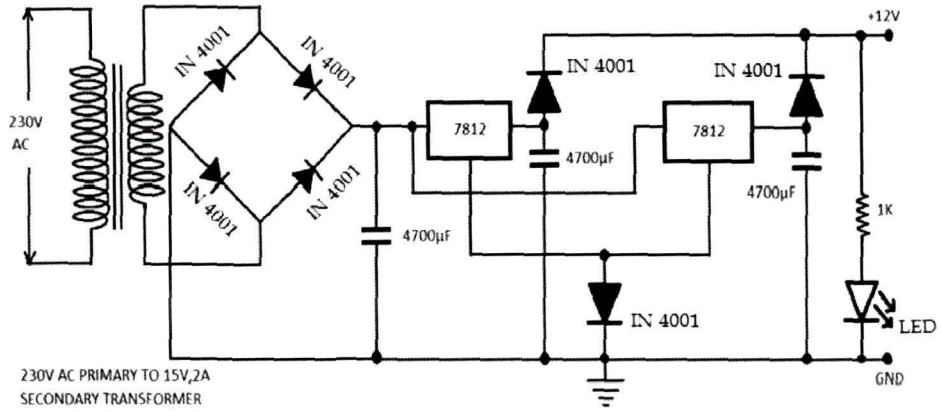

Figure 3.18: Circuit diagram of stepper motor power supply

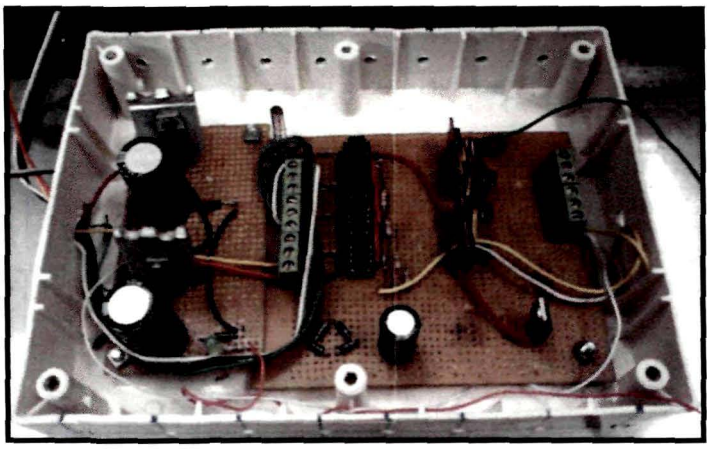

Figure 3.19: Driver circuit of Stepper motor power supply

3.6.3 The C program for generating sequence for driving stepper motor

```
#include <stdio.h>
#include <conio.h>
#include <dos.h>
#define port 0x378
void main()
{
    1   int x,PORT=0x378,y[8]={0x01,0x03,0x02,0x06,0x04,0x0c,0x08,0x09},z,i,j,l,n,k;
    2   printf("\nEnter no of loops:");
    3   scanf("%d",&x);
    4   printf("\nEnter sub loop:");
    5   scanf("%d",&z);
    6   for(j=0;j<x;j++)
    7   for(i=0;i<8;i++)
            {
            outport(PORT,y[i]);
            delay(20);
            printf("%d",y[i]);
            delay(20);
            }
    8   for(i=0;i<z;i++)
            {
            outport(PORT,y[i]);
            delay(20);
            printf("%d",y[i]);
```

```
            delay(20);
            }
    9   getch();
    10  for(k=z-2;k>=0;k--)
            {
    11  outport(PORT,y[k]);
    12  delay(20);
    13  printf("\n%d",y[k]);
    14  delay(20);
            }
    15  for(n=0;n<x;n++)
    16  for(l=7;l>=0;l--)
    17  {
    18  outport(PORT,y[l]);
    19  delay(20);
    20  printf("\n%d",y[l]);
    21  delay(20);
    22  }
    23  getch();
}
```

3. 7 Scattering Sample

The samples used for light scattering investigations using our setup were taken in two forms, (i) scattering particles suspended in some liquid media like water, (ii) scattering particles embedded in matrix medium like Polyvinyl alcohol. Depending upon the type of sample and the media, the arrangement of sample holder was adjusted.

3.7.1 Refractive index matching basin and Sample cell (for sample in a liquid suspension)

When the sample is present in some liquid media, it is taken in a cylindrically shaped Pyrex glass cuvette (diameter, 15mm). The large difference in refractive index between air and glass causes strong reflections of the incident light. To minimize the effects of these unwanted reflections, the cuvette was placed in the center of a cylindrical Pyrex glass basin filled with Glycerine which has the same refractive index as glass (n=1.5). This arrangement was amalgamated in the light scattering system to reduce the influence of undesirable strong reflections. Subsequently, the strong reflections occur farther away from the scattering sample. The Pyrex glass and Glycerine does not affect the state of polarization of passing light [232]. This is how light scattering experiments were performed for sample in suspensions.

3.7.2 Sample holder for particles embedded in a matrix medium

The small particles with the particle size ranging from nanometer to sub-micron size can also be embedded in some matrix medium supplementary to some liquid suspension. The transparent matrix used was a polymer matrix medium, which is Polyvinyl Alcohol or PVA. The major advantage of such an embedding system is that it created an environment to hold the scatterers fixed in the scattering volume. The frozen condition of scatterers (no change in position of scatterers with respect to time) enabled us to make repeated measurements on the same scattering sample to extract an average data, and this step subsequently reduced the experimental errors as well. This type of system gives information about the scattering properties of particles in embedding medium only. Thus, such a system may be used to explore the light scattering properties of polymer embedded nanostructures like CdS, ZnSe, TiO_2, ZnO, etc. The interpretation of results may be further used to improve the performance, usefulness, and accuracy of the established light scattering theories. The results of laboratory light scattering

measurements of some such particles under controlled conditions are presented in chapter IV.

In recent years, extensive work has been done in investigating different particulate matter using light scattering technique. The common practices for holding scattering sample are by using a nebulizer, or using levitation techniques, or by holding the sample in liquid suspension using some conventional means. But, the ease of fabrication, and inexpensive route of preparing such system of polymer matrices makes it a unique and convenient sample holding arrangement for light scattering systems.

3.8. Computer interfacing and data acquisition system

3.8.1 Data acquisition system - Type I

A data acquisition system type - I was indigenously designed using ADC0809 IC as shown in figure 3.20 and figure 3.21. ADC0809 is successive-approximation type analog to digital converter. Output of the photodetector is connected to pin no. 26 of the ADC0809 IC. The IC741 circuit in the analog to digital conversion unit provides the reference voltage for ADC0809 IC. The ADC unit has 8 bit resolution and result in 256 steps. The reference voltage ($+V_{ref}$) is adjusted to 5.12 volts by means of the potentiometer P so that each step is equal to

5.12volts/256=20 milivolt

The IC 555 circuit is operating as a free astable multivibrator and provides the external clock of 50 KHz clock frequency for ADC0809 IC. The pins of ADC0809 IC are interfaced to a Pentium III processor based personal computer via parallel port of the PC as shown in figure 3.21.

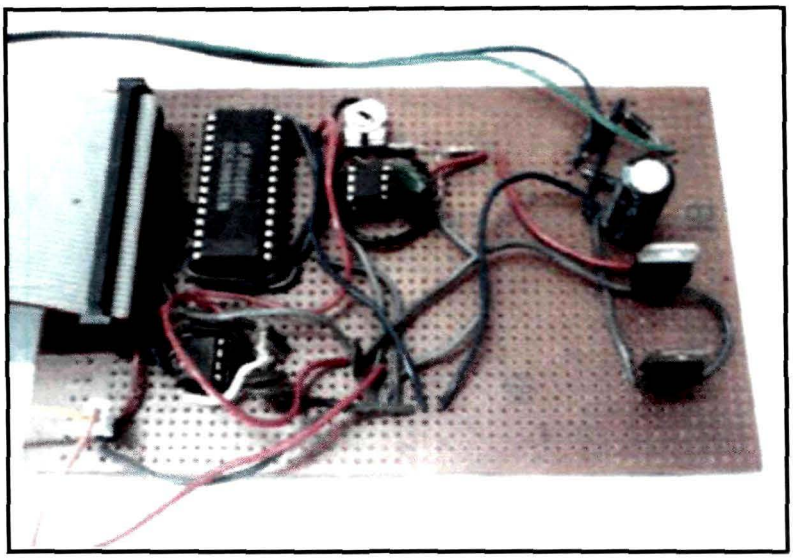

Figure 3.20: Data acquisition system - Type I

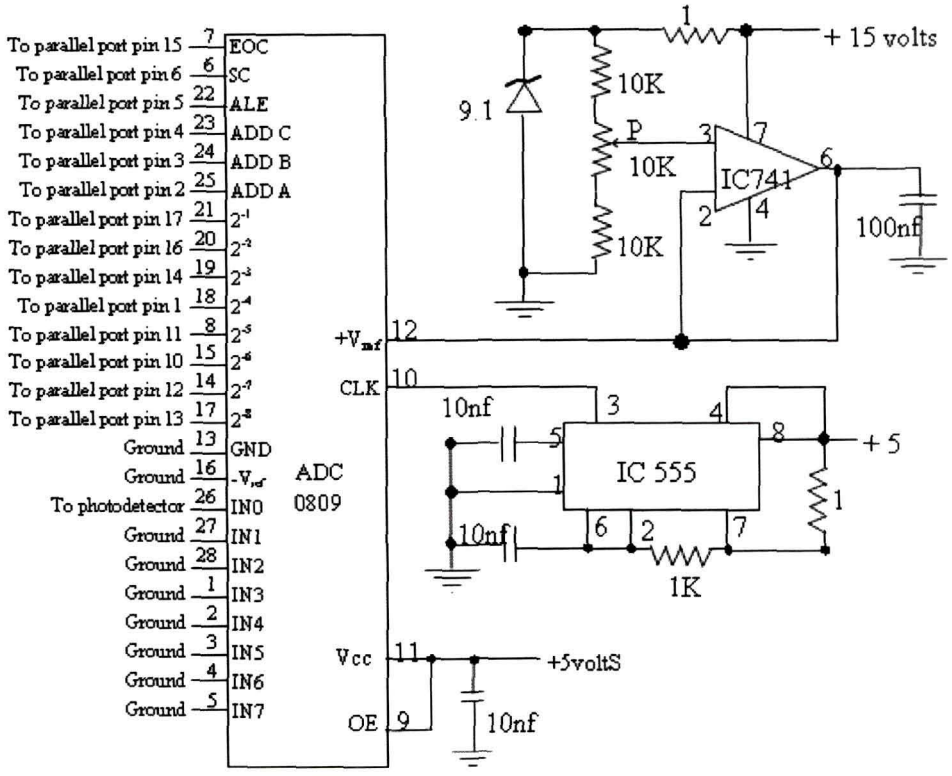

Figure 3.21: Circuit diagram of Analog to digital conversion unit

The flowchart for the data acquisition system is given in figure 3.22.

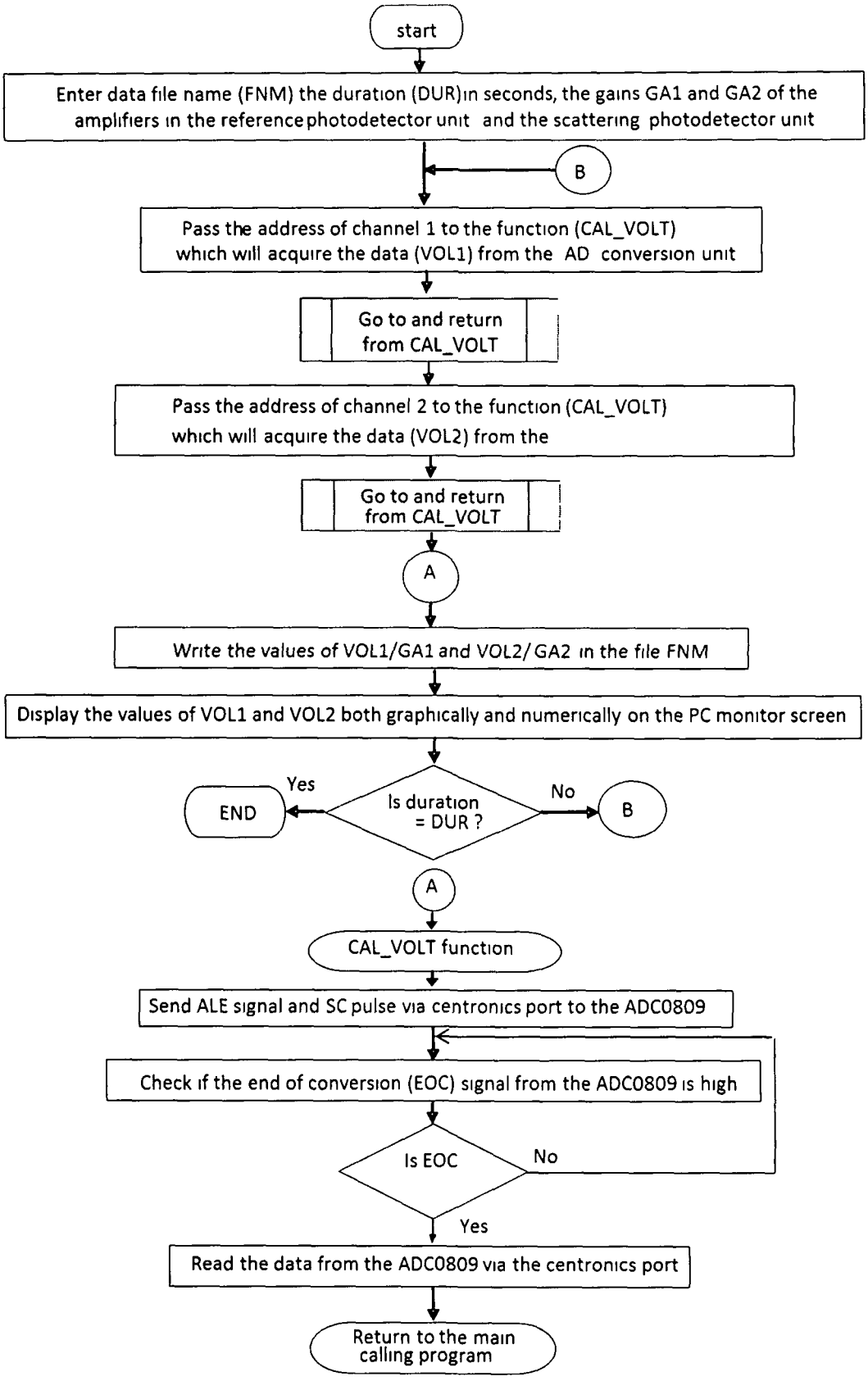

Figure 3.22: Flow chart for the Data acquisition system -Type I

The C language program corresponding to the flowchart in figure 3.22 developed for this data acquisition system is given below.

The C program for data acquisition system I

```
Line number   program
1     #include<stdio.h>
2     #include<conio.h>
3     #include<graphics.h>
4     #include<time.h>
5     #define REF 5.12
6     #define LPT1  0xd00

7     int Cal_volt(unsigned char);
8     void drawline(int *g1,int *oldg1);

9     main()
10    {
11     char add,c,fnm[10];
12     int g=20,oldg=0,dur;
13     long x;
14     float vol1,vol2,
15     float y0,oldy0=0.0,y1,oldy1=0.0,y2,oldy2=0.0;
16     float ga1=1.0,ga2=1.0;
17     FILE *file_ptr;
18     time_t first, second;
19     int GraphDriver = DETECT, GraphMode;
20     initgraph ( &GraphDriver, &GraphMode, "c:\tc\bin\.." );
21     cleardevice();
```

```
22      printf("\n\nEnter filename :");
23      scanf("%s",fnm);
24      cleardevice();
25      gotoxy(1,1);
26      printf("\nduration of reading (in seconds):");
27      scanf("%d",&dur);
28      printf("Enter gain of reference photodetector :");
29      scanf("%f",&ga1);
30     printf("Enter gain of scattering photodetector :");
31      scanf("%f",&ga2);
32      file_ptr = fopen(fnm,"w");
33      cleardevice();
34      drawline(&g,&oldg);
35      gotoxy(10,24);
36      printf("press any key");
37      c=getch();
38      gotoxy(10,24);
39      printf("          ");
40      first = time(NULL);
41      while(c!=27)          {
42              while(!kbhit())
43               {
44               vol1=(REF/256)*Cal_volt(1);
45               vol2=(REF/256)*Cal_volt(2);
46               fprintf(file_ptr,"%f,%f\n",vol1/ga1, \vol2/ga2,);
47               second = time(NULL);
48               if(dur<=difftime(second,first))
49                       {
```

```
50                  gotoxy(10,24);
51                  printf("press ESC key");
52                  goto quit;
53                  }
54              gotoxy(1,12);
55              printf("CH:1\n");
56              printf("vol %1.2f",vol1);
57              printf("\ngain\n%4.1f",ga1);
58              gotoxy(1,7);
59              printf("CH:2\n");
60              printf("vol %1.2f",vol2);
61              printf("\ngain\n%4.1f",ga2);
62             g=g+1;
63              if(g==639)
64             drawline(&g,&oldg);
65              y1=230-(vol1*15);
66              line(oldg,oldy1,g,y1);
67              oldy1=y1;
68              y2=150-(vol2*15);
69              line(oldg,oldy2,g,y2);
70              oldy2=y2;
71               oldg=g;
72             }
73      quit:
74      ;
75      c=getch();
76      }
```

```
77      fprintf(file_ptr,"%c %f",NULL,NULL);
78      fclose(file_ptr);
79      return (0);
80    }
81    Cal_volt(unsigned char add)
82    {
83            unsigned char bt[8],eoc,ale,stc,out;
84            int in,x;
85            ale = 8; stc = 16; eoc = 1;

86            out = add; outportb(LPT1,out);
87            out = add | ale; outportb(LPT1,out);
88            out = out | stc; outportb(LPT1,out);
89            outportb(LPT1,add);

90            while(eoc==1)
91                    {
92                    in=inportb(LPT1+1);
93                    if((in & 8)==0) eoc=0; else eoc=1;
94                    }
95            while(eoc==0)
96                    {
97                    in=inportb(LPT1+1);
98                    if((in & 8)==0) eoc=0; else eoc=1;
99                    }

100           outport((LPT1+2),0x04); in=inport(LPT1+1);
101           if((in & 16)==0) bt[0]=0; else bt[0]=1;
102           if((in & 32)==0) bt[1]=0; else bt[1]=1;
```

```
103             if((in & 64)==0) bt[2]=0; else bt[2]=1;
104             if((in & 128)==0) bt[3]=1; else bt[3]=0;
105             if((in & 256)==0) bt[4]=1; else bt[4]=0;
106             if((in & 512)==0) bt[5]=1; else bt[5]=0;
107             if((in & 1024)==0) bt[6]=0; else bt[6]=1;
108             if((in & 2048)==0) bt[7]=1; else bt[7]=0;
109             in=bt[0]+bt[1]*2+bt[2]*4+bt[3]*8+bt[4]*16+ \
                   bt[5]*32+bt[6]*64+bt[7]*128;
110             return in;
111             }
112   void drawline(int *g1, int *oldg1)
113   {
114   *g1=70;
115   *oldg1=70;
116   cleardevice();
117   setlinestyle(1,3,1);
118   line(70,230,640,230);
119   line(70,150,640,150);
120   line(70,70,640,70);
121   line(70,0,640,0);
122   line(70,0,70,310);
123   line(639,0,639,310);
124   setlinestyle(0,0,1);
125   return ;
      }
```

Each time an experiment is done with the light scattering system, the program is run to acquire output data. The main function is between lines 9 to 80. Lines 19 to 21 prepare the PC monitor screen for online graphical display of the data. Lines 22 to 31 presents the menu on the screen for entering data file name, duration of experiment and gains of the photodetector. Between lines 41 and 76 is a loop that runs either till the end of time duration (DUR in figure 3.22) or till the experiment is aborted by pressing the escape key (ESC) of the PC keyboard. Lines 44 and 45 acquires the values of VOL1 and VOL2 using the CAL_VOLT function given between lines 81 to 111. Line 46 writes down the data in the data file stored in the hard disk of the PC. Within this loop, lines 47 to 53 checks whether the duration DUR of reading has been exceeded and the program has to end. Lines 54 to 61 display numerical values online of VOL1 and VOL2. Lines 62 to 71 display online the values of VOL1 and VOL2, graphically and superimposed on a set of axes, which is displayed by lines 112 to 125. In the CAL_VOLT function lines 86 to 89 sends the ALE and SC pulse to the ADC0809 via the centronics port at address LPT1 to acquire data through the channel given by the address add. Lines 95 to 98 checks for the EOC signal and lines 100 to 110 reads the data via the centronics port and returns it to the calling function. The data is acquired at the rate of 26 data units per second.

3.8.2 Data acquisition system - Type II

General Description and Installation

The amplified signals are interfaced to a dedicated data acquisition system - Type II (AX5210). The AX5210 is a low cost A/D card which gives an inexpensive solution to data acquisition applications. AX5210 has a 12 bit A/D convertor with 16 single-ended analog input channels and throughput of 30 kHz of memory. The system occupies eight consecutive I/O port space, setting correct base address by DIP switch to avoid resisting other devices. Seven bits are equipped to allow us to set the base address from 200(hex) to 3F8 (hex). The following figure illustrates how the I/O port base address is used. The base address switch setting is shown in the figure 3.23 below.

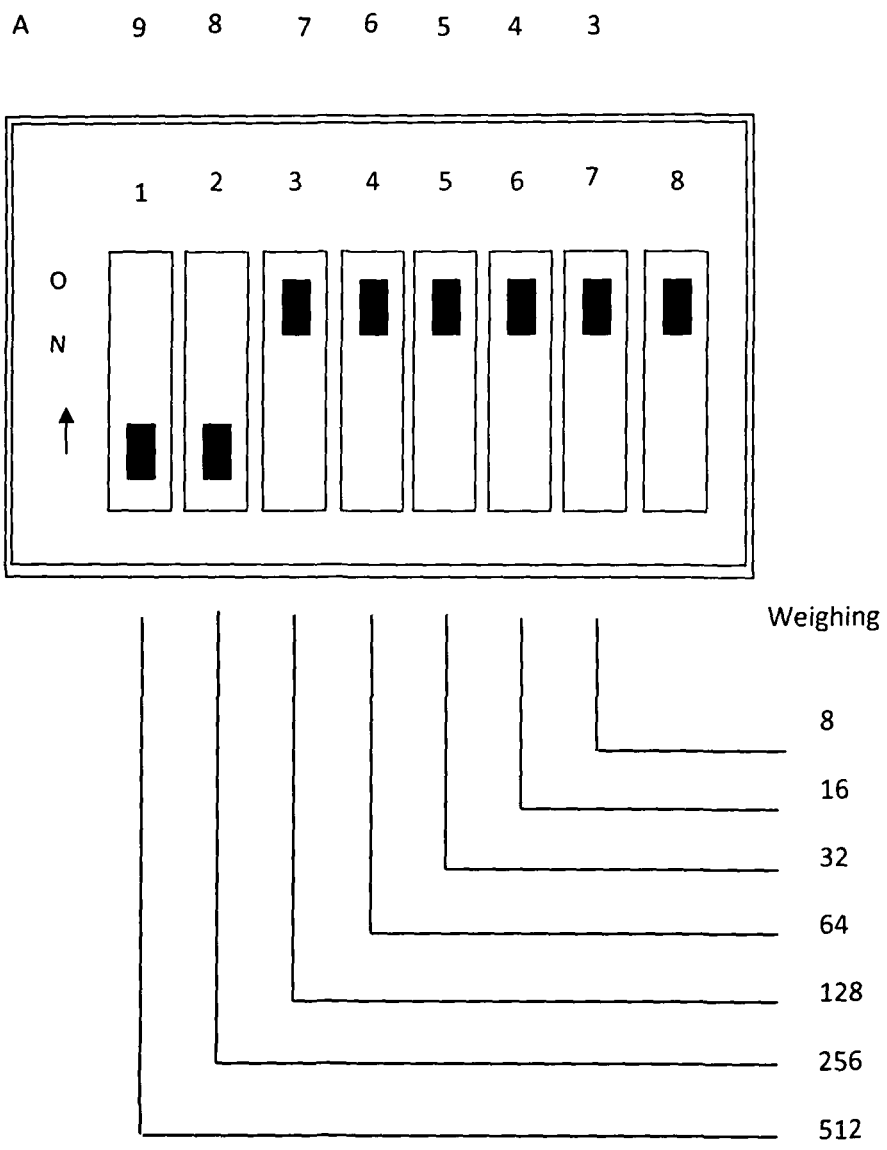

Figure 3.23: Base address setting of Data acquisition system - Type II

I/O PORT RANGE	DIP SWITCH POSITION						
Hex	1	2	3	4	5	6	7
A9	A8	A7	A6	A5	A4	A3	
000-007	0	0	0	0	0	0	0
008-00F	0	0	0	0	0	0	1
200-207	1	0	0	0	0	0	0
208-20F	1	0	0	0	0	0	1
300-307	1	1	0	0	0	0	0
308-30F	1	1	0	0	0	0	1
3F0-3F7	1	1	1	1	1	1	0
3F8-3FF	1	1	1	1	1	1	1

0=ON,1= OFF

In this data acquisition system AX5210 A/D, DIO signals are built in a single connector (CN1). The CN1 PIN assignment is shown in figure 3.24 below, followed by explanation of the PIN assignment.

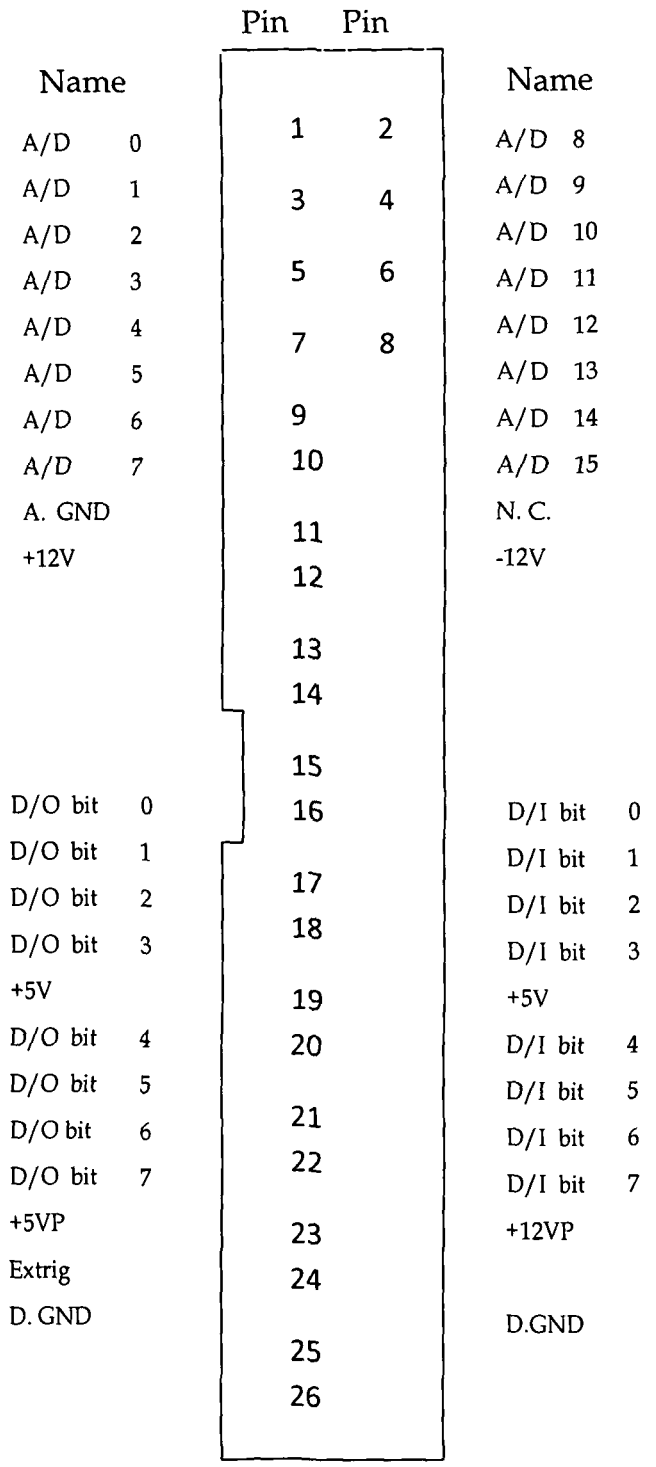

Figure 3.24: AX 5210 Pin Assignment

Note:

+12	(pin 19)	:	600mA max.
-12V	(pin 20)	:	600mA max.
+5VP	(pin 45)	:	current limited to PC power
+12VP	(pin 45)	:	current limited to PC power

PIN	NAME		I/O	FUNCTION			
1	A/D	0	Input	Channel	0	Analog	Input
2	A/D	8	Input	Channel	8	Analog	Input
3	A/D	1	Input	Channel	1	Analog	Input
4	A/D	9	Input	Channel	9	Analog	Input
5	A/D	2	Input	Channel	2	Analog	Input
6	A/D	10	Input	Channel	10	Analog	Input
7	A/D	3	Input	Channel	3	Analog	Input
8	A/D	11	Input	Channel	11	Analog	Input
9	A/D	4	Input	Channel	4	Analog	Input
10	A/D	12	Input	Channel	12	Analog	Input
11	A/D	5	Input	Channel	5	Analog	Input
12	A/D	13	Input	Channel	13	Analog	Input
12	A/D	6	Input	Channel	6	Analog	Input
14	A/D	14	Input	Channel	14	Analog	Input
15	A/D	7	Input	Channel	6	Analog	Input
16	A/D	15	Input	Channel	15	Analog	Input
17	A GND		Ground	Analog	Ground		
18	N C.						
19	+12V		Source	Analog	+12		
20	-12V		Source	Analog	-12V		
21-26	N C.						
27	D/O	0	Output	Channel	0	Digital	Output
28	D/I	0	Input	Channel	0	Digital	Input
29	D/O	1	Output	Channel	1	Digital	Output
30	D/I	1	Input	Channel	1	Digital	Input
31	D/O	2	Output	Channel	2	Digital	Output
32	D/I	2	Input	Channel	2	Digital	Input
33	D/O	3	Output	Channel	3	Digital	Output
34	D/I	3	Input	Channel	3	Digital	Input
35	+5V		Source	PC +5V			
36	+5V		Source	PC +5V			
37	D/O	4	Output	Channel	4	Digital	Output
38	D/I	4	Input	Channel	4	Digital	Input
39	D/O	5	Output	Channel	5	Digital	Output
40	D/I	5	Input	Channel	5	Digital	Input
41	D/O	6	Output	Channel	6	Digital	Output
42	D/I	6	Input	Channel	6	Digital	Input
43	D/O	7	Output	Channel	7	Digital	Output
44	D/I	7	Input	Channel	7	Digital	Input
45	+5VP		Source	PC +5V			
46	+12VP		Source	PC +12V			
47	EXTRIG		Input	External Trigger	Input		
48	N C.						
49	D G ND		Ground	Digital	Ground		
50	D GND		Ground	Digital	Ground		

AX5210 I/O Address Mapping

The data acquisition card supports several driver utilities for different languages. AX5210 uses 8 consecutive addresses in I/O spaces following (R= read, W= write) :-

Location		Function	Type
Base address	+0	A/D Low byte and Channel Start A/D or Clear INTP	R W
	+1	A/D High byte Gain & Max. scan control	R W
	+2	PCI-9812 Status PCI-9812 Control	R W
	+3	Digital Input Digital Output	R W
	+4	Counter 0	R/W
	+5	Counter 1	R/W
	+6	Counter 2	R/W
	+7	Counter Control	W

AX5210 I/O Register Description

A/D data Register (base +0 & base +1 Read Only)

7	6	5	4	3	2	1	0
D3	D2	D1	D0	C3	C2	C1	C0

Bits 0-3 C0-C3 The channel select bits are used to specify one of the 16 channels (0-15) as the input channel for A/D conversions.

Bits 4-7 D0-D3 These bits are A/D least significant data (LSB).

Software Start

A right action to base +0 will cause an A/D trigger and always initiate a conversion on software trigger for A/D.

Clear Interrupt (Start on Extrig or Start on Timer)

Writing to base +0 may clear AX5210 interrupt request (INTP) ad provides the means of acknowledging the AX5210 and re-enabling it.

7	6	5	4	3	2	1	0
D11	D10	D9	D8	D7	D6	D5	D4

MSB

Most significant A/D data.

Bits 0-7 D4-D11 These bits are A/D most significant data.

Status Register (base +2 Read Only)

7	6	5	4	3	2	1	0
X	X	X	X	EOC	INTP	T1	T0

Bits 0-1 T0-T1 Read back of the A/D start source control bits.

T1	T0	Action
0	X	Software start only.
1	0	Start on rising of external trig (extrig).
1	1	Start on internal timer trig.

X- These bits don't care

Bits 2 INTP This is the interrupt signal that is used directly to interrupt level2-7 by the jumper selection. If interrupt are disabled, INTP=0. After generation of an interrupt, INTP=1 and will remain high until reset by a write to the base +0.

Bits 3 EOC This indicates the end of a conversion cycle.
0= conversion has completed; Valid data.
1= conversion is still in process; Invalid data.
A start of A/D conversion will set the EOC=1.

Bits 4-7 X These bits do not care.

Digital Input (base +3 Read Only)

7	6	5	4	3	2	1	0
IP7	IP6	IP5	IP4	IP3	IP2	IP1	IP0

Setting Gain and Channel Number (base +1 Write Only)

7	6	5	4	3	2	1	0
X	R2	R1	R0	C3	C2	C1	C0

Bits 0-3 C0-C3 The channel select bits are used to specify one of the 16 channels (0-15) as the input channel for A/D conversions

Bits 4-6 R0-R2 These bits specify the gain.

R2	R1	R0	GAIN	RANGE
0	0	0	1	± 5V
0	0	1	2	± 2.5V
0	1	0	4	± 1.25V
0	1	1	8	± .625V
1	0	0	16	± 0.3125V

Others are invalid

Bit 7 X These bits do not care

Control Functions (base +2 Write Only)

7	6	5	4	3	2	1	0
X	X	X	X	TRGE	INTE	T1	T0

Bits 0-1 T0-T1 These bits control the source of start pulse for the A/D

T1	T0	Action
0	X	Software start only.
1	0	Start on rising of external trig (extrig).
1	1	Start on internal timer trig.

X- Meaning don't care

Bit 2 INTE This bit enables or disables PCI-9812 generated interrupts.

INTE= 0- Disable.

INTE= 1- Enable.

If INTE=1 an interrupt is generated at the end of each A/D conversion when valid data is available.

Bit 3 TRGE External trig (EXTRIG) and trig enable (TRGE) of the timer enable register are relative, because TRGE is enable for EXTRIG. The relation follows

as:

TRGE	EXTRG	TIMER
0	0	Enable
0	1	Enable
1	0	Disable
1	1	Disable

Digital Output (base +3 Write Only)

7	6	5	4	3	2	1	0
OP7	OP6	OP5	OP4	OP3	OP2	OP1	OP0

Power 'On' Initiate Condition

1. Scan Channel= 0 (base+1 cleared)
2. Gain= 1 (base +1 cleared)
3. Software trig (T1 & T0= 0)
4. Digital output all of low. (base +3 cleared)
5. EOC= 0 (No A/D trig)
6. INTP= 0 (cleared)
7. INTE= 0 (base +2 cleared)
8. TRGE= 0 (base +2 cleared)

Some Important functions of AX5210

1. Function INIT% : Initialization

The purpose of using this function is to setup base address to dio(0), and to setup interrupt level according to dio(1). It also allows checking the presence of AX5210 hardware. This function, Function Init, is needed to be executed only once, but must be performed before any other functions.

2. Function SET. CH%: Set channel range

This channel is needed to be executed only once, and must be performed before A/D conversion.

3. Function SET.GAIN% : Set gain into relative channel

This function is optional. The default gain in all channels is 1, otherwise it must be performed at least once before A/D conversion function.

4. Function SFT.TRG% : Perform single A/D conversion

This function performs A/D conversion with software trigger.

Calibration

The block diagram of data acquisition system - type II is shown in figure 3.25 below. The AX5210 calibration program (CAL5210.exe) provides a menu driven calibration procedure of A/D and digital I/O. The default I/O port address is at 300 (Hex). For amplifier offset and A/D full scale adjustment, a good digital voltage meter and a DC standard (or noise free, stable DC power supply) are necessary. The amplifier offset adjustment is executed to lessen input amplifier offset error. And the A/D full scale adjustments are performed to make sure that the A/D convertor is working with the best resolution.

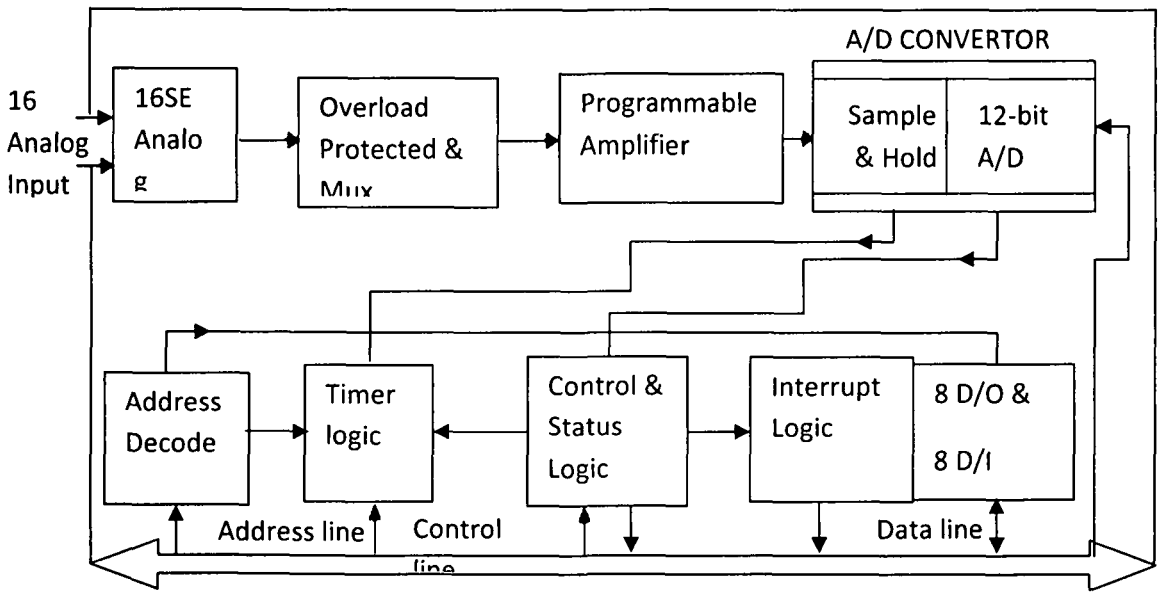

Figure 3.25: Block diagram of the Data acquisition system - Type II

Analog Input System

The basic function of analog input system (A/D system) shown in figure 3.26 is to convert the analog input signal to corresponding digital format that the computer can read. In order to benefit A/D system's stability and obtain good performance, several other additional parts such as multiplexer, amplifier, sample and hold are required. Following figure exhibits how different input signals come into the A/D system:

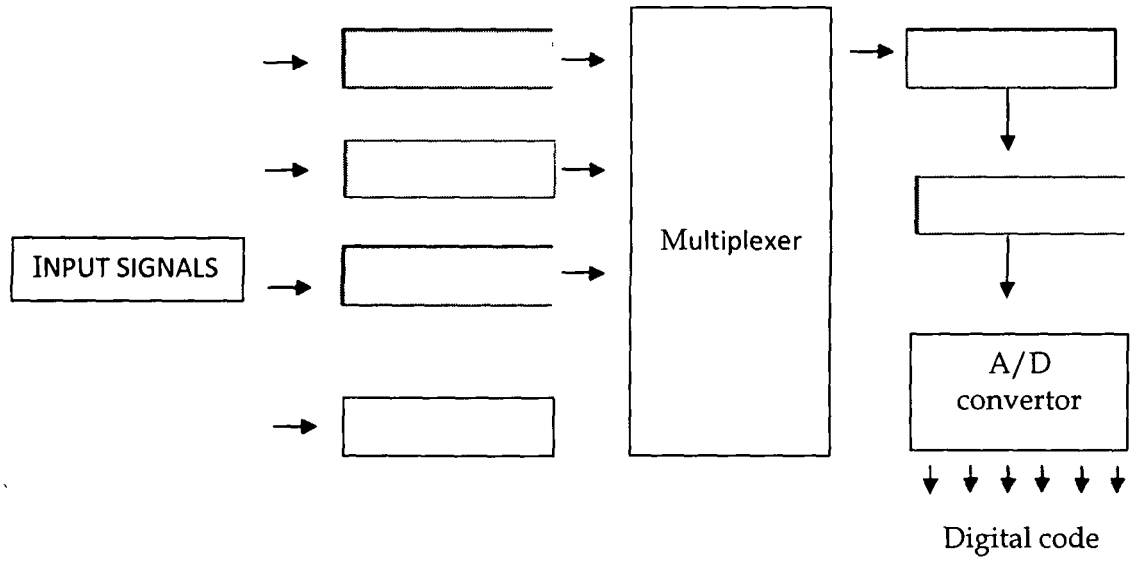

Figure 3.26: Block diagram of Analog Input System

C-program for single channel A/D conversion

```
#include "ax5210.h"
#define IOPORT 0x300 /* AX5210 IOport */
Int fun,flag;
unsigned int dio[7];
int far *ary1;
int far *ary2;

main()
```

```
{
    int   start_ch, i;

/* INITIAL AX5210 */
fun=INIT;          /* Initial function */
dio[0]=IOPORT;     /* IOport set */
dio[1]=3;          /* IRQ NO. */
flag=ax5210(fun,dio,ary1,ary2);
if (flag != 0) {
   printf (" DRIVER INITIALIZATION FAILED !,flag=%d\n",flag);
   exit(1);
   }

/* SET START & STOP CHANNEL */
start_ch=0;
stop_ch=0;
fun=SET_CH;
/* Set channel function */
dio[0]=start_ch;     /* Start channel set */
dio[1]=stop_ch;      /* Stop  channel set */
flag=ax5210(fun,dio,ary1,ary2);
if (flag !=0 ) {
   printf ("SET SCAN CHANNEL FAILED ! RE-ENTER");
   exit(1);
   }

    /* SET GAIN FOR ALL CHANNEL */
fun=SET_GAIN;
```

```
dio[0]=0;

dio[1]=1;

flag=ax5210(fun,dio,ary1,ary2);

if (flag != 0) {

   printf ("SET GAIN FAILED!,FLAG=%d\n",flag);

   exit(1);

   }


/* SOFTWARE TRIGGER */

do {

   fun=SFT_TRG;       /* Software trigger function */

   flag=ax5210(fun,dio,ary1,ary2);

   if (flag != 0) {

   printf("A/D CONVERSION FAILED !" );

   exit(1);

   }

printf("\n CHANNEL %d\n DATA %d\n " ,dio[1],dio[0]);

printf(" PRESS ANY KEY TO CONVERT NEXT CHANNEL, <e> TO EXIT\n");

} while (getche() != 'e');

}
```

The flow chart of Data Acquisition system - type II is given in figure 3.27 below. The performance of data acquisition system - type II is found to be better than type I, and is used in the light scattering system because of the ability to monitor multiple channels with one system. It has the ability to acquire a large amount of data very fast within the duration of the experiment and the facility for storing this large amount of data, and the ability to monitor online the ongoing experimental data.

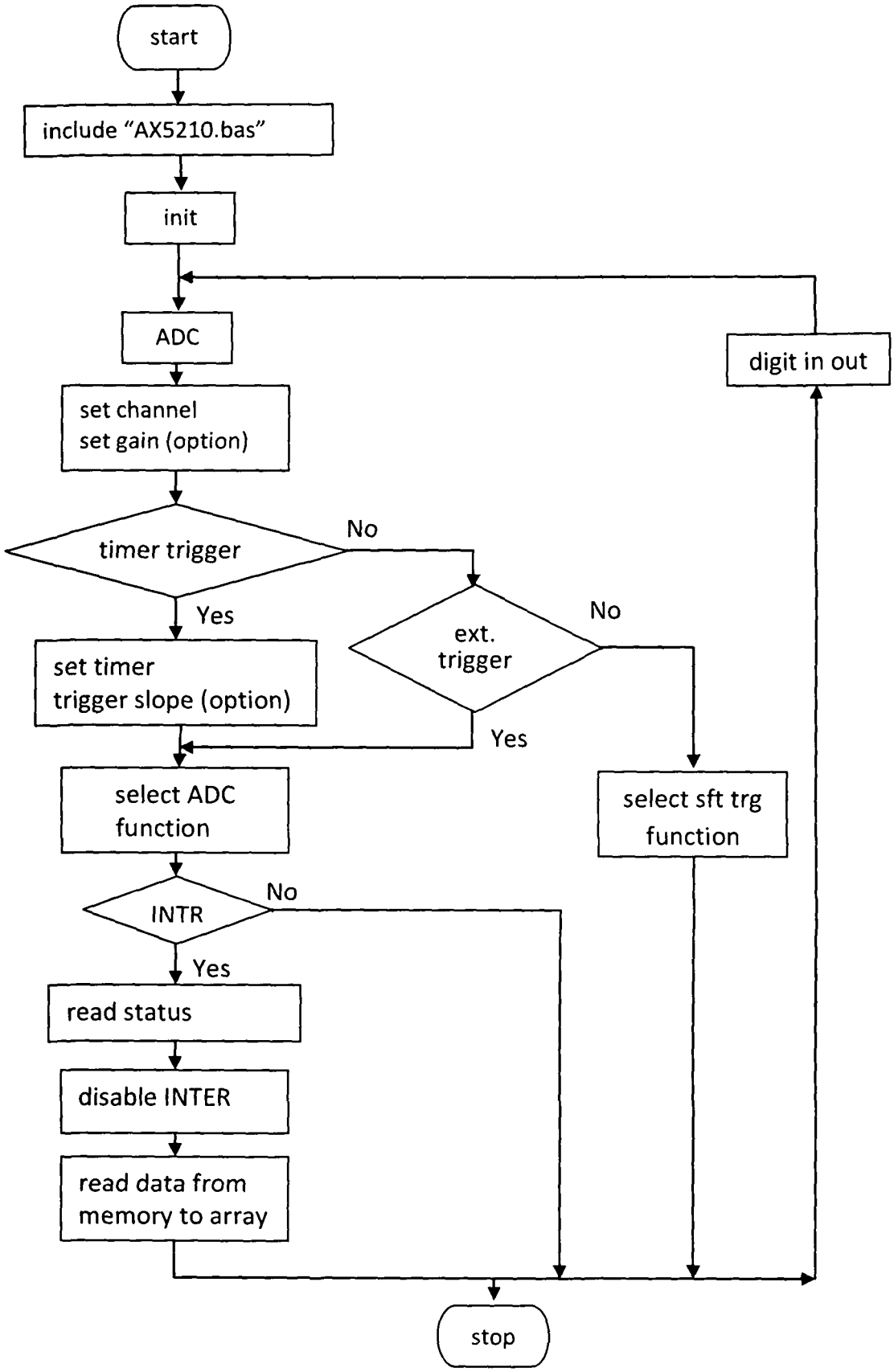

Figure 3.27: Flow chart of Data Acquisition System - Type II

3.9 Data Reduction Procedure

3.9.1 Data reduction for sample in suspension

There are several crucial error reduction steps that need to be performed during light scattering experiments. Before performing any light scattering measurements it is important to determine proper sample concentration in order to ensure that the measurements are in the single scattering regime. The results obtained from light-scattering measurements were corrected for the following factors.

(1) The changing scattering volume in the view of the rotating detector.

(2) Background scattering.

(3) Reflections at the wall of the sample holder

Samples of necessarily low concentration were used to avoid multiple scattering [232]. However, care was taken that the samples were not very diluted; else it would decrease the signal-to-noise ratio. In order to generate information about the optimal sample concentration, the detector was placed at a fixed position at θ=15°. Accordingly, sequences of measurements were made for the same sample with increasing concentration. Scattered flux from each sample was noted down. And so long as the flux was found to be proportional to the sample concentration, multiple scattering was considered to be negligible. This method enables one to determine the appropriate optimal concentration of the sample in the single scattering regime.

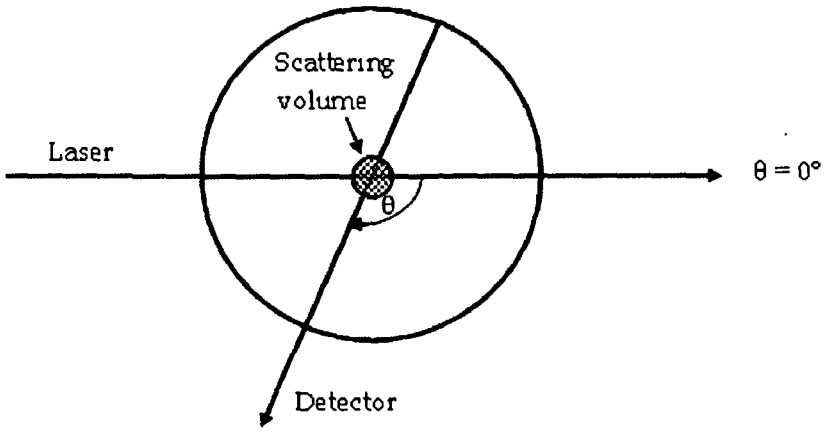

Figure 3.28: Schematic diagram of changing scattering volume in view of the detector.

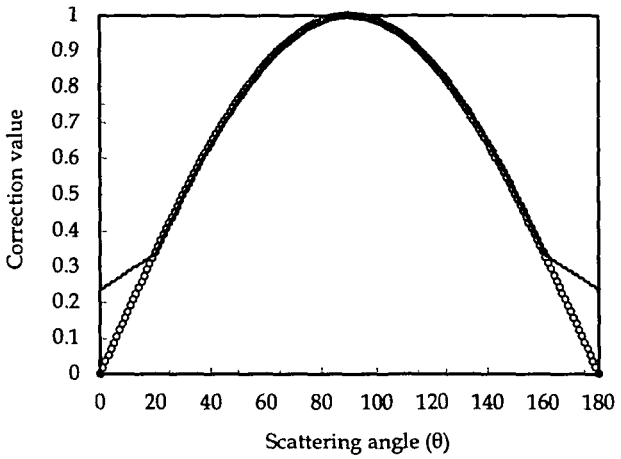

Figure 3.29: Correction function of scattering angle (shown by solid red line) to correct the measured flux for changing scattering volume as seen by the detector. This function is equal to sin θ for most of the scattering angle range (shown by black circles).

Intersection of the incident beam with the detector field of view determines the scattering volume (figure 3.28), which consequently changes with angle. The scattering volume in the view of the detector was determined by the scattering angle, the scattering volume inside the cuvette (having a length of 15 mm which is the diameter of the cuvette , and width of 1 mm

which is $2\omega_o$ of the laser beam), the distance to the photomultiplier tube which is 200mm, and by the circular pinhole in front of the photomultiplier having diameter of 5 mm. Considering this geometry and assuming that the width of the laser beam can be neglected, the correction factors as a function of scattering angle were derived. The measured flux has to be multiplied by the correction factor to correct the scattering volume as seen by the detector. The correction factor versus scattering angle graph by which the measured intensity has to be multiplied to correct the changing scattering volume seen by the detector is shown in figure 3.29[45]. Again, it is important to mention that the scattering volume is minimum for $\theta = 90°$ and gradually increases on either side of this angle, accordingly the intensity is expected to be minimum at this angle. The measured scattering intensity can be corrected for a constant scattering volume by multiplying by the correction factor sin θ [45, 232, 239]. But this sine correction is valid upto the scattering angle at which the detection area or the solid angle of the photodetector becomes equal or narrower than the path length of the beam as shown by Case I and II in figure 3.30, and outside this area the scattering volume is constant, as depicted in Case III. Thus, the standard acceptance range used in the present work is between 20° and 160°.

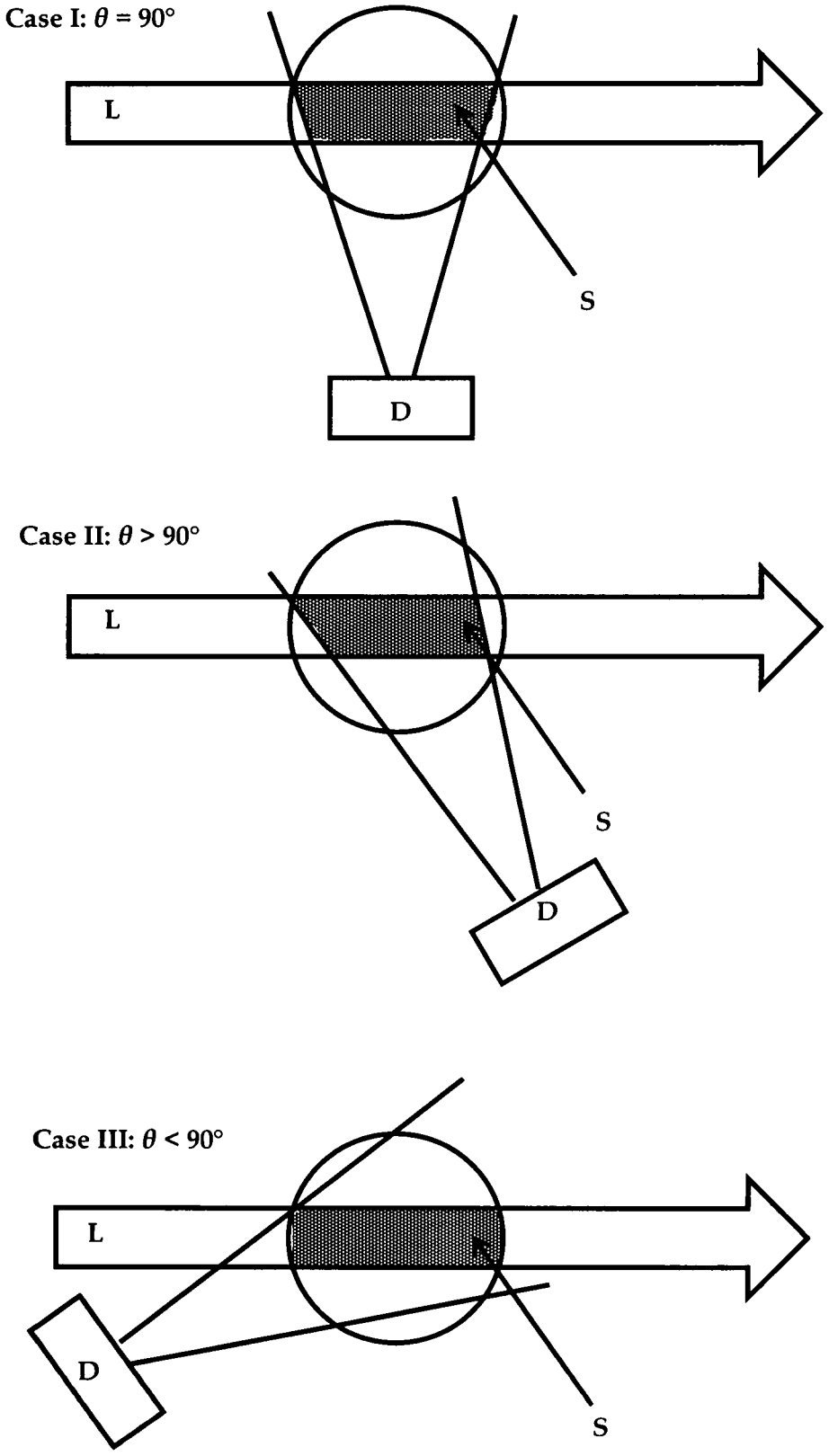

Figure 3.30: Changing scattering volume with respect to changing scattering angle. **L**: Laser beam; **D**: Detector; **S**: scattering volume.

Again, background correction is important and a necessary step to be performed when we use samples of low concentration to avoid multiple scattering. To minimize the background noise, we took our measurements in differential mode, that is, the scattered light intensity was initially measured with the cuvette containing distilled water without scattering particles, and subsequently the measurements were taken with the cuvette containing the scattering particles with distilled water. The data from the set of experiments with distilled water were then subtracted from the data of the set of experiments taken with the scattering particles suspended in distilled water. The amount of light scattering taking place from the background was subtracted from the measurements on samples such that

$$S_{11} = S_{11}^{meas} - S_{11}^{backgr} \qquad \textbf{3.9.1}$$

$$S_{12} = S_{12}^{meas} - S_{12}^{backgr} \qquad \textbf{3.9.2}$$

Where S_{11}^{backgr} and S_{12}^{backgr} are results of measurements of the cuvette filled with the same liquid medium as during the measurements of S_{11}^{meas} and S_{12}^{meas} but without the scattering sample in it. This is how it was ensured that the results obtained were independent of the medium in which the particles were suspended.

Again, while using the experimental data from static light scattering experiments on suspended particles, one must take into account the secondary reflected noise from the inner wall of the cylindrical glass cuvette because neglecting this effect may lead to false interpretation of the size or the refractive index of the scatterers [329]. The particles in the sample scatter the incoming incident light in all directions and therefore the intensities measured by the detectors consist of the actual scattered intensity at scattering angle θ along with the secondary scattering intensities from the inner wall of the glass cuvette at the scattering angle $\theta' = 180^{o} - \theta$. The contribution of this reflectivity is eliminated by introducing a semi-cylindrical blackened screen inside the

cuvette (figure 3.31). The light scattered towards the dark screen inside the cuvette is mostly absorbed. However, the strong intensity of the direct incident light gets reflected at the inner wall of the cuvette and follows its trace back and is again scattered along the path. The flux of the first-order reflected and scattered light is proportional to S_{11} (180°- θ) times the reflection coefficient R, as shown in figure 3.32[330 - 332]. We have used R =0.017 which is the reflection coefficient of Pyrex glass.

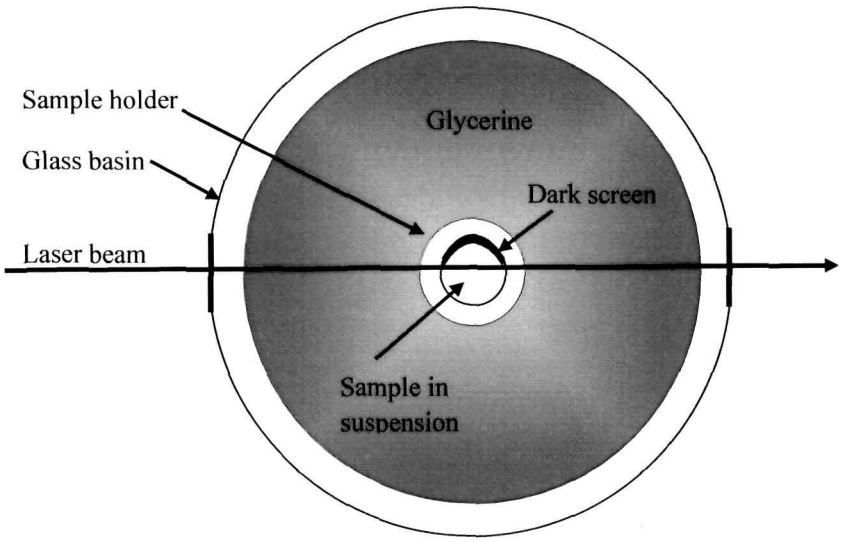

Figure 3.31: Schematic diagram of the sample holder for sample in liquid suspension.

Taking into account multiple reflections, the following expression holds for S_{11}^{uncor}, the uncorrected measured values for reflections:

$$S_{11}^{uncor}(\theta) = S_{11}(\theta) + S_{11}(180^o - \theta)R + S_{11}(\theta)R^2 + S_{11}(180^o - \theta)R^3 + \ldots \quad \textbf{3.9.3}$$

$$= [S_{11}(\theta) + S_{11}(180^o - \theta)R]\frac{1}{1-R^2} \quad \textbf{3.9.4}$$

where the expression for a geometric series was used

$$\frac{1}{1-R^2} = 1 + R^2 + R^4 + R^6 + \ldots \quad \textbf{3.9.5}$$

and S_{11} represents the real scattering function. Now, if we substitute θ by $(180^o - \theta)$ in equation 3.9.4 and multiplying by R, we obtain the following expression

$$S_{11}^{uncor}(180^o - \theta)R = [S_{11}(180^o - \theta) + S_{11}(\theta)R] \times \frac{R}{1 - R^2} \qquad \textbf{3.9.6}$$

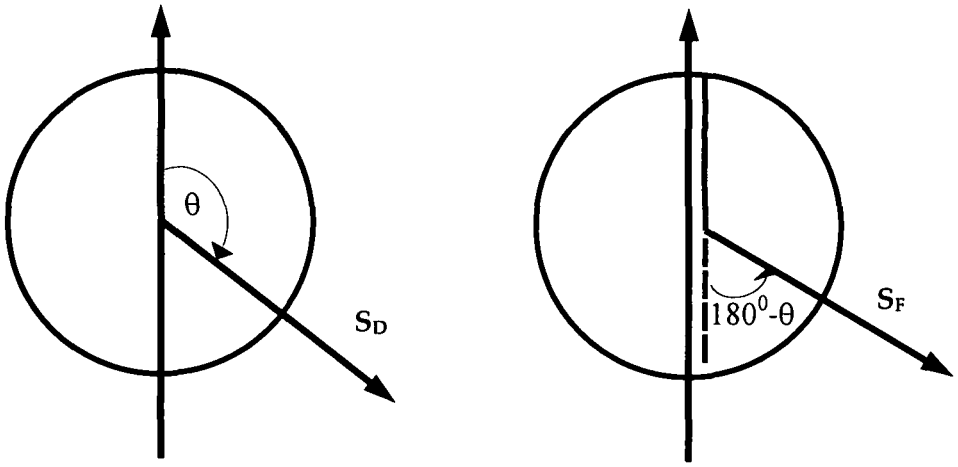

Figure 3.32: Scattering geometry for the description of the reflected light contributions. In the centre of the cylindrical glass cell the laser light is scattered in all directions. The intensity arriving at the detector consists of the directly scattered intensity(S_D)with scattering angle θ and the reflected intensity(S_F) from the glass wall opposite to the direction of detection with scattering angle $\theta' = 180° - \theta$.

Subtracting equation 3.9.6 from equation 3.9.4 yields the exact expression for the true scattering function

$$S_{11}(\theta) = S_{11}^{uncor}(\theta) - [S_{11}^{uncor}(180^o - \theta)]R \qquad \textbf{3.9.7}$$

Similarly, we obtain the actual value for $S_{12}(\theta)$ as

$$S_{12}(\theta) = S_{12}^{uncor}(\theta) - [S_{12}^{uncor}(180^o - \theta)]R \qquad \textbf{3.9.8}$$

Also, due to the stray light contamination and background light coming mainly from the reflections at the walls of the sample holder, it is usually very difficult to discriminate between the actual scattered signal and noise at lower (less than 20°) and higher (greater than 160°) phase angles and the corrected

signal could be lower than the total background contribution at such angles. In such cases, it is very important to test the stability of the polarization measurements because a small error in background correction may lead to abrupt change in the degree of linear polarization. The data reduction process for the volume scattering function $\beta(\theta)$ and the degree of linear polarization $P(\theta)$ of polystyrene spheres are discussed in Section 3.10.

3.9.2 Data reduction for sample embedded in matrix medium.

Background correction is an important step for particles embedded in a matrix medium also. The schematic diagram of the scattering particles embedded in matrix medium is presented in figure 3.33. Polyvinyl alcohol was selected as host polymer for embedding particles. The physical properties of PVA are given in table 3.3.

Table 3.3: Physical properties of PVA

Serial No.	Property	Value/Unit
1	refractive index	1.55
2	dielectric constant	2.0
3	melting point	413k
4	density	1.08 g/mol

The measurements were done in differential mode in order to minimize the background noise. The scattered light intensity was initially measured for the polyvinyl matrix medium only, and subsequently measurements were made with the matrix having the scattering particles embedded in it. The data from the set of experiments with the matrix were then subtracted from the data of the set of experiments taken with particles embedded in the medium. In this manner the measurements were corrected from background measurements. This step took care of the nominal amount of optical and

electrical noise that still remained in spite of using metallic enclosure and beam stop.

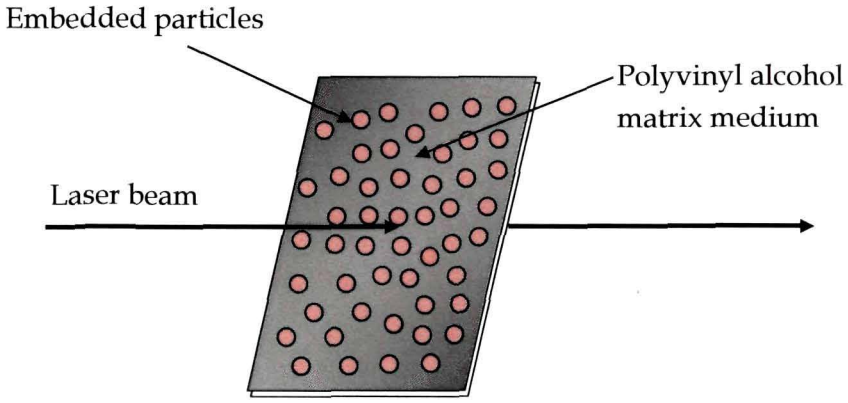

Figure 3.33: Schematic diagram of the sample embedded in matrix.

3.10 Validation of the Light scattering setup

. The most important point which must be taken into account before using any light scattering setup is to check the reliability of the setup. The performance of any light scattering setup is evaluated by conducting experiments on perfectly spherical particles and then comparing the results with the theoretical Mie calculations [30, 232, 239]. Test measurements were made on Polystyrene latex spheres. The pictorial representation for data reduction process for $\beta(\theta)$ and $P(\theta)$ at wavelength of 543.5 nm are shown in figures 3.34 and 3.35 respectively, and the same method was repeated for the other wavelengths. The test measurements were followed by comparison with Mie calculations for such spherical particles [4] having a normal Gaussian size distribution as shown in figure 3.36. In this work, extensive experiments on polystyrene spheres suspended in double-distilled water were performed at 543.5 nm, 594.5 nm and 632.8 nm incident wavelengths and the results obtained were compared with Mie calculations. Figure 3.37 shows the scanning electron microscopy (SEM) image of the polystyrene particles. The particles were found to be mostly spherical, having an average size of 0.25 μm.

We have applied the method followed by H. Volten et al. [232] to determine the highest sample concentration for which single scattering is applicable. To ensure that the measurements were in single scattering regime, the intensity of scattered light for unpolarized incident light was measured as a function of increasing particle concentration at an angle of 15°. A number of measurements were subsequently made with increasing sample concentration. The effect of multiple scattering is assumed to be negligible as long as the scattered flux is proportional to the sample concentration. In our case, we found the optimum concentration of polystyrene samples to be 4mg/L (as shown in figure 3.34). This test was performed by following the method described in sub-section 3.9.1, where the polarization was measured as a function of increasing particle concentration within the single scattering regime at a fixed phase angle [219, 333]. In our case, the degree of linear polarization, $P(\theta)$ was observed to be fairly stable at 15° as shown in figure 3.35.

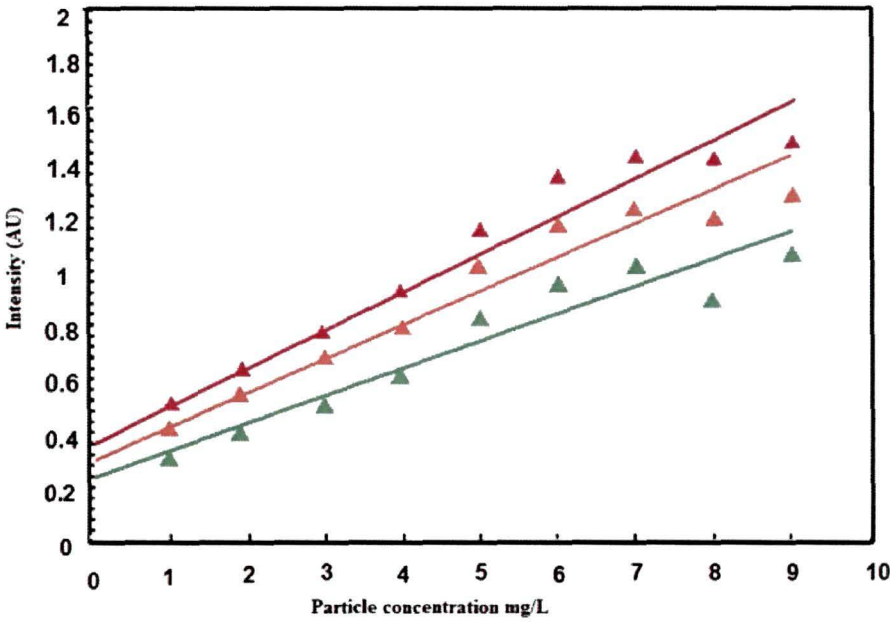

Figure 3.34: Graph for the intensity of scattered light in arbitrary units for unpolarized light versus concentration of Polystyrene spheres for a fixed position of detector at 15^0. green triangle, orange triangle, and red triangle corresponds to the results for 543.5nm, 594.5nm and 632.8nm incident laser wavelengths respectively.

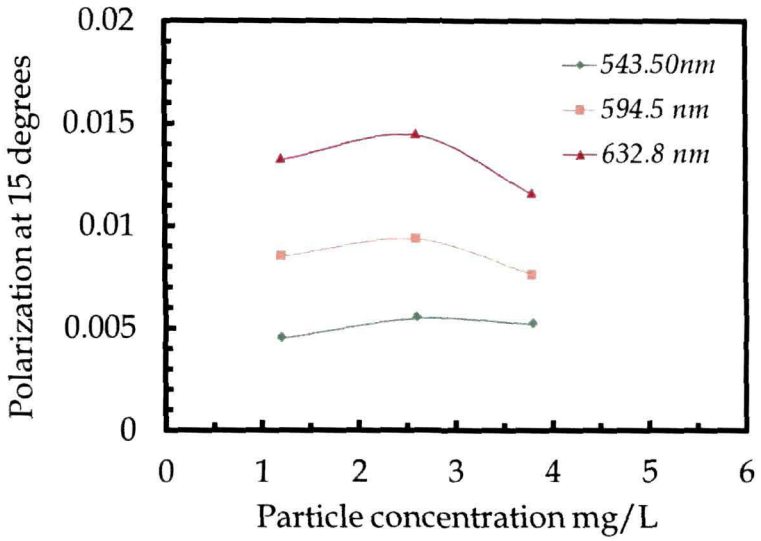

Figure 3.35: Graph for the measurement of the stability of measured polarization of polystyrene at increasing particle concentration within the single scattering regime for a fixed position of detector at 15°.

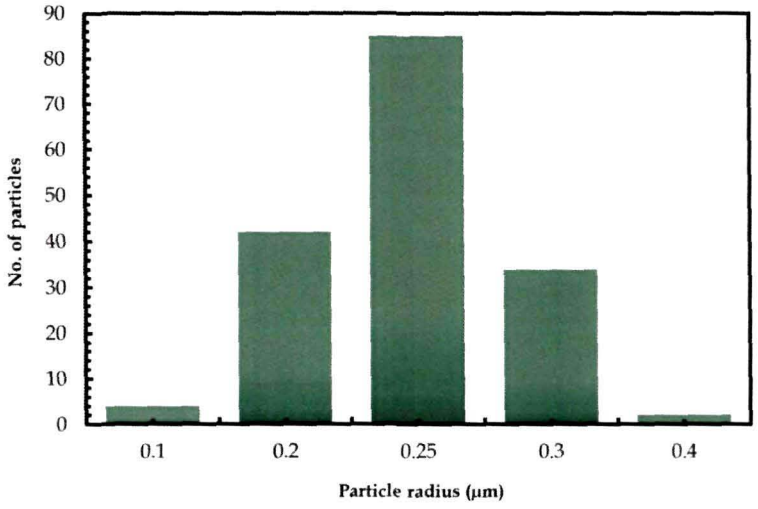

Figure 3.36: Size distribution graph of Polystyrene particles

The measured and computed values of the volume scattering function, $\beta(\theta)$ and the degree of linear polarization , $P(\theta)$ are plotted in figures 3.38 - 3.40 and 3.42 - 3.44 respectively. A closer agreement of the experimental

measurements with the theoretical calculations was found for a normal (Gaussian) distribution of particles. The dispersion formula was used for determination of the refractive indices of polystyrene spheres at three different incident wavelengths [334]. Mie oscillations were present to some extent in the experimental scattering pattern (figures 3.39 - 3.41) since the size distribution of the particles in the scattering volume was not very broad. In order to simplify the different steps involved in the data reduction procedure we have shown all the results of data reduction in the same plot in figure 3.38 and 3.42 at wavelength of 543.5 nm for $\beta(\theta)$ and $P(\theta)$ respectively. Similarly, these steps were followed for the other incident wavelengths for polystyrene sample in order to acquire the final scattering data, and subsequently for all other samples investigated in this research work. The estimated parameters required for data analysis are presented in table 3.4. The measured volume scattering phase function, $\beta(\theta)$ and the degree of linear polarization, $P(\theta)$ agree considerably well with the results drawn from Mie theory within acceptable limits of deviation as observed from the chi square fitting test, presented in Section 4.8 of Chapter IV. The deviations which are more prominent for $P(\theta)$ may be attributed to the presence of some aggregate of particles in the scattering volume as encircled in figure 3.37. We verified that after applying the data reduction method, we found goodness of fit between theoretical and experimental results for both $\beta(\theta)$ and $P(\theta)$. However, minor discrepancies still exists and found to be more prominent at small and large scattering angle for all the incident wavelengths. This step enabled us to compare our experimental results with theoretical results with greater accuracy.

Table 3.4 Important parameters for Mie calculation of polystyrene spheres.

Parameters	Value
Size distribution	Normal (Gaussian)
Model radius, *r*, of the polystyrene spheres in micrometres	0.25
Environment refractive index	1.00 + i0.000 00
Particle refractive index at 543.5 nm	1.588 + i0.000 00
Particle refractive index at 594.5 nm	1.585 + i0.000 00
Particle refractive index at 632.8 nm	1.582 + i0.000 00
Incident light wavelengths in nanometers	543.5, 594.5 and 632.8

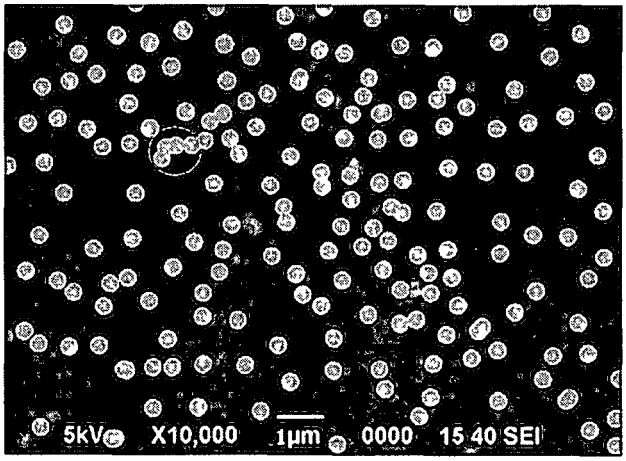

Figure 3.37: Scanning electron micrograph image of polystyrene spheres at 10,000X resolution.

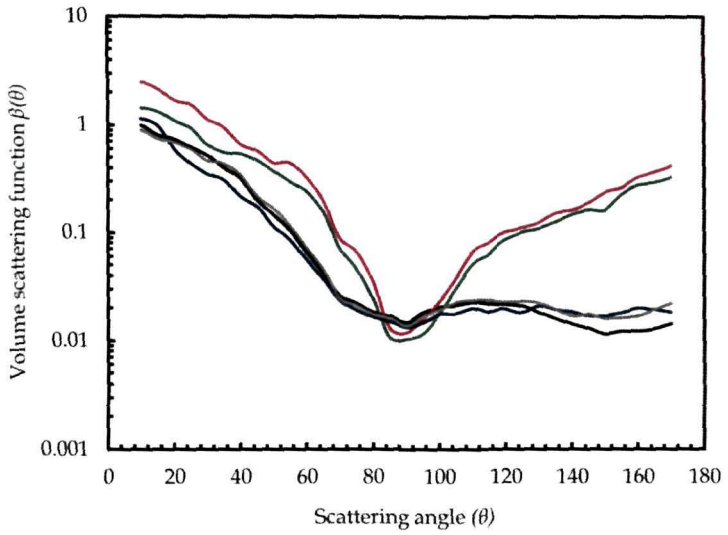

Figure 3.38: Data reduction for measured volume scattering function $\beta(\theta)$ for polystyrene spheres at 543.5nm. Plot for background scattering is shown by green line. The plot for raw uncorrected data is shown by red line. Background correction is shown by blue line. Plot after the correction for changing scattering volume is shown by grey line and the final result after correction for reflection at the walls of the cuvette is denoted by the black line.

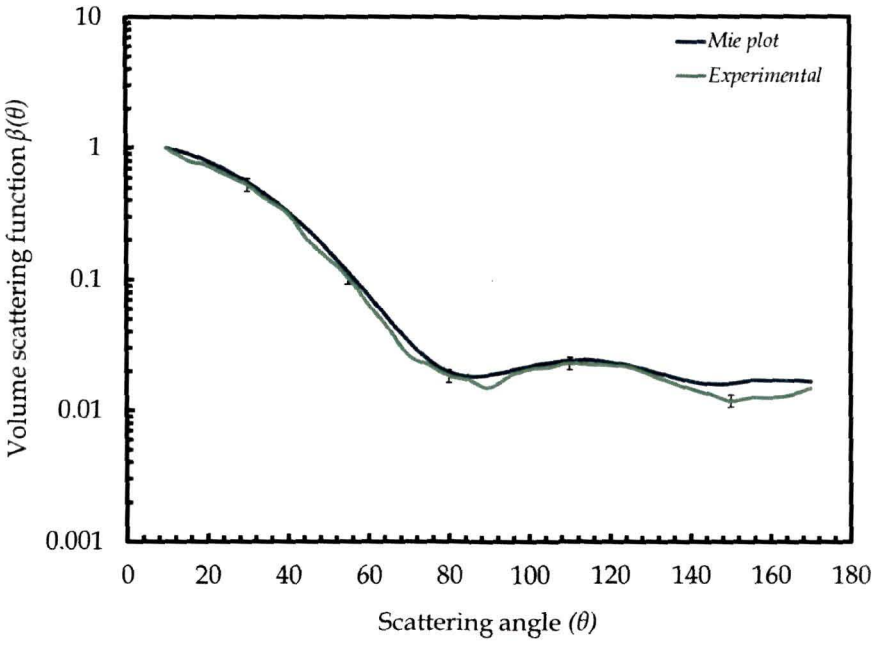

Figure 3.39: Measured volume scattering function $\beta(\theta)$ for polystyrene spheres at 543.5 nm.

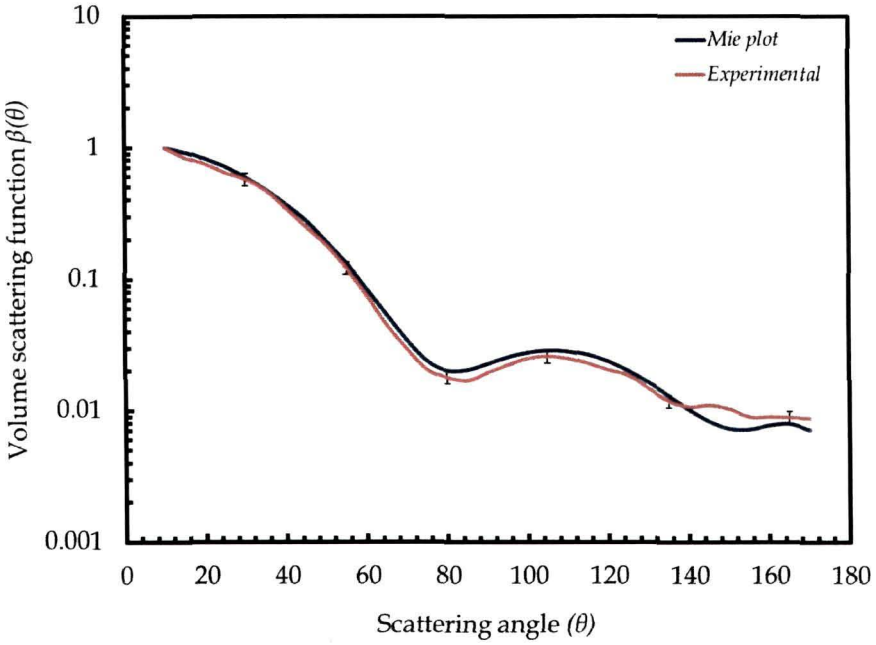

Figure 3.40: Measured volume scattering function $\beta(\theta)$ for polystyrene spheres at 594.5 nm.

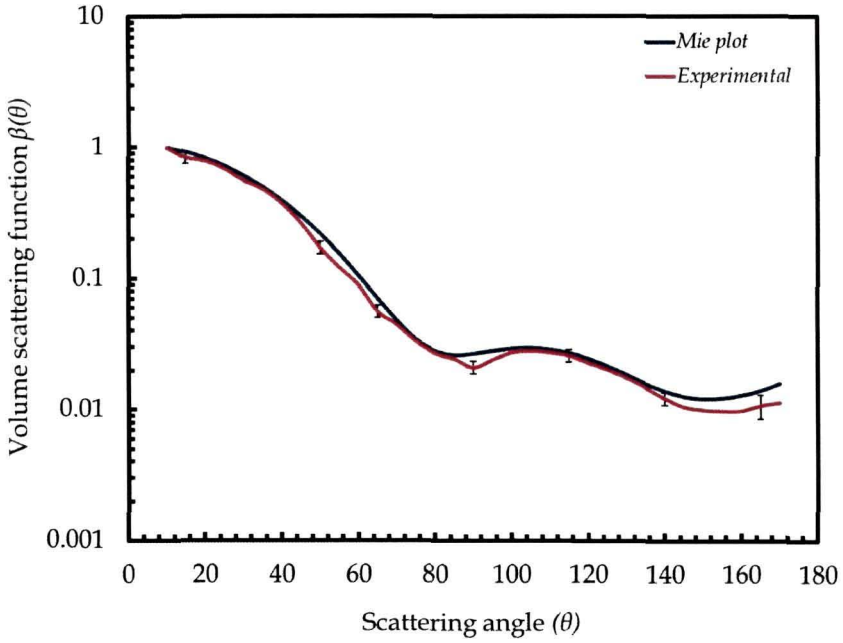

Figure 3.41: Measured volume scattering function $\beta(\theta)$ for polystyrene spheres at 632.8 nm.

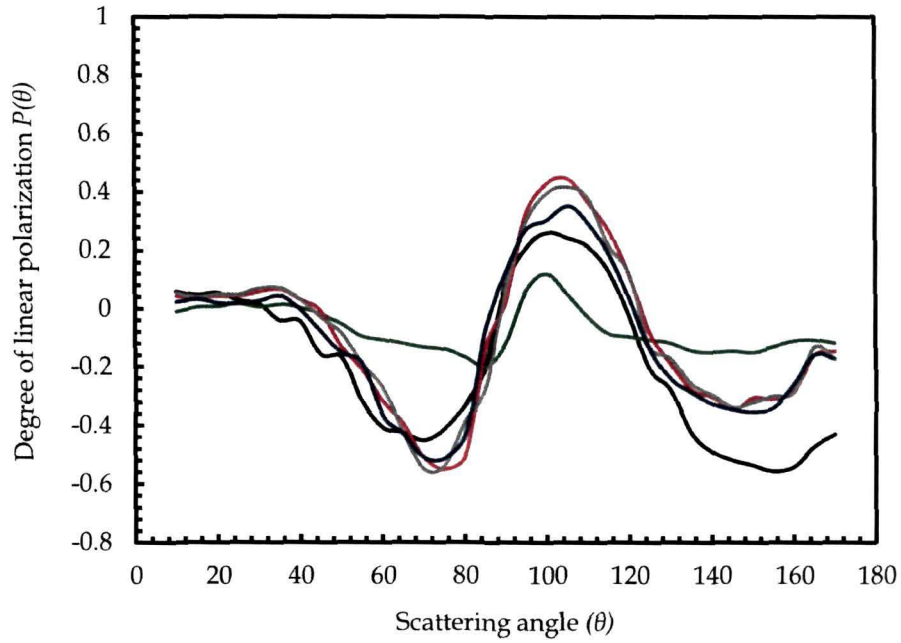

Figure 3.42: Data reduction for measured degree of linear polarization $P(\theta)$ for polystyrene spheres at 543.5nm. Plot for background scattering is shown by green line. The plot for raw uncorrected data is shown by red line. Background correction is shown by blue line. Plot after the correction for changing scattering volume is shown by grey line, and the final result after correction for reflection at the walls of the cuvette is denoted by the black line.

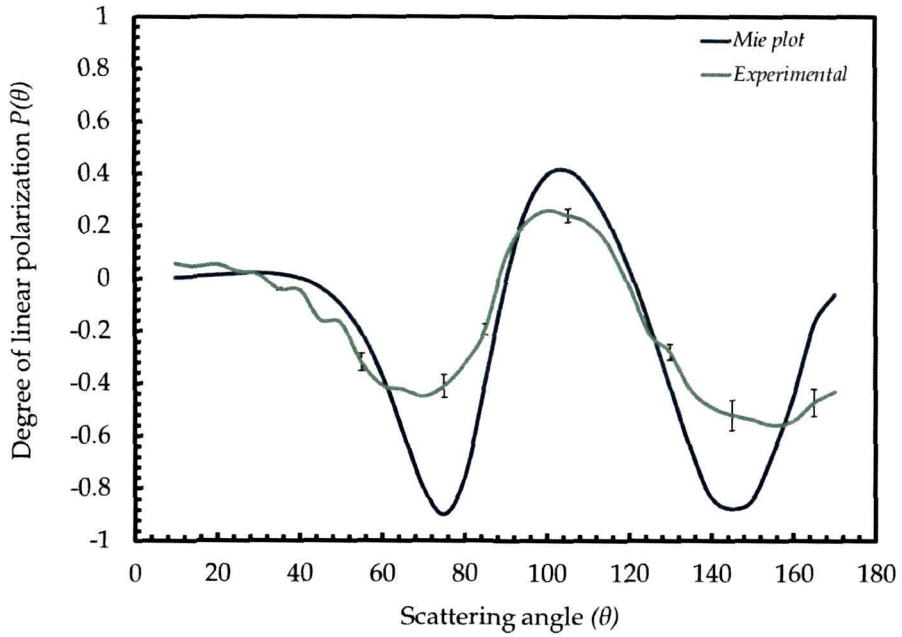

Figure 3.43: Measured degree of linear polarization $P(\theta)$ for polystyrene spheres at 543.5nm.

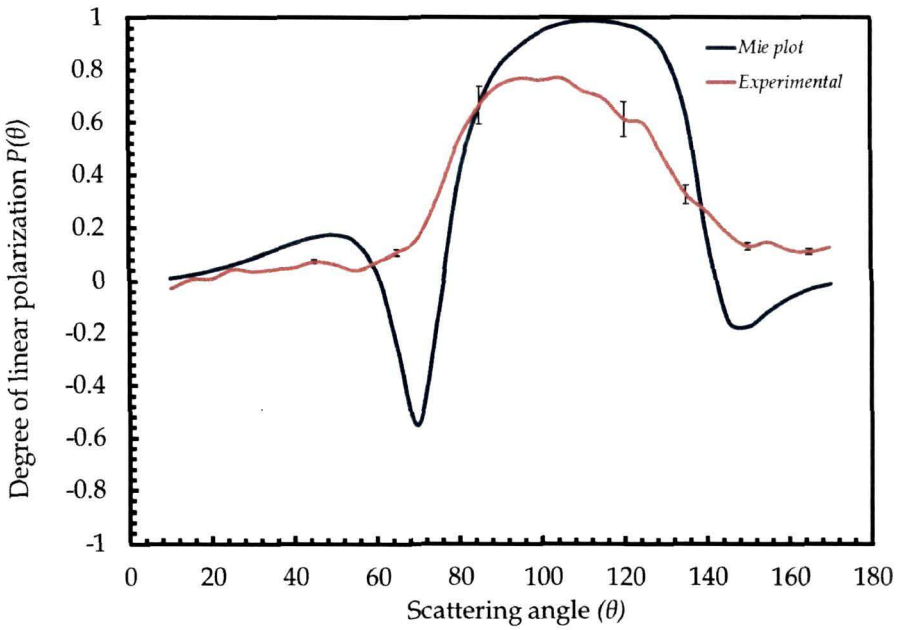

Figure 3.44: Measured degree of linear polarization $P(\theta)$ for polystyrene spheres at 594.5nm.

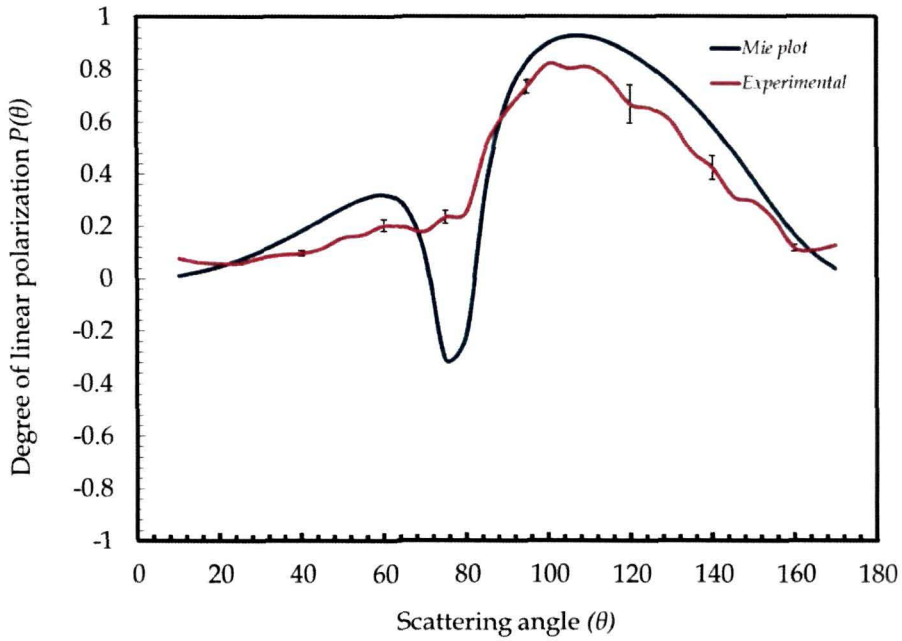

Figure 3.45: Measured degree of linear polarization $P(\theta)$ for polystyrene spheres at 632.8 nm.

3.11 Data Processing

The data is recorded in the file *filename.dat* by the data acquisition system using the program *"process.c"*, described in Section 3.8. The essential parameters of the light scattering system that are loaded into the processing program are the name of *filename.dat*, scattering angle θ, reading of refractive index of the particle n, size of the particle s , wavelength of incident light λ, which are all recorded at the time of the experiments. The program opens *filename.dat* and calculates the average of every unit of voltage data (intensity obtained in terms of volts) at each angular position of the photodetector. This averaging eliminates the negligible electromagnetic noise component in the voltage data without any significant loss in the overall pattern of the voltage data. The program computes the value of the intensity (obtained in terms of volts) of the scattered light considering a particular wavelength of light. It is seen that by taking approximately 100 sets of data using the light scattering system, yields the most significant results in case of our investigations with different samples.

CHAPTER IV

Investigations and Results with Light Scattering System

4.0 General Introduction

This chapter contains details about the experimental investigations carried out for different particles by using the designed and fabricated light scattering setup and the results. Section 4.1 presents an overview of the investigations made on different particles in the simulation chamber of the light scattering system. Section 4.2 to Section 4.7 presents the experimental results obtained with light scattering investigations on different samples outlined below. The sections also present comparisons of the experimental results with well-established theoretical results, and directs towards significant findings from the results. Section 4.8 discusses similar work done by other authors with their work presented here to make a comparative assessment of the designed and fabricated light scattering system. Finally, section 4.9 presents error analysis techniques involved in the experimental measurements of all the particles studied in this research work.

4.1 Overview of investigations made on different samples

Light scattering investigations were carried out on a number of samples namely:

i. Cadmium sulphide(CdS)
ii. Zinc selenide (ZnSe)
iii. Titanium dioxide (TiO_2)
iv. Zinc oxide (ZnO)
v. *Stapphylococcus aureus*
vi. *Camellia sinensis*
vii. *Mycobacterium smegmatis*

For every light scattering investigation, the scattering detector was first placed at an angle $\theta = 0°$. Then the measurements of scattered light signals were recorded from an angle of 10° to 170°. The plots of volume scattering function for all the experiments are represented in logarithmic scale.

It is worth mentioning that for randomly oriented non-spherical particles, light scattering properties are azimuthally independent as reported by many researchers [32, 45, 47, 179]. Still, we have carried out light scattering measurements by changing the azimuthal angle φ, for ZnO, *S. aureus*, *C. sinensis*, *M. smegmatis* non-spherical particles by using our light scattering setup. Some notable lines mentioned by Bohren and Huffman [45] which seems to be in line with our consideration are expressed as: *"It is sometimes asserted that randomly oriented non-spherical particles are somehow equivalent to spherical particles, and it is just a matter of choosing the correct size distribution. This reasoning is based, perhaps, on the realization that both systems are spherically symmetrical. But an inescapable conclusion to be drawn from the preceding paragraphs is that these assertion cannot be strictly true: regardless of the size composition of the "equivalent" spheres, symmetry precludes full equivalence"*. Accordingly, the significant reasoning of Bohren and Huffman holds correct and cannot be ruled out for practical applications where light scattering plays a key role in depicting the scattering behavior of small particles, as we witnessed similar observations. In our experimental investigation, the scattering profiles displayed by ZnO and *S. aureus* were found to be same with variation in azimuthal angle φ, whereas marked difference was observed in case of *C. sinensis* and *M. smegmatis* bio-particles with variation in φ, and this fact was found true for all the three wavelengths. Thus, the measurements substantiated the uniqueness and completeness of our light scattering setup.

4.2 Cadmium Sulphide (CdS)

Sulphide nanoparticles like CdS and ZnS are potential candidates for optoelectronic devices [335]. For example, CdS is used in photoresistors,

photovoltaic cell, solar energy materials and solar cells etc. In the recent years, II-VI semiconductor particles have been studied extensively for optoelectronic applications. Dielectric spheres with a radius comparable to the wavelength of light are efficient scatterers [336]. Mie scattering has potential as an *in situ* monitoring tool for precipitation reactions that involve such particles. Various resonance features observed in the transmission spectra, such as circumference and diameter mode contributions or shifts in the resonance peak positions due to a solvent exchange can be explained well by using Mie theory [336]. The Mie scattering effects of such particles can be considered as a colloidal or spherical analogy to the two- or three-dimensional super-lattices of photonic band gap materials. The theoretical understanding of scattering phenomena is well developed [45], but there is a need to find practical applications of this theory for such particles as well. Moreover, Mie scattering theory can be successfully extended to explain the optical properties of small particles of homogeneous nature and in different scales from nanometer to micrometer.

The CdS particles were synthesized in our laboratory via simple chemical route to maintain homogeneity of the particles [337] and it was followed by investigations based on light scattering technique. The technique outlined here for the synthesis of CdS particles in both dimensions (nanometer and micrometer) was adopted due to its simple route, cost effectiveness and high reproducibility. Poly Vinyl Alcohol (PVA, Aldrich) was selected as the host polymer for embedding these particles as it is an optically transparent aliphatic polymer. The PVA matrix was prepared by using 2.5 wt.% PVA in double distilled water under magnetic stirring at the rate of 200 rpm approximately and simultaneously heating it for about 3 hours at 60°-70°C. After preparing the matrix, Cadmium chloride ($CdCl_2$) solution of two different molar concentrations (1M and 0.1 M respectively) were taken in two stoppered conical flask maintaining a volume ratio of 2:1 with PVA matrix to prepare PVA film embedded with CdS. Different molar concentrations were

taken because the size of particle formation strongly depends upon the molar concentrations. Freshly prepared 5 wt. % (Na_2S + HCl) solution was added to the PVA and $CdCl_2$ solutions kept in the two separate flasks until their color turned yellow. The yellow color of the solution indicates the formation of CdS. The flask was then sealed and kept undisturbed for about 12 hours so that the solutions become stable. Thin films of the solution were casted over glass substrate and were dried in vacuum oven. The films were washed 2-3 times with cold water to remove Chlorine ions (Cl^-) and were dried in the oven again. The block diagram of preparation of PVA matrix embedded CdS particles is shown in figure 4.1.

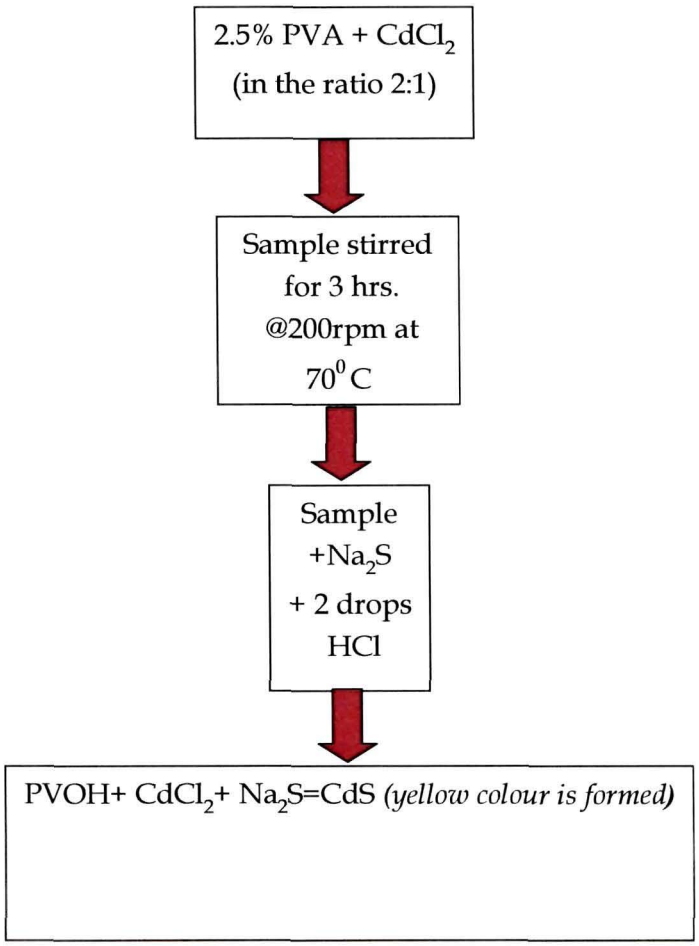

Figure 4.1: Block diagram of the route of preparation of PVA embedded CdS particles.

PVA films without the CdS particles were also prepared. Structural and morphological characterizations were carried out through high resolution Electron Microscopy. The formation of the homogenous CdS particles in a PVA matrix seems to ensure the sphericity and isotropy of the particles. From the Scanning Electron Microscopic (SEM) and Transmission Electron Microscopic (TEM) images, the shape of CdS particles was verified to be spherical (figures 4.2 & 4.3) having a normal Gaussian size distribution as shown in figure 4.4 and 4.5. The distance between particles is large enough and hence single light scattering is realized.

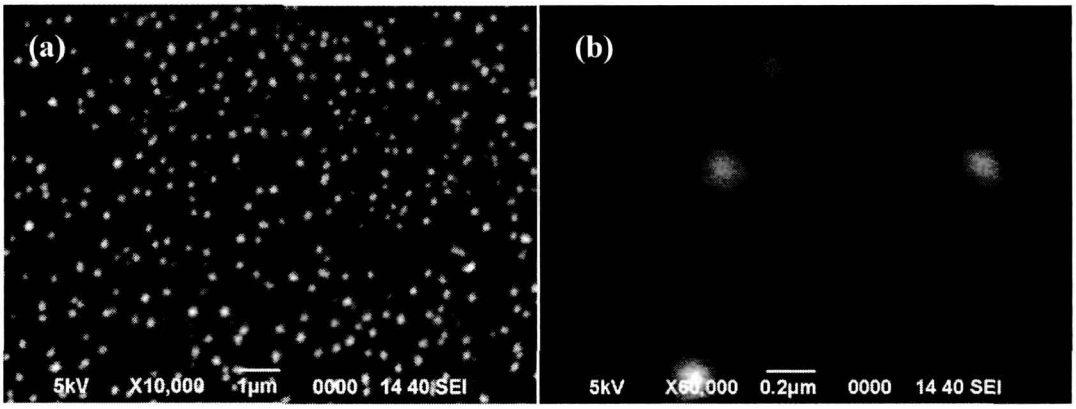

Figure 4.2: (a) SEM image of CdS at magnification of X10,000; (b) SEM image of CdS at magnification of X60, 000.

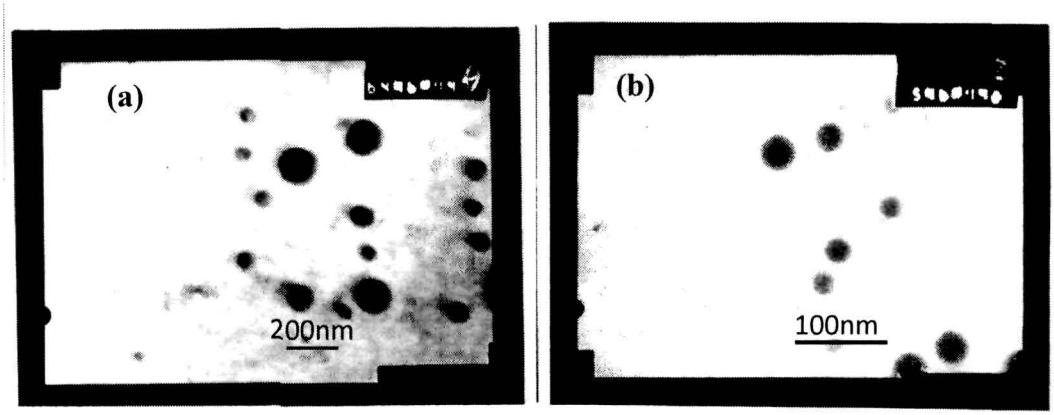

Figure 4.3: (a & b) TEM image of CdS at two different magnifications.

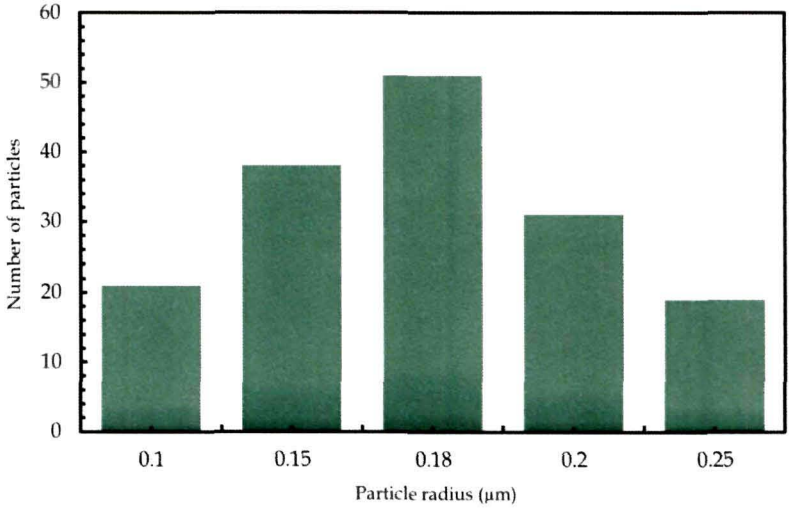

Figure 4.4: Size distribution graph of CdS particles having modal radius of 0.18 μm.

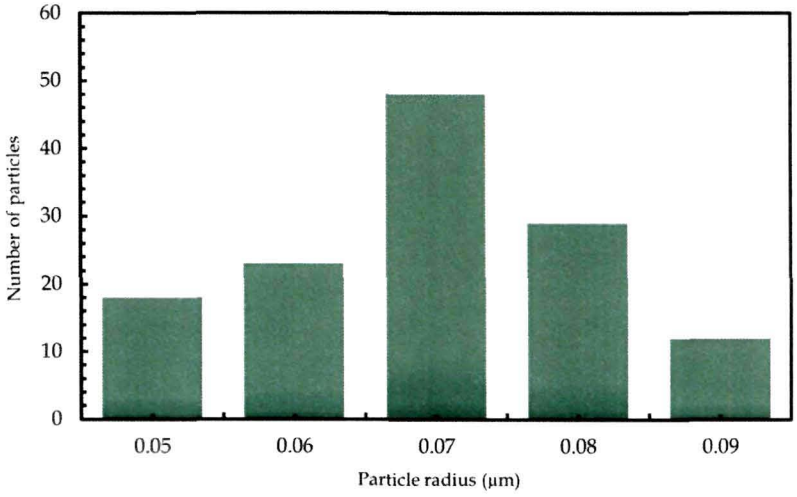

Figure 4.5: Size distribution graph of CdS particles having modal radius of 0.07 μm.

The setup comprised of 16 static silicon detectors (as described in Section 3.0 of Chapter III) was used for light scattering investigation of CdS particles. Light beam from the He-Ne laser source of wavelength of 632.8 nm was allowed to fall on the sample placed in a sample holder positioned at the centre of the circular disc and held by a mechanical support. The laser light is scattered by the sample of CdS particles. The scattered light intensity that

corresponds to the S_{11} and S_{12} element of the scattering matrix is sensed by the arrangement of 16 detectors. The scattering data was obtained for these particles in differential mode. The data was further processed using the program *'process.c'* (discussed in Section 3.11 in Chapter III) after data acquisition. Next, scattering data files were generated using the computer program as mentioned in Section 2.5 of Chapter II, to yield theoretical values of $\beta(\theta)$ and $P(\theta)$.

The data obtained were plotted and compared with the theoretically generated Mie-plot for particles having same size distribution, shape, refractive index and state of polarization. These figures depict the scattering profile of the CdS particles at different spatial angles. Some important parameters which were used for the data analysis are tabulated in Table 4.1 below.

Table 4.1: Parameters used for the data analysis of CdS particles

Parameters	Value
Particle radius (CdS of micron size) in micrometers	0.180±10
Particle radius (CdS of nano size) in micrometers	0.07±10
PVA refractive index	1.55+i0000
Particle refractive index (CdS)	2.52+i0000
Wavelength of incident light (λ) in micrometers	0.6328

For 0.18 μm CdS particles, the experimentally measured scattering phase function $\beta(\theta)$ shows sharp forward scattering lobe followed by two intense scattering peaks at around 140° and 160° (backscattering) respectively as shown in figure 4.6. The deviation from theoretical curve is prominent at larger angles (θ >100°). For 0.07 μm CdS particles, the experimentally measured $\beta(\theta)$ shows a forward scattering region where the scattering

intensity gradually decreases and shows escalation of the intensity curve at scattering angle beyond 100° as shown in figure 4.8. The scattering profiles shows backscattering around 160° with no intense scattering peaks for both the sizes of CdS particles (figures 4.6 & 4.8).

The measured degree of linear polarization $P(\theta)$ for both the sizes of CdS are shown in figures 4.7 and 4.9. Both the cases show discrepancy when compared with the theoretical predictions. In figure 4.7, alternate positive and negative branches of polarization curve with a shape dissimilar to the theoretical one is observed. The experimental values were found to be inconsistent with the theoretical values of polarization phase curve, projecting maxima of 0.395 at 100° and minima of -0.42 at 40°. Figure 4.9 also displays a dissimilar shape but with a prominent negative branch of experimental polarization curve where the negative value ranges from 95° up to 140° approximately. The maxima is 0.36 at around 60° and the minima being -0.12 at around 115°. It is important to mention that the theoretical values of the degree of linear polarization at 90° scattering angle equals to unity, that is $P(90°)= 1$ as $I_{//}$ (the scattered intensity parallel to the scattering plane) vanishes at the Rayleigh scattering regime [338], and the fact is also evident from the theoretical plot generated for CdS nanoparticles of 0.07 μm(figure 4.9). But, for larger particles, beyond the Rayleigh regime which converges to Mie scattering regime, $I_{//} \neq 0$, i.e. $P(90°)< 1$. Thus the experimentally measured $P(\theta)$ values which were found to be less than 1, revealed the possibility of cluster formation of the nanoparticles (nearly spherical cluster), at wavelength of 632.8 nm. However, the experimental curve for $P(\theta)$ seems to be far deviating from the theoretical curve for CdS nanoparticles (figure 4.9). This may be because the theory cannot accommodate well for very small particles, especially particles approximately 1/10th of λ [50], which is the wavelength of the incident light (in the present experiment, λ= 632.8 nm).

Within the limits of error of the 16 detectors and the instrument, the experimental data shows scattering patterns of approximately 0.07 μm and

0.18 μm particles, yielding comparatively better results for 0.18 μm particles. Overall, the plots of measured volume scattering function, $\beta(\theta)$ and the measured degree of linear polarization, $P(\theta)$ for CdS particles shows moderate fit with the theoretical plots. However, there is a limitation of the Mie theory when applied to nano-sized particles having a size less than 0.07 μm.

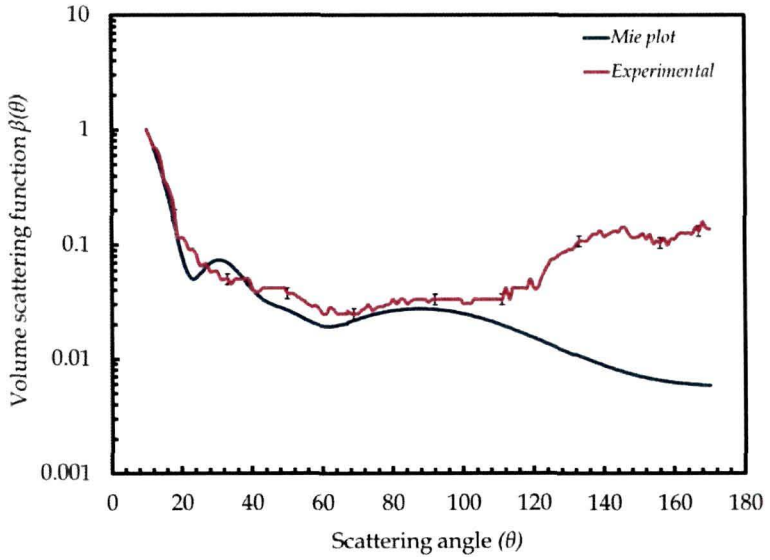

Figure 4.6: Experimentally measured Volume scattering function $\beta(\theta)$ for CdS of 0.18 μm size at wavelength of 632.8 nm.

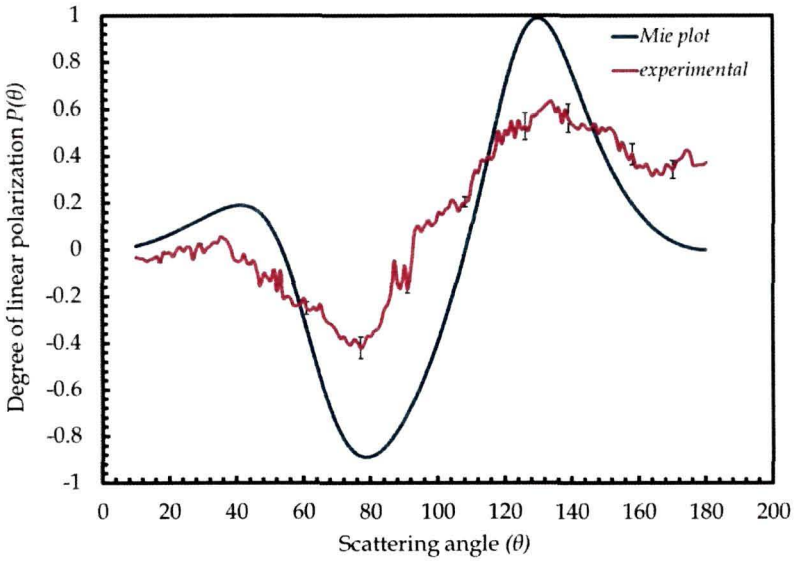

Figure 4.7: Experimentally measured Degree of linear polarization, $P(\theta)$ for CdS of 0.18 μm size, at wavelength of 632.8 nm.

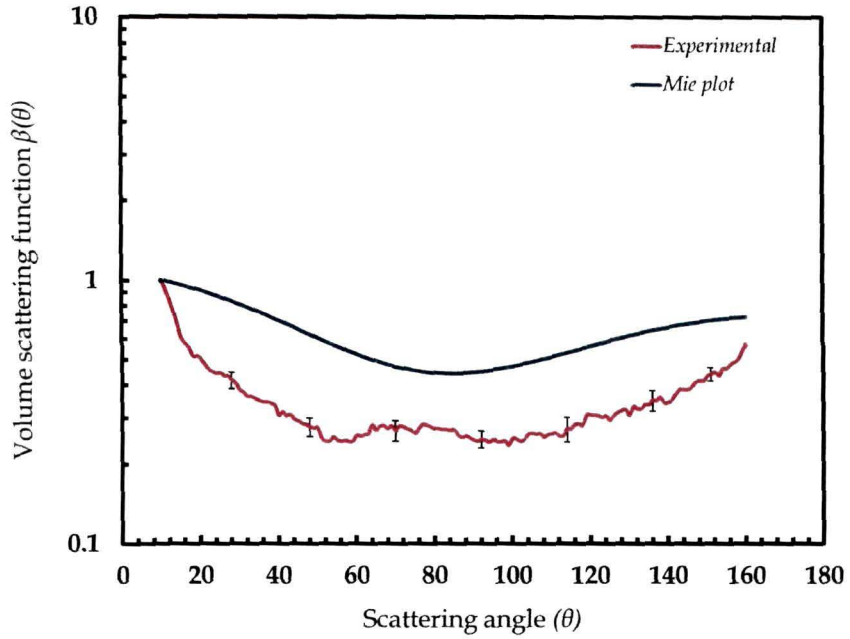

Figure 4.8: Experimentally measured Volume scattering function $\beta(\theta)$ for CdS of 0.07 μm size, at wavelength of 632.8 nm.

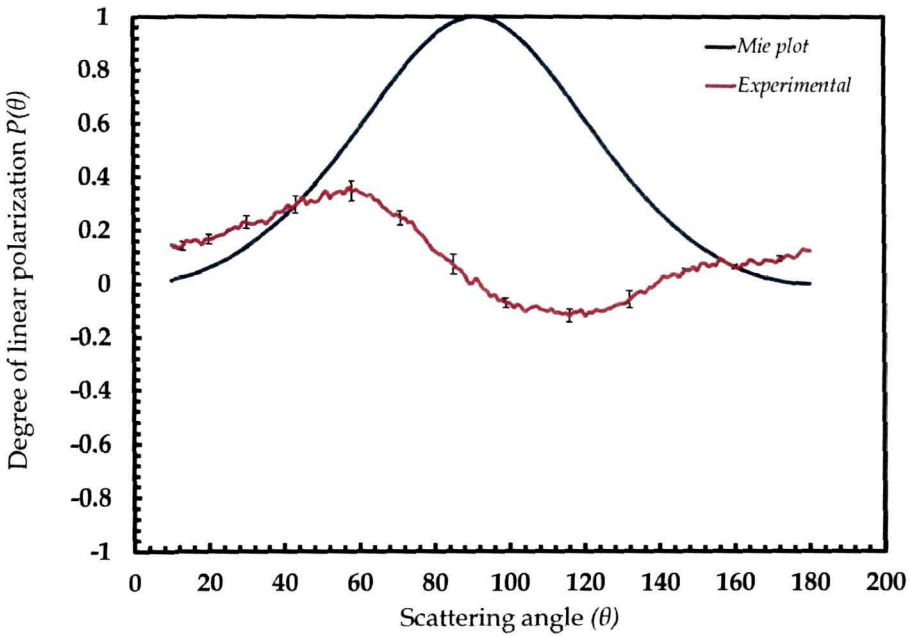

Figure 4.9: Experimentally measured Degree of linear polarization, $P(\theta)$ for CdS of 0.07 μm size, at wavelength of 632.8 nm.

The scattering plots were normalized to 1 at 10°. The results obtained showed only qualitative agreement with the established theoretical results for the volume scattering function and degree of linear polarization.

4.3 Zinc Selenide (ZnSe)

Zinc Selenide is one of the most interesting II-VI semiconductor particles [335] because of its potential application in optoelectronic devices like fabrication of light emitting diodes, blue lasers etc. The properties and applications of these particles strongly depend on the shape, size and size distributions of the particles. This fact builds up the importance of light scattering studies which can be used as an imperative tool for *in situ* monitoring and tuning such particles for proper applicability. Remarkable investigations based on computing light scattering and also simulating light scattering by different types of mineral dust and aerosols have been made in the recent years [16, 32, 69,70, 259, 285, 333]. However, reports on light scattering studies by realistic semiconductor particles and simulation of such particles are few or rather insufficient [336]. The scattering properties of these kind of particles are a vital diagnostic tool for detection and retrieval of information on physical properties which has significant applications in many disciplines.

Sol-gel method, Chemical vapour deposition, Thermal evaporation etc. are the several techniques employed earlier by many researchers to synthesize ZnSe particles [339]. In the present study, ZnSe particles were synthesized via novel elemental solvothermal route in our laboratory. A new route has been developed to synthesize sub-micron sized homogeneous Zinc selenide semiconductor particles. Transparent PVA matrix was chosen as host material for embedding these ZnSe particles in order to stop agglomeration of the particles as well as to facilitate optical characterization. The PVA matrix was prepared by following the same procedure as discussed in Section 4.2. The sample of $ZnCl_2$ solution (1 M) was added to the PVA solution drop wise

through a burette in the volume ratio of 2:1 maintaining the stirring condition. Selenium vapour was obtained by heating SeO_2 which was kept in a heating device maintained at a temperature of 200° C. The vapour was supplied through a glass tube to the mixture of PVA matrix and $ZnCl_2$ solution until the whole amount of $ZnCl_2$ solution had dropped down from the burette. After this, films were cast by pouring the semi-viscous solution over glass substrates and were dried in vacuum oven. The block diagram of preparation of PVA matrix embedded ZnSe particles is shown in figure 4.10. Energy dispersive X-ray spectroscopic investigation (EDX) was performed to ensure the formation of these particles (figure 4.11) as the particles were synthesized via elemental solvothermal route for the first time. The figure of EDX shows presence of Zinc and Selenium, without any other impurity or unwanted elements. Scanning Electron Microscopic and Transmission Electron Microscopic images were also taken in order to assess the morphology of the particles.

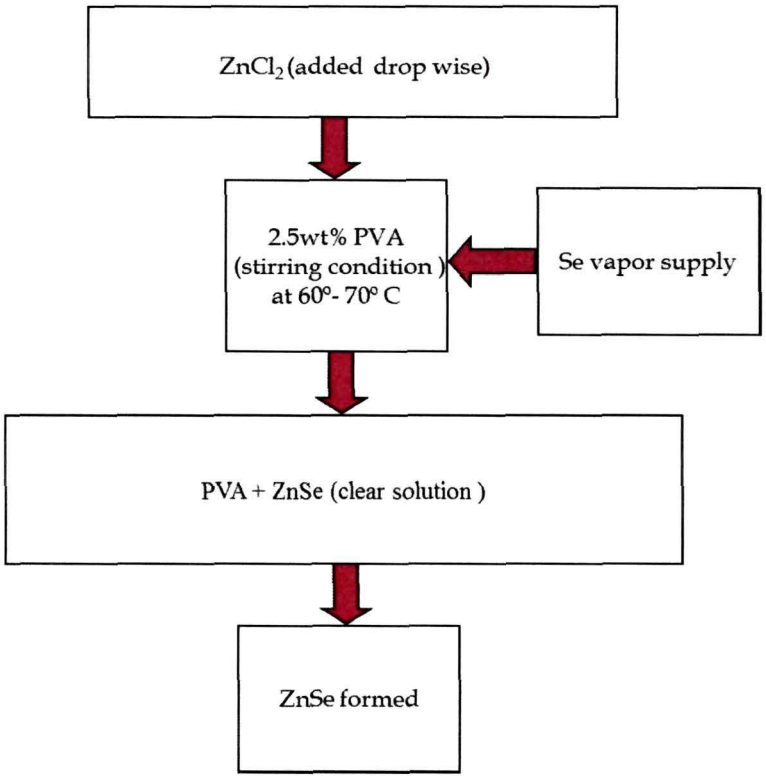

Figure 4.10: Block diagram of the route of preparation of PVA embedded ZnSe particles.

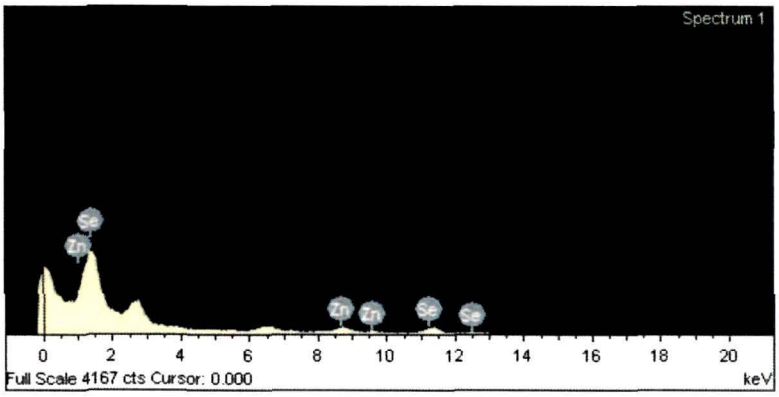

Figure 4.11: EDX image of ZnSe particles

The SEM and TEM images verified the shape of particles to be almost spherical, and are shown in figures 4.12 and 4.13 respectively. The particles were found to be having a Gaussian distribution, shown in figure 4.14, and having an approximate modal radius of 0.12 μm. The distance between particles was found to be large enough and as such single light scattering system was recognized.

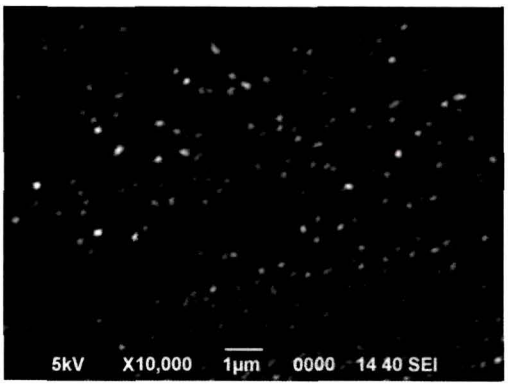

Figure 4.12: SEM image of ZnSe particles at magnification of X10, 000.

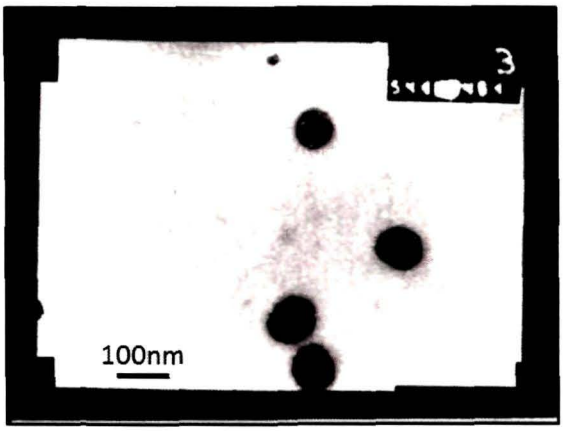

Figure 4.13: TEM image of ZnSe particles.

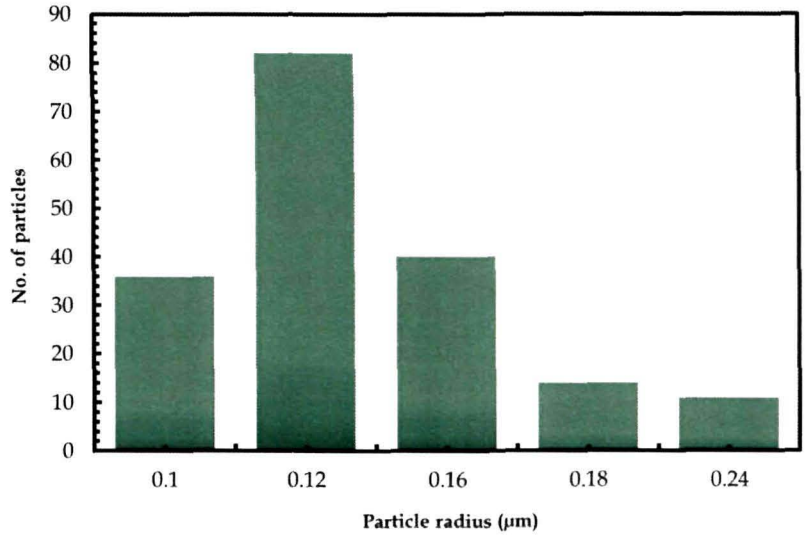

Figure 4.14: Size distribution graph of ZnSe particles

The ensemble of particles were illuminated alternately by three He-Ne laser beams of different wavelengths, 543.5nm, 594.5 nm and 632.8nm respectively, for light scattering investigations. The scattered light intensity that corresponds to the S_{11} and S_{12} element of the scattering matrix is detected by the photomultiplier tube. By quantifying the S_{11} and S_{12} element of Mueller matrix, we could measure the volume scattering function, $\beta(\theta)$ and the degree of linear polarization, $P(\theta)$ of ZnSe particles. We correlated our measurements for $\beta(\theta)$ and $P(\theta)$ with Mie calculations by using the estimated parameters

depicted in table 4.2, in order to draw a comparison of scattering measurements with Mie theoretical prediction. Again, scattering data were obtained for these particles in differential mode and the data files were successively processed using the same programs discussed in previous chapter to yield values of $\beta(\theta)$ and $P(\theta)$ values. The data obtained were plotted and compared with the theoretically generated Mie-plot for particles having same size distribution, shape and state of polarization, as shown in figures 4.15 - 4.20. All the plots for volume scattering function were normalized to 1 at 10°.

Table 4.2: Parameters used for the data analysis of ZnSe particles

Parameters	Value
Particle radius (ZnSe) in micrometers	0.120 ±10
Particle size distribution	Gaussian
Refractive index of PVA matrix	1.55+i0000
Particle refractive index(ZnSe) at 543.5 nm	2.662 46 +i0000
Particle refractive index(ZnSe) at 594.5 nm	2.618 24 +i0000
Particle refractive index(ZnSe) at 632.8 nm	2.590 73+i0000

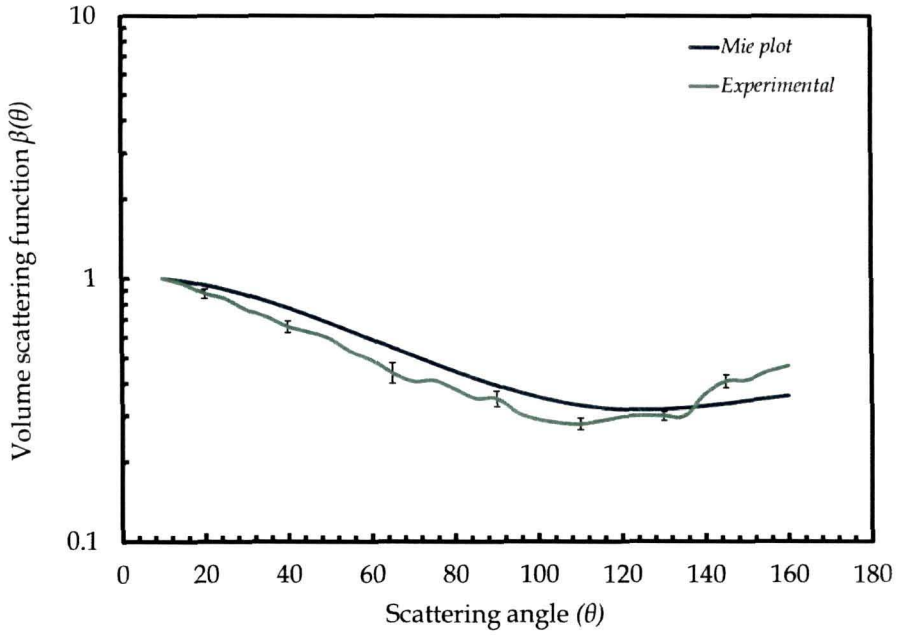

Figure 4.15: Experimentally measured Volume scattering function $\beta(\theta)$ for ZnSe at wavelength of 543.5 nm.

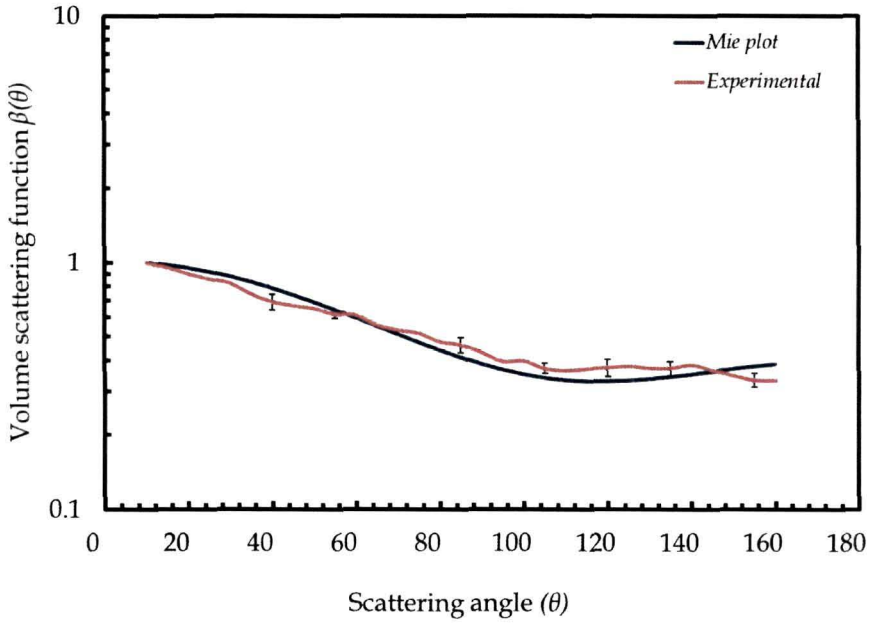

Figure 4.16: Experimentally measured Volume scattering function $\beta(\theta)$ for ZnSe at wavelength of 594.5 nm.

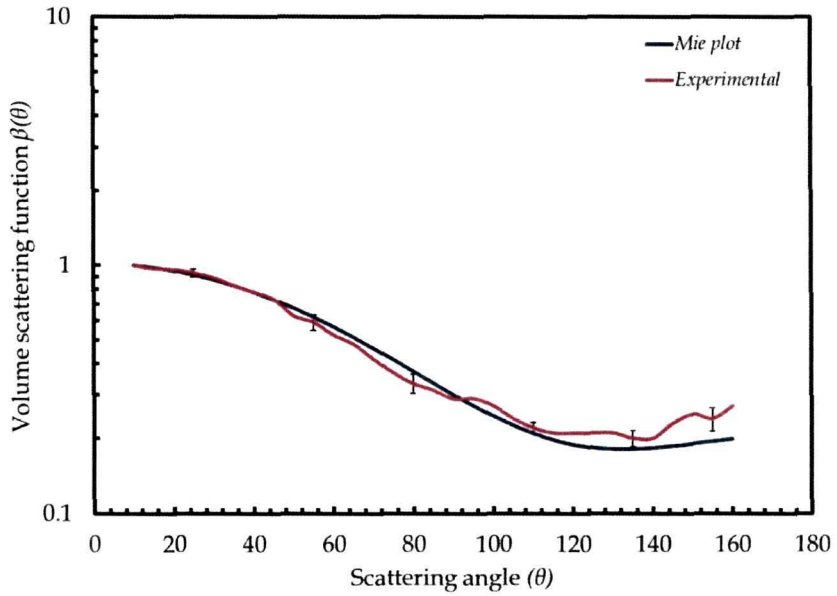

Figure 4.17: Experimentally measured Volume scattering function $\beta(\theta)$ for ZnSe at wavelength of 632.8 nm.

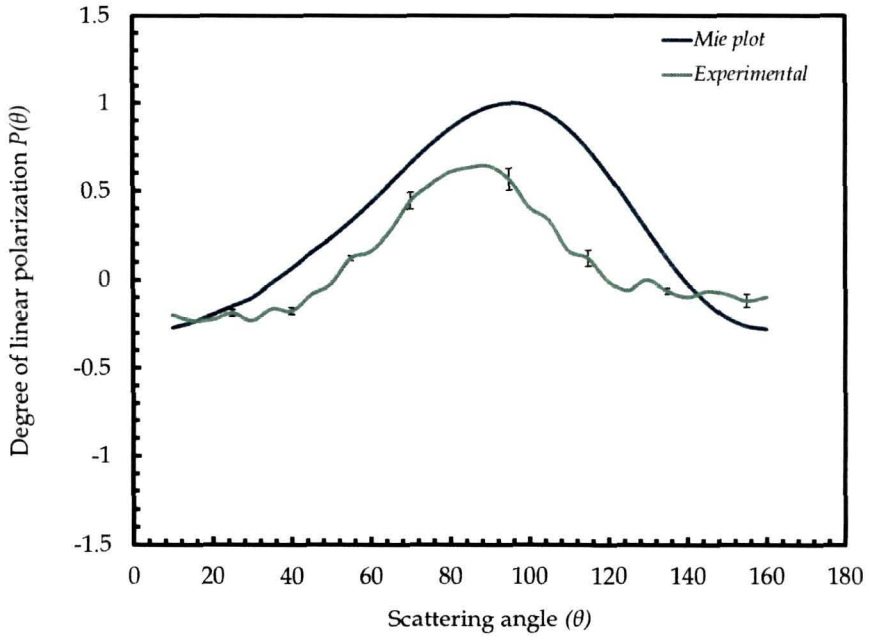

Figure 4.18: Experimentally measured Degree of linear polarization, $P(\theta)$ for ZnSe at wavelength of 543.5 nm.

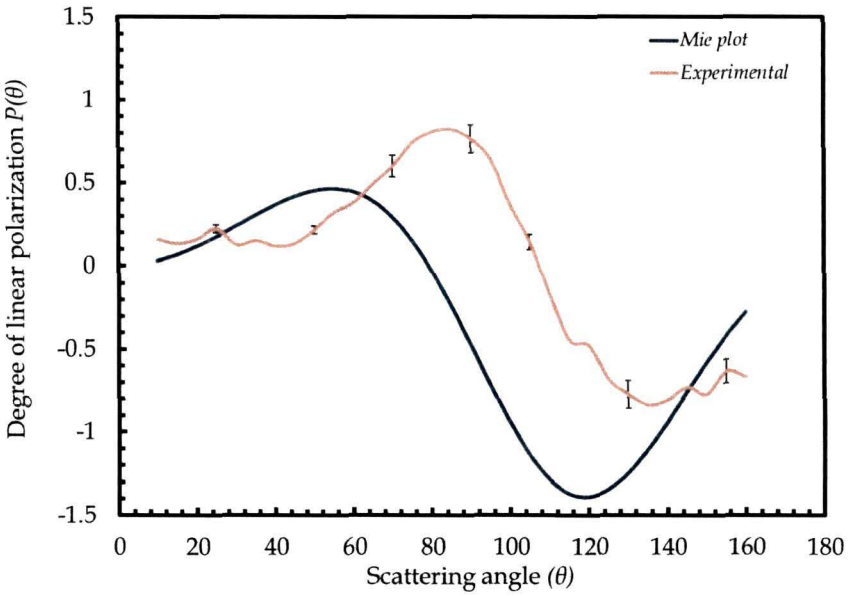

Figure 4.19: Experimentally measured Degree of linear polarization, $P(\theta)$ for ZnSe at wavelength of 594.5 nm.

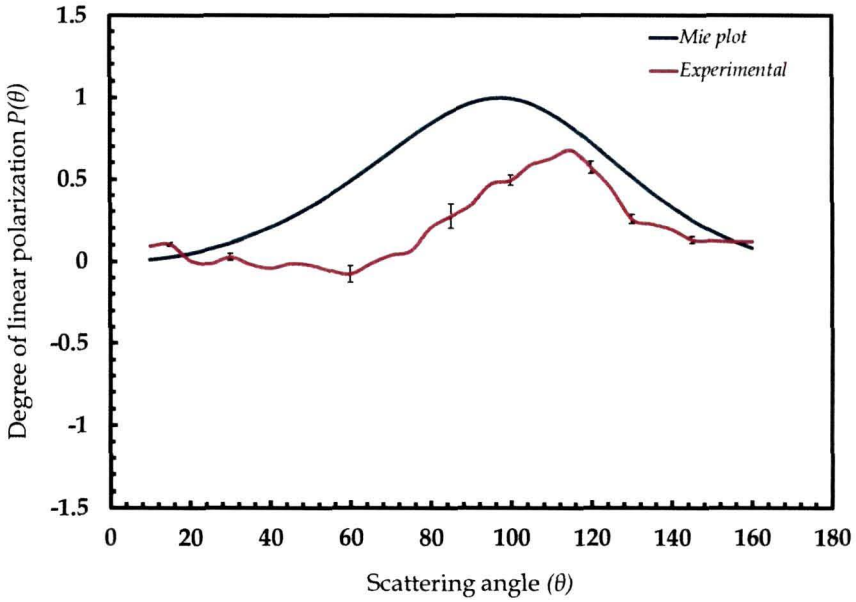

Figure 4.20: Experimentally measured Degree of linear polarization, $P(\theta)$ for ZnSe at wavelength of 632.8 nm.

The measured volume scattering function $\beta(\theta)$, displays a forward scattering lobe for all the wavelengths. The values of $\beta(\theta)$ are significantly larger than the computed values at some scattering angles in case of all the three wavelengths. This observation indicates the presence of agglomerated particles of larger sizes in the scattering volume. Although the measured $\beta(\theta)$ portrays similar shape of scattering profile when compared to theoretical phase curve, minor deviation still persists (figures 4.15 - 4.17). In view of comparative analysis of experimental data with theoretical predictions, the most agreeable signature of volume scattering function is exhibited by the ZnSe particles at wavelength of 632.8nm (figure 4.17). It is apparent from our investigations that the experimentally measured $\beta(\theta)$, agrees reasonably well with the computed values for all the three wavelengths.

The measured degree of linear polarization $P(\theta)$ (figures 4.18 - 4.20) was found to be positive at most of the scattering angles and showed some manifestation of oscillations for all the three wavelengths. It displays fluctuating behaviour with positive and negative branches of polarization phase curves. It can also be seen from the figures (figures 4.18 - 4.20) that the measured polarization curves when compared to the theoretical curves, exhibit similar trend for all the wavelengths but differs in maxima and minima. The measured $P(\theta)$ shows a characteristic bell shape for 543.5 nm and 632.8 nm incident wavelengths, whereas rather low double minima may be observed in case of 594.5nm wavelength. The maxima is 0.64 at 90° and minima is -0.231 at 30° for the wavelength of 543.5 nm. The maxima and minima are 0.72 at 85° and -0.0838 at 135° respectively for 594.5 nm. And, the maxima and minima are found to be 0.78 at 115° and -0.076 at 60° respectively for wavelength of 632.8nm.The calculated $P(\theta)$ curve reproduces the computed one considerably well, particularly for 543.5 nm and 632.8 nm (figures 4.18 and 4.20). Due to the significant discrepancy while comparing the theoretical and experimental plots of $P(\theta)$ observed in case of 594.5 nm(figure 4.19), we made an attempt to simulate the light scattering behaviour of such

particles at this wavelength, in order to correlate the results and yield better result. The results are presented in the next chapter (Chapter V). Indeed, on theoretical grounds, we expect the degree of linear polarization to be higher for smaller particles (Van de Hulst 1957, chap. 6; Bohren and Huffman, chaps. 5, 13 in references 45 & 48). In contrast, the degree of linear polarization is expected to decrease with higher refractive indices of particles. This is in agreement with the observations of measured $P(\theta)$ curves, that there was decrease in $P(\theta)$ with increasing refractive indices of ZnSe particles. It is important to mention the reasons behind the deviations of measured degree of linear polarization curves from the theoretical polarization phase curves. The reasons may be attributed to the following points:

i. Presence of size distribution, however minor it may be.
ii. Presence of non-sphericity of some particles in the scattering volume.
iii. Agglomeration of some particles in the scattering volume.
iv. Density fluctuation of the PVA matrix.
v. Resilient dependence of polarization on size parameter of the particles, pertinent for all wavelengths.

Again, the deviation of experimental plot from theoretical plot may also be attributed to the superimposition effect of the overriding scattering pattern of individual ZnSe nanoparticles over recessive scattering pattern of non-spherical clusters of the ZnSe particles.

4.4 Titanium dioxide (TiO_2) or Titania

Titania (rutile) is a non-absorbing material and rutile pigments are widely employed in industry for their extreme whiteness [340]. In this section, results of measurements of the volume scattering function and the degree of linear polarization of TiO_2 particles are presented. TiO_2 was specifically chosen for study because of its whiteness (reflecting all wavelengths strongly), its prolate shape, and having high real parts of refractive index. Transparency at visible

wavelengths is also an interesting physical property of TiO_2 particles. Due to these properties Titania is one of the most widely used white pigment for paint coatings, plastics and papers. Moreover, rutile, titania dust particles are thought to be the possible nucleation sites in oxygen rich circumstellar shells, and it is also an important component of the lunar regolith [214, 224].

The experimentally determined scattering matrix elements of a rutile sample in water has been studied earlier by Volten et al. [4], whereas Munoz *et al.* and Progra2 experimentally determined the same elements for Titania particles dispersed in air [214, 333]. In the recent years, tremendous efforts have been made in computing light scattering by such particles but still these methods were insufficient to simulate light scattering by true shapes [46, ,47, 71].

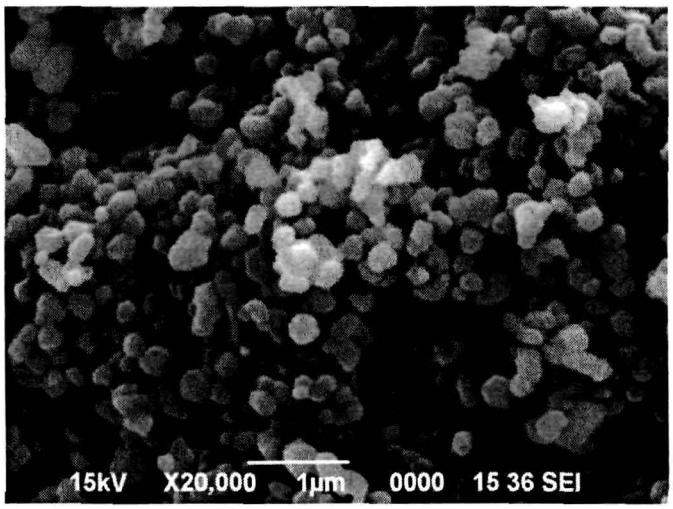

Figure 4.21: SEM image of TiO_2 particles at magnification of X20, 000.

SEM analysis of the TiO_2 particles was performed in order to correlate our light scattering measurements with the morphology of particles. The SEM image portrays prolate shape of TiO_2 particles, shown in figure 4.21. The particles showed a broad dispersion of sizes as shown in figure 4.22. The particles were found to be having a modal radius of 0.25 μm.

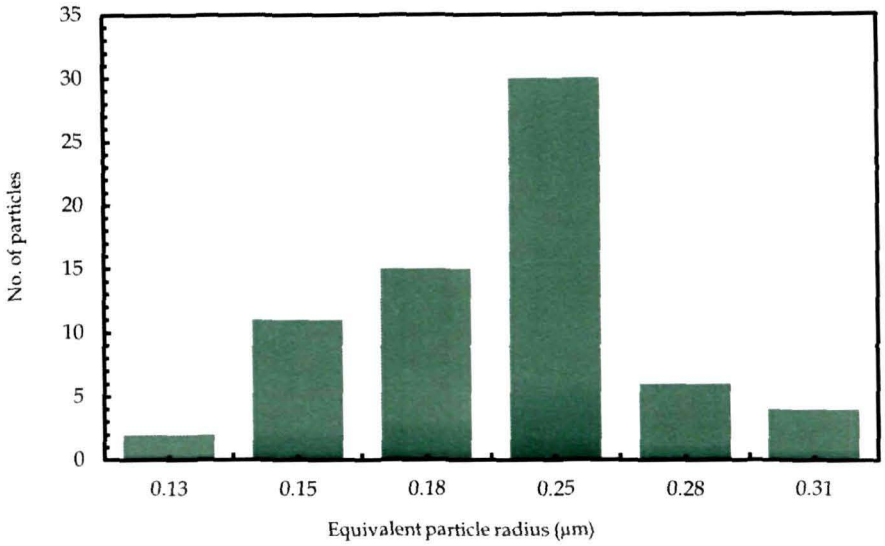

Figure 4.22: Size distribution graph of TiO_2 particles.

Light scattering measurements of the phase function and the degree of linear polarization of TiO_2 particles were carried out at wavelengths of 543.5 nm, 594.5 nm and 632.8 nm respectively. The present investigations on light scattering measurements were performed on mono-dispersed TiO_2 particles in the single scattering regime. Scattering data was obtained for the TiO_2 particles and were subsequently processed using the same analytical programs to yield values of $\beta(\theta)$ and $P(\theta)$. Some important input parameters used in the data analysis for the TiO_2 particle are given in the table 4.3.

The results of the measurements are plotted and shown in figure 4.23 - 4.28. Since it was confirmed from the SEM analysis that TiO_2 particles were definitely prolate shaped, an attempt was made to compare the experimental data with theoretical plots generated by T-matrix method instead of Mie theory, as T-matrix method is more suitable for particles with an axially symmetric morphology like TiO_2. In the same plots, the comparison of the experimental results with T-matrix theory is also shown. The graphs for volume scattering functions were normalized to 1 at 10°.

Table 4.3: Parameters used for the data analysis of TiO_2 particles

Parameters	Value
Particle size distribution	Normal (Gaussian)
Modal radius (TiO_2) in micrometers	0.25
Minimum particle radius in micrometers	0.13
Maximum particle radius in micrometers	0.31
Particle shape	Spheroidal
Particle refractive index(TiO_2) of titania at 543.5 nm	2.49965 +i0000
Particle refractive index(TiO_2) of titania at 594.5 nm	2.49577 +i0000
Particle refractive index(TiO_2) of titania at 632.8 nm	2.49366 +i0000

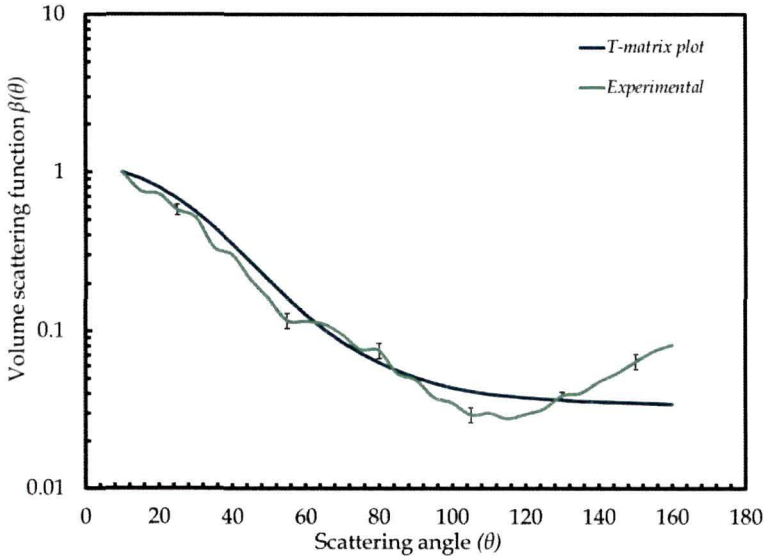

Figure 4.23: Experimentally measured Volume scattering function $\beta(\theta)$ for TiO_2 at wavelength of 543.5 nm.

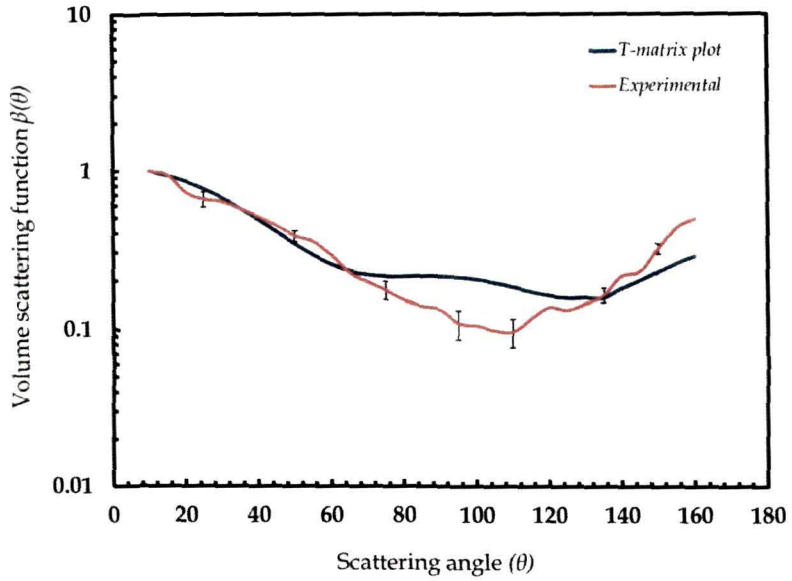

Figure 4.24: Experimentally measured Volume scattering function $\beta(\theta)$ for TiO_2 at wavelength of 594.5 nm.

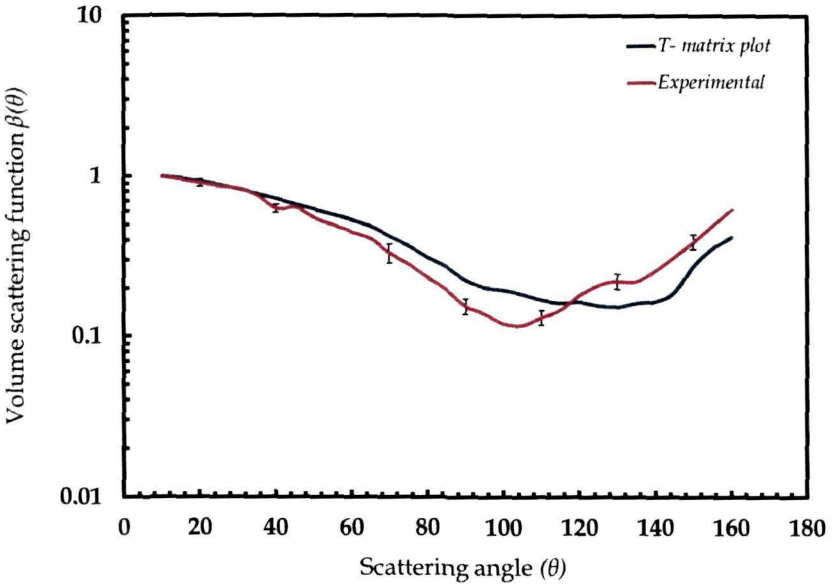

Figure 4.25: Experimentally measured Volume scattering function $\beta(\theta)$ for TiO_2 at wavelength of 632.8 nm.

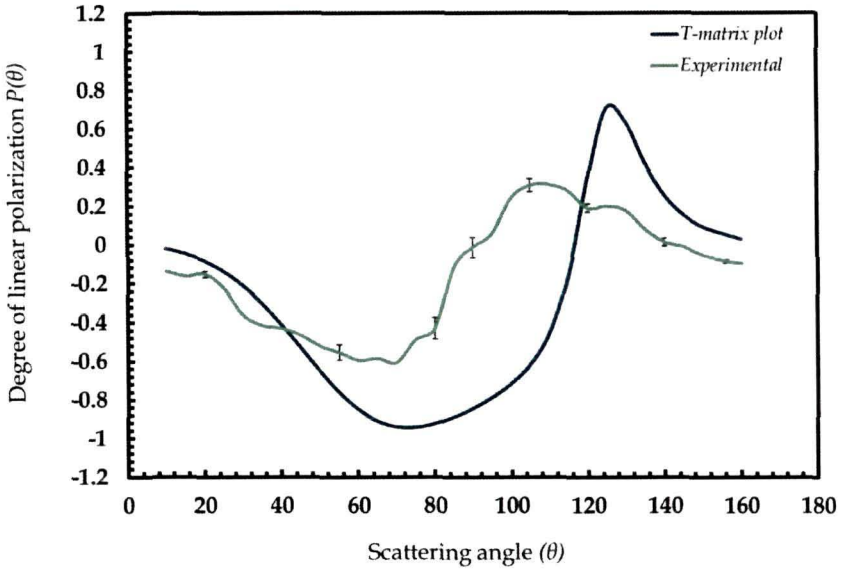

Figure 4.26: Experimentally measured Degree of linear polarization, $P(\theta)$ for TiO_2 at wavelength of 543.5 nm.

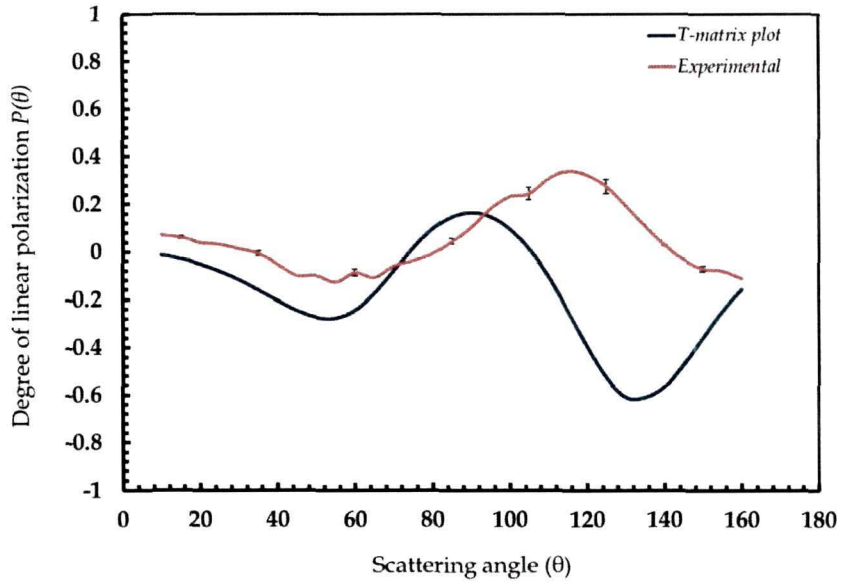

Figure 4.27: Experimentally measured Degree of linear polarization, $P(\theta)$ for TiO_2 at wavelength of 594.5 nm.

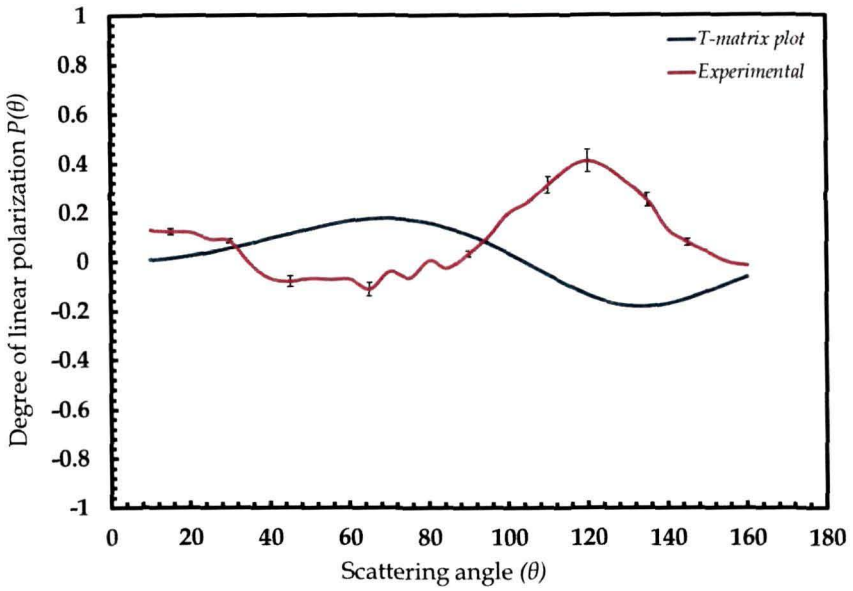

Figure 4.28: Experimentally measured Degree of linear polarization, $P(\theta)$ for TiO_2 at wavelength of 632.8 nm.

The measured $\beta(\theta)$ exhibits forward scattering lobe for all the three incident wavelengths in the range of 10° to 80° as depicted by figures 4.23 - 4.25. From the measurements, it was found that $\beta(\theta)$ show smooth signatures having fewer oscillations which indicate a wide size dispersion of the scatterers. The shapes were found to be similar to those reported for *in-situ* measurements on other aerosol particles of irregular shapes [4, 214]. As far as the wavelength dependence of the scattering phase function is concerned, it has been observed that for wavelengths, 594.5 nm and 632.8 nm, the measurements showed an extra dip around 115°. The scattering effectiveness of TiO_2 was found to be very strong, mainly at side-scattering and back-scattering angles for all the three incident wavelengths.

The measured degree of linear polarization, $P(\theta)$ exhibits similar shapes for all the wavelengths, but with positive and negative branches. As seen from the figures of $P(\theta)$ (figures 4.26 - 4.28), the negative branch is dominant at

small scattering angles. The figures also display differences in maxima and minima when compared to theoretical curves. The maxima being 0.311 at 110°, 0.339 at 115° and 0.411 at 120° for 543.5 nm, 594.5nm and 632.8 nm respectively. The minima are -0.607 at 70°, -0.127 at 55° and -0.111 at 65° for 543.5 nm, 594.5nm and 632.8 nm respectively. Significant increment in the maxima of the degree of linear polarization with increasing wavelengths was also noticeable. The measured polarization curves deviates from the theoretical curve to a greater extent in case of 632.8 nm wavelength. When compared with the results obtained from PROGRA2 experiment on TiO_2 particles, marked difference in the shape of the polarization curves was observed [333, 341]. Their results showed dominance of positive polarization throughout the angular range and strong polarization spikes at small angles around 15°. This is mainly because of the differences in size, density and structure of aggregates of TiO_2 samples used in the PROGRA2 experiment. However, the experimental results were found to be similar to those reported by O. Munoz *et al.* [214] for prolate shaped TiO_2 particles.

The reasons of deviations of experimental results from theoretical results may be due to the following reasons

i. Presence of size distribution.
ii. Minor contribution of shape distribution.
iii. Accumulation of some particles in the scattering volume.
iv. Minor effect due to variation of effective radius (of actual value from calculated value).
v. Strong dependence of polarization on size parameter of the particles.

4.5 Zinc oxide (ZnO)

Like titanium dioxide (TiO_2), zinc oxide (ZnO) is also one of the most important metal oxides. It is a stable compound having band gap of 3.22eV [342]. ZnO has high refractive index, optimum particle size, tinting strength and a high degree of whiteness (reflecting all wavelengths strongly). It is an

interesting material and finds its applications in various areas such as, optical, magnetic, gas sensing etc. [343]. In organic coatings, it provides a broad spectrum of properties like optical, chemical, biochemical and physical. Over the past century, the paint industries have utilized various aspects of those properties to a high degree, resulting in constant development of improved products. Zinc Oxide plays an important role in semiconductor ceramic elements for operation at elevated temperatures or high voltages. It is also used in UV lasers and bio-sensing. For the various applications of ZnO particles in different fields as mentioned in the preceding lines, proper tuning of size, shape etc. are important, thus light scattering measurements is one of the vital tool for such purpose. In this section, results of measurements of $\beta(\theta)$ and $P(\theta)$ of ZnO particles are presented.

Scanning electron microscopic analysis (SEM) was carried out in order to trace the morphology of the ZnO particles and to associate with light scattering measurements. The SEM image reveals that although the ZnO particles were axially symmetric, they had a wide range of shapes (figure 4.29), and had a broad dispersion of size. The equivalent spherical approximation of these particles had an average diameter of about 0.15 μm. The size distribution was Gaussian, and the graph is shown in figure 4.30.

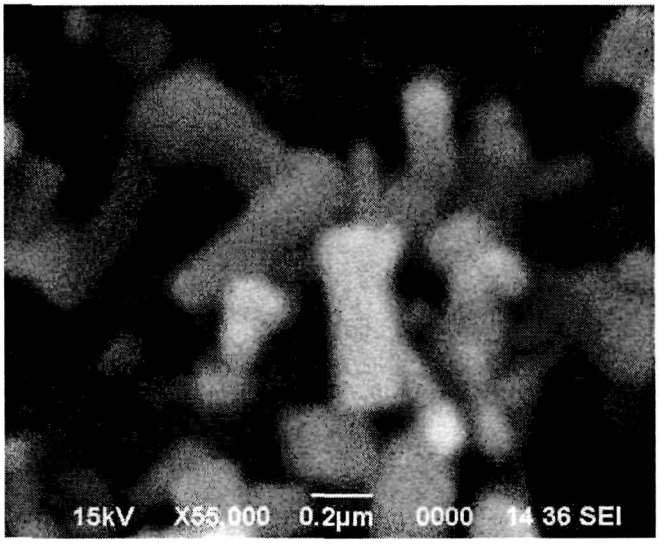

Figure 4.29: SEM image of ZnO particles at magnification of X55, 000.

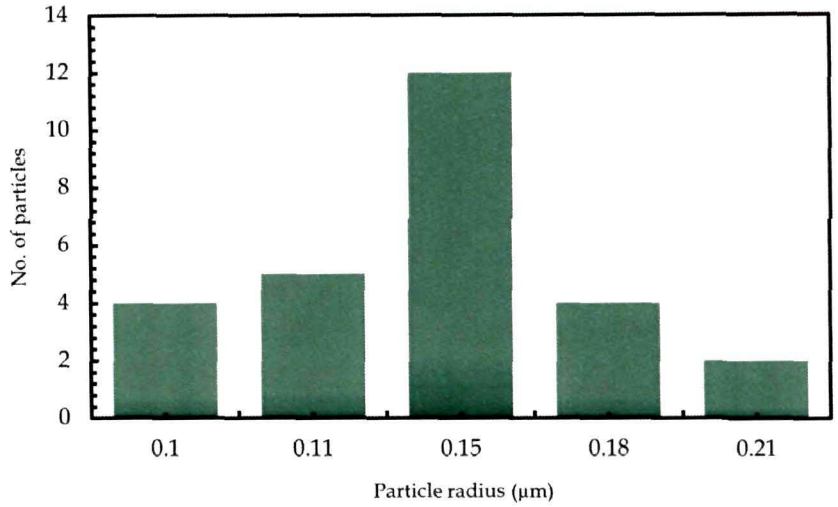

Figure 4.30: Size distribution graph of ZnO particles.

Measurements of the phase function and the degree of linear polarization of ZnO particles were carried out at three different laser wavelengths, 543.5 nm, 594.5 nm and 632.8 nm respectively. The results are shown in figures 4.31 - 4.36. Comparison of the experimental results with theoretical result based on Mie-theory is also presented in the same plots. The graphs for phase functions were normalized to 1 at 10◦. Some important parameters which were used to compute the theoretical plot for data analysis is presented in table 4.4 below.

Table 4.4: Parameters used for the data analysis of ZnO particles

Parameters	Value
Modal radius (ZnO) in micrometers	0.15 ±10
Particle size distribution	*Gaussian*
Particle refractive index(ZnO) at 543.5 nm	2.032 13 + i0000
Particle refractive index(ZnO) at 594.5 nm	2.000 84 + i0000
Particle refractive index(ZnO) at 632.8 nm	1.988 82 + i0000

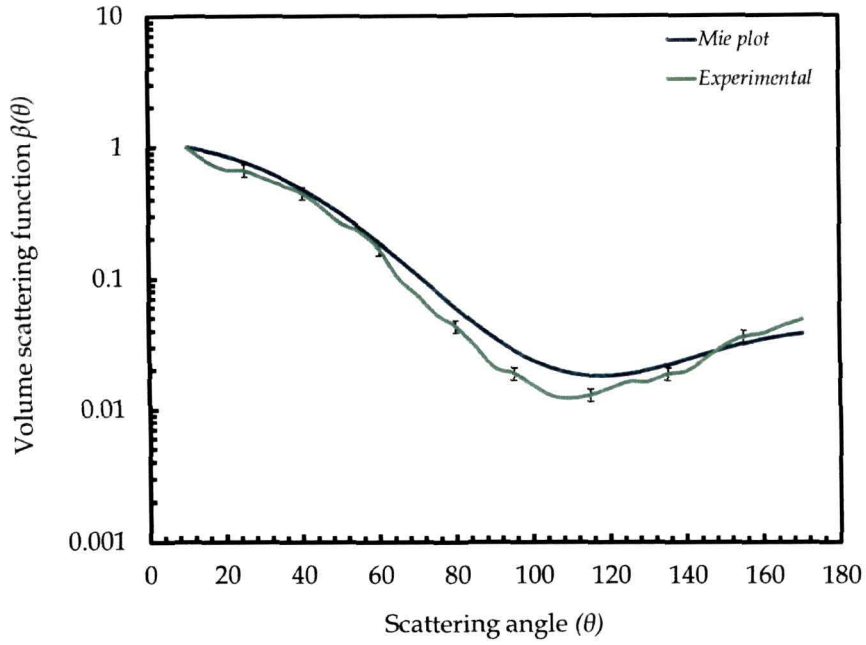

Figure 4.31: Experimentally measured Volume scattering function $\beta(\theta)$ for ZnO at wavelength of 543.5 nm.

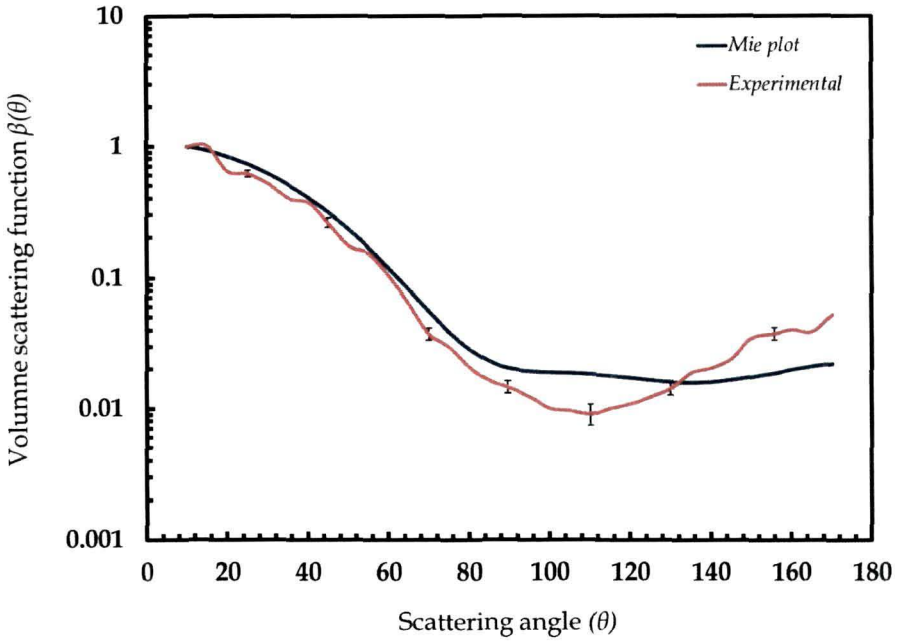

Figure 4.32: Experimentally measured Volume scattering function $\beta(\theta)$ for ZnO at wavelength of 594.5 nm.

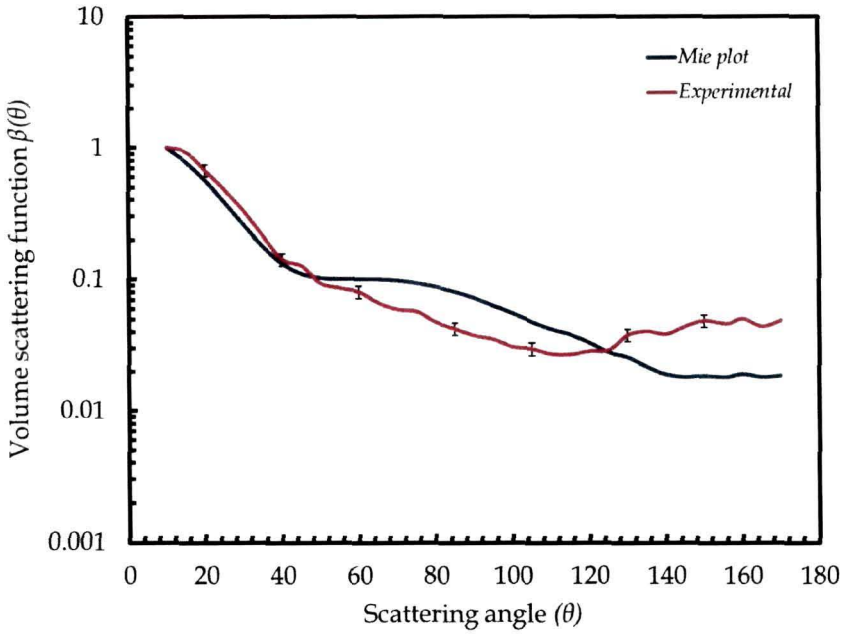

Figure 4.33: Experimentally measured Volume scattering function $\beta(\theta)$ for ZnO at wavelength of 632.8 nm.

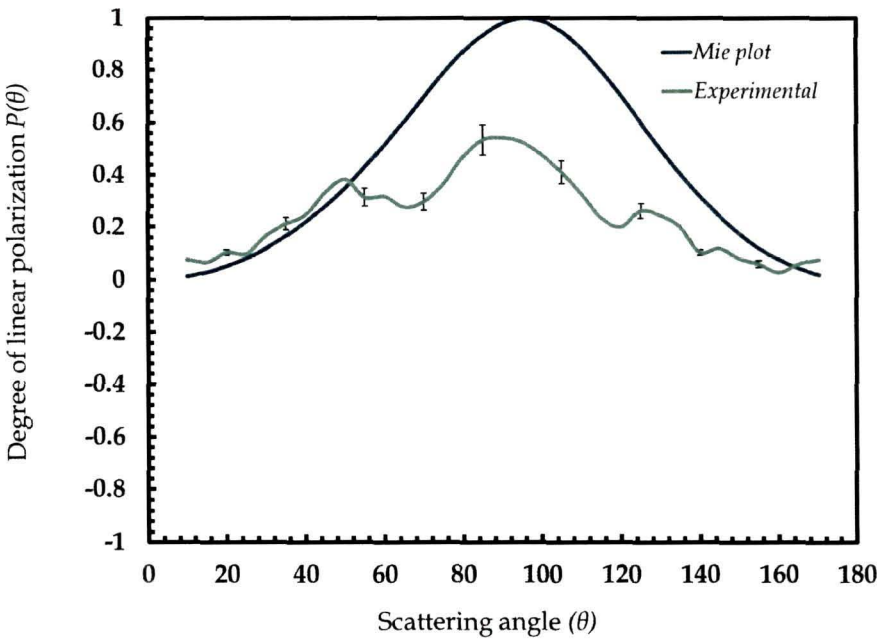

Figure 4.34: Experimentally measured Degree of linear polarization, $P(\theta)$ for ZnO at wavelength of 543.5 nm.

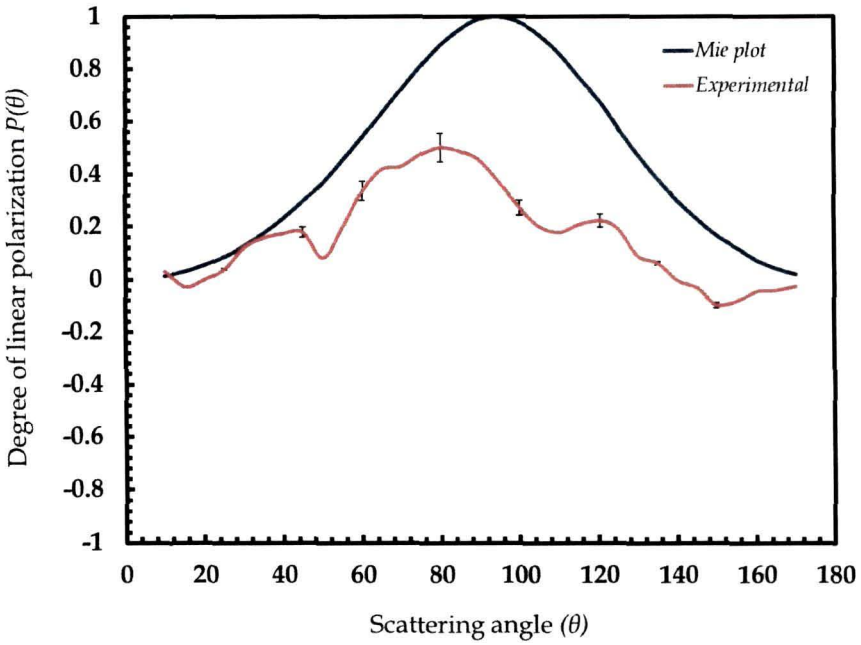

Figure 4.35: Experimentally measured Degree of linear polarization, $P(\theta)$ for ZnO at wavelength of 594.5 nm.

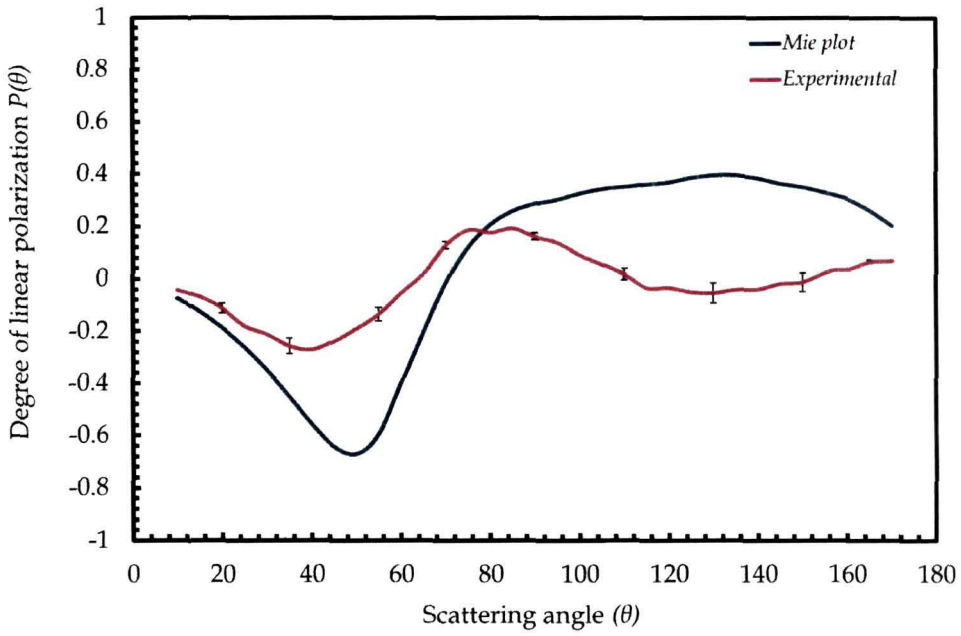

Figure 4.36: Experimentally measured Degree of linear polarization, $P(\theta)$ for ZnO at wavelength of 632.8 nm.

The measured $\beta(\theta)$ exhibits forward scattering lobe which were not equally intense for all the three incident wavelengths as depicted by scattering profiles (figures 4.31 - 4.33). The scattering effectiveness of ZnO was found to be strong, mainly at the back-scattering angles for all the three incident wavelengths, and more noticeable for wavelengths 543.5 nm and 594.5 nm. The measured values of $\beta(\theta)$ is higher at some angles perhaps because of the presence of agglomerated particles of larger size in the scattering volume. Overall, the results of measured $\beta(\theta)$ shows smooth curves (without much oscillations), indicating presence of wide size distribution of ZnO particles in the scattering volume.

The measured degree of linear polarization $P(\theta)$, for each polarization curves display a oscillating behaviour particularly for 543.5 nm and 594.5 nm wavelength (figures 4.34 and 4.35). Again, the measured degree of linear polarization was found to be positive mostly throughout the scattering angles at all the three incident wavelengths. These figures also showed low double minimum around 70° and 120° at wavelength of 543 nm, and around 50° and 115° at wavelength of 594.5 nm. In contrast, the measured $P(\theta)$ at 632.8 nm displayed a flat bell shaped characteristic curve . There is also a difference in the value of maxima for all the wavelengths. The maxima being 0.542 at 90° for 543.5 nm, 0.501 at 80° for 594.5nm and 0.181 at 70° for 632.8 nm. Significant increment in the maxima was observed with decreasing wavelengths. The reasons of deviation of measured values from theoretical values may be attributed mainly to the following points:

i. Difference in size distribution.
ii. Deviation of shape of some particles from regular shape.
iii. Difference in the density of particles.
iv. Strong dependence of measured polarization on the size parameter of ZnO particles.
v. Contributions due to presence of structure aggregates.

In other words, the experimental results showed a closer agreement for $\beta(\theta)$ than $P(\theta)$, when compared with the computed results. T-matrix method was not applied in the case of ZnO particles as their shapes did not conform to any known computable morphology. However, we ascertain a reasonable fit was observed for ZnO particles by assuming equivalent spherical particles for Mie computations, thereby proving the use of Mie theory to be a relatively good approach.

4.6 *Staphylococcus aureus*

Staphylococcus aureus is a facultative anaerobic Gram-positive coccal bacterium. It is a member of the Staphylococcae family [344]. It is an important human pathogen which has caused many epidemic outbreaks over the past 100 years. *S. aureus* is a frequent component of the human microbial flora, however, that can turn into a dangerous pathogen. The coagulase positive strain can cause severe chronic infections in human, and is capable of infecting almost every tissue and organ system in the human body [344]. The light scattered from such biological particle is rich in information and can be extracted by performing comprehensive measurements of the scattered light [190,192, 198, 254, 256, 257]. Some well-known methods used for measurement of polarization effects in biomaterial are "optical rotatory dispersion" and "circular dichroism", however, these measurements are made in the forward direction (θ= 0) and therefore do not make use of the angular information produced by the particulate matter in the sample [190].

Metal oxide nanoparticles like TiO_2, CdO, CuO, ZnO etc. are receiving great amount of attention due to their significant implication in biological applications, due to their antibacterial property [343]. Some common strains of bacteria which have been widely studied are *Staphylococcus aureus, Bacillus subtilis, Escherichia coli* etc. [189, 232, 254]. So far such bio-particles are rarely explored by using light scattering technique [189,232, 273]. It is important to mention that the studies of organic molecules may also be utilized in

interpretation of data that is obtained from Astrophysical studies on the presence of organic molecules in stellar and interstellar medium[194- 200].

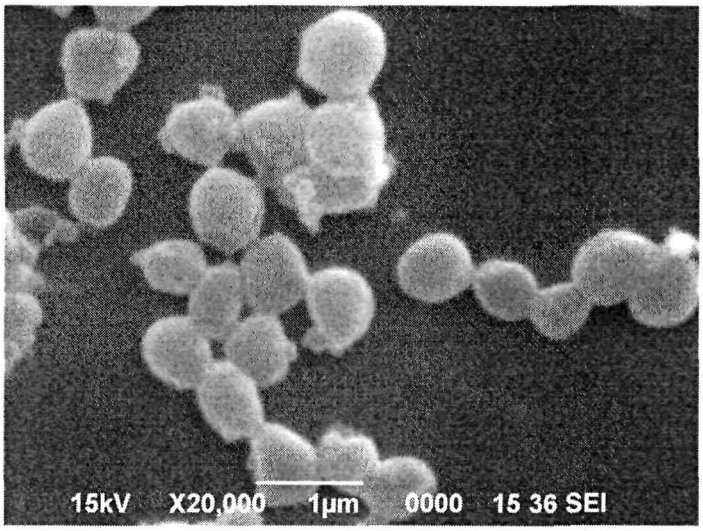

Figure 4.37: SEM of *Staphylococcus aureus* at magnification of X20, 000.

Each of the elements of the Mueller matrix contains all the information about intensities and polarization of the scattered light as a function of the scattering angle [45, 48]. Angle-resolved light scattering measurements [273] by different biological particles have been reported earlier, where light scattering was used as a powerful technique to differentiate various bio-particles according to species, strains, growth media etc. In our present work, an attempt was made to study the angle-resolved light scattering of *S. aureus* bio-particles in order to see the signatures of these particles with changing wavelength of incident light. The scattering results reveal the differences, definiteness and nature of light scattered from such systems. Light scattering technique is a very effective investigating tool when observations are to be made if a small alteration is introduced in a scattering volume. The aim of our experiment was to study subtle differences with changing incident wavelengths, especially for bio-particles by detecting significant light scattering signals. Some small morphological changes in the bio-particles under the influence of any external factors like strain, chemical treatment, metabolic change, killing techniques can be monitored *in-situ* by light

scattering. In simple words, it enables one to detect precisely what changes occur in bio-particles like bacteria as a result of some environmental or external alterations.

Scanning electron microscopic analysis (SEM) was carried out in order to find out the morphology of *S. aureus* bio-particles. From the SEM image, it was verified that the *S. aureus* bio-particles were more or less spherically celled (grape-shaped) having a modal radius of 0.45 μm, as shown in figure 4.37. The size distribution of *S. aureus* bio-particles were found to be narrow Gaussian from the SEM image, as shown in figure 4.38.

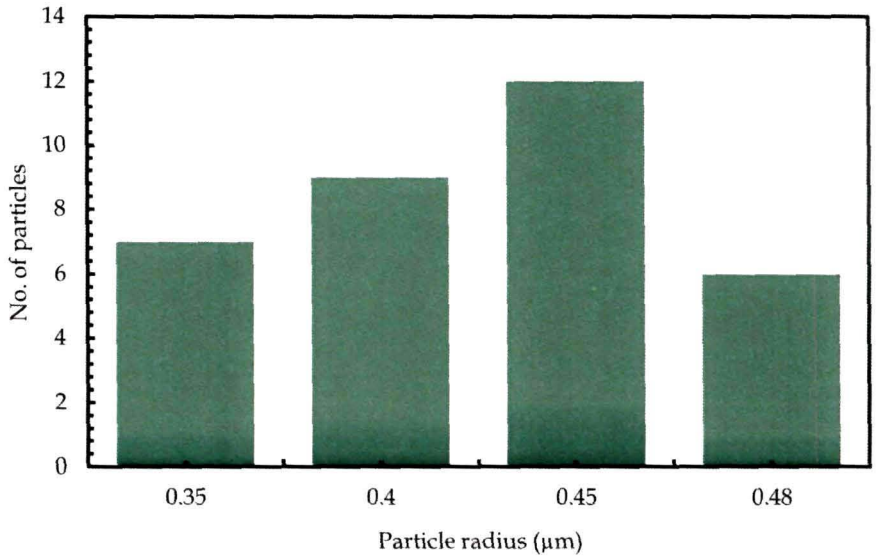

Figure 4.38: Size distribution graph of *Staphylococcus aureus* bio-particles.

Measurements of the phase function and the degree of linear polarization of *S. aureus* particles were carried out at three different laser wavelengths, 543.5 nm, 594.5 nm and 632.8 nm respectively. Scattering data files were generated and processed subsequently using the same analytical programs. The results are shown in figures 4.39 - 4.44. In the same plots we show the comparison of experimental results with Mie theory. Although Mie theory holds good for spherical homogenous particles, but bio-particles like bacteria have internal and external structures too complex to justify using Mie

calculations to model their scattering behaviours. Yet, compared to other light scattering computations, Mie calculations can be performed relatively faster and with considerable accuracy, since it requires only few input parameters which can be readily estimated or calculated [232]. Therefore, we investigated whether results of Mie calculations produce reasonable approximations of the measured results. Some important input parameters used for data analysis are given in table 4.5 below. The graphs for phase functions are presented in logarithmic scale and normalized to 1 at 10°.

Table 4.5: Parameters used for the data analysis of *Staphylococcus aureus* bio-particles

Parameters	Value
Modal radius in micrometers	0.45 ±10
Size distribution	Narrow Gaussian
Particle refractive index at visible wavelengths	1.12 + i0000

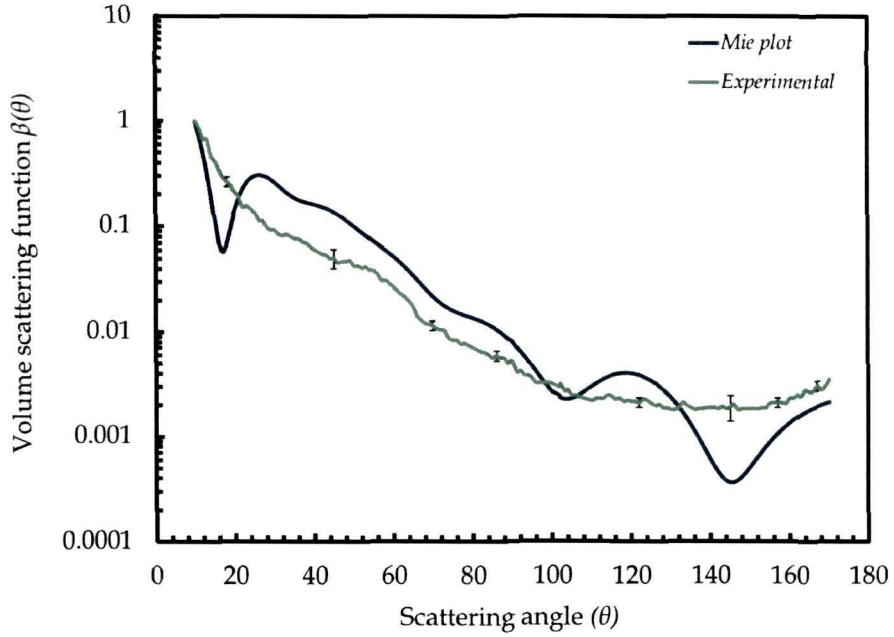

Figure 4.39: Experimentally measured Volume scattering function $\beta(\theta)$ for *S. aureus* at wavelength of 543.5 nm.

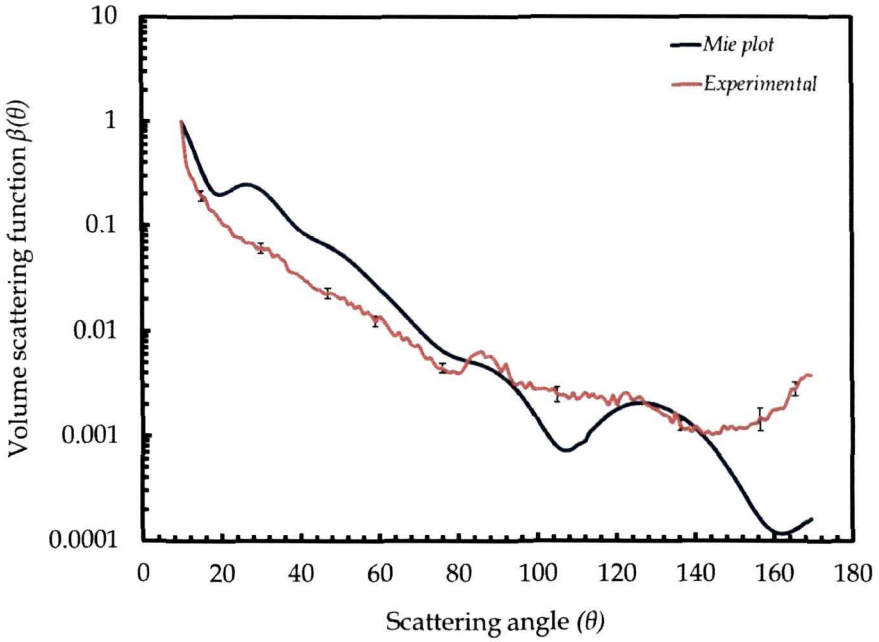

Figure 4.40: Experimentally measured Volume scattering function $\beta(\theta)$ for *S. aureus* at wavelength of 594.5 nm.

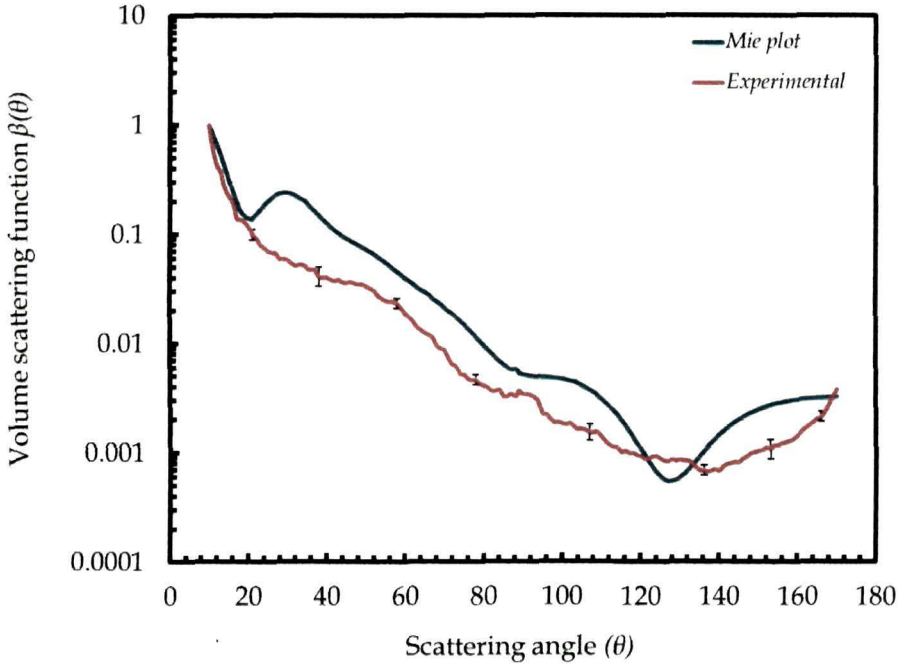

Figure 4.41: Experimentally measured Volume scattering function $\beta(\theta)$ for *S. aureus* at wavelength of 632.8 nm.

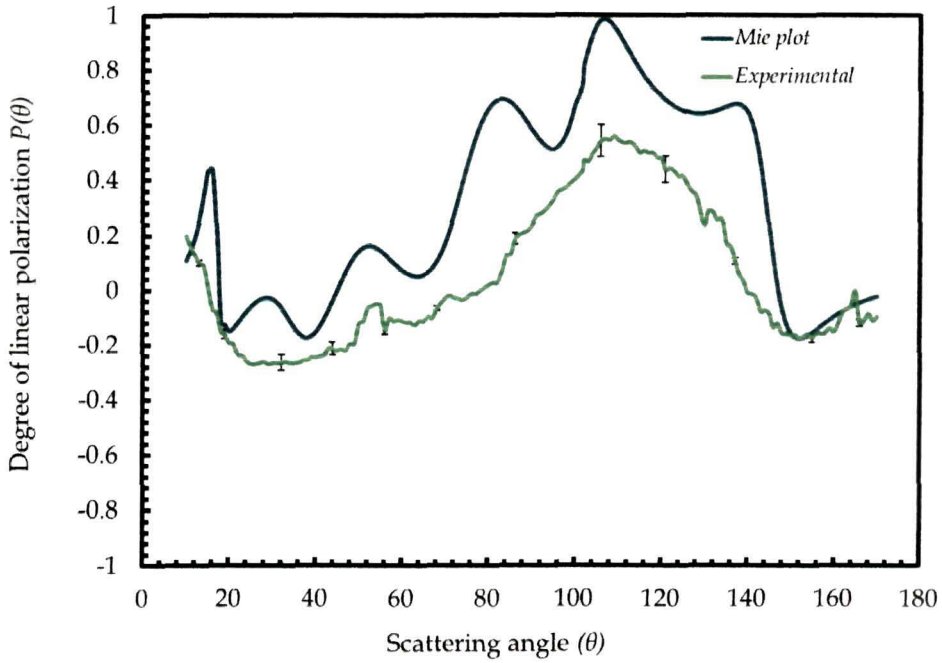

Figure 4.42: Experimentally measured Degree of linear polarization, $P(\theta)$ for *S. aureus* at wavelength of 543.5 nm.

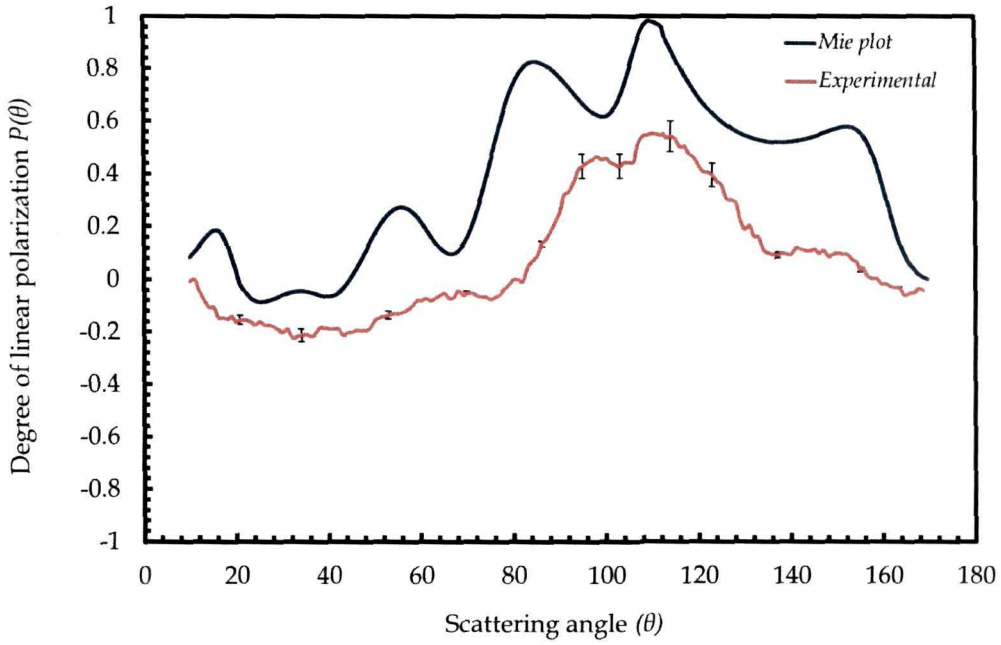

Figure 4.43: Experimentally measured Degree of linear polarization, $P(\theta)$ for *S. aureus* at wavelength of 594.5 nm.

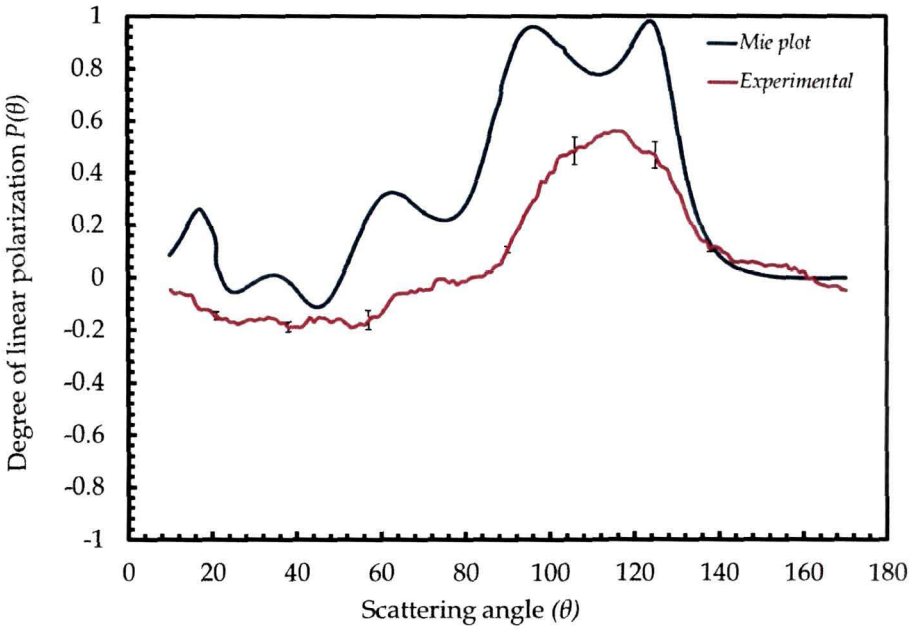

Figure 4.44: Experimentally measured Degree of linear polarization, $P(\theta)$ for *S. aureus* at wavelength of 632.8 nm.

The measured $\beta(\theta)$ are sharply peaked in the forward direction, for all the three wavelengths as depicted by figures 4.39 - 4.41. The measured plots of $\beta(\theta)$ were found to follow the same trend exhibited by the theoretical plot, but showing manifestation of prominent oscillations at some scattering angles in the theoretical curve. But, small amount of oscillations, also known as Mie oscillations were observed throughout the angular range in the experimental curve of all the wavelengths. This observation indicates presence of narrow size distribution of *S.aureus* bio-particles. The oscillating behaviour of the theoretical plot may be due to the incorporation of single size parameter in the program while generating the theoretical plot, and seemed to be more pronounced for comparatively larger particles.

The measured degree of linear polarization $P(\theta)$, for each wavelength are moderately bell-shaped, exhibiting a major positive branch and receding negative branch , and are shown in figures 4.42 - 4.44. In contrast, the theoretical curves showed dominance of positive polarization throughout the angular range and strong polarization bumps at some angles. There is a change in polarization maxima and minima as well, corresponding to changing wavelengths. The maxima being 0.552 at 107° for 543.5 nm, -0.223 at 32° for 594.5nm and 0.561 at 115° for 632.8 nm. The minima are - 0.267 at 25° for 543.5 nm, 0.167 at 112° for 594.5nm and - 0.18 at 52° for 632.8 nm. Overall, we find a goodness of fit for the bio-particles especially for the volume scattering function. The reason of deviation of measured results from computed results may be attributed mainly to the following points:

i. Presence of size distributed bio-particles, however narrow it may be.
ii. Strong dependence of polarization on the size parameter of the bio-particles.
iii. Minor contributions due to aggregation of some bio-particles.
iv. Minute morphological changes which may be due to slight change in the alteration of external environmental conditions.

4.7 *Camellia Sinensis (Tea)* dust and *Mycobacterium smegmatis*

Angular light scattering is a widely used non-destructive technique for studying particles of biological origin such a viruses, bacteria, and eucaryotic cells [89, 190, 253, 273]. Measurements of all scattering matrix elements of such particles are rare. However, the first among the researchers who worked in this area, and measured all the matrix elements successfully for a variety of biological particles was Bickel and Strafford [189, 190]. In this section, light scattering study of *Camellia sinensis* dust and *Mycobacterium smegmatis* are presented.

Tea is an important and very popular beverage used all over the world and is mainly brewed from the tender leaves of the plant species *Camellia sinensis* (L.) Kuntze. The plant is grown in many tropical regions of the world including Assam. The selected leaves and buds of tea plants are processed to produce the tea of commerce. During the processing stages in the tea industries from raw leaves to commercially packaged industrial tea, tea dust is released into the atmosphere as an effluent. It has been reported in some papers that there is possibility of the tea dust acting as a carrier for asthmatic triggers and also carrier for pathogens. The adverse effect of tea dust is mostly on the pulmonary function of tea workers who are exposed to this dust. Several authors have reported tea dust as a cause of occupational asthma, chronic respiratory disease etc. [345].

Mycobacterium tuberculosis is the etiological agent of Tuberculosis (TB). The infection of humans by *M. tuberculosis* dates back to antiquity. *M. tuberculosis* is a Gram positive bacterium with its size ranging from 0.2 to 0.4 microns. WHO declared TB as a global emergency in 1993 [346]. In view of the alarming global assessment of the disease and the ineffectiveness of the conventional first and second line of drugs used to treat TB, there is an urgent need for discovering and developing new anti-mycobacterial agents and new diagnosis and detection systems. A prerequisite in the control of *tuberculosis* is

proper understanding of the aerosolic spread and survival of *M. tuberculosis* in air. It must be emphasized that *Mycobacterium tuberculosis* is non-motile and can survive for 90 to 120 days on inanimate surfaces [347, 348]. Among the pathogens which have relatively greater likelihood of being carried by tea dust particles is *Mycobacterium tuberculosis*.

Monitoring of pathogenic aerosols in the environment around us requires very advanced detection systems which may be able to detect and distinguish these pathogenic aerosols from the normal environment conditions, especially while considering the respirable size of 1 to 10 micrometers size [188, 368]. It is highly desirable that the advanced systems are developed for such detections and are capable of generating online and rapid information about possible threats caused by these life-threatening aerosols. The fundamental information about such particle is obtained from the scattered intensity, $I(\theta, \varphi)$, where θ is the polar angle relative to the direction of incident beam and φ is the azimuthal angle relative to the scattering plane.

The present work was aimed primarily at investigating whether air-borne tea dust particles are a possible carrier of *Mycobacterium* pathogens, and secondly whether monitoring of such non-spherical particles can be done by light scattering techniques. Light scattering experiments were carried out in the single-scattering regime [253]. The effect of multiple scattering is assumed to be negligible as long as the scattered flux is proportional to the sample concentration. This was done by following the method described in Section 3.9 in Chapter 3. In this way we could determine the most favorable cell density to which single scattering applied. In our case, we found the optimum concentration of tea dust sample at three different wavelengths to be approximately 1.5×10^8 CFU/mL (figure 4.45).

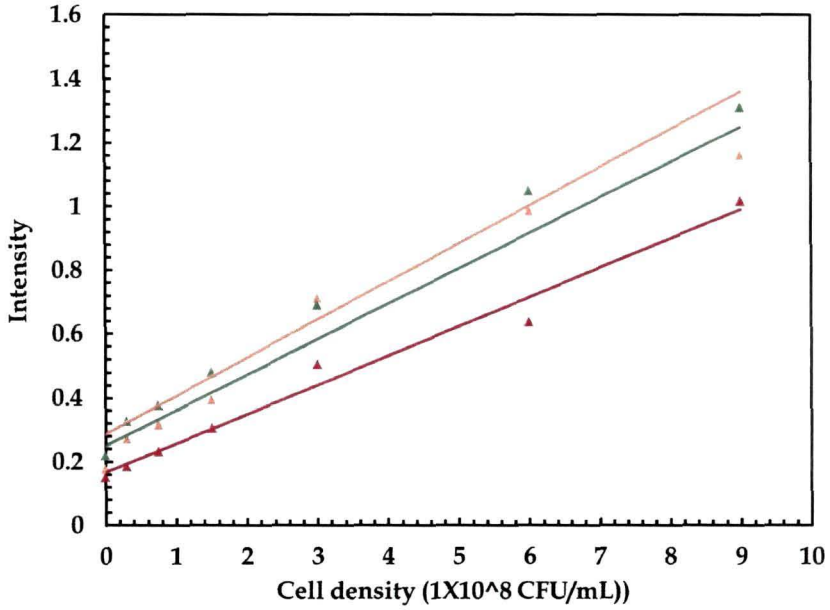

Figure 4.45: Graph for the intensity of scattered light in arbitrary units for unpolarized light versus concentration of *M. smegmatis* cells in 2.0mg/mL tea dust for a fixed position of detector at 15^0. The green triangle, orange triangle and red triangle corresponds to the results for 543.5nm, 594.5nm and 632.8nm incident laser wavelengths respectively.

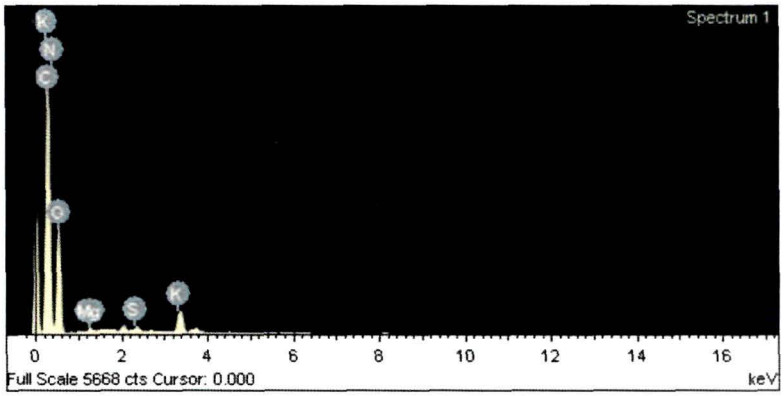

Figure 4.46: EDX image of *C. sinensis* dust particles.

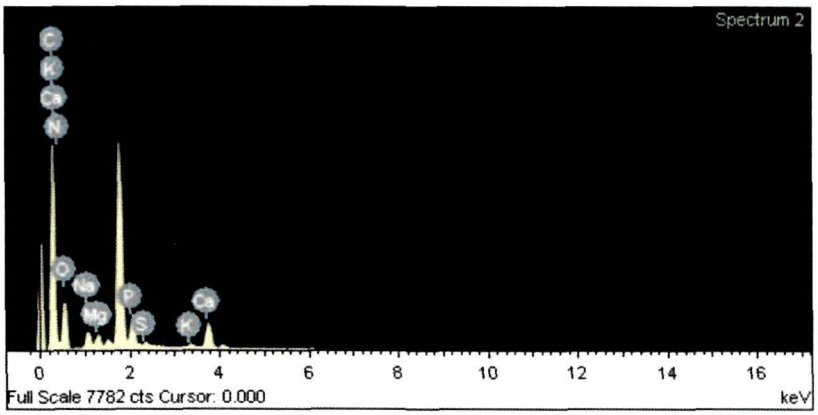

Figure 4.47: EDX image of *C. sinensis* dust particles contaminated with *M. smegmatis* bio-particles.

Energy dispersive X-ray spectroscopic investigation (EDX) was performed to check the constituents of sample of *C. sinensis* dust particles, and *C. sinensis* dust particles contaminated with the bacteria, *M. smegmatis*. The EDX images (figures 4.46 and 4.47) verified the presence of constituents like Potassium, Magnesium, Calcium, Sodium, Sulphur, Phosphorus etc. which are usually present in purely organic matter. No other impurity or unwanted elements were present. This investigation was carried out to ensure the purity of the samples chosen.

4.7.1 Sample preparation and Antimycobacterial Assay of *Camellia sinensis* dust particles

The samples of *Camellia sinensis* dust particles were collected from areas around tea factories situated in Assam, India. Agar Well Diffusion Assay [349] was performed in order to investigate whether the tea dust particles inhibit the Mycobacterial growth through polyphenols that are present in the unprocessed green tea leaves [350]. In order to maintain safe laboratory procedures, the non-pathogenic species *Mycobacterium smegmatis* which has all the characteristic properties of the pathogenic species *Mycobacterium tuberculosis* except for pathogenicity was used for the investigations. The strain *M. smegmatis* mc2 155 was cultured in Mueller Hinton Broth 2 media at

37° C for 18h. The bacterial cells were suspended in a saline solution (0.85%NaCl) and the McFarland standard of the cells were adjusted to turbidity of 0.5 (approximately 108 CFU/ml). The suspension was inoculated in Mueller Hinton Agar media and four wells (6mm) were punched. 50 µl of the sterile organic tea dust of two concentrations i.e., 20mg/ml and 50mg/ml, dissolved in 1% (v/v) DMSO(Dimethyl sulphoxide) were added to well 1 and well 2, respectively. 1% DMSO was added to well 3 and Streptomycin was used as an antibiotic control in well 4.The plates were incubated at 37° for 18h. This experiment was conducted in triplicate, that is, the Agar Well Diffusion Assay was performed three times to ascertain the validity of the biological process. Growth of the bacterial cells was not affected by 1% DMSO as shown by our control experiments in well 3 (figure 4.48). These dust particles are non-spherical and have a broad size distribution. It has been found that the size distribution of the particles is nearly Gaussian (figure 4.52). In order to differentiate between the *Mycobacterium* contaminated tea dust samples from the uncontaminated one, SEM images of both the types were taken. The control cells as well as the cells incubated with tea dust (20mg/mL) had smooth and natural surface morphology.

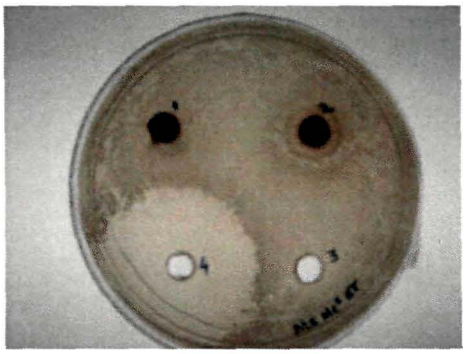

Figure 4.48: Antimycobacterial assay by the sterile *C. sinensis* dust, and dust inoculated with *M. smegmatis* culture.

Scanning electron microscopic analysis was utilized to observe the morphology of the *C. sinensis* particles and to study the morphological changes in the bacteria on being adsorbed onto tea dust. The study was done using the method of Nair et al. [351]. 100μL of bacteria adjusted to 0.5 McFarland standard was resuspended into 4 ml of 10mM sodium phosphate buffer, pH 7.4, in two different 15ml centrifuge tubes. In the solution, 100 μL of organic tea dust (20mg/ml) was added and incubated at 37 °C for 6 hours. After the incubation the bacteria were washed in the same buffer and fixed overnight at 4° C with 2.5% (v/v) glutaraldehyde (Fluka). After fixation the cells were mounted on cover slips using Poly-L-Lysine (Sigma). The cells were then rinsed with 10mM sodium phosphate buffer at pH 7.4, and dehydrated through an ethanol series for about 15 minutes each. The samples were dried at room temperature and coated with 10-15 nm thickness of platinum using a JEOL 1600 Auto Fine Coater. The samples were then examined under the SEM with an accelerating voltage of 10-15 KV. (JEOL 6390).The standard table of "McFarland standard" at *600 nm is shown in table 4.6 below.

Table 4.6: Typical McFarland Standard table

McFarland Standard No.	0.5	1	2	3	4
1.0% Barium chloride (ml)	0.05	0.1	0.2	0.3	0.4
1.0% Sulfuric acid (ml)	9.95	9.9	9.8	9.7	9.6
Approx. cell density (1X10^8 CFU/mL)	1.5	3.0	6.0	9.0	12.0
% Transmittance*	74.3	55.6	35.6	26.4	21.5
Absorbance*	0.132	0.257	0.451	0.582	0.669

The SEM images are shown in figure 4.49 to figure 4.51. In figures 4.50 and 4.51, the SEM image shows *Mycobacterium* contaminated *C. sinensis* dust sample, and verifies that the air-borne tea dust particles act as carrier of *M. smegmatis*, thereby revealing an important point that these particles might also act as carrier of pathogenic *M. tuberculosis* species. Based on the investigations using "Agar Well Diffusion" method on tea dust samples it was observed that these particles did not exhibit any antimycobacterial activity unlike the extracts of fresh tea leaves and hence it might act as a potent carrier.

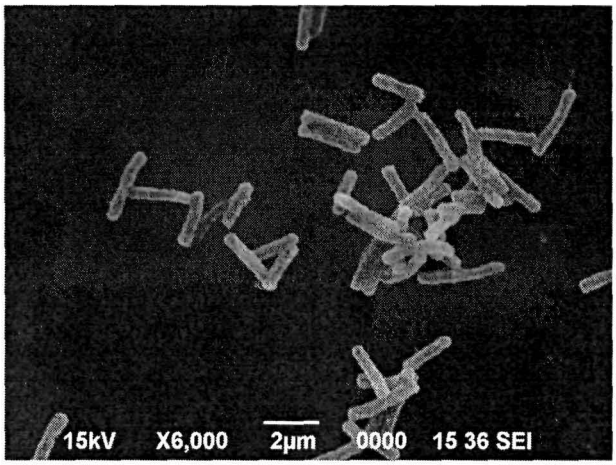

Figure 4.49: SEM image of *M. smegmatis* at magnification of X6, 000.

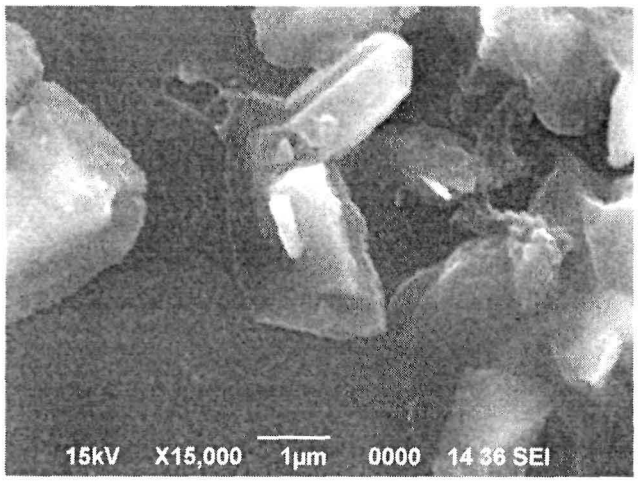

Figure 4.50: SEM image of *C. sinensis* contaminated by single *M. smegmatis* at magnification of X15, 000.

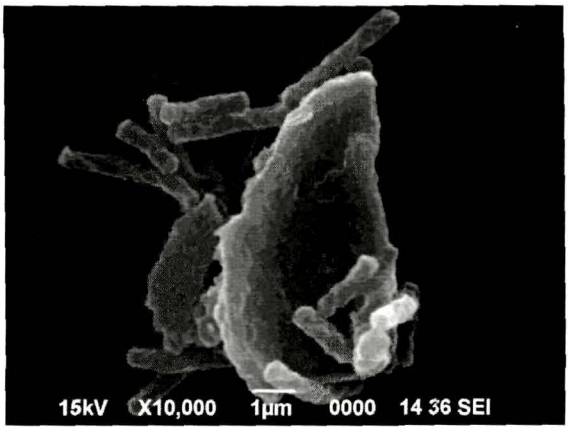

Figure 4.51: SEM image of *C. sinensis* contaminated by multiple *M. smegmatis* at magnification of X10, 000.

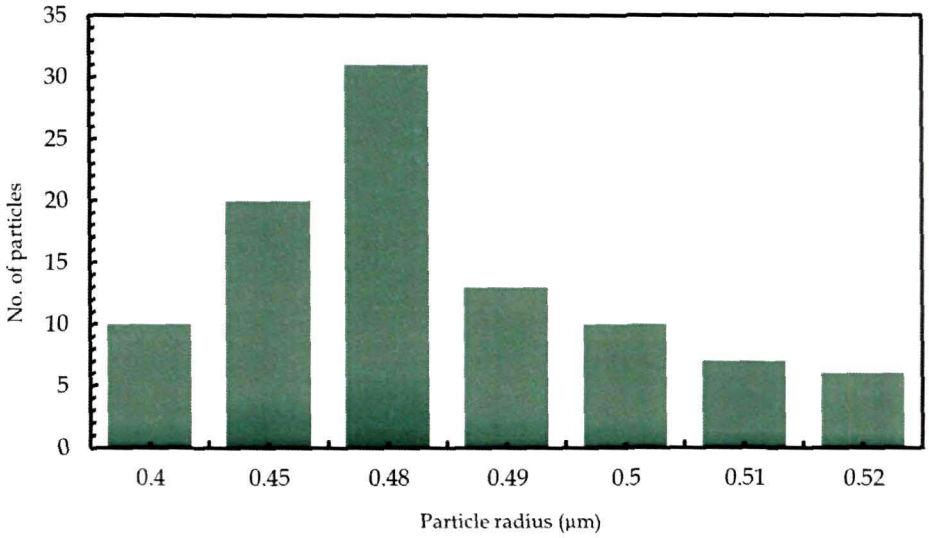

Figure 4.52: Size distribution graph of *C. sinensis* contaminated by *M. smegmatis.*

Based on the SEM image we found the size distribution of *C.sinensis* dust particles contaminated with *M. smegmatis* to be broad Gaussian, shown in figure 4.52. Scattering by single, or collection of oriented, non-spherical particles,may, unlike scattering by spheres, are azimuthally dependent. But for randomly oriented particles, light scattering properties are independent of azimuthal angle φ [45, 47]. However, azimuthally-dependant measurements were also taken along with polar-dependant measurements for sample of *C.*

sinensis, and *C. sinensis* dust with *M. smegmatis*. This is because of the reason that sometimes it is probable that the particles may get aligned along one direction or orientation when present in some liquid suspension. As reported by Quintby-Hunt *et al.* [45], there is a possibility that with change in suspension media, ensembles of non-spherical particles can exhibit non-random orientation as a result of gravitational settling, fluid dynamics flows, biological interactions etc., and we have observed similar phenomena in our studies. Light scattering investigations on such non-spherical particles was carried out for the first time, so it was necessary to ascertain the validity of our observations. Moreover, this proved to be an added step to check the reliability of our setup as well. Thus, it quantifies that the setup can be used for studying scattering properties of aligned particles too, where the importance of the dependence of azimuthal angle counts. Our investigations proved that the light scattering by such particles were found to be azimuthally dependent, the analytical part of which is described hereafter. Some important parameters used for data analysis is given in table 4.7 below.

Table 4.7: Parameters for data analysis *C. sinensis* and *M. smegmatis*

Parameters	Value
Modal radius (*M. smegmatis*) in micrometers	0.25 ±10
Modal radius (*C. sinensis*) in micrometers	0.48 (approx.)
Particle size distribution	Gaussian
Particle refractive index (*M. smegmatis*) at 543.5 nm, 594.5nm and 632.8nm respectively	1.37, 1.39 , 1.4 respectively
Particle refractive index (*C. sinensis*) at 543.5 nm, 594.5nm and 632.8nm respectively	1.453, 1.47, 1.49 respectively

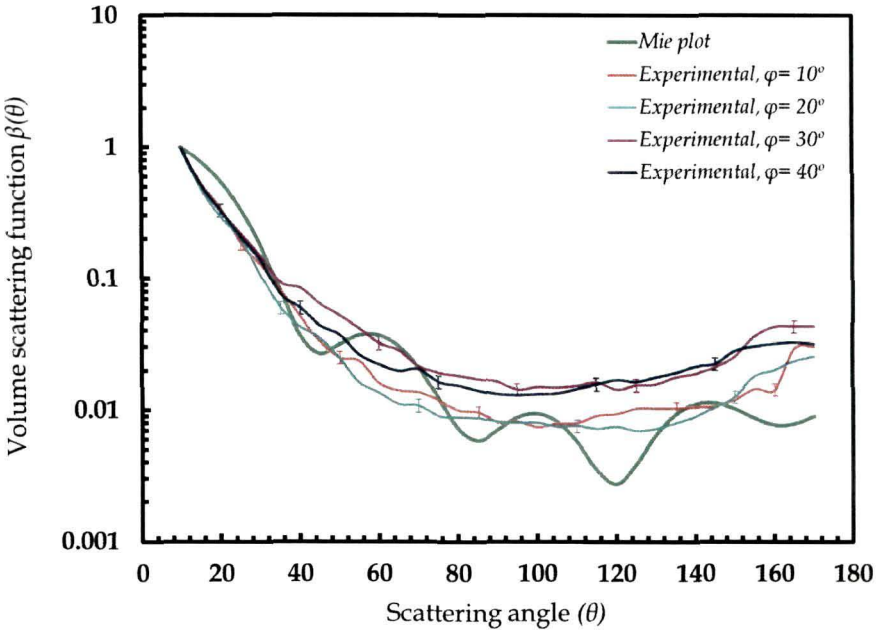

Figure 4.53: Experimentally measured Volume scattering function $\beta(\theta)$ for *C. sinensis* at wavelength of 543.5 nm.

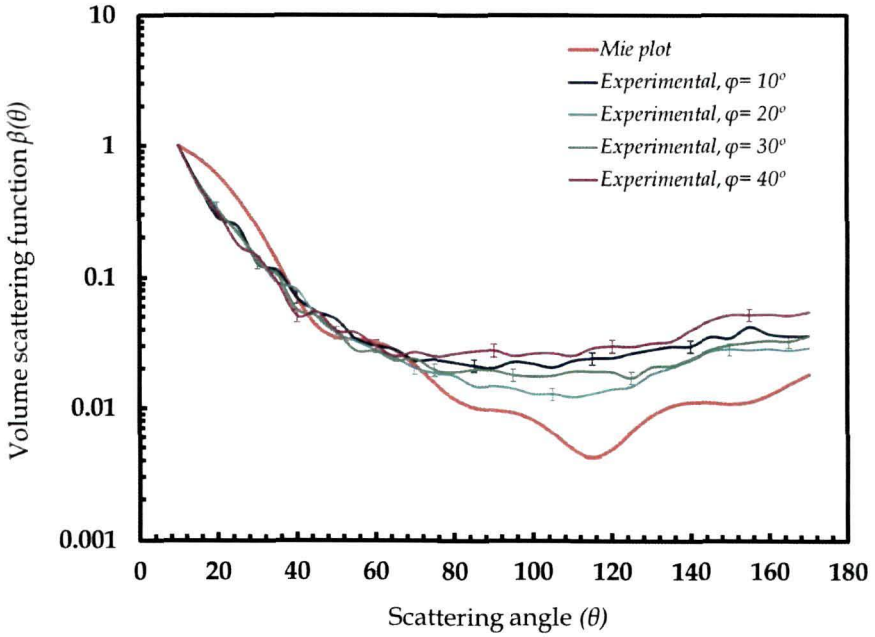

Figure 4.54: Experimentally measured Volume scattering function $\beta(\theta)$ for *C. sinensis* at wavelength of 594.5 nm.

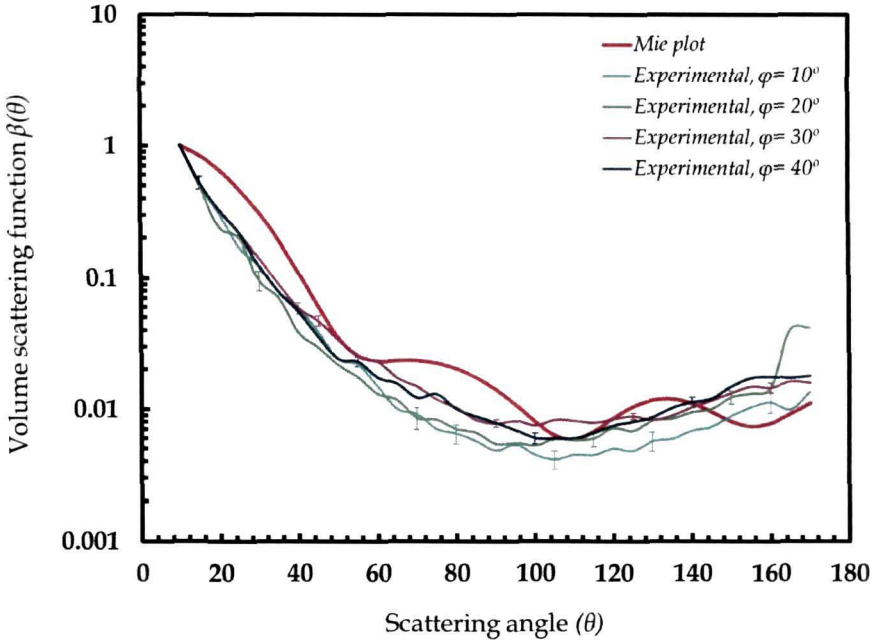

Figure 4.55: Experimentally measured Volume scattering function $\beta(\theta)$ for *C. sinensis* at wavelength of 632.8 nm.

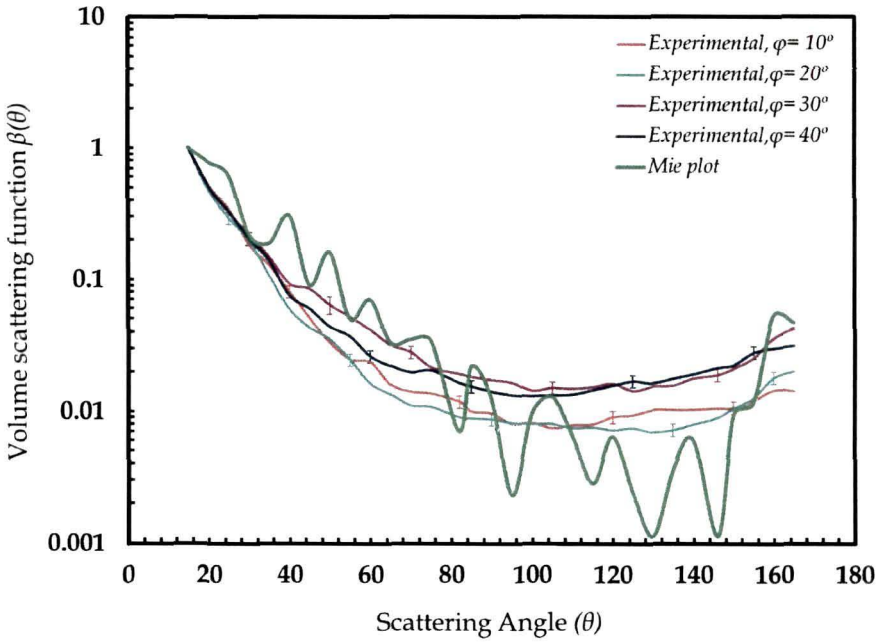

Figure 4.56: Experimentally measured Volume scattering function $\beta(\theta)$ for *C. sinensis* contaminated with *M. smegmatis* at wavelength of 543.5 nm.

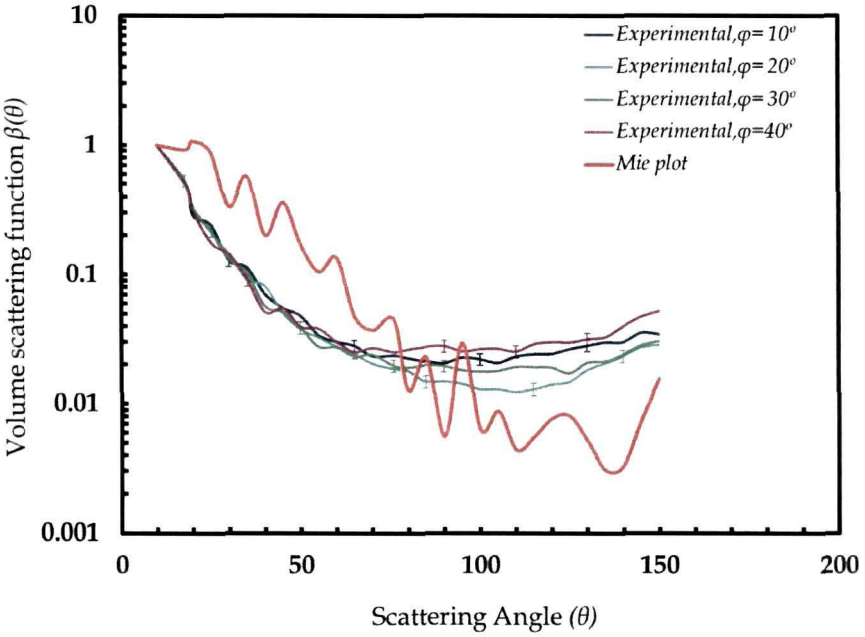

Figure 4.57: Experimentally measured Volume scattering function $\beta(\theta)$ for *C. sinensis* contaminated with *M. smegmatis* at wavelength of 594.5 nm.

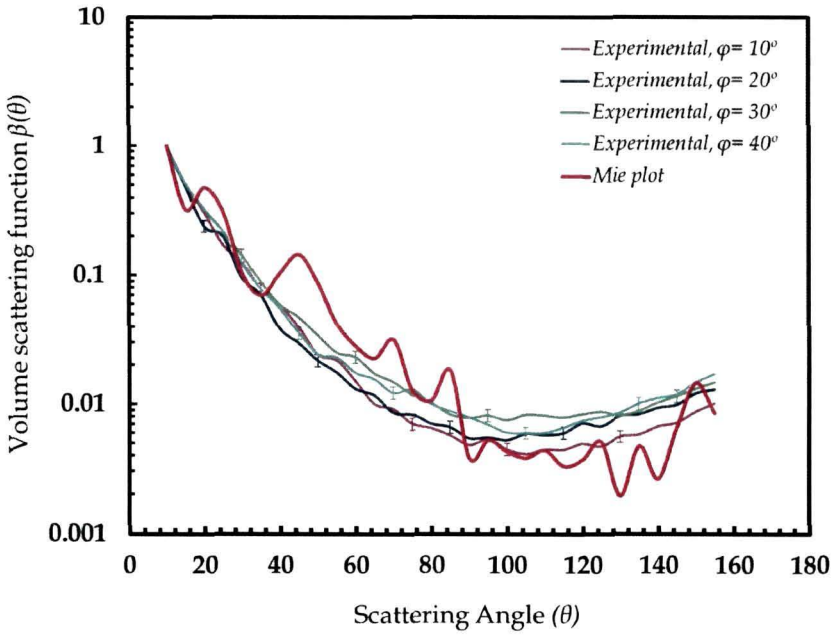

Figure 4.58: Experimentally measured Volume scattering function $\beta(\theta)$ for *C. sinensis* contaminated with *M. smegmatis* at wavelength of 632.8 nm.

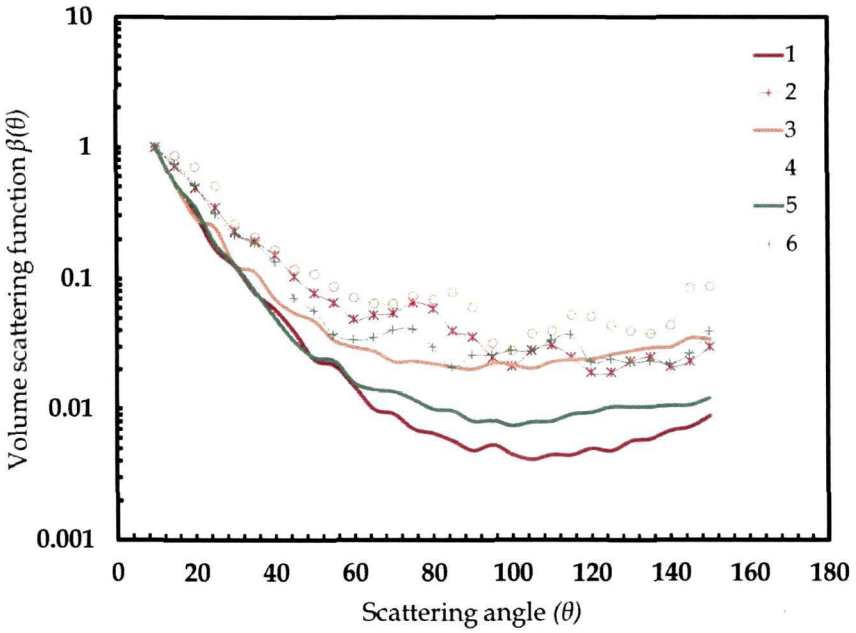

Figure 4.59 (a)

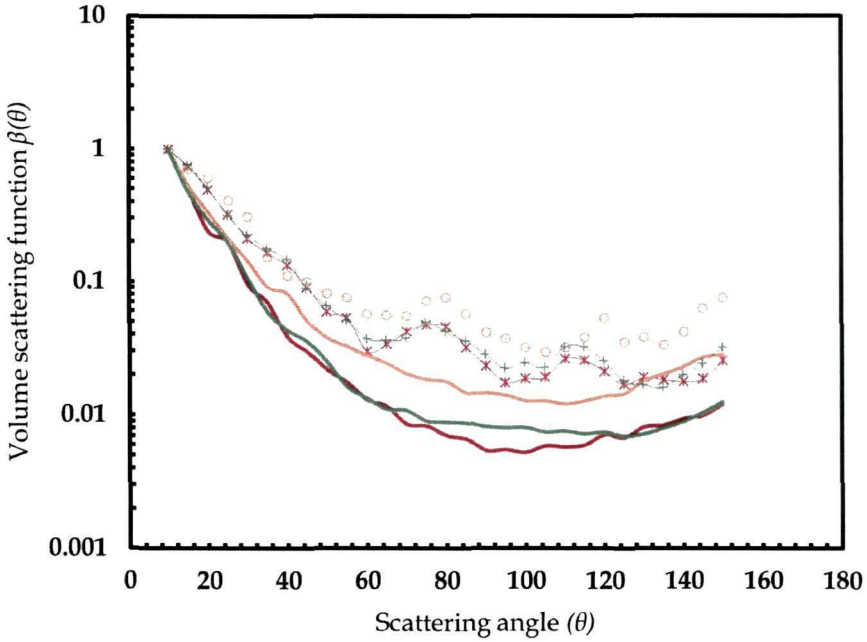

Figure 4.59 (b)

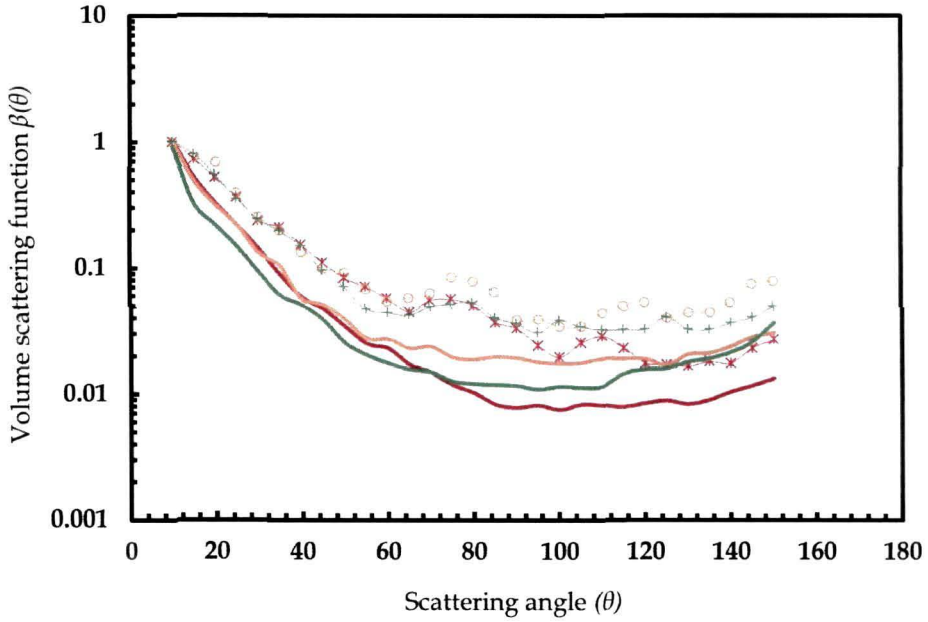

Figure 4.59 (c)

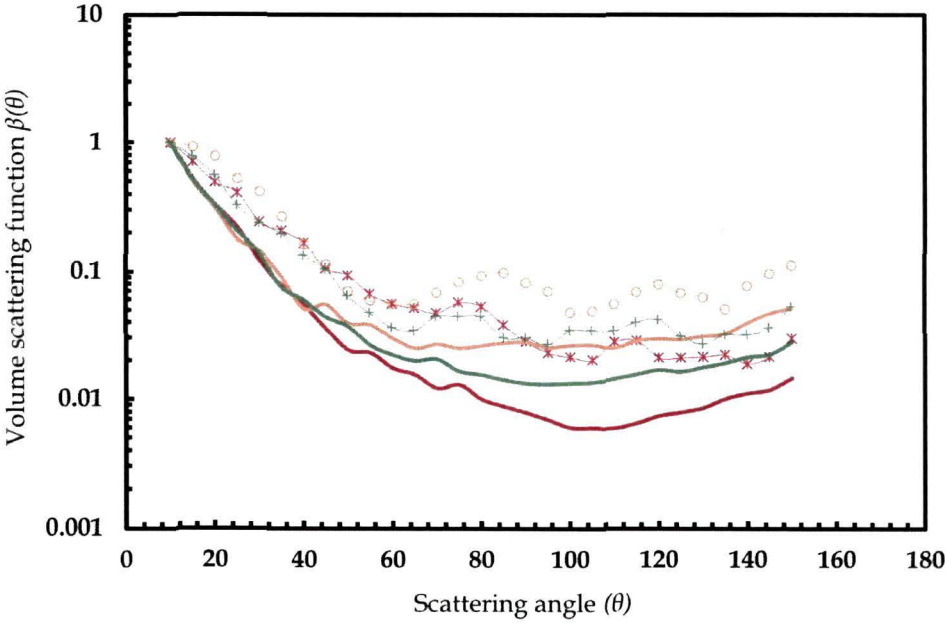

Figure 4.59 (d)

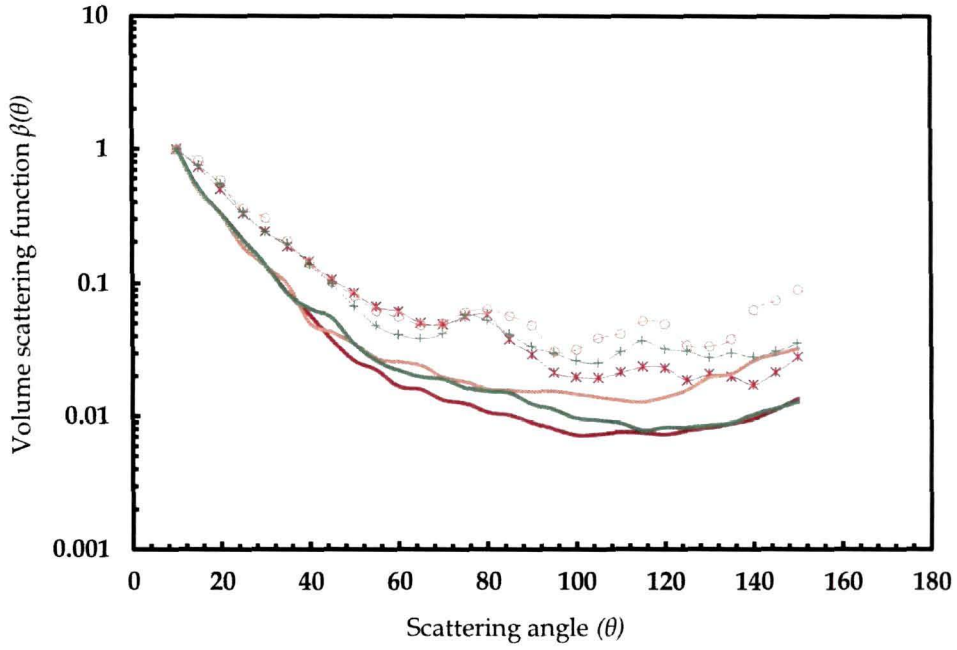

Figure 4.59 (e)

Figure 4.59: Volume scattering function, $\beta(\theta)$ for *Mycobacterium* contaminated and uncontaminated *tea* dust particles for : (a) φ= 10°, (b) φ= 20°, (c) φ= 30°, (d) φ= 40°, (e) φ= 50°. Line 1 and line 2 in the graphs (a to e) represents the *Mycobacterium* uncontaminated and contaminated intensity profile at 632.8nm respectively; Line 3 and line 4 in the graphs (a to e) represents the *Mycobacterium* uncontaminated and contaminated intensity profile at 594.5 nm; Line 5 and line 6 in the graphs (a to e) represents the *Mycobacterium* uncontaminated and contaminated intensity profile at 543.5nm laser wavelength respectively.

Measurements of the volume scattering phase function were carried out at three different laser wavelengths 543.5 nm, 594.5 nm and 632.8 nm respectively. Scattering data files obtained for the *C. sinensis* dust particles *and M. smegmatis* were processed using the same analytical program to yield values of $\beta(\theta)$. It can be observed that the measured $\beta(\theta)$ are sharply peaked in the forward direction for both *C. sinensis* dust and *C. sinensis* dust contaminated with *M. smegamatis* , in case of all the three wavelengths as depicted by figures 4.53 - 4.58. A low frequency component can be seen in all the plots of $\beta(\theta)$ for *M. smegmatis* contaminated tea dust particles in all the graphs (Figures 4.56 - 4.58). This may be due to a narrow size distribution developing due to the uniformity in size of the *M. smegmatis* bacteria. The

random size of the uncontaminated tea dust possibly got dominated by the regularity in size of the bacteria.

It can also be observed that there is higher intensity of scattering from all contaminated dust particles compared to the uncontaminated ones. This may be due to an overall increase in the size of the contaminated particles compared to the uncontaminated ones. As mentioned earlier, the investigations were carried out by mixing tea dust in phosphate buffer solution. Although the mixture was thoroughly stirred for a considerable period of time to ensure that the non-uniform tea dust particles acquired a uniformly random orientation in the medium, it is observed from figures 4.59(a) to 4.59 (e), that there is variation in the scattering plots with change in the azimuthal angle, indicating that the particles are not only non-spherical, but some amount of non-uniformity in orientation of the particles is also present. As the sample is in PBS suspension, the elongated samples may have tried to acquire a vertical alignment with the heavier end pointing downwards. This non-uniform orientation may have become more pronounced with contamination of the bacteria that has an elongated shape and a larger mass compared to the dust particles. Comparison of the experimental results with theoretical result based on Mie-theory is also presented in the same plots (figures 4.53 - 4.58). Despite the consideration of a wide size distribution of equivalent spherical particles for Mie theory predictions, it was found that there was deviation of the theoretical curves from the experimental curves. This deviation becomes more pronounced for the *M. smegmatis* contaminated *C. sinensis* sample (figures 4.56 - 4.58). The reason may be attributed to complexity in the morphology of the particles in the volume element [232]. As such, there is an urgent need to modify existing theories to characterize complex biological structures better. The measured phase functions of both *Mycobacterium* contaminated and uncontaminated tea dust particles were normalized to 1 at $\theta = 10°$. Since the experiments were dominated by the *C. sinensis* particles where the bacteria was a minor

component, and the C. *sinensis* particles were completely irregular and fluffy, preliminary test experiments on their effect on polarization of the scattered light yielded completely unpredictable and random results. Hence, these experiments, where C. *sinensis* particles played the dominant role, polarization studies for measuring the degree of linear polarization were not continued.

4.8 Error Analysis

We have determined the instrumental error of the light scattering setup by taking numerous sets of measurement for each angle throughout the angular distribution for polystyrene spheres. The instrumental error was found to be ±0.109, and indicated by errors bars in each of the experimental plots in this chapter.

Again, we have calculated the absolute error from the experimental and the theoretical values using the formula given by equation 4.8.1 below

$$Absolute\ error = \frac{Estimated\ value - Theoretical\ value}{Theoretical\ value} \qquad \textbf{4.8.1}$$

The value of absolute error for each sample investigated by using the light scattering setup is given in table 4.8.

Table 4.8: Table of absolute error calculation for the measured volume scattering function $\beta(\theta)$ and degree of linear polarization $P(\theta)$

Name of the scattering particle	Volume scattering function $\beta(\theta)$			Degree of linear polarization $P(\theta)$		
	λ= 543.5 nm	λ= 594.5 nm	λ= 632.8 nm	λ= 543.5 nm	λ= 594.5 nm	λ= 632.8 nm
Polystyrene spheres	0.073	0.045	0.071	0.193	0.117	0.231
Cadmium sulphide (0.18 μm)	-	-	0.229	-	-	0.296
Cadmium sulphide (0.07μm)	-	-	0.451	-	-	0.529
Zinc selenide	0.066	0.082	0.049	0.193	0.151	0.258
Titanium dioxide	0.048	0.045	0.046	0.483	0.498	0.612
Zinc oxide	0.051	0.048	0.096	0.476	0.470	0.484
Staphylococcus aureus	0.064	0.055	0.043	0.282	0.125	0.452
Camellia sinensis	0.054	0.047	0.051	-	-	-
Camellia sinensis with *Mycobacterium smegmatis*	0.043	0.052	0.042	-	-	-

Chi-square fitting test [252]or goodness of fit test was also done for results obtained from each type of samples to justify the comparison between theoretical results and experimental results. The chi-square statistic [252]is defined by

$$chi^2 = \sum_{i=1}^{k} \frac{(O_i - E_i)^2}{E_i} \qquad \textbf{4.8.2}$$

for i= 1,2, 3, 4.....k

Here, O_i and E_i are the observed frequencies and expected values respectively. The more the actual occurrences depart from their expected values the larger the value of chi^2. Conversely, the closer the O_i's are to E_i's the smaller is the values of chi^2, becoming zero when the two sets of frequencies are identically equal. We have calculated values of chi^2 for each sample at all the three wavelengths, and it is tabulated in table 4.9.

The observed errors may be interpreted as the errors not only due to systematic error which were introduced in the measurement of $\beta(\theta)$ due to finite angular resolution, detector sensitivity , and measurement errors of light scattering setup (mentioned in chapter III), but also due to limitations of light scattering theories that were used in modelling the actual size, shape , dispersion of size and shape distributions of the scattering particles under investigation. The absolute error calculated for polystyrene spheres were found to be minimum for both $\beta(\theta)$ and $P(\theta)$ (table 4.8) , thus proving the efficiency and reliability of our light scattering setup. Moreover, the value of chi^2 test for all the type of particles investigated (table 4.9) also substantiated the versatility of our setup.

Table 4.9: Table of Chi square fitting calculation for the measured volume scattering function $\beta(\theta)$ and degree of linear polarization $P(\theta)$

Name of the scattering particle	chi^2 for $\beta(\theta)$			chi^2 for $P(\theta)$		
	λ= 543.5 nm	λ= 594.5 nm	λ= 632.8 nm	λ= 543.5 nm	λ= 594.5 nm	λ= 632.8 nm
Polystyrene spheres	0.046	0.031	0.051	1.154	1.080	1.61
Cadmium sulphide (0.18 μm)	-	-	0.486	-	-	7.892
Cadmium sulphide (0.07μm)	-	-	0.763	-	-	14.608
Zinc selenide	0. 132	0.127	0.112	4.058	6.734	5.831
Titanium dioxide	0.304	0.686	0.782	7.131	6.296	12.15
Zinc oxide	0.186	0.298	0.151	1.878	1.515	1.872
Staphylococcus aureus	0.433	0.931	0.894	1.788	2.912	2.894
Camellia sinensis	0.416	0.237	0.431	-	-	-
Camellia sinensis with *Mycobacterium smegmatis*	0.623	0.873	0.928	-	-	-

4.9 Comparison with reported work

The present light scattering setup proved to be versatile when compared to other such instruments used for light scattering investigations around the world [25-28, 32, 35, 38]. The setup is compact and energy efficient since it uses low power laser source, a digital data recording unit which consumes minimum power, a highly sensitive and low power consuming photomultiplier tube for carrying out measurements of volume scattering

function and degree of linear polarization. The parameters like size, shape, porosity etc. of same kind of particles may differ from one sample to another, thus the light scattering results may also vary accordingly. However, the samples like Titania, *Staphylococcus aureus* etc. analysed by other workers were found to be in correspondence with our results in terms of qualitative agreement. The trends of scattering pattern were similar to those reported by other workers for such samples. The design considerations discussed by Mishchenko, Hovenier and Travis [46], Volten et al. [232], for measurement of scattering matrices are also in agreement with the light scattering system reported here. The remarkable standpoints of our setup are

- Noble design considerations of our nephelometer.
- Flexibility of measurements of all scattering matrix elements along both polar and azimuthal angles.
- Minimum power consuming detectors.
- Compact size which is easily movable.
- Different sample holding systems to hold variety of scattering particles.
- Incorporation of error reduction techniques.
- Provision for measuring rapid changes in the medium under observation made possible by incorporation of fast electronic components.
- Amalgamation of light scattering theories and subsequent experimentation to yield light scattering data successfully.
- Original software for data analysis.
- Original data acquisition software to record and store the acquired data in user defined files.

In comparison to the work reported by others based on light scattering investigations of small particles by using light scattering instruments, our designed and fabricated setup stands out as relatively flexible, compact and far more economic system. In other words, the overall response of our setup is significantly fast, reliable and effective.

CHAPTER V

Simulation of Light scattering

5.0 General Introduction

This chapter contains details about the simulation technique used for light scattering analysis of small particulate system. Section 5.1 presents an overview of Monte Carlo simulation of light scattering. Section 5.2 presents summary of original contributions. Section 5.3 presents computational results and comparison with experimental results obtained from particles like CdS, *Staphylococcus aureus* and ZnSe. Finally, the conclusion of work is presented in section 5.4.

Computer simulation has developed from basic to more advanced discipline over past four decades. Before digital computer became easily available, complex dynamic systems could not be analyzed by means of available mathematical tools. For such systems, one was forced to accept intuitive solutions. But, nowadays computer simulation has become an important tool which enables one to mimic the behavior of real-life systems, however complex it may be. It is a powerful technique that involves modeling, computer- programming and statistics for solving a wide variety of problems. In other words, simulation is copying the behavior of a system or phenomenon under study. It is basically an experimental technique. Computer simulation of experiments provide better insight into the experiments done in laboratory, besides being relatively inexpensive, faster and easier method for performing an experiment on the computer. Moreover, for systems which involve thousands and tens of thousands of variables, the complications caused by uncertainty are also very large. Thus, for such problems simulation becomes an essential tool for many researchers. However, there are no underlying principles guiding the formulation of simulation models.

5.1 Monte Carlo Simulation of Light scattering

Simulation can be carried out for both continuous and discrete systems. "Continuous systems" are those in which the state changes smoothly or continuously with respect to time, and "Discrete systems" are those in which the state changes abruptly with time.

In this work, we have done simulation of light scattering by small particle system, which again is a discrete system in which each change in the state of the system is called an *event*. Simulation in the study of discrete dynamic systems is used exclusively for systems where at least one of the variables is given by a probability distribution function. These are also known as stochastic systems. In order to simulate such random variables, a source of randomness is required. And in simulation methods, this is achieved through a source of *uniformly distributed random numbers*. These numbers are samples from a uniformly distributed random variable between some specified intervals which has equal probability of occurrence. A random number generator and its proper use is the main step in any simulation technique involving stochastic system. A sequence of numbers can be generated in computer which has the property of being random. Such deterministically generated numbers which retain the property of randomness are called *pseudorandom numbers*. The generation of these numbers is based on some recurrence relation. By generation of pseudorandom numbers, one can obtain uniformly distributed random numbers x_i's between any interval (A, B), using the relation:

$$x_i = A + (B-A).\, u_i \qquad \textbf{5.1.1}$$

where u_i's are the previously generated uniform numbers in the interval 0 and 1. There are a number of simulation experiments that require random samples from non-uniform distributions. And, there are many techniques for converting uniform random numbers into samples from various distributions.

The two most commonly used methods are the *Inverse transformation method* and the *Rejection method.*

The concept of Monte Carlo technique [352, 359, 360] was first proposed in 1777 by Comte Buffon. The application of this technique to solve real problems began by S. Ulam and J. von Neumann at the Los Alamos Scientific Laboratory. Monte Carlo simulation is the computation in which random numbers are used to obtain solutions of problems which are inherently deterministic. The Monte Carlo method, as implied by its name ("throwing the dice"), depends on random sampling of variables from definite probability distributions.

In all application of Monte Carlo method, a stochastic model is constructed in which the expected value of a certain random variable or a combination of several variables is equivalent to the value of a physical quantity to be determined. This expected value is then estimated by the average of multiple independent samples representing the random variable introduced above. For such purpose, random numbers following the distribution of the variables to be estimated are used [352, 361].

Wilson and Adam were the first to carry out Monte Carlo simulations in the field of laser-tissue interaction [283]. Various approaches and several improvements, for different applications showed vast advancement in this area [279 - 290]. In recent years, there has been an increasing interest in simulation of light transport, especially for medical applications. Scmitt et al, Emile et al. and Demos and Alfano proposed the use of polarizad light for isolating ballistic photons from diffuse background and enhance the spatial resolution in optical tomographic methods [362 - 366].

Several Monte Carlo simulations have been developed to investigate the propagation of polarized light in dense media [280]. In most of them the differential cross section of the light scattered by a sphere is assumed to be invariant by rotation around the beam direction. For example, Wang and

Jacques have presented Monte Carlo model on light transport in multi layered tissues [283]. Again, Bartel and Hielscher developed a Monte Carlo algorithm that computes all two-dimensional elements of the diffuse backscattering Mueller matrix for highly scattering media [280]. Xu has presented an interesting Monte Carlo model based on tracing the multiply scattered electric field to simulate the propagation of polarized light in a turbid media [284].

Light transport algorithms generate realistic images by simulating the emission and scattering of light in an artificial environment. Applications include neutron transport and radiative heat transfer. The simulation can score multiple physical quantities simultaneously. However, the method is statistical in nature and relies on calculating large number of photons by the computer. The number of photons required for a simulation depends largely on the precision needed, and the spatial resolution desired. In this context, we must note a point that Monte Carlo simulations are rigorous and requires significant computation time to achieve precision and resolution. Nonetheless, it is a powerful tool due to its flexibility. The main challenge with these algorithms is the high complexity of the geometric models, scattering models and illumination models that are typically used.

5.2 An original Monte Carlo technique

In this thesis, we made an attempt to develop a Monte Carlo technique that models the scattering of light by size distributed small particles. Our contributions include a new simulation model rendering algorithm. Basically, it deals with calculation of S_{11} and S_{12} element of the Mueller matrix, and also accommodates volume scattering component [46]. In the simulation program, Mie-theory for spheres was implemented. The proposed technique is an effort towards calculating scattering and polarization phase functions produced by an ensemble of randomly oriented particles, mostly spherical in nature. Simulation was carried out in order to correlate with the experimental results obtained from such particles.

5.2.1 Sampling Random Variables

We have considered a random variable 'x', which is required for the Monte Carlo simulation of light scattering (photon propagation).This variable is the angle of deflection a scattered photon experiences as a consequence of scattering event. The probability distribution function $P(x)$ that defines the distribution of 'x' over the interval (a, b) is normalized such that:

$$\int_a^b P(x)dx = 1 \qquad \textbf{5.2.1}$$

By definition, every probability distribution function increases monotonically from 0 to 1 [352]. To simulate such system, we need to choose a value for 'x' repeatedly and randomly based on a pseudo-random number generator as done by Wang et al. [283]. The computer provides a random variable n, which is uniformly distributed over the interval (0, 1). The cumulative distribution function of this randomly distributed random variable is:

$$F_n(n) = \begin{cases} 0 \; if \; n \leq 0 \\ n \; if \; 0 < n < 1 \\ 1 \; if \; n > 1 \end{cases} \qquad \textbf{5.2.2}$$

In order to sample a generally non-uniformly distributed function $P(x)$, we assume there exists a non-decreasing function $x = f(n)$, which maps $n \in (0, 1)$ to $x \in (a, b)$ as shown in figure 5.1 . The variables x and n then have a one-to-one mapping. As a result, this leads to the following equality of probabilities given by:

$$P\{ f(0) < x \leq f(n_1)\} = P\{0 < n \leq n_1\} \qquad \textbf{5.2.3(a)}$$

or,

$$P\{a < x \leq x_1\} = P\{0 < n \leq n_1\} \qquad \textbf{5.2.3(b)}$$

Again, according to the definition of Cumulative distribution function, equation 5.2.3(b) can be written as:

$$F_x(x_1) = F_n(n_1) \qquad \textbf{5.2.4}$$

On expanding the Cumulative distribution function $F_x(x_1)$ in terms of the corresponding probability density function and using equation 5.3.2, we obtain the modified equation of the form:

$$\int_a^{x_1} P(x)dx = n_1 \quad for \; n_1 \in (0,1) \qquad \textbf{5.2.5}$$

In this chapter, equation 5.3.5 is used for sampling of variable. The significant point behind the selection of x using n is to equate the probability that n is in the interval $(0, n_1)$ with the probability that x is in the interval (a, x_1).

In figure 5.1, the shaded area depicting the integral of $P(x)$ over $(0, x_1)$ is equated with the shaded area depicting $P(n)$ over $(0, n_1)$. The total areas under the curves $P(x)$ and $P(n)$ must be equal to unity owing to the condition of probability density function. In simple words, it can be asserted that $F_x(x_1)$ is equated with $F_n(n_1)$. The transformation process is shown by arrows (figure 5.1).

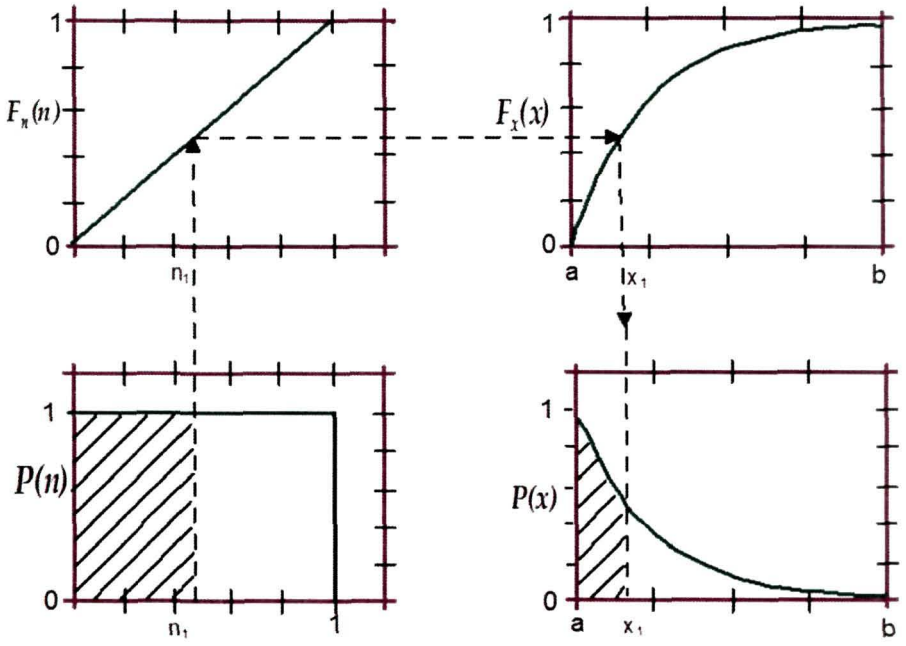

Figure 5.1: Sampling random variable

5.2.2 Programming method

The simulation program "*simscat.c*" is written in ANSI standard C and the usability has been tested in different computers and verified. A simulation runtime is an uninterrupted recording of a system's behaviour under a specified condition of controllable variables. And it is important to know for how long such simulation experiments involving randomness should be run. But, in our case the simulation is static where time plays no role. The runtime depends upon the selection of number of photons. Most simulation experiments are repeated a number of times to obtain a mean value. For example, let us consider N number of observations of an event (e_1, e_2, e_3, ..., e_N), we obtain mean as $\bar{e}$. The larger the value of N, closer is the value of $\bar{e}$ to the characteristics of a real event. In order to achieve accuracy of simulation results, *Variance reduction technique* is followed. This technique allows reduction of variance without limitless increment of the number of events N. We have used this technique to improve the efficiency of Monte Carlo simulation with many photons.

In this chapter, we have described the parameters used in the program and the algorithm of the technique. Some important points that were followed while writing the program are:

1. Adapted ANSI Standard C to make the program executable on different computers.
2. Restricted using any term similar to global variables.
3. The program checks all the parameters of simulation and stops on execution if it detects an error in the input data file.

At the end of simulation, it stores the output data file the name of which is initially specified by the input data file. This is how independent run is executed each time, and processed subsequently. Runtime is found to be approximately 3 seconds even when considering maximum number of photons.

5.2.3 Flowchart for Monte Carlo simulation

One main step followed in all the simulations of light scattering based on Monte Carlo method, is the sampling of scattering angles (θ, φ). In our study, we have considered only θ-dependent scattering function. The rejection technique is a common method that has been widely used in different simulation programs [284]. But, we have used the inverse transformation method for simulation. This method is based on random sampling of θ from probability distributions. A simple flowchart describing the simulation method is depicted by figure 5.2.

The box "C=0" initializes the photon count. $M(\theta)$ is the generated Mie plot using the developed C-program [300] with size, wavelength of source, refractive index of the particle as initial parameters. The box " $IN_0 = \int_{\theta=10}^{\theta=170} M(\theta)d\theta$" denotes the integration of the plot using composite *Trapezoidal rule* for θ ranging from 10° to 170° . Uniform random numbers were generated between 0 and 1, and we have forced these uniform random numbers into a non-uniform pattern governed by Mie theory, using it as a probability distribution function by using *Inverse transformation method* [369]. We move to the next box "$F(x) = \frac{1}{IN_0} \int_0^{\theta} M(\theta)d\theta$", where $F(x)$ is the cumulative distribution function. In this method, we assumed propagation of one single photon at a time, associated a θ to it, and stored the result. The decision box " Is $F(x) = n$? "determines whether there should be a further increment in the value of θ by a factor of 2, or to store the value of θ . The box "C= C+1" increases the photon count by 1 until it reaches the value of 100000, and displays the C versus θ result after binning. In other words, each time we perform our simulation, we check whether $F(x)$ is equal to the generated random number (n) or not. If it is found to be equal then we store the value of θ, which is the non-uniform random number conforming to Mie theory. If $F(x)$ is not found to be equal to n, then we increase the value of θ by 2 and repeat the previous step again. The simulation terminates after recording the scattered directions of 100000 photons.

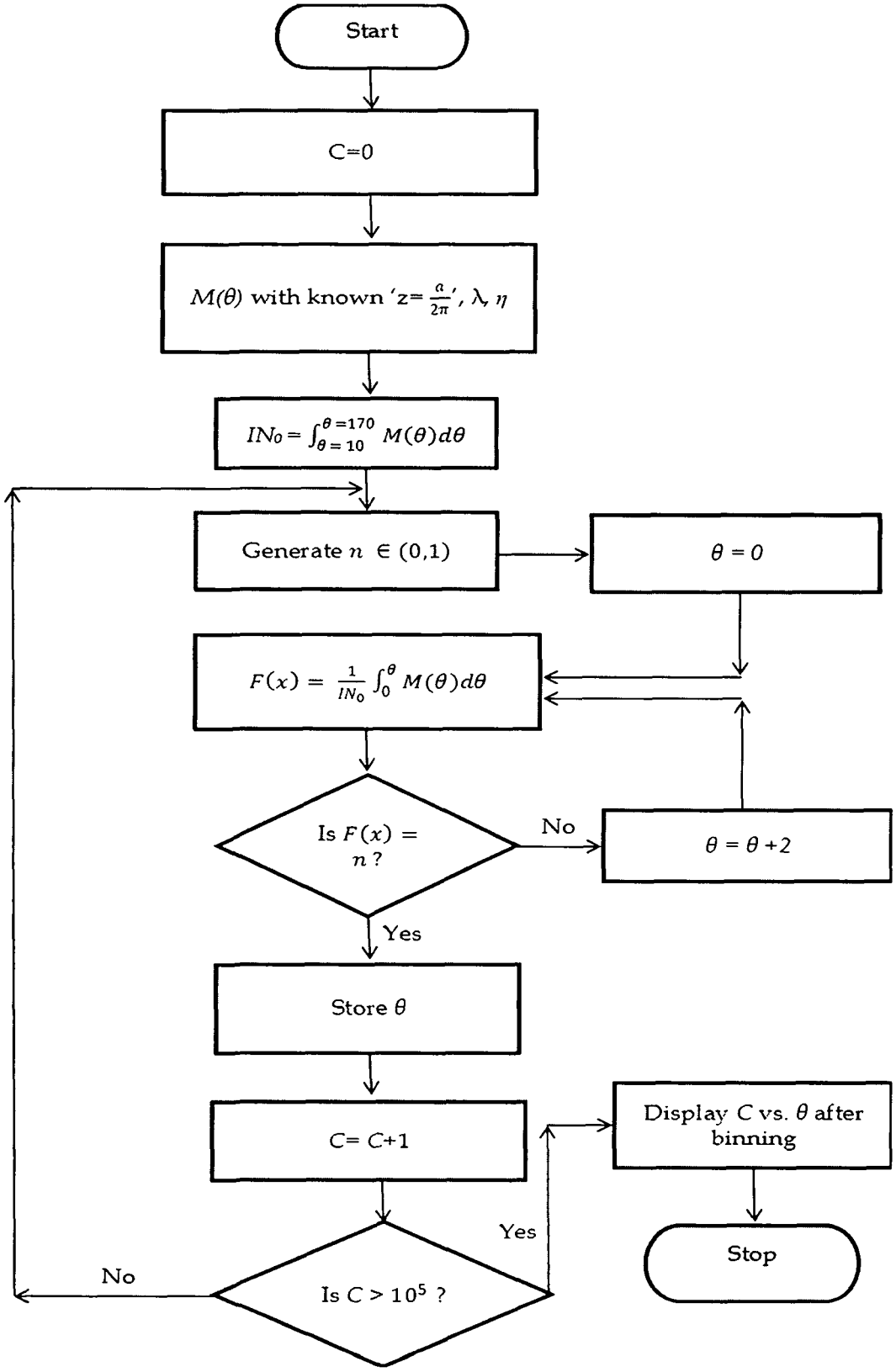

Figure 5.2: Flowchart of "*simscat.c*"

5.3 Computation Results and comparison with Experimental Results

It is worth mentioning here that we have incorporated a novel technique in order to increase the correspondence between the simulated and experimental results. The technique involves distribution of the photons in the simulation program between the particles according to their density as they were found to be governed by a Gaussian size distribution function [300]. The key idea was to have the maximum number of photons allotted to the central modal radius of size distribution and gradually decreasing the number of photons for the other radii around this central modal radius. The basis of adopting Gaussian distribution in our simulation program was based on morphology of the particles (CdS, ZnSe and *Staphylococcus aureus*) observed over a number of samples using image analysis techniques like Scanning electron microscopic image and Transmission electron microscopic image (images are shown in chapter IV).

5.3.1 Simulation of CdS

Monte Carlo simulation of light scattering using our program "*simscat.c*" was carried out for CdS particles having central modal radius of 0.18 μm, refractive index of 2.52 ± i0000 and wavelength of 632.8 nm. The range of radii of the particles incorporated in the program was chosen to be 0.17 μm to 0.19 μm. The S_{11} and S_{12} elements of the Mueller matrix was determined by following the simulation technique to yield the scattering and polarization phase functions of such size distributed, nearly spherical and randomly oriented particles.

The simulated profiles of the volume scattering function, $\beta(\theta)$ and degree of linear polarization, $P(\theta)$ as a function of scattering angle θ are shown in figure 5.3 and 5.4 respectively. From figure 5.3, it can be seen that the plot for simulated result for $\beta(\theta)$ shows good correspondence with both theoretical and experimental results for the forward scattering lobe extending

approximately to 110°. We find discrepancies between the results of simulation and experiments beyond this scattering angle. Again, the simulated results for $P(\theta)$ exhibits a similar shape of scattering profile when compared to experimental results as shown in figure 5.4. However, there is a margin of deviation which shows difference in maxima and minima. The variations may be attributed to the possibility of the experimental samples deviating from Gaussian distribution. Another aspect is that, although the sphericity of CdS particles is assumed to be perfect, there is also the probability of appearance of non-spherical particles within the sample. It must be noted that we have considered perfectly spherical particles in our simulation program. The deviations may also be attributed to the minor contribution of density fluctuations of the polyvinyl matrix in the experimental plot. This aspect is another contributing factor of the deviations between the simulated and the experimental plots. Overall, the signature of simulation shows a qualitative agreement with the experimental signature.

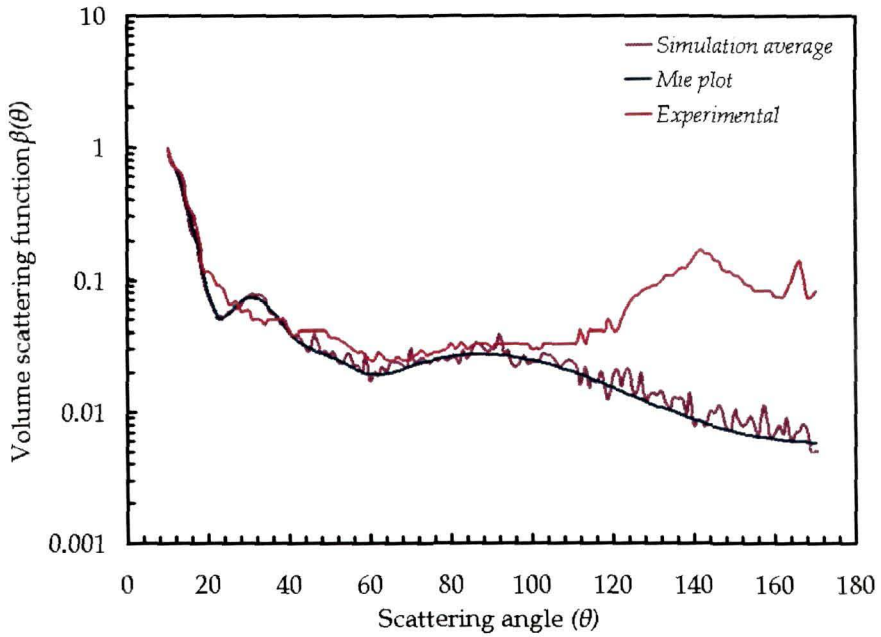

Figure 5.3: Comparative results for simulated, experimental and theoretical Volume scattering function $\beta(\theta)$ for CdS.

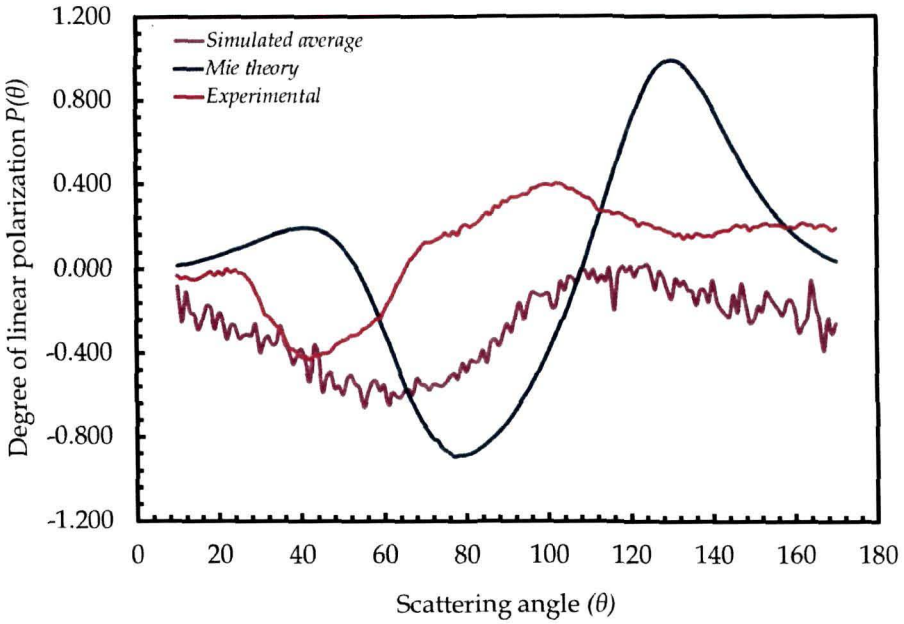

Figure 5.4: Comparative results for simulated, experimental and theoretical Degree of linear polarization $P(\theta)$ for CdS.

5.3.2 Simulation of *Staphylococcus aureus*

Simulation of light scattering was carried out usingour program *"simscat.c"* for *Staphylococcus aureus* bio-particles having central modal radius of 0.45 μm , refractive index of 1.05 ± i0000 and wavelength of 543.5 nm. The range of radii of the particles incorporated in the program was chosen to be 0.45 μm to 0.46 μm. We have calculated experimentally the S_{11} and S_{12} elements of the Mueller matrix in order to determine the scattering and polarization phase functions of such particles.

The simulated profiles of the volume scattering function, $\beta(\theta)$ and degree of linear polarization, $P(\theta)$ as a function of scattering angle θ are shown in figures 5.5 and 5.6 respectively. The scattering profiles of simulated and experimental results for $\beta(\theta)$ show overall similarity throughout the angular distribution. Both the profiles exhibit a forward scattering lobe with sharp scattering peak. However, it shows minor discrepancies when compared to the theoretical scattering profile, particularly at the forward

scattering region till 30° and in the region of 130° onwards. For $P(\theta)$, the scattering profile of *Staphylococcus aureus* exhibits a similar shape for both simulated and experimental plots, as seen from figure 5.6. Yet, there is difference in the values of maxima and minima. Again, for $P(\theta)$ the theoretical scattering profile exhibits some prominent oscillations. The oscillating behavior may be due to single size parameter of the particle which was being incorporated as input parameter to generate the theoretical plot. Moreover, we have considered perfectly spherical particles in our simulation program while generating the simulated plot. The reasons behind deviation of simulated result from experimental result for both $\beta(\theta)$ and $P(\theta)$ may also be attributed to the probability of appearance of non-sphericity in the bio-particles within the sample, due to factors like cell lysis or cell division. Again, there is a possibility of the experimental samples deviating from perfect Gaussian size distribution. Overall, for $\beta(\theta)$ and $P(\theta)$, the scattering profile for simulated result shows good agreement with the experimental result.

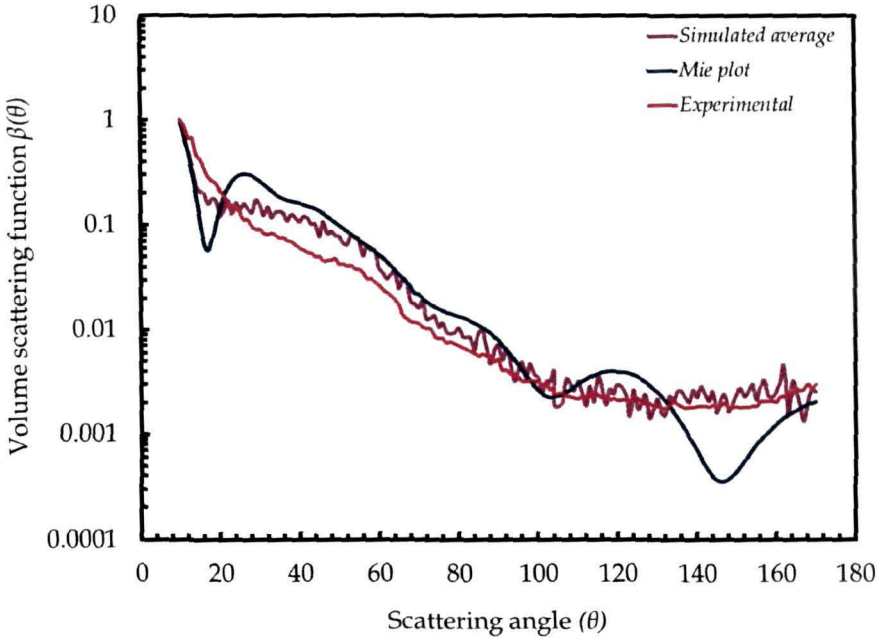

Figure 5.5: Comparative results for simulated, experimental and theoretical Volume scattering function $\beta(\theta)$ for *Staphylococcus aureus*.

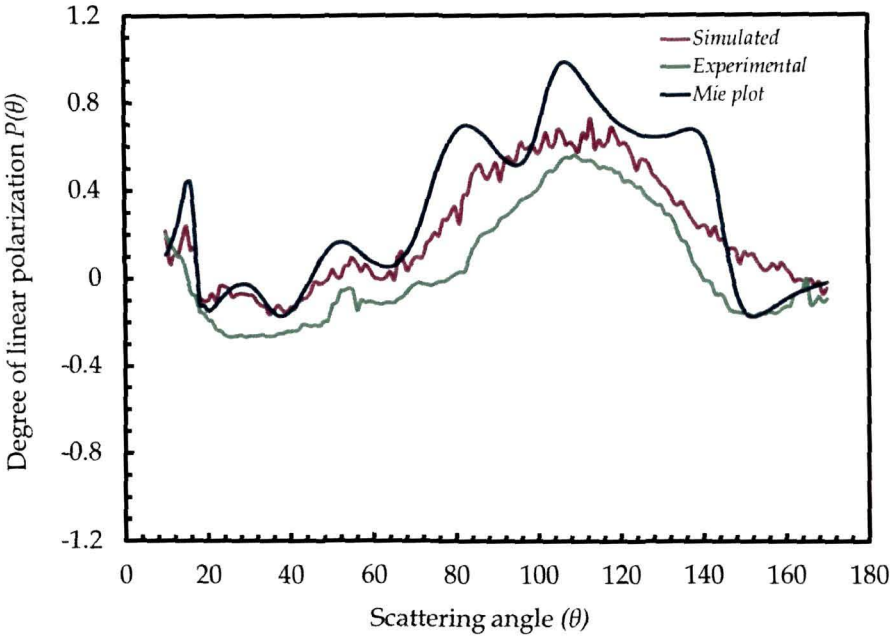

Figure 5.6: Comparative results for simulated, experimental and theoretical Degree of linear polarization $P(\theta)$ for *Staphylococcus aureus.*

5.3.3 Simulation of ZnSe

Monte Carlo simulation of light scattering was carried out for ZnSe particles having central modal radius of 0.120 μm, refractive index of 2.618 + i0000 and wavelength of 594.5 nm. The range of radii of the particles incorporated in the program was chosen to be 0.105 μm to 0.125 μm. The scattering and polarization phase functions, $\beta(\theta)$ and $P(\theta)$ of such particles were calculated by simulation.

The simulated profiles of the volume scattering function, $\beta(\theta)$ and degree of linear polarization, $P(\theta)$ as a function of scattering angle θ are shown in figure 5.7 and 5.8 respectively. The scattering profiles of simulated and experimental are found to be similar throughout the angular distribution. Both the simulated and experimental $\beta(\theta)$ shows a forward scattering lobe holding sharp scattering peak. Nevertheless, we find some discrepancy when compared to the theoretical scattering profile. The simulated $\beta(\theta)$ shows more deviation from the theoretical one when compared to the experimental one.

The scattering behavior of simulated and experimental results for $P(\theta)$ is exhibited by the scattering profile as seen from figure 5.8. There is difference in the values of maxima and minima for all the three profiles (figure 5.8). The overall trend of the scattering profiles of the simulated plot shows similarity with the experimental plot, however, the maxima is approximately around 60° (extending to 80°) for simulated plot, whereas the maxima is around 90° for experimental plot. For $P(\theta)$, there is more correspondence between these results at an angle of 90° and onwards. Again, the theoretical scattering profile for $P(\theta)$ shows marked deviation when compared to the simulated and experimental profiles. In order to find out the level of efficiency of the simulation technique, the particular case of light scattering from ZnSe nanoparticles using 594.5 nm laser line was selected.

Incorporation of condition of perfect sphericity of particles in our simulation program may be the reason of the discrepancies between the simulated and experimental result. The possibility of the experimental samples deviating from perfect Gaussian size distribution also cannot be ruled out. Moreover, agglomeration of some particles in the experimental sample may be a contributing factor for such deviations. And most importantly, the strong dependence of polarization on modal size parameter of the particles is another aspect of the deviations between the simulated and the experimental plots. Overall, for $\beta(\theta)$ and $P(\theta)$, the scattering profile of simulation agrees quite well with the experimental profile, however, for $P(\theta)$ incongruities are a bit more.

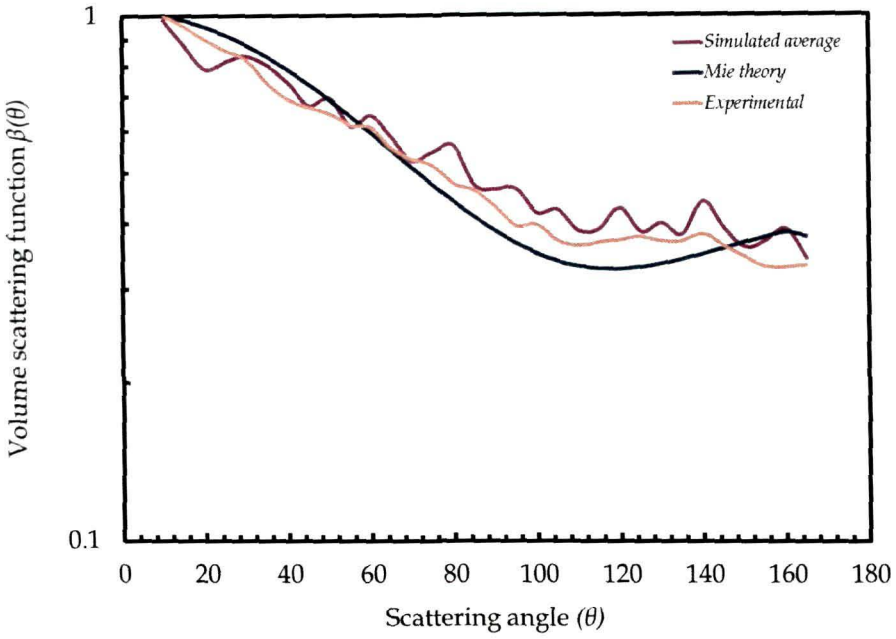

Figure 5.7: Comparative results for simulated, experimental and theoretical Volume scattering function $\beta(\theta)$ for ZnSe.

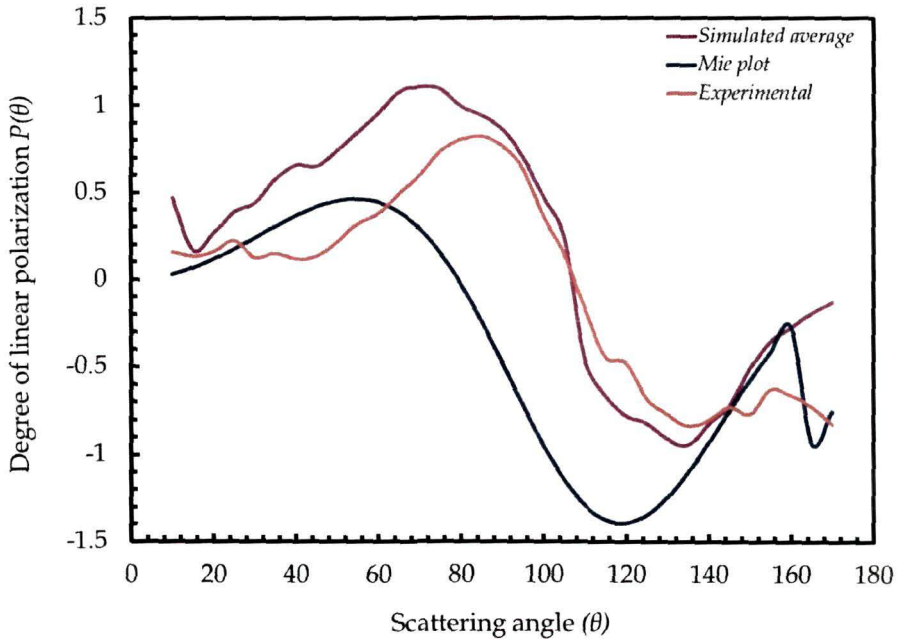

Figure 5.8: Comparative results for simulated, experimental and theoretical Degree of linear polarization $P(\theta)$ for ZnSe.

5.4 Conclusions

We have modelled a Monte-Carlo-based algorithm that models the single-scattering event according to Mie theory, for small particles. The simulations reproduced well, the two elements of Mueller matrix, S_{11} and S_{12} respectively. We used the program *"simscat.c"* for simulating light scattering of CdS, *Staphylococcus aureus*, and ZnSe to determine the volume scattering function $\beta(\theta)$ and degree of linear polarization $P(\theta)$ of these particles. Three different wavelengths were incorporated in the program for the three different samples, and simulation was carried out successfully. The results validate the usability of our program with different wavelength of incident light for the investigation of such bio-particles and particles ranging from nano-size to micron-size.

The program is fast and the user time is nearly 2-3 seconds to generate output data file. The experimental results correspond almost accurately with the simulated results for both $\beta(\theta)$ and $P(\theta)$. However, the results obtained from simulations shows some discrepancies when compared with the experiments, which becomes more noticeable for $P(\theta)$ in all the cases. More prominent fluctuations occur when simulating the other matrix elements. The agreement between experimental and simulated results reveals the possibility of modeling the complete Mueller matrix for different types of small particles.

Attempts may be made to tackle and minimize the deviations by incorporating other parameters in the simulation program, like inclusion of perfect size distribution of particles and minor contribution of shape distribution etc. We can also incorporate increased photon count ($> 10^5$) in order to realize a more realistic depiction of simulated result. Furthermore, an effort can be made to improve the program for systematic studies on non-spherical particles using T-matrix as the theoretical background.

CHAPTER VI

Conclusions and Future Prospects

An original light scattering setup was designed and fabricated in an attempt to incorporate a higher level of versatility and accuracy in comparison to such setups developed by earlier workers. Test measurements with polystyrene sphere samples and subsequently comparing the results with Mie calculations validated that the setup is quite accurate for light scattering measurements. The setup was successfully used for investigation of several types of particulate matter. The results were obtained after systematic and careful experimentation along with theoretical analysis, supported by computer simulation.

Following are the main conclusions drawn from the present work:

1. Experiments with semiconductor nanoparticles like Cadmium sulphide (CdS) and Zinc selenide (ZnSe) showed characteristic properties of such particles. Synthesis of the scattering samples via simple route in the laboratory ensured homogeneity of the particles under investigation. Moreover, the route provides valuable information about attaining desirable size of particles by changing the molar concentration, although size distribution was also observable. A significant finding of a novel route for synthesis of ZnSe particles is also reported here. The scattering results also revealed some valuable information, particularly for CdS nanoparticles which were in the transitional domain of Rayleigh and Mie scattering regime. The observation calls for a modification in the existing theories and also builds up the necessity of developing new theories applicable for analysing particles in the intermediate size domain. The experiments on nanoparticles and sub-micron particles have a direct importance in

understanding interaction of light with such low-dimensional structures.

2. Light scattering measurements of metal oxides like TiO_2 (Titania) and Zinc oxide (ZnO) were made effectively. Such metal oxides have wide applications in the area of optoelectronics, astrophysical issues, biological applications etc. [34, 190, 198, 199, 214, 224,189]. Scattering measurements portrayed the characteristic scattering properties of TiO_2 and ZnO. The results may prove to be very useful if comparative analyses of such particles are made, when used as anti-bacterial agents. Moreover, the measurements may expose dynamic information when multiple samples of Titania (differing in parameters like size, shape, porosity, density etc.), are examined with similar experimental technique. Conclusions drawn from such investigations and observations are important in regard of the fact that TiO_2 particles are possible nucleation sites in oxygen rich circumstellar shells.
3. Light scattering results of one type of strain of bacteria, *Staphylococcus aureus* MTCC 737 was studied. Light scattering technique being an indestructible tool proved to be a successful means in providing scattering information of such strain precisely. Furthermore, it substantiated the key role of the technique for *in-situ* monitoring of such particles when alterations in the morphology of particles become effective due to external factors. Use of Mie calculations during comparative analysis produced reasonable approximations of the measured results, and therefore shows the possibility to analyse other bacterial strains.
4. We found interesting results while doing experimentation on *Camellia sinensis* dust particles and *Mycobacterium smegmatis* bio-particles. The light scattering measurements made on *C. sinensis* dust particles (both contaminated and uncontaminated by *M. smegmatis*) revealed a remarkable finding that the dust particles may be a potent carrier of

life threatening bacteria, *Mycobacterium tuberculosis*. Light scattering proved to be an important diagnostic tool to identify bacterial pathogens [253, 369]. The scattering measurements also showed an interesting result of self-alignment of particles in suspension. Although the particles were non-spherical and randomly--oriented, they were found to be dependent on azimuthal angle. This fact provided vital information about such organic particles sometimes attaining self-alignment due to several factors [45, 46]. Thus, it provides a new outlook that we cannot rule out the azimuthal dependency of randomly-oriented particles in suspension. This information suggests the need of making extensive measurements of such particles one step forward, in order to obtain the actual scattering information. Therefore, our work may provide novel clues in developing new models of light scattering from complex forms.

5. A Monte Carlo code ('*simscat.c*') for simulating light scattering from small particles was developed and successfully implemented in simulating the scattering behaviour of CdS, ZnSe, and *S. aureus* particles. The simulated results were found to be in correspondence with the experimental results. Two significant elements of Mueller matrix, S_{11} and S_{12} were reproduced by our simulation technique considerably well. Thus, we could yield simulated volume scattering function, $\beta(\theta)$ and degree of linear polarization, $P(\theta)$ of the above mentioned particles. And, in general it was observed that the simulation plots corresponded with the experimental plots better than the theoretical plots.

Future prospects of work:

1. The limitations of investigation with only He-Ne lasers, operating at wavelengths of 543.5 nm, 594.5 nm and 632.5 nm may be overcome by using other laser sources like organic dye laser having tunable wavelength, Nd:YAG laser , CO_2 laser, Ruby laser, Argon laser operating at different wavelengths like 1.06 μm 0.6943 μm, 0.488 μm, 0.514 μm respectively [227, 228].The use of different incident wavelengths will be fruitful particularly for studying atmospheric particles, astrophysical particles and bio-particles which are mostly exposed to sunlight.
2. Our investigations can be broadened further by modifying our setup with replacement of existing photodetectors so that it may be used to retrieve information of particles even in the Rayleigh and Raman scattering domain.
3. More precise information about the scattering and extinction coefficients of small particulate matter can be obtained by transforming our setup (functional at angular scale of 10° - 170°). This can be done by changing the polar angular distribution from 10° - 170° to a lower limit of < 3° (very small angles) and upper limit of > 177° (near backscattering angles). This can be made practically effective by taking into account the design considerations of a Point visibility meter in the existing light scattering setup.
4. The limitations of generating theoretical results for particles having complex morphologies, and also requiring numerous input parameters, may be overcome by using more powerful computers with larger memories and multiprocessors in parallel for data recording and processing unit of the light scattering setup.
5. The use of Electro-optic modulator (EOM) for controlling the polarization state of the beam of incident light can also be incorporated into the existing setup. Measurements of all the

scattering matrix elements to get complete information of the scattering particles (like size and shape characteristics) can be made possible by incorporating polarizers and analyzers at both the source end and detector end of our light scattering setup.

6. The investigation results with our light scattering setup may be used for analysis of unknown particulate matter using Light Detection and Ranging (LIDAR) systems.
7. A nebulizer can be used as a source of generating floating particles, so as to enable measurements on other important atmospheric particles, and yield realistic profiles.
8. Since the present setup has provision for light scattering measurements along both polar and azimuthal angles, it can be used for studying axis-symmetric and aligned particles of different origin.
9. The setup can be used to make quantitative measurements on particles of different shapes like star-shaped, chebyshev, oblate-spheroids etc.
10. The simulation results revealed successful interpretation of volume scattering function and degree of linear polarization. This leads towards the possibility of simulating the other scattering elements of the Mueller matrix by modifying the present Monte Carlo code ('*simscat.c*') to achieve a complete simulated result.
11. Furthermore, the code can be modified to meet the requirement of simulating non-spherical particles too.
12. Some other efficient light scattering theories like DDA, T-matrix method, SVM etc. can be used instead of Mie theory by making necessary modifications in the present simulation software, to broaden its applicability.

Thus, with the rapid development of lasers, high quality instrumentation, efficient software, faster and more powerful computers, the field of light scattering studies has a very bright future with probable applications in almost all the frontier areas of science and technology.

REFERENCES

1. Ahmed, G. A., Mazumdar, G. K. D. and Choudhury, A. Investigations by a designed and fabricated laser based Air Quality monitoring system, *J. Inst. Soc. of India*, **26** (3) , 734-738, 1996.
2. Kuik, F., Stammes, P., and Hovenier, J.W. Experimental determination of scattering matrices of water droplets and quartz particles, *Appl. Opt.*, **30**(33), 4872 - 4881, 1991.
3. Stammes, P., de Haan, J. F. and Hovenier, J. W. The polarized internal radiation field of planetary atmosphere, *Astron. Astrophys.*, **225**, 239-259, 1989.
4. Volten, H., et al. Laboratory Measurements and T-Matrix Calculations of the Scattering Matrix of Rutile Particles in Water, *Appl. Opt.*, **38**(24), 5232-5240, 1999.
5. Xu, Y.I., and Gustafson, B. Å. S. Experimental and theoretical results of light scattering by aggregates of spheres, *Appl. Opt.*, **36**,8026 - 8030, 1997.
6. Kolokolova, L., et al. Properties of cometary dust from color and polarization, *Icarus*, **126**, 351-361, 1997.
7. Mishchenko, M. I. and Hovenier, J. W. Depolarization of light backscattered by randomly oriented nonspherical particles, *Opt. Lett.*, **20**, 1356-1358, 1995.
8. Sharma, S. and Somerford, D. J. *Light scattering by optically soft particles: Theory and applications*, Praxis Publishing, Chichester, UK, 2006.
9. Sassen, K., Zhao, H. and and Yu, B. -K., et al. Backscatter laser depolarization studies of simulated stratospheric aerosols: Crystallized sulphuric acid droplets, *Appl. Opt.*, **28**, 3024- 3029, 1989.
10. Hovenier, J. W. and van der Mee, C. V. M. Testing scattering matrices: A compendium of recipes, *J. Quant. Spectrosc. Radiat. Transfer*, 55, 649-661, 1996.
11. Waterman, T.H. Polarization patterns in submarine illumination, *Science*, **120**, 927- 932, 1954.

12. Waterman, T. H. Polarization of marine light fields and animal orientation, *Proc. SPIE*, **925**, 431- 437, 1988.
13. Quintby- Hunt, M. S. and Hunt, A. J. Effects of structure on scattering from marine organisms: Rayleigh- Debye and Mie predictions, *Proc. SPIE*, **925**, 288-295, 1988.
14. Takano, Y. and Liou, K. N. Solar radiative transfer in cirrus clouds. III. Light scattering by irregular ice crystals, *J. Atmos. Sci*, 52, 818-837, 1995.
15. Xu, Yu-lin. Scattering Mueller matrix of an ensemble of variously shaped small particles, *J. Opt. Soc.Am. A*, **20**(11), 2093-2105, 2003.
16. Ulanowski, Z. Ice analog halos, *Appl. Opt.*, **44**(27), 5754-5758, 2005.
17. Muinonen, K., Lumme, K., Peltoniemi, J. and Irvine, W. M. Light scattering by randomly oriented crystals, *Appl. Opt.*, **28**, 3051-3060, 1989.
18. Muinonen, K. Introducing the Gaussian shape hypothesis for asteroids and comets. *Astron. Astrophys.*, **332**, 1087- 1098, 1998.
19. Orendorff, C. J., et al. Light scattering from gold nanorods: tracking material deformation, *Nanotechnology*, **16**, 2601-2605, 2005.
20. Chu, B. and Liu, T. Characterization of nanoparticles by scattering techniques, *J. Nanoparticle Research*, **2**, 29-41, 2000.
21. Gonçalves M. R. and Marti, O. Experimental observation of the scattering of light by planar metallic nanoparticles, *New J. of Physics*, **5**, 160.1-160.14, 2003.
22. Schmitt, J. M. and Kumar, G. Turbulent nature of refractive-index variations in biological tissue, *Opt. Lett.*, **21**, 1310- 1312, 1996.
23. Schmitz, K. S. *An introduction to dynamic light scattering by macromolecules*, Academic press, San Diego. pp:32, 1990.
24. Ulanowski, Z, Hesse, E., Kaye, P.H., Baran, A.J. Light scattering by complex ice-analogue crystals, *J. Quant. Spectrosc. Radiat. Transfer*, **100**(1-3): 382-92, 2006.
25. Pritchard, B. S. and Elliott, W. G. Two instruments for atmospheric optics measurements, *J. Opt. Soc. Am.*, **50** (3), 191-202, 1960.

26. Barkey, B. and Liou, K. N. Polar nephelometer for light-scattering measurements of ice crystals, *Opt. Lett.*, **26**(4), 232- 234, 2001.
27. Kaye, P. H. Spatial light-scattering analysis as a means of characterizing and classifying non spherical particles, *Meas. Sci. Technol.*, **9**, 141-149, 1998.
28. Volten, H., et al. WWW scattering matrix database for small mineral particles at 441.6 and 632.8 nm, *J. Quant. Spectrosc. Radiat. Transfer*, **90**, 191-206, 2005.
29. Roy, S., Gogoi, A. and Ahmed, G.A. Size Dependent Optical Characterization of CdS semiconductor particles embedded in dielectric polymer matrix, *Indian J. Phys.*, **84** (10), 1405-1411, 2010.
30. Daugeron, D., et al. Laboratory polarization nephelometer for measurements of optical properties of aerosols, *Meas. Sci. Technol.*, **18**, 632-638, 2007.
31. Hadamcik. E., et al. Laboratory light scattering measurements on 'natural' particles with the PROGRA2 experiment: an overview. *J. Quant. Spectrosc. Radiat. Transfer*, **79-80**, 679-693, 2003.
32. Muñoz, O., et al. Experimental determination of scattering matrices of dust particles at visible wavelengths: The IAA light scattering apparatus, *J. Quant. Spectrosc. Radiat. Transfer* , **111**, 187-196, 2010.
33. Hovenier, J. W. Measuring scattering matrices of small particles at optical wavelengths. In: *Light scattering by nonspherical particles*, Mishchenko, M. I., Hovenier, J. W. and Travis, L. D. Academic, San Diego, CA, 355-365, 2000.
34. Bickel, W. S. and Stafford, M. E. Polarized scattered light as a probe for structure and change in bioparticles. In Ultrasensitive biochemical diagnostics, **2680** (4-15), 1st edn. SPIE, San Jose, CA, 1996.
35. Quinby-Hunt M. S., et al . Polarized-light scattering studies of marine *chlorella. Limnol. Oceanogr.*, **34**(8),1587-1600, 1989.
36. Gordon, H. R. Light scattering and absorption by randomly-oriented cylinders: dependence on aspect ratio for refractive indices applicable for marine particles, *Opt. Express*, **19**(5) / 4673-4691, 2011.

37. Ulanowski, Z., et al. Scattering of light from atmospheric ice analogues. *J. Quant. Spectrosc. Radiat. Transfer*, **79-80**, 1091-1102, 2003.

38. Das, D., et al. Investigations on atmospheric humidity profile at varying oxygen levels with a laser based monitoring system, *Asian J. Phys.*, **10**(3), 323-330, 2001.

39. Kokhanovsky, A. A. (Editor) *Light Scattering Reviews 2 Remote sensing and Inverse Problems*, Praxis Publishing Ltd, Chichester, UK, 2007.

40. Kokhanovsky, A. A. (Editor) *Light Scattering Reviews 3 Light Scattering and Reflection*, Praxis Publishing Ltd, Chichester, UK, 2008.

41. Hadamick, E., et al. Light scattering by fluffy particles with the PROGRA2 experiment: Mixtures of materials, *J. Quant. Spectrosc. Radiat. Transfer*, **100**, 143-156, 2006.

42. Gupta, R., et al. Scattering properties and Composition of Cometary Dust, *Astrophys. Space Sci.*, **301**, 21-31, 2006.

43. Hahn, D. W. *Light scattering theory*, Academic press, New York, 1-13, 2009.

44. Mishchenko, M. I. Multiple scattering by particles embedded in an absorbing medium. 2. Radiative transfer equation, *J. Quant. Spectrosc. Radiat. Transfer*, **109**, 2386- 2390, 2008.

45. Bohren, C. F. and Huffman, D. R. *Absorption and scattering of light by small particles* , John Wiley & Sons Inc, New York, 1983.

46. Mishchenko, M. I., Hovenier, J. W. and Travis, L. D. *Light scattering by nonspherical particles: Theory, Measurements, and Applications* , San Diego, Academic Press, California, 2000.

47. Mishchenko, M. I., Hovenier, Travis, L. D. and Lacis, A. A. *Scattering, Absorption, and Emission of Light by Small Particles*, Electronic Edition, Goddard Institute for Space Studies, New York, 2004, url: http://www.giss.nasa.gov/~crmim/ books.html.

48. van de Hulst, H. C. *Light scattering by small particles*, Dover Publications, New York, 1981.

49. Kokhanovsky, A. A. (Editor) *Light Scattering Reviews Single and Multiple Light Scattering*, Praxis Publishing Ltd, Chichester, UK, 2006.

50. Lecler, S. *Light scattering by sub-micrometric particles*, PhD thesis, Louis Pasteur University - Strasbourg I, 2005.
51. Mishchenko, M. I. Light scattering by randomly oriented axially symmetric particles, *J. Opt. Soc. Am. A*, **8**, 871-882, 1991.
52. Mishchenko, M. I. Extinction and polarization of transmitted light by partially aligned nonspherical grains, *Astrophys. J.*, **367**, 561-574, 1991.
53. Mishchenko, M. I. and Travis, L. D. Light scattering by polydisperse, rotationally symmetric nonspherical particles: Linear polarization, *J. Quant. Spectrosc. Radiat. Transfer*, **51**, 759- 778, 1994.
54. Xu, Yu-lin. Scattering Mueller matrix of an ensemble of variously shaped small particles, *J. Opt. Soc. Am. A*, **20**(11), 2093-2105, 2003.
55. Min, M., Hovenier, J. W. and Koter, A. de. Shape effects in scattering and absorption by randomly oriented particles small compared to the wavelength, *Astron. & Astrophys.*, 404, 35- 46, 2003.
56. Huffman, P. J. and Thursby, W. R. Light scattering by ice crystals, *J. Atmos. Sci.*, 26, 1073-1077, 1969.
57. Huffman, P. Polarization of light scattered by ice crystals, *J. Atmos. Sci.*, 27, 1027-1028, 1970.
58. Pollack, J. B. and Cuzzi, J. N. Scattering by nonspherical particles of size comparable to the wavelength: a new semi-empirical theory and its application to tropospheric aerosols, *J. Atmos. Sci.*, **37**, 868-881, 1980.
59. Cai, Q. and Liou, K. N. Polarized light scattering by hexagonal ice crystals: theory, *Appl. Opt.*, **21**, 3569-3580, 1982.
60. Greenler, R. *Rainbows, Halos, and Glories*, Cambridge Univ. Press, New York, 1990.
61. Martin, P. G. *Cosmic Dust*, Oxford Univ. Press, Oxford, 1978.
62. Sassen, K., et al. Effects of ice crystal structure on halo formation: Cirrus cloud experimental and ray tracing modelling studies, *Appl. Opt.*, **33**, 4590-
63. 4601, 1994.Sassen K. Optical backscattering from near-spherical water, ice, and mixed phase drops, *Appl. Opt.*, **16**, 1332-1341, 1977.

64. Murayama, T., et al. application of lidar depolarization measurement in the atmospheric boundary layer: Effects of dust and sea-salt particles, *J. Geophys. Research*, **104** (D 24), 31,781- 31,792, 1999.

65. Könen, G. and Tinbergen, J. Polarization structures in parhelic circles and in 120° parhelia. *Appl. Opt.*, **37**, 1457- 1464, 1998.

66. Kaye, P. H. Spatial light-scattering analysis as a means of characterizing and classifying non-spherical particles, *Meas. Sci. Technol.*, **9**, 141- 149, 1998.

67. Loiko, V. A. and Molochko, V. I. Influence of the director field structure on extinction and scattering by a Nematic Liquid-crystal Droplet, *Appl. Opt.*, **38**, 13 2857- 2861, 1999.

68. Dick, V. P., Loiko, V. A. and Ivanov, A. P. Light transmission by a monolayer of particles: comparison of experimental data with calculation as a single-scattering approximation, *Appl. Opt.*, **36**, 24, 4235-4240, 1997.

69. Vilaplanaa, R., Moreno, F., Molina, A. Study of the sensitivity of size-averaged scattering matrix elements of non-spherical particles to changes in shape, porosity and refractive index, *J. Quant. Spectros. Radiat. Transfer*, **100**, 277-287, 2006.

70. Vilaplanaa, R., Moreno, F. and Molina, A. Computations of the single scattering properties of an ensemble of compact and inhomogeneous rectangular prisms: implications for cometary dust, *J. Quant. Spectros. Radiat. Transfer*, **88**, 219–231, 2004.

71. Kahnert, M., Nousiainen, T. and Mauno, P. On the impact of non-sphericity and small-scale surface roughness on the optical properties of hematite aerosols, *J. Quant. Spectros. Radiat. Transfer*, **112**, 1815- 1824, 2011.

72. Muinonen, K. Light scattering by Gaussian random particles: Rayleigh and Rayleigh-Gans approximation, *J. Quant. Spectros. Radiat. Transfer*, **55**, 603-613, 1996.

73. Hecht, E. *Optics*, 4th Edition, Pearson Education, India, 2003.

74. Born, M. and Wolf, E. *Principles of Optics*, 7th Expanded Edition, Cambridge University Press, Cambridge, 1999.

75. Hazarika, F. B., Rai, S. N. and Baruah, G. D. An analysis of lasing without inversion in a three level system in terms of vector representation, *Optik - International Journal for Light and Electron Optics*, **122** (2), 95-98, 2009.
76. Chylek, P. and Klett, J. D. Extinction cross sections of nonspherical particles in the anomalous diffraction approximation, *J. Opt. Soc. Am. A*, **8**(2), 274-281, 1991.
77. Farone, W. A. and Robinson, M. J. The range of validity of the anomalous diffraction approximation to electromagnetic scattering by sphere. *Appl. Opt.*, **7**(4), 643- 646, 1968.
78. Mishchenko, M. I. Gustav Mie and the fundamental concept of electromagnetic scattering by particles: A perspective, *J. Quant. Spectrosc. Radiat. Transfer*, **110**, 1210- 1222, 2009.
79. Mie, G. Beiträge zur Optik trüber Medien, speziell kolloidaler Metallösungen, *Annalen der Physik*, **25**(3), 377- 445, 1908.
80. Mie, G. *Contributions on the optics of turbid media, particularl of colloidal metal solutions*, Translation: Sandia Laboratories, Albuquerque, New Mexico, SAND 78- 6018. National Translation Center, Chicago, ILL, Translation 79-21946, 1978.
81. Mie, G. *Contributions to the optics of turbid media, particularly of colloidal metal solutions*, Royal Aircraft Establishment- Lit- Trans, 1976.
82. Kerker, M. *The Scattering of Light and Other Electromagnetic Radiation*, Academic Press, San Diego, 1969.
83. Kerker, M. Founding fathers of light scattering and surface-enhanced Raman scattering, *Appl. Opt.*, **30**, 4699- 4705, 1991.
84. Laven, P. Simulation of rainbows, coronas and glories using Mie theory and the Debye series, *J. Quant. Spectroc. Radiat. Transfer*, **89**, 257-269, 2004.
85. Min, M., et al. Shape effects in scattering and absorption by randomly oriented particles small compared to the wavelength, *Astron. Astrophys.*, **404**, 35-46, 2003.

86. Fratalocchi, A., et al. Three-dimensional ab initio investigation of light-matter interaction in Mie lasers, *Phys. Rev. A: At. Mol. Opt. Phys.*, **78**, 013806, 2008.

87. Wriedt, T. Mie theory 1908 on the mobile phone, *J. Quant. Spectrosc. Radiat. Transfer*, **109**, 1543-1548, 2008.

88. Ren, K. F., et al. Scattering of a Gaussian beam by an infinite cylinder in the framework of generalized Lorenz-Mie theory: formulation and numerical results, *J. Opt. Soc. Am. A*, **14** (11), 3014-3025, 1997.

89. Laven, P. Simulation of rainbows, coronas, and glories by use of Mie theory, *Appl. Opt.*, **42** (3). 436-444, 2003.

90. Graaff, R., et al. Reduced light-scattering properties for mixtures of spherical particles: a simple approximation derived from Mie calculations, *Appl. Opt.*, **31** (10), 1370-1376, 1992.

91. Shah, G. A. Numerical methods for Mie theory of scattering by a sphere, *Kodalkanal Obs. Bull. Ser. A*, **2**, 42-63, 1977.

92. Gouesbet, G. T-matrix formulation and generalized Lorentz-Mie theories in spherical coordinates, *Opt. Commun.*, **283**, 517-521, 2010.

93. Ross, W.D. Computation of Bessel Functions in Light Scattering Studies, *Appl. Opt.*, **11** (9), 1919-1923, 1972.

94. Peňa, O. and Pal, U. Scattering of electromagnetic radiation by a multilayered sphere, *Comput. Phys. Commun.*, **180**, 2348-2354, 2009.

95. Wolf S. and Voshchinnikov, N. V. Mie scattering by ensembles of particles with very large size parameters, *Comput. Phys. Commun.*, **162**, 113-123, 2004.

96. Wiscombe, W. J. Improved Mie scattering algorithms, *Appl. Opt.*, **19** (9), 1505-1509, 1980.

97. Roy, S. and Ahmed, G. A. Computation of Mueller scattering matrices of spherical particles with a Gamma size distribution, *J. Opt.*, **39**(2), 76-81, 2010.

98. Deirmendjien, D. *Electromagnetic scattering on spherical polydispersions*, Elsevier, New York, 1969.

99. Yang, P. and Liou, K. N. Light scattering by hexagonal ice crystals: comparison of finite-difference time domain and geometric optics models, J. Opt. Soc. Am. A, 12(1), 162-176, 1995.

100. Liou, K. N. and Hansen, J. E. Intensity and polarization for single scattering by polydisperse spheres: a comparison of ray optics and Mie theory, *J. Atmos. Sci.*, **28**, 995-1004, 1971.

101. Macke, A., et al. Scattering of light by large nonspherical particles: ray-tracing approximation versus T-matrix method, *Opt. Lett.*, **20**(19), 1934-1936, 1995.

102. Ravey, J. C. and Mazeron, P. Light scattering in the physical optics approximation; application to large spheroids, *J. Optics (Paris)*, **13**(5), 273-282, 1982.

103. Zhang, Z., et al. Geometrical-optics solution to light scattering by droxtal ice crystals, *Appl. Opt.*, **43** (12), 2490-2499, 2004.

104. Macke, A. Scattering of light by polyhedral ice crystals. *Appl. Opt.*, **32**, 2780- 2788.

105. Macke, A., et al. Scattering of light by large nonspherical particles: Ray tracing approximation versus T-matrix method. *Opt. Lett.*, **20**, 1934- 1936, 1995.

106. Asano, S. and Yamamato, G.Light scattering by a spheroidal particle, *Appl. Opt.*, **14**, 29- 49, 1975.

107. Oguchi, T. Scattering properties of oblate raindrops and cross polarization of radio waves due to rain: Calculations at 19.3 and 34.8 GHz, *J. Radio Res. Lab. Jpn.*, **20**, 79- 118, 1973.

108. Voshchinnikov, N. V. and Farafonov, V. G. Optical properties of spheroidal particles, *Astrophys. Sapce. Sci.*, **204**, 19- 86, 1993.

109. Aden, A. L. and Kerker, M. Scattering of electromagnetic waves from two concentric spheres, *J. Appl. Phys.*, **22**, 1242-1246, 1951.

110. Bhandari, R. Scattering coefficients for a multilayered sphere: analytic expressions and algorithms, *Appl. Opt.*, **24**(13), 1960- 1967, 1985.

111. Bohren, C. F. Scattering of Electromagnetic Waves by an Optically Active Cylinder, *J. Colloid Interface Sci.*, **66**(1), 105-109, 1978.

112. Farafonov, V. G., et al. Light scattering by a core-mantle spheroidal particle, *Appl. Opt.*, **35**(27), 5412-5426 (1996).

113. Voshchinnikov, N. V. Electromagnetic scattering by homogeneous and coated spheroids: Calculations using the separation of variables method, *J. Quant. Spetrosc. Radiat. Transfer.*, **55**(5), 627-636, 1996.

114. Rother, T. Generalization of the separation of variables method for non-spherical scattering on dielectric objects, *J. Quant. Spectrosc. Radiat.* Transfer, **60** (3), 335-353, 1998.

115. Yee, S. K. Numerical solution of initial boundary value problems involving Maxwell's equations in isotropic media. *IEEE Trans Antennas Propag.*, 14, 302- 307, 1966.

116. Holland, R., Cable, V. R. and Wilson, L. C. Finite-volume time-domain (FVTD) techniques for EM scattering, *IEEE Trans. Electromagn. Compat.*, 33, 281- 293, 1991.

117. Kunz, K. S. and Luebbers, R. J. *The Finite Difference Time Domain Method for Electromagnetics*, CRC Press, Florida, 1993.

118. Itoh, T. (Editor) *Numerical Techniques for Microwave and Millimeter-Wave Passive Structures*, John Wiley & Sons, New York, 1989.

119. Yang, P., et al. efficient Finite-Difference Time-Domain Scheme for Light Scattering by Dielectric Particles: Application to aerosols, *Appl. Opt.*, **39**(21), 3727- 3737, 2000.'

120. Dunn, A., et al. Finite difference time domain simulation of light scattering from single cells, *J. Bimed. Opt.*, **2**(3), 262-266, 1997.

121. Gratton, E., et al. Measurements of scattering and absorption changes in muscle and brain, *Philos. Trans. R. Soc. Lond. B: Biol. Sci.*, **352**(1354), 727-735, 1997.

122. Sun, W., Fu, Q. and Chen, Z. Finite-difference time-domain solution of light scattering by dielectric particles with a perfectly matched layer absorbing boundary condition, *Appl. Opt.*, 38(15),3141- 3151, 1999.

123. Yang, P. and Liou, K. N. Finite-difference time-domain method for light scattering by small ice crystals in three-dimensional space, *J. Opt. Soc. Am. A*, **13**(10), 2072-2085, 1996.

124. Sun, W., et al. Examination of Surface Roughness on Light Scattering by Long Ice Columns by use of a Two-Dimensional Finite-Difference Time-Domain Algorithm, *Appl. Opt.*, **43** (9), 1957-1964, 2004.

125. Silvester, P. P. and Ferrari, R. L. *Finite Elements for Electrical Engineers*, Cambridge Univ. Press, New York, 1996.

126. Itoh, T. (editor) *Numerical Techniques for Microwave and Millimeter-Wave Passive Structures*, John Wiley & Sons, New York, 1989.

127. Wriedt, T. and Comberg, U. Comparison of computational and scattering methods, *J. Quant. Spectrosc. Radiat. Transfer*, **60** (3), 411-423, 1998.

128. Thiele, E. S. and French, R. H. Light scattering properties of representative, morphological rutile TiO2 particles studied using a Finite-Element method, *J. Am. Ceram. Soc.*, **81**(3), 469-479, 1998.

129. Arridge, S. R., et al. The finite element model for the propagation of light in scattering media: A direct method for domains with nonscattering regions, *Med. Phys.*, **27**(1), 252-264, 2000.

130. Arridge, S. R., et al. A finite element approach for modeling photon transport in tissue. *Med. Phys.*, **20**(2 Pt. 1), 299-309, 1993.

131. Volakis, J. L., et al. Review of the finite-element method for three-dimensional electromagnetic scattering, *J. Opt. Soc. Am. A*, **11** (4), 1422-1433, 1994.

132. Wiscombe, W. J. and Mungai, A. *Single scattering from non-spherical chebyshev particles: a compendium of calculations*, NASA Ref. Publ. 1157 NASA/GSFC Greenbelt, MD, 1986.

133. Kahnert, F. M. Numerical methods in electromagnetic scattering theory, *J. Quant. Spectrosc. Radiat. Transfer*, 79-80, 775-824, 2003.

134. Wreidt, T. A Review of elastic light scattering theories, *Part. Part. Syst. Charact.*, 15, 67- 74, 1998.

135. Nieminen, T. A., et al. Calculation of the T-matrix: general considerations and application of the point-matching method, *J. Quant. Spectrosc. Radiat. Transfer*, **79-80**, 1019- 1029, 2003.

136. Su, C. -C. Electromagnetic scattering by a dielectric body with arbitrary inhomogeneity and anisotropy, *IEEE Trans. Antennas Propag.*, **37**, 384- 389, 1989.

137. Iskander, M. F., Chen, H. Y. and Penner, J. E. Optical scattering and absorption by branched chains of aerosols, *Appl. Opt.*, **28**, 3083- 3091, 1989.

138. Draine, B. T. The discrete-dipole approximation and its application to interstellar graphite grains. *Astrophys. J.*, **333**, 848- 872. 1988.

139. Draine, B. T. Interstellar Dust Grains, *Annu. Rev. Astron. Astrophys.*, **41**, 241–289, 2003.

140. Draine, B. T. and Flatau, P. J. Discrete-dipole approximation for periodic targets: theory and tests, *J. Opt. Soc. Am. A*, **25**(11), 2693-2703, 2008.

141. Dungey, C. E. and Bohren, C. F. Light scattering by nonspherical particles: A refinement to the coupled-dipole method, *J. Opt. Soc. Am. A*, **8**, 81- 87, 1991.

142. Lumme, K. and Rahola, J. Light scattering by porous dust particles in the discrete dipole approximation, *Astrophys. J.*, **425**, 653- 667, 1994.

143. Peterson, B. and Strom, S. T-matrix for electromagnetic scattering from an arbitrary number of scatterers and representations of E(3)*, *Phys. Rev. D*, **8**, 3661-3678, 1973.

144. Lakhatia, A., Varadan, V. K. and Varadan, V. V. Scattering and absorption characteristics of lossy dielectric, chiral, nonspherical objects, *Appl. Opt.*, **24**, 4146- 4154, 1985.

145. Waterman, P. C. and Truell, R. Multiple scattering of waves, *J. Math Phys.*, **2** (4), 512-537, 1961.

146. Waterman, P.C. New formulation of acoustic scattering, *J. Accoust. Soc. Am.*, **45** (6), 1417-1429, 1968.

147. Waterman, P.C. Symmetry, unitary, and geometry in electromagnetic scattering, *Phys. Rev. D: Part. Fields*, **3**, 825-839, 1971.

148. Wriedt, T. Using the T-matrix Method for Light Scattering Computations by Non-axisymmetric Particles: Superellipsoids and Realistically Shaped Particles, *Part. Part. Syst. Charact.*, **19**, 256-268, 2002.

149. Doicu, A., et al. Projection schemes in the null field method, *J. Quant. Spectrosc. Radiat. Transfer*, **63**, 175-189, 1999.

150. Doicu, A. and Wriedt, T. Calculation of the T-matrix in the null-field method with discrete soureces, *J. Opt. Soc. Am. A*, **16**, 2539-2544, 1999.

151. Schmidt, K., et al. The equivalence of applying the Extended Bounded Condition and the contimuity conditions for solving electromagnetic scattering problems, *Opt. Commun.*, **150**, 1- 4, 1998.

152. Mackowski, D. W. and Mishchenko, M. I. Calculation of the T matrix and the scattering matrix for ensembles of sphere, *J. Opt. Soc. Am. A*, **13**, 2266-2278, 1996.

153. Mishchenko, M. I., et al. T-matrix Computations of Light Scattering by Nonspherical Particles: A Review, *J. Quant. Spectrosc. Radiat. Transfer*, **55**(5), 535-515, 1996.

154. Mishchenko. M. I., et al. Scattering of light by polydisperse, randomly oriented, finite circular cylinders, *Appl. Opt.*, **35**, 4927-4940, 1996.

155. Mishchenko, M. I. and Travis, L. D. T-matrix computations of light scattering by large spheroidal particles, *Opt. Commun.*, **109**, 16-21, 1994.

156. Quirantes, A. A T-matrix method and computer code for randomly oriented, axially symmetric coated scatterers, *J. Quant. Spectrosc. Radiat. Transfer*, **92**, 373-381, 2005.

157. Petrov, D., et al. The T-matrix technique for calculation of scattering properties of ensembles of randomly oriented particles with different size, *J. Quant. Spectrosc. Radiat. Transfer*, **102**, 85-110, 2006.

158. Baron, A. J., Yang, P. and Havemann, S. Calculation of the Single-Scattering Properties of Randomly Oriented Hexagonal Ice Columns: A Comparison of the T-Matrix and the Finite-Difference Time-Domain Methods, *Appl. Opt.*, **40**, 4376-4386, 2001.

159. Mackowski, D. W., Mishchenko, M. I. A multiple sphere T-matrix Fortran code for use on parallel clusters, *J. Quant. Spectrosc. Radiat. Transfer*, **112**, 2182- 2192, 2011.

160. Mishchenko, M. I. and Travis, L. D. Capabilities and limitations of a current FORTRAN implementation of the T-matrix method for randomly oriented, rotationally symmetric scatterers, *J. Quant. Spectrosc. Radiat. Transfer* , **60**, 309-324, 1998.

161. Mishchenko, M. I., Mackowski, D. W. and Travis, L. D. Scattering of light by bispheres with touching and separated components, *Appl. Opt.*, **34**, 4589- 4599, 1995.

162. Mackowski, D.W. Discrete dipole moment method for calculation of the T-matrix for nonspherical particles, *J. Opt. Soc. Am. A*, **19**, 881-893, 2002.

163. Mishchenko, M. I., et al. Scattering of light by polydisperse, randomly oriented, finite circular cylinders, *Appl. Opt.*, **35**, 4927-4940, 1996.

164. Wriedt, T. and Doicu, A. Formulations of the extended boundary condition method for three dimensional scattering using the method of discrete sources, *J. Mod. Opt.*, **45**, 199–213, 1998.

165. Khlebtsov, N.G. Orientational averaging of light scattering observables in the T-matrix approach, *Appl. Opt.*, **31**, 5359-5365, 1992.

166. Quirantes, A. and Delgado, A. Experimental determination of spheroidal particles via the T-matrix method, *J. Quant. Spectrosc. Radiat. Transfer*, **60**(3), 463-474, 1998.

167. Riefler, N. and Wriedt, T. T-matrix simulation of plasmon resonances of particles on or near a surface, *Progress in Electromagnetic Research Symposium*, Cambridge, USA, March 26-29, 2006.

168. Ben-David, A. Backscattering Measurements of Atmospheric Aerosols at CO_2 Laser Wavelengths: Implications of Aerosol Spectral Structure on Differential-Absorption Lidar Retrievals of Molecular Species, *Appl. Opt.*, **38**, 2616-2624, 1999.

169. Muñoz O., et al., Experimental determination of scattering matrices of olivine and Allende meteorite particles, *Astron. Astrophys.*, **360**, 777-788, 2000.

170. Stam, D. M., et al. Integrating polarized light over a planetary disc applied to starlight reflected by extrasolar planets, *Astron. Astrophys.*, **452**, 669-683, 2006.

171. Nicolae, D. N., et al., Analytical averaging method in scattering of light by ensembles of nonspherical aerosols, *J. Optoelec. Advanc. Mat.*, **6**(3), 831-840, 2004.

172. Hess, M., et al. Optical Properties of Aerosols and Clouds: The Software Package OPAC, *Bull. Am. Meterol. Soc.*, **79**(5), 831-844, 1998.

173. Pinnick, R. G., Rosen, J. M. and Hofmann, D. J. Measured Light-Scattering Properties of Individual Aerosol Particles Compared to Mie Scattering

174. Theory, *Appl. Opt.*, **12**(1), 37- 41, 1973.Hirst, E., Kaye, P. H. and Guppy, J. R. Light scattering from nonspherical airborne particles: experimental and theoretical comparisons, *Appl Opt.*, **33**(30) 7180- 7186, 1994.

175. Fierz-Schmidhauser, R. Measured and predicted aerosol light scattering enhancement factors at the high alpine site Jungfraujoch, *Atmos. Chem. Phys.*, **10**, 2319–2333, 2010.

176. Reid, J. P. Particle levitation and laboratory scattering, *J. Quant. Spectrosc. Radiat. Transfer*, 10, 1293–1306, 2009.

177. Dubovik, O., et al. Non-spherical aerosol retrieval method employing light scattering by spheroids, *Geophys. Research Lett.*, **29**(10), 54 - 1- 54 - 4, 2002.

178. Cluff, D. L. and Patitsas, A. J. Size characterization of Asbestos Fibers by means of electrostatic Alignment and Light -scattering techniques, *Aerosol Sci.Technol.*, **17**, 186- 198, 1992.

179. Muñoz, O. and Hovenier, J.W. Laboratory measurements of single light scattering by ensembles of randomly oriented small irregular particles in air. A review, *J. Quant. Spectros. Radiat. Transfer*, **112**, 1646–1657, 2011.

180. Muñoz, O., et al. Scattering matrices of volcanic ash particles of Mount St. Helens, Redoubt, and Mount Spurr Volcanoes, *J. Geophys Research*, **109** (D16201),1- 16, 2004.

181. Renard, J. -B, et al. Light scattering by dust particles in microgravity: polarization and brightness imaging with the new version of PROGRA2 instrument, *Appl. Opt.*, **41**(4), 609- 618, 2002.

182. Levasseur- Regourd, A. C. Cosmic dust physical properties and the ICAPS facility on board the ISS, *Adv. Space Res.*, **31**(12), 2599- 2606, 2003.

183. Levasseur- Regourd, A. C., et al. The LS- CODAG experiment for light scattering measurements by dust particles and their aggregates, *Adv. Space Res.*, **23**(7), 1271- 1277, 1999.

184. Levasseur- Regourd, A. C., et al. Physical properties odf dust in the solar system: Relevance of computational approach of measurements under microgravity conditions, *Adv. Space Res.*, **20**(8), 1585- 1594, 1997.

185. Gupta, R.,et al. Scattering properties and Composition of Cometary Dust, *Astrophys. Space Sci.*, **301**, 21-31, 2006.

186. Gupta, R., et al. Interstellar extinction by spheroidal dust grains, *Astron. Astrophys.*, **441**, 555–561, 2005.

187. Sen, Asoke K. On the Variation of Cometary Polarisation, *ESO Symposia: High Resolution Infrared Spectroscopy in Astronomy*, 546-549, 2005.

188. Pan, Y., et al. Characterizing and monitoring respiratory aerosols by light scattering, *Opt. Lett.*, **28**(8), 589-591, 2003.

189. Bickel W.S. Optical system for light scattering experiments. *Appl. Opt.*, **18**(11), 1707-1709, 1979.

190. Bickel, W.S., et al. Applications of polarization effects in light scattering: A new biophysical tool, *Proc. Nat. Acad. Sci. USA*, **73**(2), 486-490, 1976.

191. Sivaprakasam, V., et al. Classification and selective collection of individual aerosol particles using laser-induced florescence. *Appl. Opt*, **48**(4), B 126-136, 2009.

192. Pan, Y., et al. Single-shot fluorescence spectra of individual micrometer-sized bioaerosols illuminated by a 351- or a 266-nm ultraviolet laser, Opt. Lett., **24**(2), 116-118, 1999.

193. Hill, S. C., et al. Fluorescence from airborne microparticles: dependence on size, concentration of fluorophores, and illumination intensity, *Appl. Opt.*, **40**(18), 3005-3013, 2001.

194. Hoyle, F. and Wickramasinghe, C. "*Our Place In The Cosmos*", *Life Did Not Begin On Earth - It Arrived From Space And Is Still Arriving* Phoenix Publications, 1993.

195. Rauf, K. and Wickramasinghe, C. Evidence for biodegradation products in the interstellar medium, *Int. J. Astrobiol.*, **9**(1), 29-34, 2010.

196. Rauf, k., et al. Study of putative microfossils in space dust from the stratosphere, *Int. J. Astrobiol.*, **9**(3), 183-189, 2010.

197. Wickramasinghe, N.C. Spectroscopic evidence of cosmic life, *Int. J. Astrobiol.*, 11, 3476-3488, 2010.

198. Wickramasinghe, N.C. The astrobiological case for our cosmic ancestry, *Int. J. Astrobiol.*, **9**, 119-129, 2010.

199. Wickramasinghe, C. Bacterial morphologies supporting cometary: a reappraisal, *Int. J. Astrobiol.*, **10**, 25-30, 2011.

200. Wickramasinghe, N.C., et al. Evolution of primordial planets in relation to the cosmological origin of life, *Proc. SPIE*, **7819**, 2010.Mukai, S., et al. Removal of scattered light in the Earth atmosphere, *Earth Planets Space*, **50**, 595-601, 1998.

201. Wang, Y. and Yang, C. Regularizing active set method for retrieval of the atmospheric aerosol particle size distribution function, *J. Opt. Soc. Am. A*, 25(2), 348- 356, 2008.

202. Liou, K. N. Light Scattering by Ice Clouds in the Visible and Infrared: A Theoretical study, *J. Atmos. Sci.*, **29**, 524-536, 1972.

203. Stephens, G. L. and Webster, P. J. Clouds and Climate: Sensitivity of Simple Systems, *J. Atmos. Sci.*, **38**, 235-247, 1981.

204. Liou, K. N. and Takano, Y. Light scattering by nonspherical particles: remote sensing and climatic applications, *Atmos. Res.*, **31**, 271-298, 1994.

205. Yang, P. and Liou, K. N. Geometrics-optics-integral-equation method for light scattering by nonspherical ice crystals, *Appl. Opt.* 35 (33), 6568-6584, 1996.

206. Kokhanovsky, A. A. *Cloud Optics*, Springer,The Netherlands, 2006.

207. Liou, K. N. Light Scattering by Ice Clouds in the Visible and Infrared: A Theoretical study, *J. Atmos. Sci.*, **29**, 524-536, 1972.

208. Takano, Y. and Jayaweera, K. Scattering phase matrix for hexagonal ice crystals computed from ray optics, *Appl. Opt.*, **24** (19), 3254-3263, 1985.

209. Takano, Y. and Liou, K. N. Solar radiative transfer in cirrus clouds. Part I: single scattering and optical properties of hexagonal ice crystals. *J. Atms. Sci.*, **46**(1), 3-19, 1989.

210. Kokhanovsky, A. A. and Zege, E. P. Scattering optics of snow, *Appl. Opt.*, **43** (7), 1589-1602, 2004.

211. Barkey, B. and Liou, K. N. An analog light scattering experiment of hexagonal icelike particles. Part I: Experimental apparatus and test measurements, *J. Atms. Sci.*, **56**, 605-612, 1999.

212. Barkey, B. and Liou, K. N.Polar nephelometer for light-scattering measurements of ice crystals, *Opt. Lett.*, **26**(4), 232–234, 2001.

213. Borovoi, A. and Kustova, N. Specular scattering by preferentially oriented ice crystals, *Appl. Opt.*, **48**, 3878-3885, 2009.

214. Muñoz, O., et al. Experimental and computational study of light scattering by irregular particles with extreme refractive indices: hematite and rutile, *Astron. Astrophys.*, **446**, 525-535, 2006.

215. Ulanowski, Z., et al. Light scattering by complex ice-analogue crystals, *J. Quant. Spectrosc. Radiat. Transfer*, **100** (1-3), 382-392, 2006.

216. Yang, P., et al. Single-scattering properties of droxtals, *J. Quant. Spectrosc. Radiat. Transfer*, **79-80**, 1159-1169, 2003.

217. Haywood, J. M., Ramaswamy, V. and Soden, B. J. et al. Tropospheric aerosol climate forcing in clear-sky satellite observations over the oceans, *Science*, **283**, 1299- 1303, 1999.

218. Randles, C. A., Russell, L. M. and Ramaswamy, V. Hygroscopic and optical properties of organic sea salt aerosol and consequences for climate forcing, *Geophys. Research Lett.*, **31**(L16108), 1- 4, 2004.

219. Worms, J.-C, et al. Results of the PROGRA^2 Experiment: An experimental study in microgravity of scattered polarized light by dust particles with large size parameter, *Icarus*, **142**, 281- 297, 1999.

220. Volten, H., et al. Scattering matrices of mineral aerosol particles at 441.6 nm and 632.8 nm, *J. Geophys. Res.*, **106** (D15), 17375-17401, 2001.

221. Weiss-Wrana, K. Optical properties of interplanetary dust - Comparison with light scattering by larger meteoritic and terrestrial grains, *Astron. Astrophys.*, **126**, 240-250, 1983.

222. Moroz, V. I., et al. Aerosol vertical profile on Mars from the measurements of thermal radiation on the limb, *Planet. Space Sci.*, **42** (10), 831-845, 1994.

223. Koepke, P. and Hess, M. Scattering functions of tropospheric aerosols: the effects of nonspherical particles, *Appl. Opt.*, **27**(12), 2422- 2430, 1988.

224. Jeong, K. S., et al., Self-consistent modeling of the outflow from the O-rich Mira IRC -20197, *Astron. Astrophys.* , **407**,191- 206, 2003.

225. Pluchino, A. B. et al, Refractive-index measurements of single micron-sized carbon particles, *Appl. Opt.*, **19**(19), 3370- 3372, 1980.

226. Batten, C. E. Spectral optical constants of soots from polarized angular reflectance measurements, *Appl. Opt.*, **24**(8), 1193- 1199, 1985.

227. Westphal, A. J., et al. Analysis of "Midnight" Tracks in the Stardust Interstellar Dust Collector: Possible Discovery of a Contemporary Interstellar Dust Grain, 41st Lunar and Planetary Science Conference, March 1-5, 2010. The Woodlands, Texas. LPI Contribution No. 1533, p. 2050.

228. Brownlee, D. E., et al. Stardust: Comet and interstellar dust sample return mission, *J. Geophys. Res.*, **108** (E10), 8111(15PP), doi: 10.1029/2003JE002087, 2003.

229. Nousiainen, T., Muinonen, K. and Räisänen, P. Scattering of light by large Saharan dust particles in a modified ray optics approximation, *J. Geophys. Res.*,108, 4025, 17 pp., doi:10.1029/2001JD001277, 2003.

230. Quirantes, A. and Bernard, S. Light scattering by marine algae: two-layered spherical and non-spherical models, *J. Quant. Spectrosc. Radiat. Transfer*, **89**(1- 4), 311- 321, 2004.

231. Ormerod, M. G., et al., Discrimination of apoptotic thymocytes by forward light scatter, *Cytometry*, **21**, 300- 304, 1995.

232. Volten, H. et al. Laboratory measurements of angular distributions of light scattered by phytoplankton and silt, *Limnol. Oceanogr.*, **43** (6), 1180-1197, 1998.

233. Gilev, K. V., et al. Comparison of the discrete dipole approximation and the discrete source method for simulation of light scattering by red blood cells, *Opt. Express*, **18**(6), 5681- 5690, 2010.

234. Yurkin, M. A., et al. Experimental and theoretical study of light scattering by individual mature red blood cells by use of scanning flow cytometry and a discrete dipole approximation, *Appl. Opt.*, **44**(25), 5249–5256 (2005).

235. Preizzhev, A., Nikitin, S. Y. and Lugovtsov, A. E. Ray- wave approximation for calculation of laser light scattering by transparent dielectric particles, mimicking red blood cells or their aggregates, *J. Quant. Spectrosc. Radiat. Transfer*, **110**, 1535- 1544, 2009.

236. Streekstra, G. J., et al. Light scattering by red blood cells in ektacytometry: Fraunhofer versus anomalous diffraction, *Appl. Opt.*, **32**(13), 2266- 2272, 1993.

237. Stramski, D., et al. The role of seawater constituents in light backscattering in the ocean, *Prog. Oceanogr.*, **61**, 27-56, 2004.

238. Kerker, M. and Mer, V. K. L. Particle Size Distribution in Sulfur Hydrosols by Polarimetric Analysis of Scattered Light, *J. Am. Chem. Soc.*, **72**, 3516-3525, 1950.

239. Jonasz, M. and Fournier G. R. *Light Scattering by Particles in water Theoretical and Experimental Foundations*, Elsevier, Amsterdam, 2007.

240. Lotsberg, J. K., et al. Laboratory measurements of light scattering from marine particles, *Limnol. Oceanogr.:Methods*, **5**, 34-40, 2007.

241. Morel. A. Optics of marine particles and marine optics, *Particle Analysis in Oceanography*, **G27**, 141-188, 1991.

242. Mobley, C. D. et al. Comparison of numerical models for computing underwater light climate, *Appl. Opt.*, **32**(36), 7484-7504, 1993.

243. Di Toro, D. M. Optics of turbid estuarine waters: approximations and applications, *Water Res.*, **12**, 1059-1068, 1978.

244. Morel, A. and Gentili, B. Diffuse reflectance of oceanic waters: its dependence on sun angle as influenced by the molecular scattering contribution, *Appl. Opt.*, **30**(30), 4427-4438, 1991.

245. Chami, M. et al. Variability of the relationship between the particulate backscattering coefficient and the volume scattering function measured at fixed angles, *J. Geophys. Res.*, 111, C05013, doi: 10.1029/2005JC003230, 2006.

246. Bricaud, A. and Morel, A. Light attenuation and scattering by phytoplanktonic cells: a theoretical modelling, *Appl. Opt.*, **25**, 571-580, 1986.

247. Petzold, T. T. Volume scattering functions of selected ocean waters (Scripps Institution of Oceanography, Visibility Lab., University of California, San Diego. Ref. 72-78, October 1972).

248. Witkowski, K., et al. A Light-Scattering Matrix for Unicellular Marine Phytoplankton, *Limnol. Oceanogr.*, **43** (5), 859-869, 1998.

249. Dekker, A. G., et al. Angular scattering functions of algae and silt: an anlysis of backscattering to scattering fraction (In: Steven G. Ackleson. Editor. Proc. SPIE Vol. 2963, Ocean Optics XIII, Halifax, Canada 22-25 October, 1996) 392-400.

250. Sokolov, A., et al. Parameterization of volume scattering function of coastal waters based on the statistical approach, *Opt. Express*, **18** (5), 4615-4636, 2010.

251. Ben-David, A. and Ren, H. Detection, Identification and Estimation of Biological Aerosols and Vapors with a Fourier-Transform Infrared Spectrometer, *Appl. Opt.*, **42**, 4887-4900, 2003.

252. Berkmen, R. M., Wyatt, P. J. and Phillips, D. T. Rapid detection of penicillin sensitivity in *Staphylococcus aureus*, Nature (London), **228**, 458-460, 1970.

253. Roy, S., et al. Monitoring of pathogen carrying air-borne tea dust particles by light scattering, *J. Quant. Spectrosc. Radiat. Transfer*, 112, 1784- 1791, 2011.

254. Bronk, B. V., et al. Measuring diameters of rod-shaped bacteria in vivo ith polarized light scattering, *Biophys. J.*, **69**, 1170- 1177.

255. Van de Merwee, W. P., Polarized light scattering for rapid observation of bacterial size changes, *Biophys. J.*, **73**, 500- 506, 1997.

256. Benson, M. C., McDougal, D. C. and Coffey, D. S. The application of perpendicular and forward light scatter to access nuclear and cellular morphology, *Cytometry*, **5**, 515- 522, 1984.

257. Gorman, A. M., et al. Use of flow cytometry techniques in studying mechanisms of apoptosis in leukemic cells, *Cytometry*, **29**, 97- 105, 1997.

258. Latimer, P. Light scattering and absorption as methods of studying cell population parameters, *Ann. Rev. Biophys. Bioeng.*, **11**, 129- 150, 1982.

259. Aslan, M. M., et al. Size and shape prediction of colloidal metal oxide MgBaFeO particles from light scattering measurements, *J. Nanoparticle Research*, **8**, 981- 994, 2006.

260. Messina, E., et al. Plasmon-Enhanced optical trapping of gold nanoaggregates with selected optical properties, *ACS NANO*, **5**(2), 905-913, 2011.

261. Bayan, S., Mohanta, D. Directed growth characteristics and optoelectronic properties of Eu-doped ZnO nanorods and urchins, *J. Appl. Phys.*, 108, 023512, 2010.

262. Shu, J., et al. Elastic light scattering from nanoparticles by monochromatic vacuum-ultraviolet radiation. *The J. of Chem. Phys.*, **124**, 034707-1-034707-9, 2006.

263. Pecora, R. Dynamic light scattering measurement of nanometer particles in liquids, *J. Nanoparticle Research*, **2**, 123-131, 2000.

264. Chu, B. and Liu, T. Characterization of nanoparticles by scattering techniques, *J. Nanoparticle Research*, **2**, 29-41, 2000.

265. Chen, K., et al., Nanoparticle sizing with a resolution beyond the diffraction limit using UV light scattering spectroscopy, *Opt. Commun.*, **228**, 1-7, 2003.

266. Jillavenkatesa, A. and Kelly, J. F. Nanopowder characterization: challenges and future directions, *J. Nanoparticle Research*, **4**, 463-468, 2002.

267. Chen, Z., et al. Backscattering enhancement of light by nanoparticles positioned in localized optical intensity peaks, *Appl. Opt.*, **45**, 632-638, 2006.

268. Gebauer, G. and Winter, J. *In situ* nanoparticle diagnostics by multiwavelength Rayleigh-Mie scattering ellipsometry, *New J. Physics*, **5**, 38.1-38.17, 2003.

269. Orendorff, C. J., et al. Light scattering from gold nanorods: tracking material deformation, *Nanotechnology*, **16**, 2601-2605, 2005.

270. Mishra, A., Ram, S. and Ghosh, G. Dynamic Light Scattering and Optical Absorption in Biological Nanofluids of Gold Nanoparticles in Poly(vinyl pyrrolidone) Molecules, *J. Phys. Chem. C*, **113** (17), 6976–6982, 2009.

271. Lechner, M. D. Influence of Mie scattering on nanoparticles with different particle sizes and shapes: photometry and analytical ultracentrifugation with absorption optics, *J. Serb. Chem. Soc.*, **70**(3), 361-369, 2005.

272. S. Roy and G.A.Ahmed, Investigation of light scattering properties of laboratory synthesized sub-micron CdS semiconductor particles, J. Opt. 39(4) 181-184 (2010).

273. Roy, S., et al. Light scattering study of ZnO nanoparticles for the application of its anti-bacterial property, *AAPP| Journal of Mathematical, Physical and Natural Sciences*, DOI: 10.1478/C1V89S1P001, 2011.

274. Kruzewski, S., Surface enhanced Raman scattering, *Crys. Res. Technol.*, **41**(6), 562-569, 2006.

275. Ampion, A. C. and Ambhampati, P. K. Surface enhanced Raman scattering, *Chemical Society Reviews*, **27**, 241-250, 1998.

276. Fazio, B., et al. Re-radiation enhancement in polarized surface-enhanced resonant Raman scattering of randomly oriented molecules on self-organized gold nanowires, *ACS NANO*, **5**(7), 5945- 5956, 2011.

277. Wriedt, T., Doicu, A. Light scattering from a particle on or near a surface, *Opt. Commun.*, **152**, 376-384, 1998.

278. Voshchinnikov, N. V. and Karjukin, V. V. Multiple scattering of polarized radiation in circumstellar dust shells, *Astron. Astrophys.*, **288**, 883-896, 1994.

279. Chuah, H. T. and Tan, H. S. A Monte Carlo Backscatter model for radar backscatterer from a half space random medium, *IEEE Trans. Geosci. Remote Sens.*, **27**, 86-93, 1998.

280. Bartel, S. and Hielscher, A. H. Monte Carlo simulations of the diffuse backscattering Mueller matrix for highly scattering media, *Appl. Opt.*, **39**, (10), 1580-1588, 2000.

281. Wang, X. and Wang, L. V. Propagation of polarized light in birefringent turbid media: a Monte Carlo study, *J. Biomed. Opt.*, **7**, 279 2002.

282. Wang, X., et al. Polarized light propagation through scattering media: time-resolved Monte Carlo simulations and experiments, *J. Biomed. Opt.*, **8**, 608 (2003); doi:10.1117/1.1606462.

283. Wang, L., Jacques, S. L. and Zheng, L. MCML-Monte Carlo modeling of light transport in multilayered tissues, *Comput. Methods Programs Biomed.*, **47**, 131-146 , 1995.

284. Xu, M. Electric field Monte Carlo simulation of polarized light propagation in turbid media, Optics Express, 12, 26, 6530-6539 (2004).

285. Mikrenska, M., et al. Direct simulation Monte Carlo ray tracing model of light scattering by a class of real particles and comparison with PROGRA^2 experimental results, *J. Quant. Spectrosc. Radiat. Transfer*, **100**, 256–267, 2006.

286. Mikrenska, M. and Koulev P. Simulation of light scattering by large particles with randomly distributed spherical or cubic inclusions, *J. Quant. Spectrosc. Radiat. Transfer*, **110**, 1411–1417, 2009.

287. Kaplan, B., Ledanois, G. and Drévillon, B. Mueller matrix of dense polystyrene latex sphere suspensions: Measurements and Monte Carlo simulation, *Appl. Opt.*, **40**, 2769–2777, 2001.

288. Xia, M., et al. Monte Carlo simulation of backscattering signal from bubbles under water, *J. Opt. A: Pure Appl. Opt.*, **8**, 350-354, 2006.

289. Barber, P. W. and Hill, S. C. *Light scattering by particles: Computational methods*, World scientific, Singapore, 1990.

290. Yuan, Y. J., et al. Extended geometrical optics approximation and Monte Carlo ray tracing for light scattering by an irregular object, *In 15th Int. Symp. on Applications of Laser Techniques to Fluid Mechanics*, Lisbon, Portugal, 05-08 July, 2010.

291. Kocifaj, M. Light pollution simulations for planar ground-based light sources, *Appl. Opt.*, **47**(6), 792- 798, 2008.

292. Pathak, A. and Rastogi, S. Modeling the interstellar aromatic infrared bands with co-added spectra of PAHs, *Astron. Astrophys.*, **485**, 735–742, 2008.

293. Ghosh, N., et al. Mueller matrix polarimetry for the characterization of complex random medium like biological tissues, *PRAMANA- Journal of Physics*, **75**(6), 1071- 1086, 2010.

294. Antonelli, M.-R., et al. Mueller matrix imaging of human colon tissue for cancer diagnostics: how Monte Carlo modeling can help in the interpretation of experimental data, *Opt. Express*, **18**(10), 2010.

295. Dlugach, J. M., et al. Numerical exact computer simulations of light scattering by densely packed, random particulate media, *J. Quant. Spectrosc. Radiat. Transfer*, **112**, 2068- 2078, 2011.

296. Bogucki, D. J., et al. Monte Carlo simulation of propagation of a short light beam through turbulent oceanic flow, *Opt. Express*, **15**(21), 13988-13996, 2007.

297. Saunders, C., et al. Preliminary laboratory studies of the optical scattering properties of the crystal clouds, *Ann. Geophysics*, **16**, 618-627, 1998.

298. Takano, Y., et al. Solar radiative transfer in Cirrus clouds. Part I: Single scattering and optical properties of hexagonal ice crystals, *J. Atmosph. Sci.*, **46**(1), 3-19, 1989.

299. Muller, D., Wandinger, U. and Ansmann, A. Microphysical Particle Parameters from Extinction and Backscatter Lidar Data by Inversion with Regularization: Theory, *Appl. Opt.*, **38**, 2346-2357, 1999.

300. Roy, S. and Ahmed, G. A. Monte Carlo simulation of light scattering from size distributed sub-micron spherical CdS particles in a volume element, *Optik-Int. J. Light Electron Opt.* , **122**, 1000-1004, 2011.

301. Hunt, A. J. and Huffman, D. R. A new polarization-modulated light scattering instrument, *Rev. Sci. Instrum.*, **44**(12), 1763-1773, 1973.

302. Huffman, D. R. Optical properties of particulates, *Astrophys. Space Sci.*, **34** (1), 175-184, 1975.

303. Thompson, R. C., et al. Measurement of polarized light interaction via the Mueller matrix, *Appl. Opt.*, **19**, 1323-1332, 1980.

304. Anderson, R. Measurement of Mueller matrices, *Appl. Opt.*, **31**, 11-13, 1992.

305. van der Mee, C. V. M. and Hovenier, J. W. Expansion coefficients in polarized light transfer, *Astron. Astrophys.*, 228, 559- 568, 1990.

306. van der Mee, C. V. M. and Hovenier, J. W. Structure of matrices transforming Stokes parameters, *J. Math. Phys.*, 33, 3574- 3584, 1992.

307. Valentine, M. T., et al. Microscope-based static light-scattering instrument, *Opt. Lett.*, **26**(12), 890-892, 2001.

308. Holland, A.C. and Gagne, G. The scattering of polarized light by polydisperse systems of irregular particles, *Appl. Opt.*, **9**, 1113-1121, 1970.

309. Castagner, J.L. and Bigio, I. J. Particle sizing with a fast polar nephelometer, *Appl. Opt.*, **46**(4), 527- 532, 2007.

310. Quirantes, A., et al. Correction factors for a total scatter/ backscatter nephelometer, *J. Quant. Spectrosc. Radiat. Transfer*, **109**, 1496- 1503, 2008.

311. Doherty, S. J., et al. Measurement of the lidar ration for atmospheric aerosols with a 180° backscatter nephelometer, *Appl. Opt.*, **38**(9), 1823- 1832, 1999.

312. Stewart, H. S. and Curcio, J. A. The influence of field of view on measurements of atmospheric transmission, *J. Opt. Soc. Am.*, **42**, 801- 805, 1952.

313. Curcio, J.A., et al. An experimental study of atmospheric transmission, *J. Opt. Soc. Am.*, **43**, 97-102, 1953.

314. Gibbons, M.G. Transmission and scattering properties of a Nevada Desert atmosphere under cloudy conditions, *J. Opt. Soc. Am.*, **51**, 633-640, 1961.

315. Clay, M.R. and Lenham, A.P. Transmission of electromagnetic radiation in fogs in the 0.53 to 10.1 micron wavelength range, *Appl. Opt.*, **20**, 3831-3832, 1981.

316. Roberts, R.E., Selby, J.E.A. and Biberman, L.M. Infrared continuum absorption by atmospheric water vapour in the 8-12 micrometer window, *Appl. Opt.*, **15**, 2085-2090, 1976.

317. Eldrige, R.G. and Jhonson, J.C. Diffuse transmission through real atmospheres, *J. Opt. Soc. Am.*, **48**, 463-468, 1958.

318. Winstanley, J.V. and Adams, M.J. Point visibility meter: a forward scatter instrument for the measurement of aerosol extinction coefficient, *Appl. Opt.*, **14**, 2151-2157, 1975.

319. Nefedov, A.P., et al. Application of a forward-angle-scattering transmissiometer for simultaneous measurements of particle size and number density in an optically dense medium, *Appl.Opt.*, **37**, 1682-1689, 1998.

320. Killinger, D.K. and Menyuk, N. Laser remote sensing of the atmosphere, *Science*, **235**, 37-45, 1987.

321. Remsberg, E.E. and Gordley, L.L. Analysis of differential absorption lidar from the space shuttle, *Appl. Opt.*, **17**, 624-630, 1978.

322. Browell, E.V., Wilkerson, T.D. and McIlrath, T.J. Water vapour differential-absorption lidar development and evaluation, *Appl. Opt.*, **18**, 3474-3483, 1978.

323. Fredriksson, K., et al. Mobile lidar system for environmental probing, *Appl.Opt.*, **20**, 4181-4189, 1981.

324. Toon, O.B. and Pollack, J.B. Atmospheric aerosols and climate, *Am. Sci.*, **68**, 268-278, 1980.

325. Devera, P.C.S., et al. Lidar for Environmental Monitoring, *J.Instrument Soc.India*, **26** (3), 62-67, 1996.

326. Roy, S., Gogoi, A. and Ahmed, G. A. Size dependent optical characterization of semiconductor particle: CdS embedded in polymer matrix, *Indian J. Phys.*, **84** (10), 1405-1411, 2010.

327. General Purpose Linear Devices Databook, *National Semiconductor*, 1987.

328. GE Solid State Data Book on Optoelectronics, GE/RCA/*Intersil Semiconductors*, 1987.

329. Schnablegger, H. and Glatter, O. Simultaneous determination of size distribution and refractive index of colloidal particles from static light scattering experiments, *J. Colloid Interface Sci.*, **158**, 228–42, 1993.

330. Schreurs, R. *Light scattering algae: Fitting experimental data using Lorenz-Mie theory*. Graduation report, Free Univ., Amsterdam, 1996.

331. Sugihara, S., Kishino, M., and Okami, N. Back-scattering of light by particles suspended in water, *Phys. Chem. Res.*, **76**, 1-8, 1982.

332. Schnablegger, H. and Glatter, O. Simultaneous determination of size distribution and refractive index of colloidal particles from static light-scattering experiments. *J. Colloid Interface Sci.*, **158**, 228- 242, 1993.

333. Hadamcik, E., et al. Polarization of light scattered by fluffy particles (PROGRA2 Experiment), *Icarus*, **155**, 497–508, 2002.

334. Nikolova, S., et al. Analysis of the dispersion of optical plastic materials, *Optical Materials*, **29**, 1481- 1490, 2007.

335. Nabok, A., et al. Optical studies on II- VI semiconductor nanoparticles in Langmuir- Blodgett films, IEEE transactions on Nanotechnology, **2**(1), 44-49, 2003.

336. Scholz, S.M., et al. Mie scattering effects from monodispersed ZnS nanospheres, *J. Appl. Phys*, **83**(12), 7860–7866, 1998.

337. ohanta, D., Mishra, N. C. and Choudhury, A. SHI-induced grain growth and grain fragmentation effects in polymer-embedded CdS quantum dot systems, *Materials Letters*, **58**, 3694–3699, 2004.

338. Setien, B., et al. Spectral behaviour of the linear polarization degree at right-angle scattering configuration for nanoparticle systems, *New Journal of Physics*, **12**, 103031 (14pp), 2010.

339. Zhong, H., et al. Monodispersed ZnSe Colloidal Microspheres: Preparation, Characterization, and Their 2D Arrays, *Langmuir*, **23**(17), 9008–9013, 2007.

340. McNeil, L. E. and French, R. H. Multiple scattering from rutile TiO2 particles, *Acta Mater.* **48**, 4571- 4576, 2006.

341. Hadamcik, E., et al. Polarimetric study of levitating dust aggregates with the PROGRA2 experiment, Planet. Space Sci., **50**, 895–901, 2002.

342. Marinkovic, M., et al. Light trapping of zinc oxide nano particle films, 218th ECS Meeting, The Electrochemical Society, 2010.

343. Sharma, D., et al. Synthesis of ZnO nanoparticles and study of their antibacterial and antifungal properties, *Thin Solid films*, **519**, 1224- 1229, 2010.

344. Sibbald, M. J. J. B., et al., Mapping the Pathways to Staphylococcal Pathogenesis by Comparative Secretomics, *Microbiology and Molecular Biology reviews*, **70**, 755-788, 2006.

345. Zuskin, E., et al. Organic dust disease of airways, *International Archives of Occupational and Environmental Health*, **65**, 135-140, 1993.

346. WHO Report 2009 Global Tuberculosis Control Epidemiology Strategy Financing.

347. Kunz, R. and Gundermann, K.C. The survival of Mycobacterium tuberculosis on surfaces at different relative humidities. *Zent Bakl Hyg.*, **176**(B), 105-115, 1982.

348. Rubin, J. Mycobacterial disinfection and control, *In: Seymour S. Bock Lea and Flebiger editors. Disinfection, sterilization and preservation*, 4th edition, 377-383, 1991.

349. Perez, C., Paul, M. and Bazerque, P .Antibiotic assay by agar well diffusion method, *Acta Biol. Med. Exp.*, **15**,113–15, 1990.

350. Anand, P.K., Kaul. B.D. and Sharma, M. Green tea polyphenols inhibits Mycobactrium tuberculosis survival within human macrophages, *Int. J. Biochem. Cell Biol.*, **38**(4), 600-609, 2006.

351. Nair, D.G., et al. Antimicrobial activity of omwaprin, a new member of the waprin family of snake venom proteins, *J. Biochem.*, **402**, 93-104, 2007.

352. Deo, N. *System Simulation with Digital Computer*, Prentice- Hall of India Private Limited, New Delhi, 1993.

353. Jackson, J.D. *Classical Electrodynamics*, Wiley Eastern Ltd., New Delhi, 1975.

354. Hovenier, J. W., et al. Laboratory studies of scattering matrices for randomly oriented particles: potentials, problems, and perspectives, *J. Quant. Spectroc. Radiat. Transfer*, **79-80**, 741-755, 2003.

355. Ghatak, A.K., Goyal, I.C. and Chua, S.J. *Mathematical Physics*, Macmillan India Ltd., New Delhi, 1995.

356. Junge, C.E. Comments on "Concentration and Size Distribution Measurements of Atmospheric Aerosols and a Test of the Theory of Self-Preserving Size Distributions", *J. Atmos. Sci.*, **26**, 603-608, 1969.

357. Mishchenko, M. I. and Travis, L. D. Capabilities and limitations of a current fortran implementation of the T-matrix method for randomly oriented, rotationally symmetric scatterers, J. Quant. Spectrosc. Radiat. Transfer, **60**(3), 309-324, 1998. http://www.giss.nasa.gov/&crmin.

358. ScatLab light scattering software, http://www.scatlab.org/.

359. Lux., I., and Koblinger, L. *Monte Carlo particle transport methods: Neutron and Photon Calculations*, CRC Press, 1991.

360. Kalos, M. H., and Whitlock, P.A. *Monte Carlo methods, I: Basics*, John Wiley & Sons Inc., 1986.

361. Marsaglia, G., Generating exponential random variables, *Ann. Math. Stat.*, **32**, 899, 1961.

362. Demos, S. G. and Alfano, R. R., Optical polarization imaging, *Appl. Opt.*, **36**(1), 150- 155, 1997.

363. Demos, S. G. and Alfano, R. R., Temporal gating in highly scattering media by the degree of optical polarization, *Opt. Lett.*, **21**(2), 161- 163, 1996.

364. Demos, S. G., Radousky, H. B. and Alfano, R. R., Deep subsurface imaging in tissues using spectral and polarization filtering, *Opt. Express*, **7**(1), 23- 28, 2000.

365. Schmitt, J. M., Gandjbakhche, A. H. and Bonner, R. F. Use of polarized light to discriminate short-path photons in a multiply scattering medium, *Appl. Opt.*, **31**(30), 6535- 6546, 1992.

366. Emile, O., Bretenaker, F., and Le Floch, A. Rotating polarization imaging in turbid media, *Opt. Lett.*, **21**(20), 1706- 1708, 1996.

367. Rai, R. K. and Rastogi, S. The scattering and extinction properties of nanodiamonds, *Mon. Not. R. Astron. Soc.*, 401, 2722–2728, 2010.

368. OPN, Optics & Photonics News, OSA, **22**(10), 21- 27, 2011.

369. Chandra, S. *Applications of Numerical Techniques with C*, Narosa Publishing House, 2006.

LIST OF PUBLICATIONS

Papers published in referred journals

1. Roy, S., Mohanta, D. and Ahmed, G. A. Modeling of Light Scattering from Size distributed ZnSe Nanoparticles, *International Journal of Nanotechnology and Applications*, **5** (4), 471 - 476, 2011.
2. Roy, S., Barua, N., Buragohain, A. K. and Ahmed, G. A. Light scattering study of ZnO nanoparticles for the application of its anti-bacterial property, *AAPP| Journal of Mathematical, Physical and Natural Sciences*, DOI: 10.1478/C1V89S1P001, 2011.
3. Roy, S., Mahatta, R., Barua, N., Buragohain, A. K. and Ahmed, G. A. Monitoring of pathogen carrying air-borne tea dust particles by light scattering, *J. Quant. Spectrosc. Radiat. Transfer*, **112** 1784 - 1791, 2011.
4. Roy, S. and Ahmed, G. A. Monte Carlo simulation of light scattering from size distributed sub-micron spherical CdS particles in a volume element, *Optik-Int. J. Light Electron Opt.* , **122**, 1000 - 1004, 2011.
5. Roy, S., Gogoi, A. and Ahmed, G. A. Size Dependent Optical Characterization of CdS semiconductor particles embedded in dielectric polymer matrix, *Indian J. Phys.*, **84** (10), 1405 - 1411 (2010).
6. Roy, S. and Ahmed, G.A. Investigation of light scattering properties of laboratory synthesized sub-micron CdS semiconductor particles, *J. Opt.*, **39**(4), 181-184, 2010.
7. Roy , S., Boro, M., Mohanta, D., Choudhury, A. and Ahmed, G. A. Size quantification of sub-micron ZnSe semiconductor particles by laboratory scattering methods, *Indian J. Phys.*, **84** (6), 705 - 709, 2010.
8. Roy, S. and Ahmed, G. A. Computation of Mueller scattering matrices of spherical particles with a Gamma size distribution, *J. Opt.*, **39** (2), 76 - 81, 2010.

Papers in conference proceedings

1. Roy, S., Boruah, M., Barua, N., Buragohain, A. K., and Ahmed, G. A. Investigations on antibacterial property of ZnO nanoparticles applying optical techniques, *AIP Conf. Proc.* 1391, 721, 2011; doi: 10.1063/1.3643660.
2. Roy, S., Mahatta, R., Barua, N., Buragohain, A. K. and Ahmed, G. A. Monitoring of pathogen carrying air-borne *Camellia Sinensis* dust particles by light scattering, 250-253; Editors: Muinonen, K., Penttila, A., Lindqvist, H., Nousiainen, T. and Videen, G. *Proc. Of 12th Electromagnetic and Light Scattering Conference,* June 28-July 2, 2010, University of Helsinki, Finland.
3. Roy, S. Simulation of Light Scattering from Spherical Particles in a Volume Element, ICOP 2009-in *Proc. of International Conference on Optics and Photonics,* CSIO, Chandigarh, India, 30 Oct.-1 Nov., 2009.
4. Roy, S., Ahmed, G. A. Computation of Mueller Scattering Matrices of Spherical Particles with size distribution, in *Proc. of XXXIII Optical Society of India (OSI) Symposium 2007,* 98-100, edited by: Sahu, P. P. and Deb, P., Tezpur University, Tezpur, Assam, India, December 18-20, 2007.

Presentation in Conferences

1. Contributed Oral presentation in the 13th Electromagnetic and Light Scattering Conference, University of Messina, held at Taormina, Italy, 26-30th September, 2011.
2. Contributed Oral presentation in the National conference on "Nuclear and Atomic Techniques based Pure and Applied Physics", at Tezpur University, 1-3rd February, 2011.
3. Contributed Poster presentation in the National conference on Smart Nanomaterials, at Tezpur University, 18th-20th January, 2011.

4. Contributed Oral presentation in the National Conference on Laser and Optical Sciences, DHSK College, Dibrugarh, 11 -13th October 2010.Contributed Oral presentation in the 7th National Conference of Physics Academy of North East, Manipur University, 5-6th October 2010.
5. Contributed Oral presentation in the 12th Electromagnetic and Light Scattering Conference, University of Helsinki, Finland, 27th June-3rd July 2010.
6. Contributed Oral presentation in 6th National Conference of Physics Academy of North East, Tripura University, 4-6th April, 2010.
7. Contributed Oral presentation in the International Conference Optics and Photonics, at Central Scientific and Industrial Research Organization (CSIO), Chandigarh, 30th October-2nd November, 2009.
8. Contributed Oral presentation in the 13th National conference on "Condensed Matter days", at Tezpur University, 29th August- 1st September,Viswa Bharati University, Shantiniketan,2008.
9. Contributed Poster presentation on the XXXIII OSI Symposium on Optics and Optoelectronics, 18-22nd December 2007, at Tezpur University.

Workshops attended

1. DIT sponsored workshop on "Possibilities of Electronics R&D and Application in the North East", 29th July 2011, at Tezpur University.National Science Academics Lecture Workshop on Non-Linear Dynamics, 26th-28th April 2011, at Tezpur University.
2. Contributed Oral presentation in the National Seminar on Photon and Quantum Structures, 4th -6th November, 2009 at Tezpur University.
3. Workshop on Recent Trends on Astronomy & Astrophysics, 21st- 23rd October, 2009 at Tezpur University.
4. Technical Session of Assam Science Society, February 4th, 2009 at Tezpur University.